



HAL
open science

Theoretical study of electronic and thermoelectric nanodevicesbased on strained graphene junctions

Mai Chung Nguyen

► **To cite this version:**

Mai Chung Nguyen. Theoretical study of electronic and thermoelectric nanodevicesbased on strained graphene junctions. Condensed Matter [cond-mat]. Université Paris Saclay (COMUE), 2016. English. NNT : 2016SACLS460 . tel-01553413

HAL Id: tel-01553413

<https://theses.hal.science/tel-01553413>

Submitted on 3 Jul 2017

HAL is a multi-disciplinary open access archive for the deposit and dissemination of scientific research documents, whether they are published or not. The documents may come from teaching and research institutions in France or abroad, or from public or private research centers.

L'archive ouverte pluridisciplinaire **HAL**, est destinée au dépôt et à la diffusion de documents scientifiques de niveau recherche, publiés ou non, émanant des établissements d'enseignement et de recherche français ou étrangers, des laboratoires publics ou privés.

NNT: 2016SACLS460

THÈSE DE DOCTORAT
DE
L'UNIVERSITÉ PARIS-SACLAY
PRÉPARÉE À
L'UNIVERSITÉ PARIS-SUD

ÉCOLE DOCTORALE 575 EOBÉ
Electrical, optical, bio-physics and engineering

Spécialité de doctorat: Physique

Par

Mme. Mai Chung NGUYEN

Etude théorique de nanodispositifs électroniques et thermoélectriques à base de jonctions contraintes de graphène

Thèse présentée et soutenue à Orsay, le 2 Décembre 2016:

Composition du Jury:

M. Henri HAPPY	Université de Lille 1, IEMN	Président
Mme. Mireille MOUIS	CNRS, IMEP-LAHC, Grenoble	Rapporteur
M. Nicolas CAVASSILAS	Université d'Aix-Marseille, IM2NP	Rapporteur
M. Viet Hung NGUYEN	IMCN, Université Catholique de Louvain	Examineur
M. Huy-Viet NGUYEN	Institute of Physics Hanoi	Co-directeur de thèse
M. Philippe DOLLFUS	CNRS, C2N, Orsay	Directeur de thèse

Acknowledgements

Firstly, I would like to express my sincere gratitude to my supervisors, Dr. Philippe DOLLFUS and Dr. HuyViet NGUYEN for their support, patience, motivation, and immense knowledge in all the time of study and writing of this thesis. I also express my deepest thanks to Dr. VietHung NGUYEN, who has ever kept a post-doc position in our group (COMICS), for his training, helping and sharing in research. To be honest, I am really very lucky to work with them. Without their guidance and encouragement, this work would have taken a longer time to complete.

Besides my advisors, I would like to take this opportunity to thank all my colleagues in COMICS group (Prof. Arnaud Bournel, Dr. Jerome Saint-Martin, Dr. Damien Querlioz, Dr. Michele Amato, Mr. Christophe Chassat, Dr. Tran Van Truong, Dr. Jerome Larroque, Dr. Thanayut Kaewmaraya, Mr. Jean Choukroun, Mr. Brice Davier, Ms. Li Su and others) for stimulating discussions, a friendly atmosphere and all the fun (we have) in life as well as in work.

My sincere thanks also goes to Universit Paris-Sud, Universit Paris-Saclay and CNRS (Centre National de la Recherche Scientifique), University Science and Technology of Hanoi (USTH) and Vietnamese government for the financial supports.

Last but not least, I would like to thank to my parents, my husband, my sisters and brothers for supporting and encouraging me spiritually throughout writing this thesis, without that this work could not finished on time.

Thank you very much, everyone!

Orsay, 23th August, 2016

MaiChung NGUYEN

Abstract

Due to its outstanding physical properties, graphene is expected to become a new generation material, able to replace or complement traditional semiconductors in device technology. Hence, many studies have been led to explore the potential of this material immediately after the successful fabrication of a single layer of graphene in 2004. However, applications of graphene in electronic devices are still questionable due to the gapless character of this material. In particular, regarding electronic applications, the absence of energy bandgap in the band structure makes it difficult to switch off the current in graphene devices like transistors. Regarding thermoelectric properties, the gapless character is also a strong drawback since it prevents the separation of the opposite contributions of electrons and holes to the Seebeck coefficient. Thus, a sizable bandgap in graphene is a requirement to overcome the disadvantages of graphene and to fully benefit from its excellent conduction properties. It has been shown that many nanostructuring techniques can be used to open such a bandgap in graphene, e.g., graphene nanoribbons, graphene bilayer with a perpendicular electric field, graphene nanomesh lattices, channels based on vertical stack of graphene layers, mixed graphene/hexagonal boron nitride structures, nitrogen doped graphene, and so on. However, each of these methods has its own fabrication issues and/or need to be further confirmed by experiments. In this work, we focus on strain engineering, which offers a wide range of opportunities for modulating the electronic properties of graphene nanostructures. For this theoretical work, all calculations were performed using essentially two main methods, i.e., an atomistic tight binding Hamiltonian model to describe the electronic structure and the non-equilibrium Green's function approach of quantum transport. The main aim is to analyze in details the strain effects in graphene and to provide strategies of strain engineering to improve the performance of both electronic (transistors and diodes) and thermoelectric devices.

After introducing the general context of this work and the numerical techniques developed for this purpose, we first analyze the only effect of strain. Actually, if uniformly applied, a strain of large amplitude ($> 23\%$) is required to open a bandgap in the band structure of graphene. However, we show that with a strain of only a few percent, the strain-induced shift of the Dirac point in k-space may be enough to open a sizable conduction gap (500 meV or more) in graphene heterojunctions made of unstrained/strained junctions, though the strained material remains gapless. After analyzing in details this property according to the amplitude and direction of strain and the direction of transport, we exploit this effect using appropriate strain junctions to improve the behavior and performance of several types of devices. In particular, we show that with a strain of only 5%, it is possible to switch-off transistors efficiently, so that the ON/OFF current ratio can reach 10^5 , which is a strong improvement with respect to pristine graphene transistors where this ratio cannot exceed 10. Then we show that by combining strain and doping engineering in such strain junctions the Seebeck coefficient can reach values higher than 1.4 mV/K, which is 17 times higher than in gapless pristine graphene. It can contribute to make graphene an excellent thermoelectric material. Finally, we study the effect of negative differential conductance (NDC) in graphene diodes made of either as single gate-induced strained barrier or a p-n junction. We show that appropriate strain engineering in these devices can lead to very strong NDC effects with peak-to-valley ratios of a few hundred at room temperature.

Contents

Résumé	1
Introduction	8
1 OVERVIEW	12
Part I Properties of graphene and strain effects	14
1.1 Graphene material	14
1.2 Strain Engineering	17
1.2.1 Uniform Strain	18
1.2.2 Local Strain	18
1.3 General theory of stress and strain	19
1.3.1 Stress tensor	20
1.3.2 Strain tensor	21
1.3.3 The relationship between stress and strain	23
1.4 Effect of strain on the electronic properties of materials	25
1.5 Experimental techniques to generate strain in graphene	27
1.6 Conclusions	31
Part II Numerical techniques	33
1.7 Tight-binding method	33
1.7.1 Secular equations	34
1.7.2 Tight-binding calculations for carbon structures	36
1.8 Non-equilibrium Green's function technique	41
1.8.1 Basic equations	41
1.8.1.1 Transmission	42

1.8.1.2	Density of states (DOS) and local density of states (LDOS)	43
1.8.1.3	Electric current	44
1.8.1.4	Conductance	45
1.8.2	Numerical techniques for Green's function calculation	45
1.8.2.1	Calculation of the self energy	45
1.8.2.2	Device Green's function calculation	52
1.9	Conclusions	53

2 ELECTRONIC PROPERTIES OF STRAINED GRAPHENE JUNCTIONS **54**

2.1	Introduction	54
2.2	Electronic properties of graphene nanostructures	55
2.2.1	Monolayer graphene	55
2.2.2	Graphene nanoribbon structures	59
2.2.3	Bilayer graphene	62
2.2.4	Graphene nanomesh	64
2.3	Electronic properties of strained graphene	71
2.3.1	Basic equations	72
2.3.2	Opening of bandgap under large strain	77
2.3.3	The shift of Dirac point by a small strain of a few percent	80
2.4	Opening of a conduction gap (transport gap) in strained graphene junctions	81
2.4.1	The opening of conduction gap with strain of a few percent	82
2.4.2	The dependence of conduction gap on strain amplitude (σ), direction of applied strain (θ) and transport direction (ϕ) in both of tensile and compressive cases	85
2.4.2.1	Armchair transport direction ($\phi = 0$)	85
2.4.2.2	Zigzag transport direction ($\phi = 30^\circ$)	87
2.4.2.3	Any transport direction ($0 < \phi < 30^\circ$)	88
2.4.2.4	Compressive and tensile-strained graphene junctions	91
2.5	Conclusion	94

3 APPLICATION OF STRAINED JUNCTIONS IN GRAPHENE HETEROCHANNELS	95
3.1 Introduction	95
3.2 Improved performance of graphene transistors	96
3.2.1 Field-effect transistor (FET)	97
3.2.2 Different types of graphene transistors	99
3.2.3 A high ON/OFF ratio in strained graphene transistor	101
3.3 Enhanced thermoelectric effect	104
3.3.1 What is the thermoelectric effect?	105
3.3.2 The Seebeck effect in monolayer and bilayer graphene, graphene nanoribbons and graphene nanomesh	107
3.3.3 The enhancement of Seebeck effect in graphene heterochannels by strain and doping engineering	110
3.3.3.1 Strained device with uniform doping ($\Delta U = 0$)	112
3.3.3.2 Strained device with both strain and doping engineering ($\Delta U \neq 0$)	113
3.3.3.3 Strained device with large doping	116
3.4 Enhanced negative differential conductance (NDC) effect	119
3.4.1 What is the NDC effect?	119
3.4.2 Enhanced NDC effect in strained graphene channels	121
3.4.2.1 Enhanced NDC effect in single potential barrier structure	123
3.4.2.2 Enhanced NDC effect in PN junction	128
3.5 Conclusion	133
Summary and perspectives	134
A The relationship between the bond lengths in cases of (σ, θ) and $(-\sigma, \theta + 90^\circ)$	137
B The equation of transmission	139
Bibliography	143

Résumé

Le graphène, une couche unique d'atomes de carbone disposés en nid d'abeille possède de nombreuses caractéristiques fascinantes. On en attend qu'il devienne un matériau d'avenir, susceptible de remplacer ou compléter des matériaux conventionnels. Tout d'abord, il faut dire que le graphène offre de nombreux avantages tels que la haute mobilité des porteurs et la haute conductivité thermique, qui laissent espérer des applications prometteuses dans le domaine électronique. En outre, l'inconvénient du graphène lié à l'absence de bande interdite dans sa structure de bande peut être surmonté de nombreuses façons: découpage de nanorubans de graphène, bicouche de graphène avec application d'un champ électrique transverse, percement d'un réseau périodique de nano-trous (nanomesh), structures mixtes de graphène et de nitrure de bore, dopage du graphène à l'azote. À présent, le graphène est considéré comme l'un des matériaux les plus étudiés avec un nombre gigantesque de publications au cours de ces 10 dernières années.

En comparaison avec des matériaux conventionnels, le graphène est bien connu pour ses caractéristiques extraordinaires. Cependant, dans ce travail, nous nous concentrons sur ses propriétés mécaniques, c'est-à-dire la flexibilité de ce matériau avec une haute résistance à la déformation qui peut être exploitée pour moduler ses propriétés électroniques. Au moyen d'ingénierie de contrainte, nous proposons des canaux de graphène combinant sections contraintes et non-contraintes. Il est à noter que tous les calculs ont été effectués en utilisant essentiellement deux méthodes, à savoir, un modèle d'Hamiltonien atomistique de liaisons fortes liaison pour décrire la structure électronique et l'approche des fonctions de Green hors-équilibre du transport quantique. L'objectif principal est d'analyser en détail les effets de déformation dans le graphène et de fournir des stratégies d'ingénierie de la contrainte pour améliorer les performances de dispositifs électroniques (transistors et diodes) et de dispositifs thermoélectriques (coefficient Seebeck).

En fait, ce projet de thèse a été établi dans le cadre d'une collaboration entre l'Institut de Physique (IoP - VAST, Hanoi, Vietnam) et l'Institut d'Électronique

Fondamentale (IEF, CNRS, Université Paris Sud, France) dans le but de développer des outils théoriques efficaces pour étudier le transport électronique et les effets thermoélectriques dans des hétérostructures de graphène contraintes. Il s'agit également d'étudier en détail les effets de contrainte sur les propriétés électroniques et d'en déduire des propositions de dispositifs performants pour des applications électroniques et thermoélectriques.

Dans le détail, la thèse est présentée dans quatre chapitres et deux annexes. Son contenu est organisé comme suit:

Le chapitre 1 présente les bases nécessaires et le contexte de l'étude avec deux parties principales: La première est une introduction élémentaire du graphène, et plus particulièrement de ses propriétés mécaniques. Ensuite, nous présentons des techniques d'ingénierie de contrainte à la fois uniforme (globale) et locale. Une contrainte uniforme couvre l'ensemble du substrat. Une contrainte locale peut être obtenue dans un semiconducteur standard par "shallow trench-isolation" des couches épitaxiales et/ou par dépôt de couches de nitrure fortement contraintes. Puis, nous discutons des effets de déformation sur les propriétés électroniques des matériaux, en particulier du graphène. En principe, la contrainte peut modifier la structure de bandes qui décrit les états d'énergie dans l'espace du moment cristallin entre les électrons et les trous, ce qui peut conduire à des changements profonds des propriétés électronique du matériau. Dans le graphène, la contrainte induit également le déplacement du point de Dirac dans l'espace réciproque. Par conséquent, l'ingénierie de la contrainte a été proposée comme une approche alternative pour surmonter l'absence de bande interdite dans sa structure de bande. Dans cette partie, nous mentionnons également quelques techniques pour créer expérimentalement une contrainte locale dans le graphène, avec en particulier un travail extraordinaire de Ji-Li et al.. Ce travail propose un processus basé sur la pression de choc induit par laser pour générer une déformation locale dans la feuille de graphène. Plus intéressant encore, la longueur de canal de la plupart de nos dispositifs varie de quelques dizaines à une centaine de nm, de sorte que l'étude de Ji-Li et al (également d'autres groupes tels que cités dans les références) est considéré comme une validation de la notion de contrainte locale dans le graphène, ce qui rend réalistes les concepts de dispositifs développés dans notre travail. La deuxième partie introduit les techniques numériques développées et utilisées dans notre travail. En particulier, nous présentons en détail le modèle de liaison forte pour décrire les états de charge du réseau de graphène et l'approche des fonctions de Green hors-équilibre (NEGF) pour examiner les propriétés de transport dans les dispositifs à l'échelle nanométrique. Le modèle de liaisons

fortes est le plus souvent utilisés pour décrire les états de charge dans les structures de graphène et permet d'explorer les caractéristiques importantes telles que la structure électronique et les phénomènes de transport. En comparaison avec les calculs ab initio, le modèle de liaisons fortes est plus simple, et permet des calculs beaucoup plus rapides. Pour examiner les propriétés de transport dans les dispositifs nanométriques, l'approche NEGF combinée à un hamiltonien de liaisons fortes s'est avérée être une méthode très efficace. Elle est adaptée à des simulations de transport quantique tenant compte des effets de couplage à des contacts, des défauts, impuretés, phonons, etc. De plus, l'approche de NEGF a démontré son utilité pour la simulation de transistors à l'échelle nanométrique, tels que MOSFETs Si conventionnels, FETs à nanotubes de carbone et transistors moléculaires. Quelques aspects principaux de ces techniques sont donnés comme suit.

Dans la méthode des liaisons fortes, les énergies propres de l'électron $E_i(\vec{k})$ sont obtenues en résolvant l'équation séculaire. En appliquant cette technique au graphène, nous obtenons une expression de la structure de bandes donnée par

$$E_{g2D}(\vec{k}) = \frac{\epsilon_{2p} \pm t\omega(\vec{k})}{1 \pm s\omega(\vec{k})} \quad (1)$$

où les signes + dans le numérateur et le dénominateur vont donner la bande π de l'état liant, et de même pour les signes -, qui donnent l'a bande π^* de l'état anti-liant. La fonction $\omega(\vec{k})$ est donnée par

$$\omega(\vec{k}) = \sqrt{3 + 2\cos(\sqrt{3}k_y a) + 4\cos(\frac{\sqrt{3}}{2}k_y a)\cos(\frac{3}{2}k_x a)} \quad (2)$$

Ici, les trois paramètres ϵ_{2p} , t et s sont fournis soit par l'expérience soit par des calculs ab initio. La pratique la plus courante consiste à ajuster le modèle de liaisons fortes à une description correcte des bandes π au point K . Cela donne $\epsilon_{2p} = 0$, t entre -2,5 et -3,0 eV, et s en dessous de 0,1. Comme s est petit, il est habituellement négligé. Nous



Figure 1: Modèle général du transistor à effet de champ avec un canal central connecté aux contacts de source et de drain et contrôlé par une grille.

considérons l'application de la méthode de la fonction de Green dans des dispositifs à l'échelle nanométrique. Une structure schématique d'un dispositif simulé typique est représentée sur la Fig. 1. En principe, il comprend trois parties principales: un canal (zone active), les contacts (gauche et droite, ou source et drain) et une électrode de grille. La fonction de Green de la région active est maintenant

$$G_D = (E - H_D - \Sigma_L - \Sigma_R)^{-1} \quad (3)$$

où H_D est le hamiltonien de la région active. $\Sigma_{L(R)}$ est la self-énergie du contact de gauche (droite) et est déterminé par

$$\Sigma_{L(R)}^s = H_{DL(R)} g_{0(N)}^{L(R)} H_{L(R)D} \quad (4)$$

où H_{DL} (H_{LD}) est le hamiltonien décrivant le couplage entre le dispositif et le contact et $g_{0(N)}^{L(R)}$ est la fonction de Green de surface du contact de gauche (droite).

En régime de transport balistique, la transmission du système peut être calculé par la fonction de Green

$$T = \text{trace}[\Gamma_L G_D \Gamma_R G_D^\dagger] \quad (5)$$

où $\Gamma_{L(R)} = i[\Sigma_{L(R)} - \Sigma_{L(R)}^\dagger]$ est l'élargissement du niveau d'énergie à gauche (droite) contact.

Il est à noter qu'une fois la transmission obtenue, d'autres quantités de transport peuvent également être calculées, à savoir, le courant, la conductance, le coefficient Seebeck, etc.

Le chapitre 2 commence par l'introduction de certaines techniques pour remédier à l'inconvénient majeur du graphène lié qu'est l'absence de bande interdite dans sa structure de bandes. Nous passons en revue les caractéristiques et les propriétés électroniques du graphène monocouche et ses nanostructures à fort bandgap, à savoir, nanorubans de graphène, bicouche de graphène sous champ électrique transverse et graphène nanomesh. Ensuite, ce travail se concentre sur l'utilisation de l'ingénierie de contrainte comme une technique alternative pour modifier la structure de la bandes du graphène. En fait, une forte contrainte ($\gtrsim 23\%$) peut ouvrir une bande interdite dans le graphène, mais cela représente un défi expérimental. Par conséquent, ce travail suggère l'utilisation astucieuse de petites déformations, à savoir, seulement quelques pour cent. Une faible contrainte suffit en effet à provoquer le déplacement de points de Dirac dans l'espace des k , ce qui peut conduire à des modifications importantes des propriétés de transport électronique dans une jonction graphène contraint / graphène non-contraint. On montre qu'un gap de conduction ou de transport de

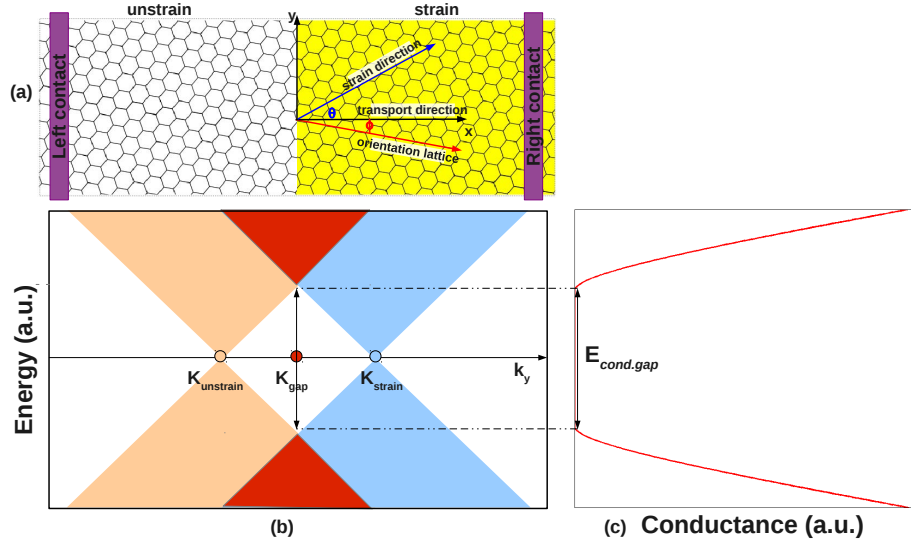


Figure 2: (a) Jonctions de graphène contraint/non-contraint. (b) Structure des bords de bandes illustrant le changement induit par déplacement des points Dirac le long de la direction k_y qui mène à l'ouverture d'un gap de conduction (c).

quelques centaines de meV peut s'ouvrir dans de telles structures, comme on le voit sur la Fig. 2. Par ailleurs, le gap de conduction dépend de manière significative de l'amplitude de la contrainte, de sa direction et de l'orientation du réseau, aussi bien pour une tension que pour une compression.

Le chapitre 3 est une étude des potentialités de ces hétérojonctions contraintes pour la conception de dispositifs électroniques. Nous nous concentrons d'abord sur des transistors avec un canal de graphène contraint. Ce travail a été principalement mené par V. H. Nguyen *et al*, et nous en présentons les principaux résultats. Il a été démontré que l'utilisation d'une hétérostructure faiblement contrainte (5%) peut grandement améliorer les performances d'un FET de graphène avec un fort rapport de courant ON/OFF de et une bonne saturation du courant. En effet, un gap de conduction de 360 meV peut être obtenu avec une contrainte de seulement 5% et une valeur plus élevée peut même être obtenue avec une plus grande contrainte. Ce gap est la clé importante menant à la possibilité de couper le courant et donc d'atteindre un rapport ON/OFF élevé, typiquement 10^5 pour $V_{gs} = 0.35V$. Ensuite, nous continuons l'étude en examinant la possibilité d'améliorer la pouvoir thermoélectrique (coefficient de Seebeck) dans des dispositifs de graphène par l'ingénierie de contrainte et de dopage. On voit que, si une contrainte locale peut entraîner le désalignement des cônes de Dirac dans l'espace des k - entre les sections de graphène contraintes et non-contraintes, l'ingénierie de dopage conduit à leur déplacement en énergie. Par

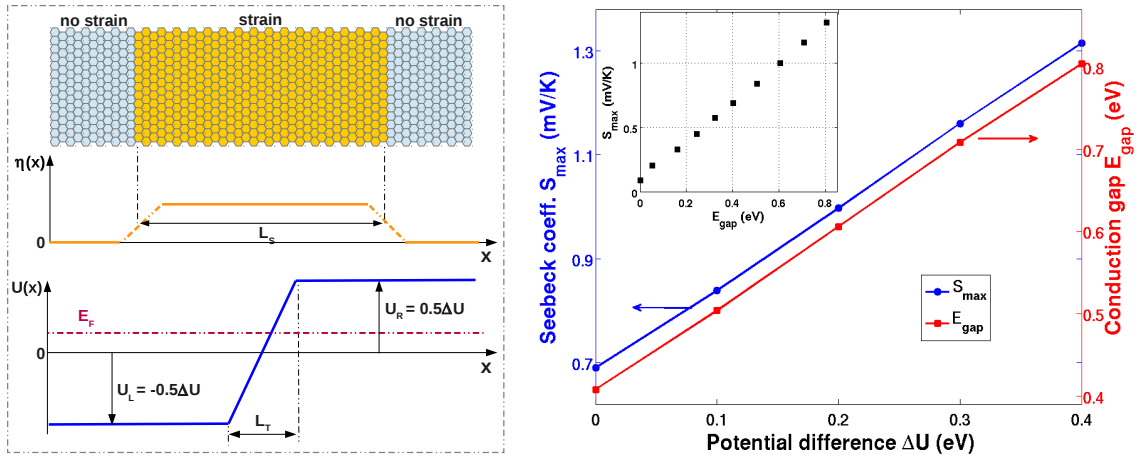


Figure 3: Vue schématique de la structure de graphène constituée d'une diode PN avec une zone contrainte localement (a) et coefficient Seebeck maximal (S_{\max}) et gap de conduction (E_{gap}) en fonction de ΔU (b).

la combinaison de ces deux effets, nous démontrons que le gap de conduction aussi élevé que quelques centaines de meV peut être atteint, ce qui permet d'atteindre des valeurs de coefficient Seebeck supérieures à 1.4 mV / K, comme on peut le voir en Fig. 3. En comparaison, cette valeur est 17 fois plus élevée que dans le graphène pristine sans gap. Dans la dernière partie de ce chapitre 3, nous montrons que ces effets de contrainte locale peuvent être exploités afin de générer une forte conductance différentielle négative (NDC) dans des structures à simple barrière (induite par une grille) et dans des jonctions tunnel p-n, comme on le voit sur la Fig. 4. Lorsque la déformation locale est appliquée de façon appropriée, le rapport de courant pic / vallée (PVR) peut atteindre quelques centaines. En outre, la dépendance de l'effet NDC en fonction des paramètres de la structure est étudiée systématiquement. En particulier, une forte NDC est obtenue dans les structures à simple barrière avec une grande région contrainte, tandis que le PVR n'est pas très sensible à la longueur de transition dans les jonctions p-n.

Le chapitre 4 conclut le travail de thèse en résumant les principales contributions de l'étude, et mentionne certains travaux qui restent à réaliser dans la continuité de celui-ci, à savoir, prendre en compte des effets de la direction du réseau, de la déformation de cisaillement et de la déformation de cisaillement pur.

La liste des références ainsi que les publications de l'auteure relatives à ces travaux sont données ensuite.

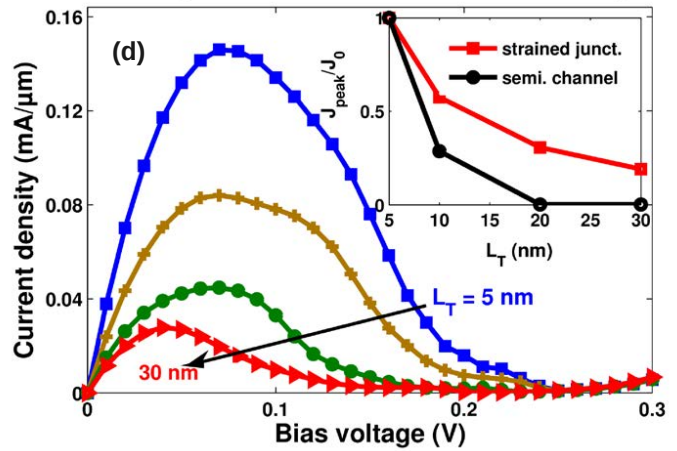
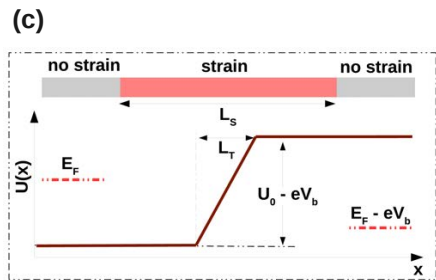
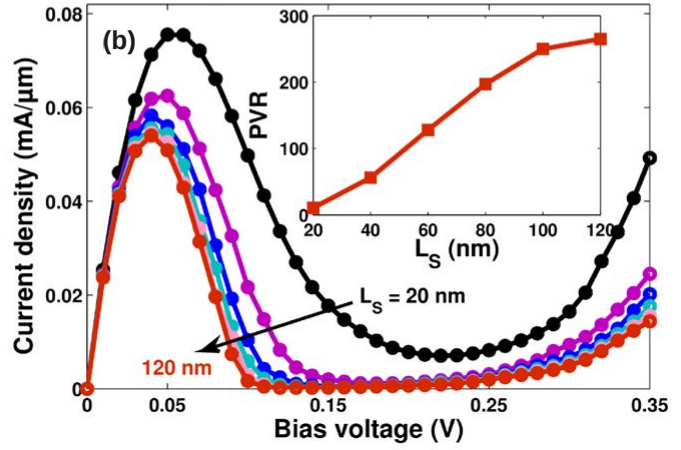
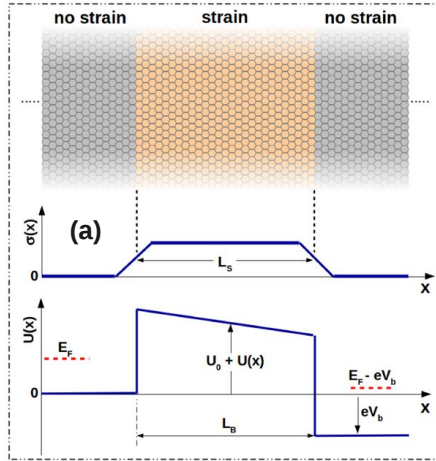


Figure 4: Représentation schématique des structures à simple barrière (a) et caractéristiques à $I - V$ correspondantes calculées pour différentes longueurs L_S de la région contrainte (b). Structure des jonctions tunnel p-n (c) et caractéristiques $I - V$ correspondantes du dispositif pour différentes longueurs de transition L_T (d).

Introduction

Graphene, a single layer of carbon atom arranged in a honeycomb lattice has many fascinating properties and is considered as a very promising new material likely to replace conventional materials. First, it should be mentioned that graphene offers many advantages such as high carrier mobility, high thermal conductivity and ability to sustain large strain, which makes it suitable for many applications. Additionally, the drawback of graphene related to its gapless character can be overcome by many ways in lots of nanostructures of this material such as graphene nanoribbons, bilayer graphene under vertical electric field, graphene nanomesh, graphene/hexagonal boron nitride, nitrogen-doped graphene, and etc. Until now, graphene is one of the most studied materials from both theoretical and experimental viewpoints with a huge number of publications in only one decade.

Compared with conventional materials, graphene benefits from lots of outstanding properties. However, in this work, we focus on the mechanical properties of graphene and the use of strain engineering to overcome its gapless disadvantage. The motivation came from many theoretical and experimental studies which investigated the possibility and usefulness of strain engineering to modify the electronic structure of semiconducting materials. Moreover, this technique has been proposed as an alternative approach to open a bandgap in graphene. In this PhD work, we mainly design and study graphene channels made of unstrained/strained graphene junctions. We use the tight binding (TB) model to describe charge states in graphene structures and devices. In fact, this approach is used most extensively in condensed matter physics and it allows us to simulate the important characteristics such as electronic structure and properties of lots of graphene structures. Besides, we apply the atomistic non-equilibrium Green's function (NEGF) approach for studying quantum transport, which has been proved to be very efficient in the field of nanodevice simulation.

In fact, this Ph.D project has been established in the frame of collaboration between the Institute of Physics (IoP - VAST, Hanoi, Vietnam) and the Institute of Electronic Fundamental (IEF - CNRS, University Paris Sud, France) (whose new

name is Centre for Nanoscience and Nanotechnology, C2N) with the aim of developing efficient theoretical tools to study the electronic transport and thermoelectric effects in strained graphene heterostructures.

In detail, the manuscript is presented in three chapters, a conclusion and two appendices, with content organized as follows:

In Chapter 1 we present the necessary background in two main parts. In the first one, we introduce the main features of graphene with a special emphasis on the mechanical properties. Next, we present some strain engineering technologies to generate both uniform (global) and local strain types. The former one, uniform strain, is identified as the case where stress covers the entire substrate area while the latter, i.e. the local strain corresponds to the case where stress is engineered on a limited area of the device by means, e.g., of shallow-trench-isolation, epitaxial layers and/or highly stressed nitride capping layers. Then, we discuss about the strain effect on the general electronic properties in semiconductor materials, especially in graphene. In principle, strain can modify the band structure, i.e., the energy state of carrier in the crystal momentum space, which leads to changes in the electronic properties of the materials. In graphene, strain especially induces a shift of Dirac points in k -space. Hence, strain engineering has been proposed as an alternative approach to overcome the gapless character of this material. In this part, we also mention some experimental techniques to create uniform as well as local strain, and we emphasize the work of Ji-Li et al. who have reported a scalable manufacturing process to generate three-dimensional (3D) nanostructures by laser-induced shock pressure and thus induce local strain in the graphene sheet. Interestingly, the size of the resulting strain area is similar to the channel length of the devices proposed in the present work. It makes realistic the device designs investigated in this work.

The second part introduces the numerical techniques used in our work. In particular, we present in detail the tight binding model used to describe the charge states of graphene lattice and the non equilibrium Green's (NEGF) function approach applied to consider the transport properties in nanoscale devices. The tight binding model is more simple and much faster than the ab initio calculations and much more appropriate to treat large devices with some thousands atoms. To consider the transport properties in nanoscale devices, the NEGF approach combined with a TB Hamiltonian has been proven to be a very efficient method. It is suitable for quantum transport simulations, taking into account effects of coupling to contacts, defects, impurities, phonons, etc. Additionally, the NEGF approach has demonstrated its

usefulness for simulating nanoscale transistors, from conventional Si MOSFETs to carbon nanotube FETs and molecular transistors.

In Chapter 2 we start with the introduction of some techniques to overcome the drawback of graphene related to its gapless character. To show this clearly, we review the properties of graphene and its nanostructures with sizable bandgap, i.e., graphene nanoribbons, bilayer graphene under vertical electric field and graphene nanomesh. Then, we focus on the use of strain engineering as an alternative technique to modify the band structure of graphene. It is shown that a large strain ($\gtrsim 23\%$) can open a bandgap in pristine graphene, but achieving experimentally such a strain level is a big challenge. Instead, this work suggests the appropriate use of small local strain, i.e., of only a few percent. We see that though a small strain cannot change graphene's gapless character, it causes the shift of Dirac points in k-space which may lead to dramatic changes of electronic transport features. In particular, in unstrained/strained graphene junctions, a conduction gap or transport gap, that is defined as a finite gap of conductance, can be opened. In this work, based on a tight binding model, we suggest two methods to evaluate and describe the conduction gap, i.e., from Green's function calculations and from bandstructure analysis, respectively. We study in details the dependence of conduction gap on strain amplitude, strain direction and transport direction in both cases of tensile and compressive strain.

In Chapter 3 we study some possibilities of using strained graphene junctions to design the channel of electronic devices. We focus first on transistor with strained channel. Our study shows that a strain of only a few percent can improve significantly the performance of graphene transistors. In particular, the ON/OFF current ratio increases strongly to over 10^5 for a strain of 5%. Then, we find that the combination of strain and doping engineering can lead to a conduction gap of a few hundreds meV in strain junctions. As a consequence, the Seebeck coefficient can reach a value higher than 1.4 mV/k in doped graphene junctions by applying a local strain. Finally, we demonstrate that strain can strongly enhance negative differential conductance (NDC) in two types of diodes. This effect is shown in single gate-induced barrier structure and in p-n junctions. It results in high peak-to-valley ratio (PVR) in the I-V characteristics. The dependence of NDC effect on structure parameters the is investigated systematically in this chapter.

A conclusion briefly closes the manuscript by summarizing the main contributions, and mentioning some works that can be further performed. It is for instance suggested to analyze in details the effects of transport direction, shear strain and pure shear

strain. Two appendices, the bibliography and the list of author's publications can be found at the end of the manuscript.

Chapter 1

OVERVIEW

In this chapter, we introduce two main parts related to the material, the engineering as well as the numerical methods used for this PhD work. Therefore, it is organized as follows. In the first part, the first section 1.1 is a review of graphene material regarding its main properties and application abilities. The section 1.2 is an introduction to strain engineering, including the two main forms: uniform strain and local strain. In the section 1.3, we summarize some basic knowledge of the stress/strain theory. The effect of strain on the electric properties of materials (section 1.4) and the experimental techniques to generate strain in graphene (section 1.5) are the subject of very important sections, related directly to the relevance of this work. In, the second part of this chapter, we present the numerical techniques related to the two main methods developed and used in this work, i.e., the tight binding and Green's function formalisms, respectively, which have been demonstrated to be good approaches to investigate the properties of graphene and its nanostructures.

Part I. Properties of graphene and strain effects

1.1 Graphene material

Graphene, experimentally isolated in 2004 by Novoselov *et al* [1], is a single two-dimensional (2D) sheet of carbon atoms arranged in a honeycomb lattice. The technique to obtain such a layer is really simple. It consists of rubbing highly oriented pyrolytic graphite against another surface (like using a pencil). This leaves a variety of flakes on the surface. Most of these flaky materials are composed of more than ten layers, but surprisingly, a single layer flake can result from this technique. In fact, some basic allotropes of carbon atoms have been identified and studied, such as carbon nanotubes, graphite as well as fullerenes, as shown in Fig. 1.1. Actually, carbon nanotubes can be seen as rolled-up sheets of graphene, graphite comes from stacks of many graphene layers weakly coupled by Van der Waals forces and fullerenes (C_{60}) are molecules consisting of wrapped graphene. In comparison, graphene is known as a very attractive material with many superlatives associated with its properties. It is known as the thinnest material in the universe and, mechanically, the strongest ever tested [2]. Its low-energy carriers offer giant intrinsic mobility, have zero effective mass, and can travel for micrometers without scattering at room temperature. The charge transport in graphene can be described by a Dirac-like equation, which allows for the investigation of relativistic quantum phenomena in experiment. Therefore, graphene rapidly become a hot topic of many researchers in experiment and theory as well as researchers in device applications (see in reviews [1, 2, 3, 4] and references therein).

Further, among systems of only carbon atoms, graphene has many interesting properties originated from the very specific conical shape of electronic bandstructure, in particular, at the six edge corner points (often named the Dirac points or K, K' -points) of the hexagonal Brillouin zone. The low energy particles around these points are massless, chiral and Dirac fermions. This particular dispersion mimics the physics of quantum electrodynamics (QED) for massless fermions except for the fact that the Dirac fermions in graphene move with a speed v_F , which is about 300 times smaller than the speed of light c . Hence, many unusual properties of QED can be seen in graphene but at much smaller speeds [5, 6]. Dirac fermions behave in unusual ways when compared to ordinary electrons if subjected to magnetic fields, leading to new physical phenomena [7] such as the anomalous integer quantum Hall effect (IQHE) measured experimentally [8]. Besides being qualitatively different from the IQHE observed in Si and GaAlAs (heterostructures) devices, the IQHE in graphene can be

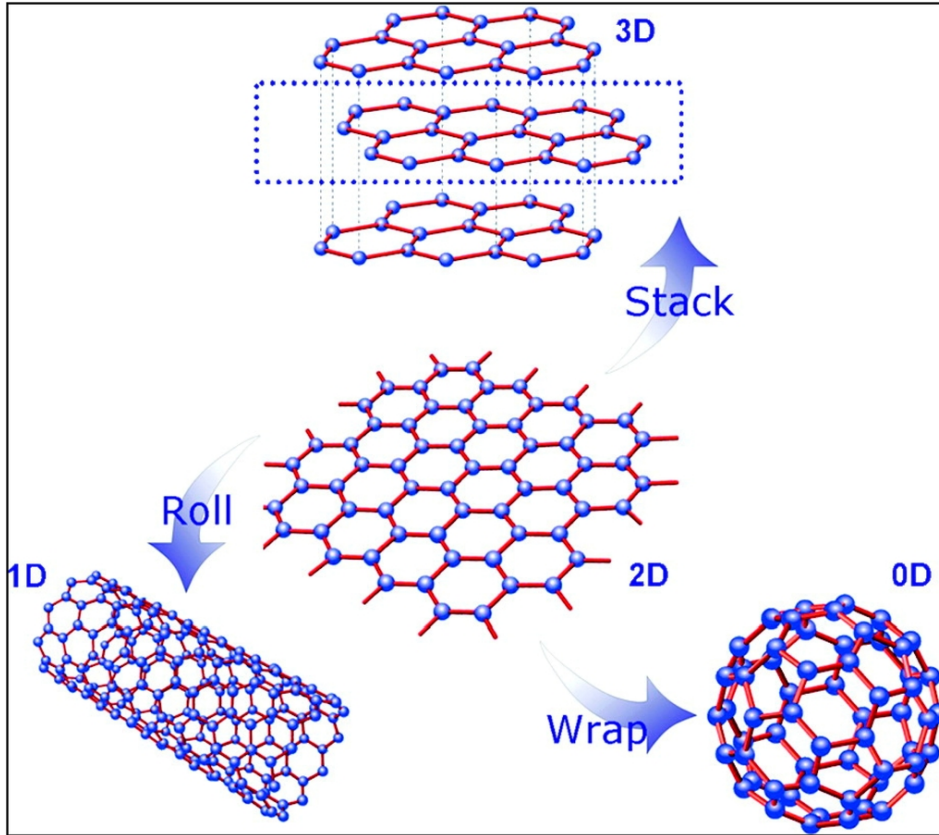


Figure 1.1: Graphene: mother of all graphitic forms. It is a $2D$ building element for carbon material of all other dimensionalities, i.e., it can be stacked into $3D$ graphite, rolled into $1D$ nanotubes or wrapped up into $0D$ buckyballs (fullerenes C_{60}). From X. Wan *et al.* [4]

observed at room temperature because of the large cyclotron energies for "relativistic" charges [9].

Another interesting feature observed in graphene structure is the Klein tunneling of relativistic-like particles through potential barrier [6, 10]. This phenomenon is characterized by the fact that Dirac fermions can be transmitted with probability 1 through a barrier having any height and width. That manifestation is called the Klein's paradox and it strongly contrasts to the conventional and non-relativistic tunneling processes where the transmission probability decays exponentially with increasing the barrier height. This relativistic effect can be attributed to the fact that a sufficiently strong potential, being repulsive for electrons, is attractive for holes and results in states inside the barrier, which align in energy with the electron continuum outside. Essentially, good matching between electron and hole wave-functions across the barrier can result in high tunneling probability [11]. In the framework of the

QED, the reason this feature can be realized is that states at positive (electrons) and negative (holes) energies are intimately linked (conjugated), being described by two different components of the same spinor wave-function. This fundamental property of Dirac fermions is often referred to as the charge conjugation symmetry.

After the success of experiments and by lots of special properties as mentioned above, graphene became indeed a material of choice for numerous researchers, which is illustrated by the dramatic increase of the number of publications on graphene (according to ISI Web of KnowledgeSM), as shown in Fig. 1.2. As a result, the Nobel Prize in 2010 was awarded to Andre Geim and Konstantin Novoselov for groundbreaking experiments regarding the two-dimensional material graphene.

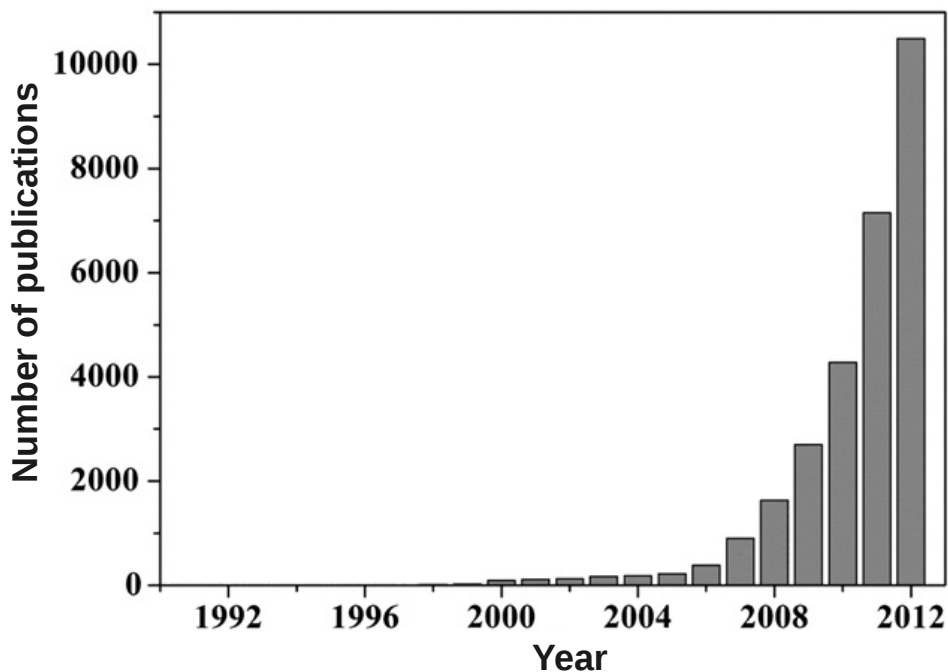


Figure 1.2: Number of publications on graphene [12].

Graphene, of course, offers a wide range of potential applications due to its excellent mechanical, electrical, thermal, optical properties and its large surface-to-weight ratio, e.g., 1 g of graphene can cover several football fields [13, 14]. Moreover, these properties suggest that graphene could replace other materials in existing applications. In this work, we exploit deeply the mechanical properties of graphene and especially explore their influence on electronic properties.

The first systematic experimental analysis of elastic properties and strength exhibited by monolayer graphene has been reported by C. Lee *et al* [15]. It was experimentally found that graphene shows both non-linear elastic behavior and brittle

fracture. The non-linear elastic response of graphene to tensile load is described as:

$$\sigma = E\epsilon + D\epsilon^2 \quad (1.1)$$

where σ , ϵ , E and D are the applied stress, the elastic strain, the Young modulus, and the third-order elastic stiffness, respectively. These parameters will be detailed in next sections.

In the experiment of C. Lee *et al* [15], the value of Young modulus E has been found to be extremely large and close to that of carbon nanotubes, i.e., $E = 1.0TPa$. Besides, brittle fracture of graphene occurs at a critical stress equal to its intrinsic strength of $\sigma = 130GPa$ [15]. This value is the highest ever measured for any materials.

The discussed experimental data on the Young modulus ($E = 1TPa$) and the intrinsic strength ($\sigma = 130GPa$) exhibited by pristine graphene are consistent with computer simulations [16] showing values of $E = 1.05TPa$ and $\sigma = 110GPa$. The extremely large values of E and σ make graphene to be very attractive for mechanical applications because it can be easily bent.

1.2 Strain Engineering

It is shown that the semiconductor industry is always facing lots of critical challenges such as the high gate leakage current for very thin gate dielectrics, the difficulty to maintain a high I_{on}/I_{off} ratio, short channel effects, and the high power dissipation for small transistors. Innovative techniques such as strain engineering have to be used to solve or circumvent the arising problems. It is widely believed that strain engineering takes a key position among other technological changes for the next technology nodes after 90, 65, and 45 nm technology nodes. The studies of the influence of strain on the intrinsic mobility of Si was first investigated in the early 1950s [17, 18]. In 1992, it was first demonstrated that n-channel MOSFETs on a strained Si substrate, exhibit a 70% higher effective mobility than those on unstrained substrates [19]. Ever since semiconductor industry has adopted several different technologies to introduce strain in the Si channel of MOSFETs.

Generally, two approaches for introducing strain in MOSFETs can be identified: a uniform (global) one, where stress is introduced/covered across the entire substrate, and a local approach, where stress is engineered into the device by means of shallow-trench-isolation, epitaxial layers and/or highly stressed nitride capping layers.

1.2.1 Uniform Strain

Uniform (global) strain engineering that uses strained semiconductor-on-insulator as the starting material is a promising method for future technology nodes and is compatible with thin-channel device processing. It is shown that some studies have ever worked on strained *Si* focused on biaxial global strain generated by epitaxy of a thin strained *Si* layer on a thick relaxed *SiGe* virtual substrate [19]. In these works, due to the lattice mismatch between *Si* and *SiGe*, the lattice of the *Si* layer is biaxially tensile strained in the plane of the interface. In particular, on [001] oriented substrates this deformation results in enhanced carrier transport in the strained *Si* layer, and mobility enhancements of 110% for electrons and 45% for holes have been demonstrated on sub-100 nm strained *Si* MOSFETs [20].

Besides, using layer transfer and wafer bonding techniques, uniform strain can also be integrated in *Si* on insulator substrate. Electron and hole mobility enhancement comparable with the enhancement of wafers without the insulating layer were observed in ultra-thin strain *Si* layers on *SiGe* in insulator [21, 22] and strained *Si* layer directly on insulator. Technologies using ultra thin strained *Si* directly on insulator are especially promising, since in those structures the *SiGe* layer is eliminated before transistor fabrication, hence critical process-integration problems related to *SiGe* layer can be avoided. However, a major drawback common to all uniform strain techniques for CMOS technology is that they can provide only one type of strain. Since the mobilities of electrons and holes are differently affected by strain, a uniform strain configuration, for example, compressive biaxial strain, can be beneficial for p-channel MOSFETs, but deteriorates the n-channel MOSFETs performance. This problem is circumvented by local strain techniques, which are able to provide different strain patterns for n-channel and p-channel MOSFETs.

1.2.2 Local Strain

Several process-induced local stress techniques, such as (i) the contact etch stop liner technique (CESL), (ii) the stress memorization technique (SMT), (iii) a technique based on selective epitaxial growth (SEG) of the source/drain regions, and (iv) stress from shallow trench isolation (STI), were introduced in mass production of integrated circuit [23]. It is well known that the favorable strain configuration for short channel drive current increase is uniaxial tensile and compressive strain for nFETs and pFETs, respectively. Unlike biaxial strain, under uniaxial strain the effective transport mass is modulated. Hence the performance enhancement is maintained even at

short channel or under high carrier confinement [23]. Moreover, various CMOS fabrication processes can be exploited to induce strain in the transistor channel. Since these processes generate local strain that depends on the position in the MOSFET channel, techniques based on process-induced strain are frequently called local strain techniques. Starting from the late 1990's effects related to local stress arising from various process steps on the performance of MOSFETs were investigated. It was found that mainly the following process steps are relevant to generate stress in transistor channels, i.e., (i) shallow trench isolation, (ii) the formation of silicide at the source/drain region, and (iii) nitride contact etch stop layers [24]. Even though process-induced strain was not initially able strain levels as large as in the case of uniform strain, the local techniques benefit from some of advantages [23, 24] such as (i) strain can be independently tailored to optimize performance enhancement for both n-channel and p-channel MOSFETs, (ii) the threshold voltage shift is smaller in uniaxially stressed MOSFETs, and (iii) local stress techniques are cheaper and more compatible with standard CMOS technology. Since the local strain approach was more promising for industrial applications, the first strain engineering technologies were developed on the basis of uniaxial process induced stress.

1.3 General theory of stress and strain

In this work, we investigate the potential of strain engineering in modulating the properties of graphene material and its nanostructures. So, it is essential to understand the basis of engineering mechanics like stress, strain, and mechanical properties of the material. Within the elastic limit the property of solid materials to be deformed under the application of an external force/load and to regain their original shape after the force is removed is referred to as elasticity. It is Hooke's law, which describes the elastic relationship between the mechanical constraint and the deformation that the material will undergo. The external force applied on a specified area is known as stress, while the amount of deformation is called the strain. In this section, the theory of stress, strain, and their interdependence is briefly presented.

By definition, stress – strain analysis is an engineering discipline covering methods to determine the stresses and strains in materials and structures subjected to forces or loads. In continuum mechanics, stress is a physical quantity that expresses the internal forces that neighboring atoms of a continuous material exert on each other, while as mentioned above strain is the measure of the deformation of the material. Strain is a description of deformation in terms of relative displacement of particles

in the body that excludes rigid-body motions. In a continuous body, a deformation field results from a stress field induced by applied forces or is due to changes in the temperature field inside the body. In this case, the continuum completely recovers its original configuration. On the other hand, irreversible deformations can remain even after stresses have been removed. One type of irreversible deformation is plastic deformation, which occurs in material bodies after stresses have reached a certain threshold value known as the elastic limit or yield stress, and are the result of slip, or dislocation mechanisms at the atomic level.

In the case of elastic deformations, the response function linking strain to the deforming stress is the compliance tensor of the material. In this work, we only consider elastic deformations.

1.3.1 Stress tensor

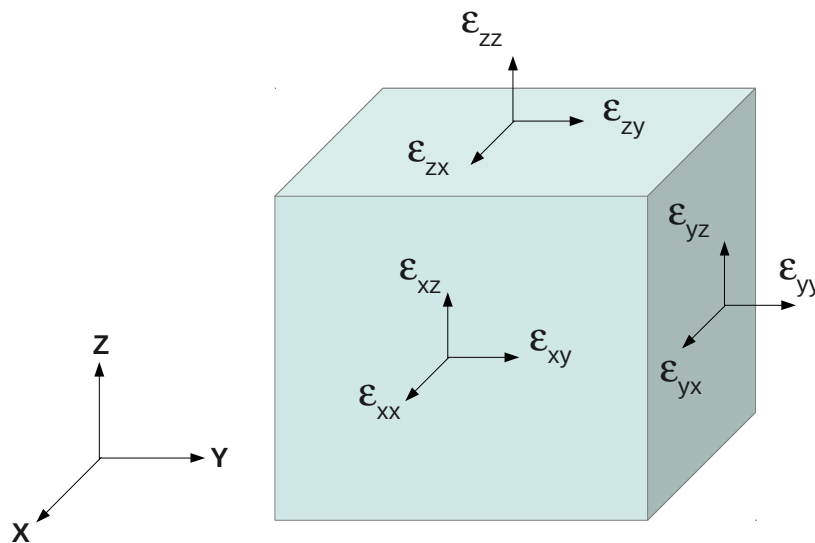


Figure 1.3: Stress tensor components acting on the surface of cube.

Stress is defined as the forces/loads in response to strain in a unit area. Stress has nine components and is a second-rank tensor. In particular, the stress distribution is displayed in Fig. 1.3, where ε_{xx} represents a force applied in the x direction, a unit area of the plane whose outward-drawn normal lies in the x direction, and ε_{xy} represents a force applied in the x direction to a unit area of the plane whose outward-drawn normal lies in the y direction. The stress tensor is symmetric just as the strain tensor, which will be shown below.

In case the force of components along the coordinate axes, i.e., F_{xx} , F_{xy} , F_{xz} , the stress components in this plane are [25]

$$\varepsilon_{xx} = \frac{F_{xx}}{A}, \quad \varepsilon_{xy} = \frac{F_{xy}}{A}, \quad \varepsilon_{xz} = \frac{F_{xz}}{A}$$

where A is the area of the stressed region.

We now study some simple stress cases to determine the stress tensors.

1. Hydrostatic pressure:

Under a hydrostatic pressure P , each shear stress component is zero. Stress along any principle direction is $-P$, namely,

$$\varepsilon = \begin{bmatrix} -P & 0 & 0 \\ 0 & -P & 0 \\ 0 & 0 & -P \end{bmatrix} \quad (1.2)$$

Here, the sign convention is that tensile stress is positive and compressive stress is negative.

2. Uniaxial stress T along the $[001]$ direction: For a uniaxial stress T along the $[001]$ direction, all stress components are zero, excepted $\varepsilon_{zz} = T$. So, we have

$$\varepsilon = \begin{bmatrix} 0 & 0 & 0 \\ 0 & 0 & 0 \\ 0 & 0 & T \end{bmatrix} \quad (1.3)$$

3. Uniaxial stress T along the $[110]$ direction: The case for a uniaxial stress along the $[110]$ direction is a little more complicated and is determined by

$$\varepsilon = \frac{T}{2} \begin{bmatrix} 1 & 1 & 0 \\ 1 & 1 & 0 \\ 0 & 0 & 0 \end{bmatrix} \quad (1.4)$$

Because a stress tensor is symmetric, the six coefficients ε_{xx} , ε_{yy} , ε_{zz} , ε_{xy} , ε_{yz} , and ε_{zx} completely define the stress. A second-rank stress tensor can be reduced to a 1D array form.

1.3.2 Strain tensor

Strain is created by deformation and is defined as the relative lattice displacement as shown in Fig. 1.4. In this Fig. 1.4(a), we use two unit vectors \vec{x} and \vec{y} to represent the unstrained lattice, and in a simple square lattice, they correspond to the lattice basis vectors. Under a small uniform deformation of the lattice, the two vectors are

distorted in both orientation and length, as shown in Fig. 1.4(b). The new vectors \vec{x}' and \vec{y}' may be written in terms of the old vectors [25]:

$$\begin{aligned}\vec{x}' &= (1 + \sigma_{xx})\vec{x} + \sigma_{xy}\vec{y} \\ \vec{y}' &= \sigma_{yx}\vec{x} + (1 + \sigma_{yy})\vec{y}\end{aligned}\tag{1.5}$$

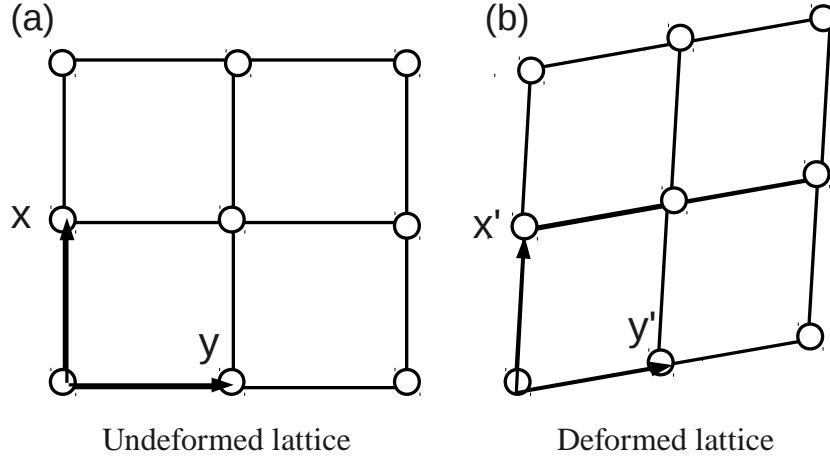


Figure 1.4: Schematic for (a) an undeformed lattice and (b) a deformed lattice

Similarly, in the 3D case, we also have

$$\begin{aligned}\vec{x}' &= (1 + \sigma_{xx})\vec{x} + \sigma_{xy}\vec{y} + \sigma_{xz}\vec{z} \\ \vec{y}' &= \sigma_{yx}\vec{x} + (1 + \sigma_{yy})\vec{y} + \sigma_{yz}\vec{z} \\ \vec{z}' &= \sigma_{zx}\vec{x} + \sigma_{zy}\vec{y} + (1 + \sigma_{zz})\vec{z}\end{aligned}\tag{1.6}$$

The strain coefficients $\sigma_{\alpha\beta}$ define the deformation of the lattice and are dimensionless. The 3×3 matrix

$$\sigma = \begin{bmatrix} \sigma_{xx} & \sigma_{xy} & \sigma_{xz} \\ \sigma_{yx} & \sigma_{yy} & \sigma_{yz} \\ \sigma_{zx} & \sigma_{zy} & \sigma_{zz} \end{bmatrix}\tag{1.7}$$

is called the strain tensor.

Suppose a lattice point originally located at $\vec{r} = x\vec{x} + y\vec{y} + z\vec{z}$, then with a uniform deformation this point will be at $\vec{r}' = x'\vec{x}' + y'\vec{y}' + z'\vec{z}'$. For a general varying strain, the strain tensor may be written

$$\sigma_{\alpha\beta} = \frac{\partial u_{\alpha}}{\partial x_{\beta}}\tag{1.8}$$

with

$$u_\alpha = u_x, u_y, u_z \quad \text{and} \quad x_\beta = x, y, z$$

where u_α is the displacement lattice point under study along x_α . A strain tensor is symmetric, i.e.,

$$\sigma_{\alpha\beta} = \sigma_{\beta\alpha} = \frac{1}{2} \left(\frac{\partial u_\alpha}{\partial x_\beta} + \frac{\partial u_\beta}{\partial x_\alpha} \right) \quad (1.9)$$

The antisymmetric part of tensor shown in Eq. 1.7 represents a rotation of the entire body.

Otherwise, we can work with another set of strain components, the diagonal elements of which are simply defined as

$$e_{xx} = \sigma_{xx}, \quad e_{yy} = \sigma_{yy}, \quad e_{zz} = \sigma_{zz} \quad (1.10)$$

that describe infinitesimal distortions associated with a change in volume, while the other strain components e_{xy} , e_{yz} , and e_{zx} are defined in terms of changes of angle between the basis vectors.

$$\begin{aligned} e_{xy} &= \vec{x}^i \vec{y}^j = \sigma_{xy} + \sigma_{yx} \\ e_{yz} &= \vec{y}^j \vec{z}^l = \sigma_{yz} + \sigma_{zy} \\ e_{zx} &= \vec{z}^l \vec{x}^i = \sigma_{zx} + \sigma_{xz} \end{aligned} \quad (1.11)$$

These six coefficients completely define the strain tensor as

$$e = \begin{bmatrix} e_{xx} & e_{xy} & e_{xz} \\ e_{yx} & e_{yy} & e_{yz} \\ e_{zx} & e_{zy} & e_{zz} \end{bmatrix} = \begin{bmatrix} \sigma_{xx} & \sigma_{xy} + \sigma_{yx} & \sigma_{zx} + \sigma_{xz} \\ \sigma_{xy} + \sigma_{yx} & \sigma_{yy} & \sigma_{yz} + \sigma_{zy} \\ \sigma_{zx} + \sigma_{xz} & \sigma_{yz} + \sigma_{zy} & \sigma_{zz} \end{bmatrix} \quad (1.12)$$

1.3.3 The relationship between stress and strain

The relationship between stress and strain is given by Hooke's law and can be mathematically written as [25]

$$\varepsilon_{ij} = \sum_{\alpha\beta} C_{ij\alpha\beta} \sigma_{\alpha\beta} \quad (i, j, \alpha, \beta = x, y, z) \quad (1.13)$$

where the coefficients $C_{ij\alpha\beta}$ are called elastic stiffness constants. Elastic stiffness constants are a fourth-rank tensor. Because of the symmetry of both the strain tensor and the stress tensor, we have

$$C_{ij\alpha\beta} = C_{ji\alpha\beta} = C_{ij\beta\alpha} \quad (1.14)$$

so we may write both strain and stress tensor as a six-component array as

$$\sigma = (\sigma_{xx}, \sigma_{yy}, \sigma_{zz}, \sigma_{xy}, \sigma_{yz}, \sigma_{zx}) \quad (1.15)$$

and

$$\varepsilon = (\varepsilon_{xx}, \varepsilon_{yy}, \varepsilon_{zz}, \varepsilon_{xy}, \varepsilon_{yz}, \varepsilon_{zx}) \quad (1.16)$$

which reduces the elastic stiffness tensor to a 6×6 matrix such as

$$\varepsilon_i = \sum_m C_{im} \sigma_m \quad (1.17)$$

This 6×6 matrix has a very simple form in cubic crystals due to the high symmetry. It has only three independent components and takes the form

$$C_{ij} = \begin{bmatrix} C_{11} & C_{12} & C_{12} & 0 & 0 & 0 \\ C_{12} & C_{11} & C_{12} & 0 & 0 & 0 \\ C_{12} & C_{12} & C_{11} & 0 & 0 & 0 \\ 0 & 0 & 0 & C_{44} & 0 & 0 \\ 0 & 0 & 0 & 0 & C_{44} & 0 \\ 0 & 0 & 0 & 0 & 0 & C_{44} \end{bmatrix} \quad (1.18)$$

In many cases it is convenient to work with the inverse of the elastic stiffness tensor, which is defined through the relation between strain and stress

$$\sigma_{\alpha\beta} = \sum_{ij} S_{\alpha\beta ij} \varepsilon_{ij} \quad (1.19)$$

The fourth-rank tensor $S_{\alpha\beta ij}$, called the compliance tensor, can also be reduced to a 6×6 matrix. Under cubic symmetry, it has the same form as the stiffness tensor

$$\begin{bmatrix} S_{11} & S_{12} & S_{12} & 0 & 0 & 0 \\ S_{12} & S_{11} & S_{12} & 0 & 0 & 0 \\ S_{12} & S_{12} & S_{11} & 0 & 0 & 0 \\ 0 & 0 & 0 & S_{44} & 0 & 0 \\ 0 & 0 & 0 & 0 & S_{44} & 0 \\ 0 & 0 & 0 & 0 & 0 & S_{44} \end{bmatrix} \quad (1.20)$$

and the strain-stress relation can be written as

$$\sigma_m = \sum_i S_{mi} \varepsilon_i \quad (1.21)$$

Since the elastic stiffness tensor and compliance tensor are inverse to each other, so it is easy to work out the relations between the components as

$$\begin{aligned} S_{11} &= \frac{C_{11} + C_{12}}{(C_{11} - C_{12})(C_{11} + 2C_{12})} \\ S_{12} &= \frac{-C_{12}}{(C_{11} - C_{12})(C_{11} + 2C_{12})} \\ S_{44} &= \frac{1}{C_{44}} \end{aligned} \quad (1.22)$$

In mechanical engineering, the modulus of elasticity E (also called Young's modulus) and Poisson's ration ν are commonly used. For a homogeneous, isotropic material, strain is related to stress through

$$\begin{aligned}\sigma_{xx} &= \frac{1}{E}(\varepsilon_{xx} - \nu(\varepsilon_{yy} + \varepsilon_{zz})) \\ \sigma_{yy} &= \frac{1}{E}(\varepsilon_{yy} - \nu(\varepsilon_{zz} + \varepsilon_{xx})) \\ \sigma_{zz} &= \frac{1}{E}(\varepsilon_{zz} - \nu(\varepsilon_{xx} + \varepsilon_{yy}))\end{aligned}\tag{1.23}$$

In cubic systems Young's modulus and Poisson ration ν are related to the compliance constants by

$$E = \frac{1}{S_{11}}, \quad \nu = -\frac{S_{12}}{S_{11}}\tag{1.24}$$

It is noted that, in one-dimensional systems, the Hooke's law relates 1D normal stress and 1D extensional strain, leading to

$$\sigma = E\varepsilon\tag{1.25}$$

1.4 Effect of strain on the electronic properties of materials

In general theory, the band structure describes the states of energy in the crystal momentum space that electrons and holes are allowed to have. It presents the electronic dispersion relation under the influence of the potential of the solid. The band structure determines several important characteristics of a material, e.g., electronic properties. Many theoretical and experiment studies have demonstrated the alterability of band structure in semiconducting materials thanks to strain engineering [26, 27, 28, 29, 30].

One can say that strain is not a new topic in semiconductor physics. It has been shown that strain may result from phonon-induced lattice vibrations, lattice mismatched film growth, and applied external stress. In principle, strain induces the shift of conduction band energy in material. This displacement is accounted by the deformation potential theory of Bardeen and Shockley [31, 32]. After that in 1955, Herring and Vogt used deformation potentials to model transport in strained semiconductors [33]. In that theory, the strain induced band edge shift is proportional to the strain tensor, which depends on the deformation. Until now, deformation potential theory is still the primary method to model the band shift and warping via band calculations.

It has been shown that while hydrostatic strain merely shifts the energy levels of a band, uniaxial and biaxial strain removes the band degeneracy. These energy shifts can either be extracted from the full-band structure calculated numerically including strain, or obtained analytically using the linear deformation potential theory. For example, the effect of strain on the conductivity of semiconductors, e.g., *Si*, was first investigated by C. C. Smith [18]. The principal finding of his experimental work was the observation of a change in the Si resistivity on applying uniaxial tensile stress. This change occurs due to a modification of the electronic band structure. Microscopically, the modification stems from a reduction in the number of symmetry operations allowed, which in turn depends on the way the crystal is stressed. This breaking of the symmetry of the *Si* lattice can result in a shift in the energy levels of the different conduction and valence bands, their distortion, removal of degeneracy, or any combination.

It has been reported from the simulation results of carrier velocity and drive current in strained-Si n-MOSFETs with gate length of 100 nm that the increase in mobility can result in higher drive current even under a constant saturation velocity model. Besides, recent experimental and theoretical results (see in [23] and Refs. therein) have shown that the drive current of MOSFETs with gate lengths of 100 – 50 nm is roughly proportional to the square root of low-field mobility. These results strongly suggest that low-field mobility is still important for, at least not fully disconnected from the current drive in short-channel MOSFETs. On the other hand, carrier velocity is also affected by the scattering probability of high energy carriers, typically reflecting in the energy relaxation time. It is also shown that strain induces band splitting, which can lead to longer energy relaxation time and higher velocity. Thus, device simulations taking accurately non-stationary transport effects and detailed band structures into account are mandatory for quantitative understanding of the current drive of short-channel MOSFETs.

Among them, strained-Si channels [34] have been recognized as a technology applicable to near term technology nodes, thanks to the recent progress in so-called local strain techniques, and have actually been included in most recent logic CMOS technologies [35]. The mobility enhancement obtained by applying appropriate strain can provide higher carrier velocity in MOS channels, resulting in higher current drive under fixed supply voltage and gate oxide thickness. This means that thicker gate oxides and/or lower supply voltage can be used under a fixed current drive, leading to the mitigation of the trade-off relationship among current drive, power consumption and short-channel effects. As a result, the strain engineering, with resulting increase

in channel mobility, has been regarded as a device technology mandatory for future technology nodes, as well.

Regarding graphene, it has been mentioned in previous section that one of many outstanding properties of graphene relates to the mechanical deformation. This material might exhibit a high enough strain endurance to meet the requirement of flexible electronics. Lots of works in theories and experiments have investigated the possibility and usefulness of strain engineering applied in graphene to modify the electronic structure of this material. Moreover, strain engineering has been proposed as an alternative approach to overcome its gapless character in this work. That interesting point will be discussed in chapter 2.

1.5 Experimental techniques to generate strain in graphene

Graphene was suggested to be able to sustain a much larger strain than conventional semiconductors. Many theoretical works have predicted that extreme strains in graphene might achieve over 10% [29, 36, 37], while some reports from experiments have shown the highest strains in a controlled, reversible and reproducible way only about a few percent [38, 39, 40]. That can be explained that experimental studies still have difficult problems to control the magnitude and type of strain in graphene devices. However, up to now, lots of recent works [41, 42, 43, 44, 45, 46] have demonstrated techniques to generate extreme strains in graphene with both uniform and local forms in a controlled and nondestructive way. This interesting point will be discussed below.

A. Uniform strain in graphene. Several experimental studies [39, 40, 43, 47] have reported the changes in the electrical transport properties of strained graphene on flexible substrates, a schematized for example in Fig. 1.5. In addition, the control of uniaxial strain with both tensile and compressive forms have also been demonstrated by bending a flexible substrates onto which graphene was deposited in [30, 48]. However, due to the dependence of strain on bending of the substrate, these methods only allow to engineer a limited amplitude of strain, i.e., of a few percent.

Additionally, it has been shown that on a pre-stretched polydimethylsiloxane substrate, graphene can exhibit a stable sheet resistance up to 11% stretching, with only one order change in this resistance up to 25% stretching. Especially, in two works [41, 42], techniques to generate extreme strains ($> 10\%$) in graphene in a controlled and nondestructive way have been suggested. In particular, the first one of Garza et

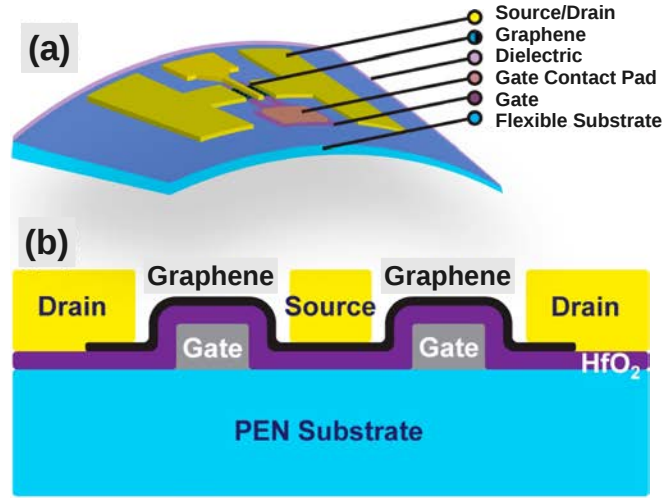


Figure 1.5: Schematic (a) for GFET fabricated on a flexible poly-ethylene naphthalate (PEN) substrate and (b) for cross-sectional schematic of flexible GFET device [39].

al. [41] demonstrated the generation of uniaxial strains by pulling graphene using a tensile-MEMS (micro-electro-mechanical systems). The system offers the possibility to tune and accurately reach the extremely high strain desired in the suspended part of graphene sheet. The second one of H. Shioya et al. [42] have introduced a method to control strain in graphene using thin-film-shrinkage (the effect of recrystallization of metallic films and condensation polymerization of organic insulating films). These methods in this work not only allow for inducing strain higher than 10% without the need for bending the substrate, but also achieve both biaxial strained states and isotropic compressive strained states of graphene in a controlled manner. In conclusion, these studies hold the promise for the development of strain engineering of graphene and help explore novel physics in strained graphene.

B. Local strain in graphene. Some different experimental techniques to generate local strains at the nanoscale in graphene and 2D materials have been explored [26, 27, 44, 46, 49]. It has been shown that a large localized uniaxial strain (up to 2.5% tensile) in few layer MoS_2 samples (3 to 5 layers) has been achieved [26], as seen in Fig. 1.6(a). Here, the fabrication process of localized uniaxial strain in wrinkled MoS_2 nanolayers is described as follows: MoS_2 flakes are deposited onto an elastomeric substrate which is pre-stretched by 100%. As a consequence, the tension in the elastomeric substrate is suddenly released, generating well-aligned wrinkles in the MoS_2 layers. It is found that this fabrication exhibit wrinkles in thin MoS_2 layers with the height from 50 to 350 nm. The distance between these wrinkles is about a few micrometers. For the thin MoS_2 flakes, the estimated uniaxial strain ranges

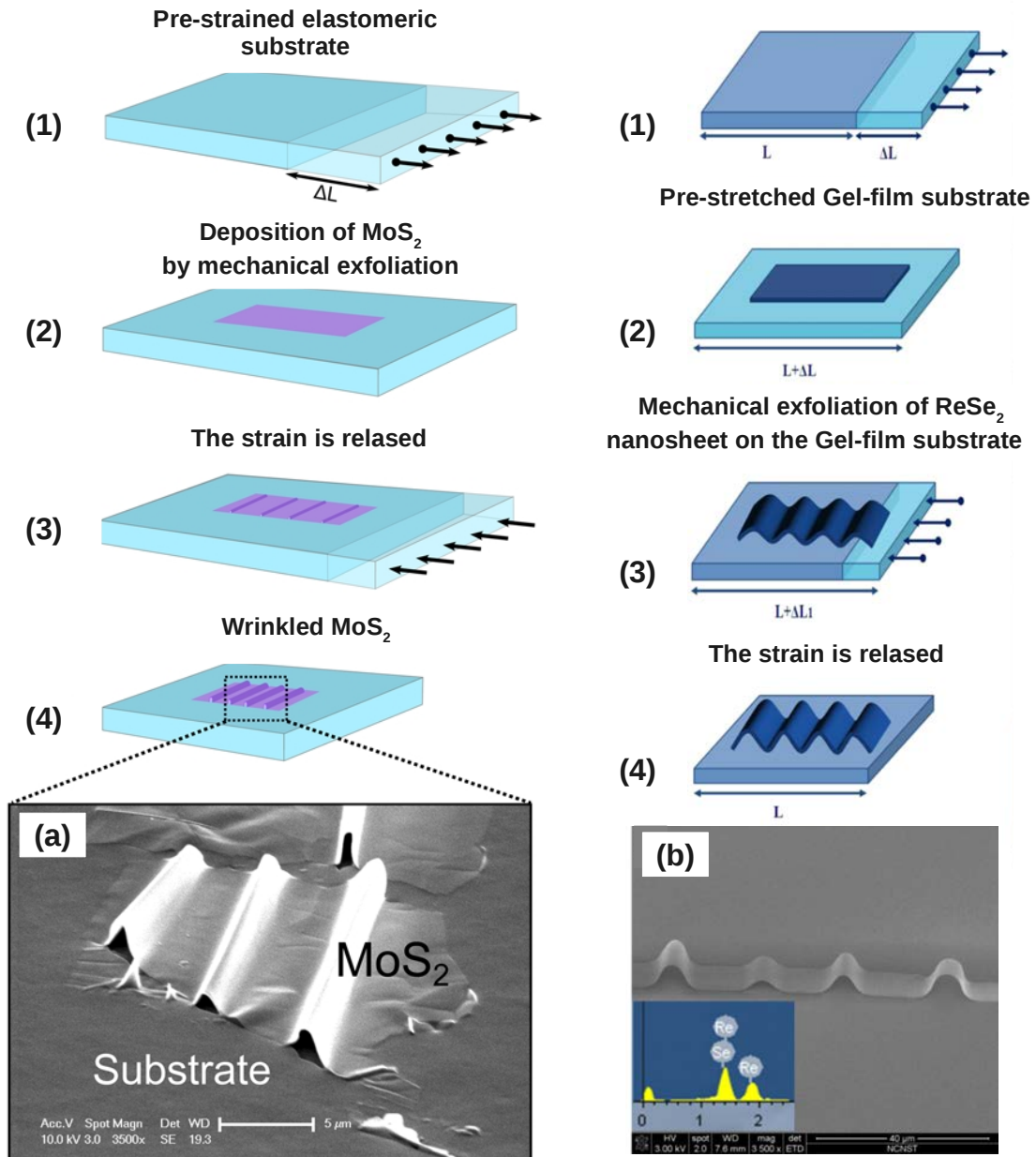


Figure 1.6: Localized uniaxial strain in MoS_2 [26] and $ReSe_2$ [27].

from 0.2% to 2.5%. Especially, in this work, it was shown that the wrinkles are stable in time, and no slippage has been found. Otherwise, this technique has been applied to create local strain (about 1.64%) through formation of $ReSe_2$ wrinkles [27] with the width and height of micrometers, separated by more than 10 μm as seen in Fig. 1.6(b).

Regarding the fabrication of local strain in graphene, an amazing work has been reported by Ji-Li et al. [44]. The Scalable strain engineering techniques were devel-

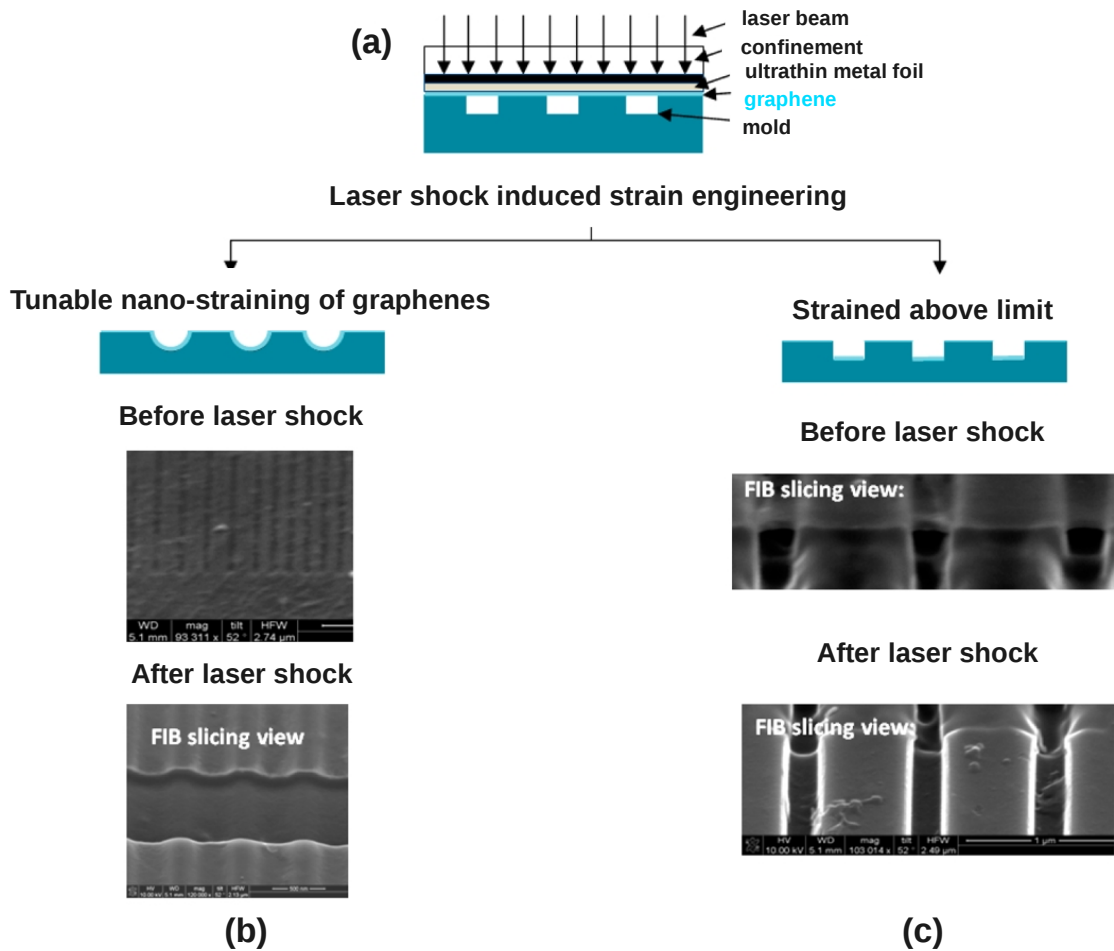


Figure 1.7: Illustration of the laser shock induced straining of graphene [44]. (a) setup of of the laser-induced strain engineering, (b) tunable 3D nanostraining of the graphene film when the strain limit is not exceeded. (c) graphene straining above the strain limit.

oped to control the area as well as the limit of local strain. This work presents a scalable manufacturing process to generate three-dimensional (3D) nanostructures, illustrated in Fig. 1.7, by laser-induced shock pressure and thus to induce local strain in the graphene sheet. It has been shown that the graphene film is attached to the mold surface after the laser shock due to the Van der Waals force. As a result, the strained shapes remain after the process. With this technique, the strain takes place in a circular mold, the size of which is related to the strain amplitude. It turns out that a strain of a few percent can be achieved in molds of size in the range from 50 to a few hundred nm, i.e, a circular mold ~ 50 nm in diameter with strain of 12%. Moreover, it is presented that the combination of the existing scalable patterning technique such as photolithography, laser interference lithography, and e-beam

lithography, the treated area in the proposed laser straining process might be further scaled up to roll to roll process by changing laser beam size and scanning speed. In conclusion, this is a fast, efficient, and quite "easy" technique, so it is expected to be applicable to lots of graphene systems in nanoelectronic devices.

An important point is here that these results are very attracting for us because the channel length of most of our devices ranges from a few ten nm to one hundred nm. So, the studies of Ji-Li et al and other groups as cited in references are considered as a validation of the concept of local strain in graphene, which makes realistic in the short term the experimental demonstration of the device designs investigated in the present work.

1.6 Conclusions

In the first part, I have introduced some basic and outstanding properties of graphene as well as its prospects in applications. Besides, I have also discussed the use of strain engineering to modify the band structure of semiconducting materials. Many fabrications of uniform and local strain forms are mentioned in this part to conclude that strain technique might be believed to overcome the gapless drawback of graphene. We have to say that until now although there are lots of techniques have been investigated to open a bandgap for graphene, each technique still has its own drawbacks and need to be confirmed by experiments. That is also the reason why the opening bandgap for graphene is still a necessary work. These interesting points will be mentioned in our work and in next chapter 2 and 3.

Part II. Numerical techniques

This theoretical work focuses on the electronic and thermoelectric properties of heterodevices made of graphene with strain engineering. The aims are to find good guides to improve the performance of graphene devices for practical applications and to demonstrate novel device concepts. To study some graphene nanostructures such as single graphene lattice, graphene nanoribbons, bilayer graphene, graphene nanomesh, and strained graphene lattice, I have used two quantum formalisms and the corresponding numerical methods: the tight-binding (TB) approach and the non-equilibrium Green's function (NEGF) technique.

In fact, it has ever been shown that ab initio method (Density Functional Theory (DFT)) is considered to be the most powerful one to investigate material properties in condensed matter physics with the highest possible level of accuracy. However, though ab initio is a almost perfect method for calculations in small system with limited number of atoms (a few tens of atoms), its applications have to face with many challenges in large systems (a few hundreds or thousands of atoms or even more). The tight-binding model is more simple and much faster in comparison with ab initio calculations. This method has been used most extensively to describe charge states in graphene structures, and, in principle, allows us to explore important characteristics such as electronic structure and transport phenomena. More interesting, at low energy around Dirac point of graphene with good selected parameters, it has been investigated that conduction bands obtained by tight binding model band calculations correspond to the DFT paradigm [50], even it might also give a good agreements with experimental results. Hence, in this work, we use the tight binding techniques as an useful tool for investigation of graphene system with reasonable computational design and time.

To consider the transport properties in nanoscale devices, the NEGF approach combined with a TB Hamiltonian has been proven to be a very efficient method. It is suitable for quantum transport simulations, taking into account effects of coupling to contacts, defects, impurities, phonons, etc. Additionally, the NEGF approach has demonstrated its usefulness for simulating nanoscale transistors, from conventional Si MOSFETs to carbon nanotube FETs and molecular transistors. Therefore, the details of these techniques are discussed in this part.

1.7 Tight-binding method

Among other semi-empirical methods like $k.p$ [51] and pseudo-potential [52] approaches, it has been demonstrated that the tight binding model [53, 54] is a suitable

approach to calculate the electronic band structure in solid-state physics. By using an approximate set of wave functions based upon superposition of wave functions for isolated atoms located at each atomic site, this model describes the properties of tightly-bound electrons in solids. The method is closely related to the LCAO method (linear combination of atomic orbitals method) used in chemistry. Here, the electrons should be tightly bound to the atom to which they belong and should have limited interaction with states and potentials on surrounding atom. As a result, the wave function of the electron will be rather similar to the atomic orbital of the free atom which it belongs to. This method has been initially developed by Bloch in 1928 by considering only the s atomic orbital. In 1934, Jones, Mott and Skinner introduced other atomic orbitals [55].

The tight binding model can be applied to a wide variety of solids. The model gives good quality results in many cases and can be combined with other models, i.e., density functional theory (DFT) that gives better results and can be used as a reference when the tight-binding model fails. Besides, the tight binding approach also provides basic information for materials like the surface states, applied to various kinds of many-body problems as well as quasiparticle calculations. It is also a common practice to use optimized tight binding methods, in which the values of the matrix elements are derived approximately or fitted to experiment or other more accurate theories like ab initio calculation [53].

1.7.1 Secular equations

Before the introduction of tight binding calculations in carbon structures, i.e., in graphene, we review here some secular equations, which are actually given in detail in [56]. First, the wave function of the lattice in Bloch's theorem is written by

$$T_{\vec{a}_i}\psi = e^{i\vec{k}\vec{a}_i}\psi \quad (i = 1, 2, 3) \quad (1.26)$$

where $T_{\vec{a}_i}$ is a translational operation along the lattice vector \vec{a}_i , and \vec{k} is the wave vector.

There are lots of possible functional forms of ψ to satisfy the equation above. However, in the tight-binding model of electronic structures, single electron wave functions are normally expanded in terms of atomic orbitals. So, another functional form $\phi_j(\vec{k}, \vec{r})$ based on the j^{th} atomic orbital in the unit cell (or atom), which satisfies Eq. 1.26, is given as

$$\phi_j(\vec{k}, \vec{r}) = \frac{1}{\sqrt{N}} \sum_{\vec{R}} e^{i\vec{k}\vec{R}} \varphi_j(\vec{r} - \vec{R}) \quad (j = 1, 2, \dots, n) \quad (1.27)$$

where \vec{R} is the position of the atom and $\varphi_j(\vec{r} - \vec{R})$ is the atomic wavefunction in state j . N and n denote the number of unit cells and atomic wave functions, respectively. There are n Bloch functions in the solid for a given \vec{k} . It is easy to verify that this function satisfies the Bloch condition

$$\begin{aligned}\phi_j(\vec{k}, \vec{r} + \vec{a}) &= \frac{1}{\sqrt{N}} \sum_{\vec{R}} e^{i\vec{k}\vec{R}} \varphi_j(\vec{r} + \vec{a} - \vec{R}) \\ &= e^{i\vec{k}\vec{a}} \frac{1}{\sqrt{N}} \sum_{\vec{R}-\vec{a}} e^{i\vec{k}(\vec{R}-\vec{a})} \varphi_j[\vec{r} - (\vec{R} - \vec{a})] \\ &= e^{i\vec{k}\vec{a}} \phi_j(\vec{k}, \vec{r})\end{aligned}\quad (1.28)$$

In a solid, the eigenfunctions $\psi_j(\vec{k}, \vec{r})$ ($j = 1, 2, \dots, n$) are defined as a linear combination of Bloch functions

$$\psi_j(\vec{k}, \vec{r}) = \sum_{j'=1}^n C_{jj'}(k) \phi_{j'}(\vec{k}, \vec{r}) \quad (1.29)$$

Here, $C_{jj'}(k)$ are coefficients which have to be determined.

The eigenvalues of the system described by the Hamiltonian H are given by

$$E_j(\vec{k}) = \frac{\langle \psi_j | H | \psi_j \rangle}{\langle \psi_j | \psi_j \rangle} = \frac{\int \psi_j^*(\vec{k}, \vec{r}) H \psi_j(\vec{k}, \vec{r}) dr}{\int \psi_j^*(\vec{k}, \vec{r}) \psi_j(\vec{k}, \vec{r}) dr} \quad (1.30)$$

Now, substituting $\psi_j(\vec{k}, \vec{r})$ as defined above leads to

$$E_i(\vec{k}) = \frac{\sum_{j,j'=1}^n C_{ij}^* C_{ij'} \langle \phi_j | H | \phi_{j'} \rangle}{\sum_{j,j'=1}^n C_{ij}^* C_{ij'} \langle \phi_j | \phi_{j'} \rangle} = \frac{\sum_{j,j'=1}^n H_{jj'}(\vec{k}) C_{ij}^* C_{ij'}}{\sum_{j,j'=1}^n S_{jj'}(\vec{k}) C_{ij}^* C_{ij'}} \quad (1.31)$$

where $H_{jj'}(\vec{k})$ and $S_{jj'}(\vec{k})$ are the transfer and overlap matrices, respectively, and are defined by

$$H_{jj'}(\vec{k}) = \langle \phi_j | H | \phi_{j'} \rangle; \quad S_{jj'}(\vec{k}) = \langle \phi_j | \phi_{j'} \rangle \quad (1.32)$$

For a given \vec{k} value, the coefficient $C_{jj'}^*(\vec{k})$ is optimized so as to minimize $E_i(\vec{k})$

$$\frac{\partial E_i(\vec{k})}{\partial C_{ij}^*(\vec{k})} = \frac{\sum_{j,j'=1}^n H_{jj'}(\vec{k}) C_{ij'}(\vec{k})}{\sum_{j,j'=1}^n S_{jj'}(\vec{k}) C_{ij}^*(\vec{k}) C_{ij'}(\vec{k})} - \frac{\sum_{j,j'=1}^n H_{jj'}(\vec{k}) C_{ij}^*(\vec{k}) C_{ij'}(\vec{k})}{[\sum_{j,j'=1}^n S_{jj'}(\vec{k}) C_{ij}^*(\vec{k}) C_{ij'}(\vec{k})]^2} \sum_{j'=1}^n S_{jj'}(\vec{k}) C_{ij'}(\vec{k}) = 0 \quad (1.33)$$

This can be rewritten as

$$\frac{\sum_{j,j'=1}^n H_{jj'}(\vec{k}) C_{ij'}(\vec{k})}{\sum_{j,j'=1}^n S_{jj'}(\vec{k}) C_{ij}^*(\vec{k}) C_{ij'}(\vec{k})} - \left[\frac{\sum_{j,j'=1}^n H_{jj'}(\vec{k}) C_{ij}^*(\vec{k}) C_{ij'}(\vec{k})}{\sum_{j,j'=1}^n S_{jj'}(\vec{k}) C_{ij}^*(\vec{k}) C_{ij'}(\vec{k})} \right] \frac{\sum_{j'=1}^n S_{jj'}(\vec{k}) C_{ij'}(\vec{k})}{\sum_{j,j'=1}^n S_{jj'}(\vec{k}) C_{ij}^*(\vec{k}) C_{ij'}(\vec{k})} = 0 \quad (1.34)$$

which can be readily simplified as

$$\sum_{j'=1}^n H_{jj'}(\vec{k}) C_{ij'}(\vec{k}) - E_i(\vec{k}) \sum_{j'=1}^n S_{jj'}(\vec{k}) C_{ij'}(\vec{k}) = 0 \quad (1.35)$$

Rewriting this equation in a matrix form we get

$$\{[H] - E_i(\vec{k})[S]\}\{C_i(\vec{k})\} = 0 \quad (1.36)$$

If the matrix $[H] - E_i(\vec{k})[S]$ has an inverse, the vector $C_i(\vec{k})$ will be identically zero, which leads to the trivial solution. Thus, non-trivial solutions require

$$|[H] - E_i(\vec{k})[S]| = 0 \quad (1.37)$$

This equation is called the secular equation, whose eigenvalues $E_i(\vec{k})$ give the energy bandstructure.

1.7.2 Tight-binding calculations for carbon structures

In the tight binding method, the one-electron energy eigenvalues $E_i(\vec{k})$ are obtained by solving the secular equation. The eigenvalues $E_i(\vec{k})$ are periodic functions in the reciprocal lattice, and thus can be fully described within the first Brillouin zone. In a two or three dimensional solid, it is difficult to display the energy dispersion relations over the whole range of \vec{k} values, and thus we plot $E_i(\vec{k})$ along the high symmetry directions of the Brillouin zone. The actual procedure of the tight binding calculation is as follows [56]:

(i) specify the unit cell and the unit vectors, \vec{a}_i . Specify the coordinates of the atoms in the unit cell and select n atomic orbitals which are considered in the calculation.

(ii) specify the Brillouin zone and the reciprocal lattice vectors, \vec{b}_i . Select the high symmetry directions in the Brillouin zone, and the \vec{k} points along the high symmetry axes.

(iii) for the selected \vec{k} points, calculate the transfer and the overlap matrix elements, H_{ij} and S_{ij} , respectively.

(iv) for the selected \vec{k} points, solve the secular equation, and obtain the eigenvalues $E_i(\vec{k})$ ($i=1,2,\dots,n$) and the coefficients $C_{ij}(\vec{k})$

When applying these calculation methods to real systems, the symmetry of the problem is considered in detail on the basis of a tight binding approach where the transfer and overlap matrix elements are often treated as parameters selected to

reproduce the band structure of the solid obtained either experimentally or from first principle calculations.

In graphene, we consider the unit cell and the Brillouin zone of the two dimensional lattice in Fig. 1.8, where \vec{a}_1 and \vec{a}_2 are unit vectors in real space, and \vec{b}_1 and \vec{b}_2 are the reciprocal lattice vectors. In the real space, the unit real vectors of the hexagonal lattice are expressed as

$$\vec{a}_1 = a\left(\frac{3}{2}, \frac{\sqrt{3}}{2}\right), \quad \vec{a}_2 = a\left(\frac{3}{2}, -\frac{\sqrt{3}}{2}\right) \quad (1.38)$$

where $a = 1.42\text{\AA}$ is the lattice constant of graphene. The corresponding unit vectors \vec{b}_1 and \vec{b}_2 of the reciprocal lattice are given by:

$$\vec{b}_1 = \frac{2\pi}{3a}(1, \sqrt{3}), \quad \vec{b}_2 = \frac{2\pi}{3a}(1, -\sqrt{3}) \quad (1.39)$$

corresponding to a lattice constant of $4\pi/a\sqrt{3}$ in reciprocal space. The direction of

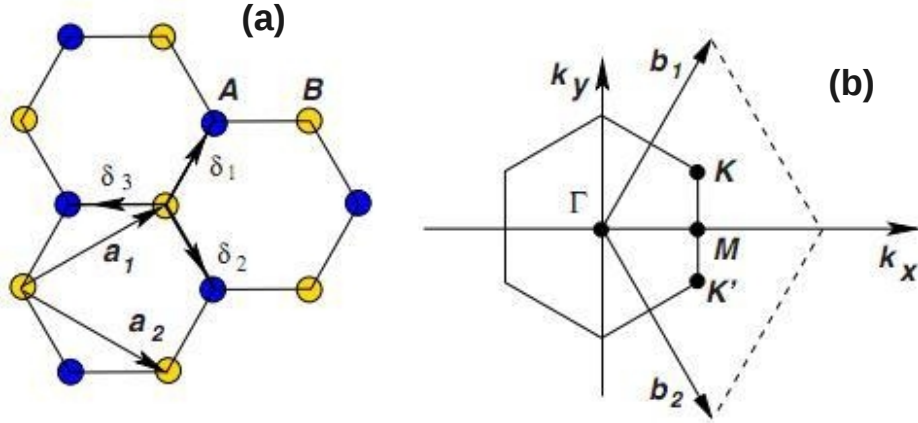


Figure 1.8: Graphene lattice and its Brillouin zone. (a) lattice structure of graphene, made out of two interpenetrating triangular lattices (\vec{a}_1 and \vec{a}_2 are the lattice unit vectors). (b) corresponding Brillouin zone with two reciprocal lattices \vec{b}_1 and \vec{b}_2 . The Dirac cones are located at the K and K' points [3].

the unit vectors \vec{b}_1 and \vec{b}_2 of the reciprocal hexagonal lattice is shown in Fig. 1.8 from the unit vectors \vec{a}_1 and \vec{a}_2 of the hexagonal lattice in real space. By selecting the first Brillouin zone as in Fig. 1.8(b), the highest symmetry is obtained for the Brillouin zone of 2D graphite. Here we define the three high symmetry points, Γ , K and M as the center, the corner, and the center of the edge, respectively. The energy dispersion relations are calculated for the triangle ΓKM .

It has been shown that the three σ -bonds for 2D graphite hybridize in a sp^2 configuration, while the other $2p_z$ orbital, which is perpendicular to the graphene plane, forms π covalent bands. Here, we consider only π energy bands for 2D graphite, because we know that the π energy bands are covalent and are the most important for determining the solid state properties of graphite.

The unit cell of graphene defined as a box represented by the dotted lines in Fig. 1.9, with two carbon atoms (A and B) in the unit cell. The Bloch orbitals consisting of A and B atoms are given by

$$\Phi(r) = \frac{1}{\sqrt{N}} \sum_{R_\alpha} e^{ikR_\alpha} \varphi(r - R_\alpha) \quad \text{with } \alpha = A, B \quad (1.40)$$

where the summation is taken over the atom site coordinate R_α for the A and B carbon atom in the solid.

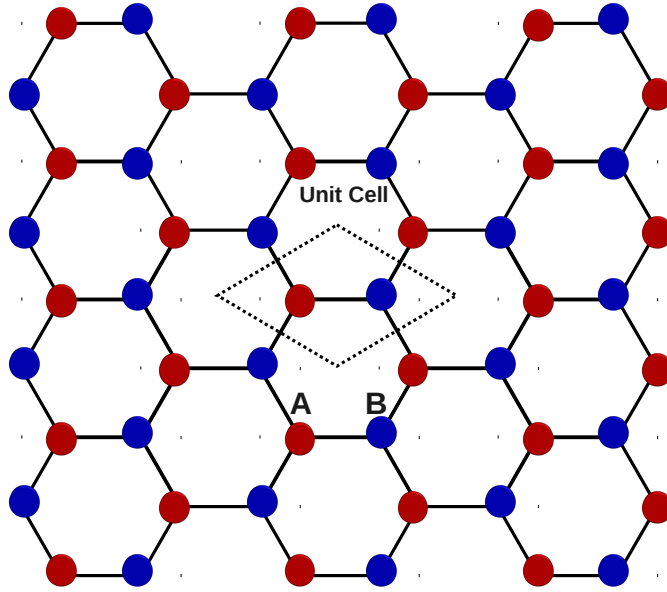


Figure 1.9: Graphene lattice is composed of two triangular sub-lattices A and B. Unit cell is shown in figure with two atoms. It is noted that the lattice constant is a ($a = 1.42\text{\AA}$).

The (2×2) matrix Hamiltonian, $H_{\alpha\beta}$ ($\alpha, \beta = A, B$), is determined as follows

$$\begin{aligned} H_{AA}(r) &= \langle \phi_A(r) | H | \phi'_A(r) \rangle \\ &= \frac{1}{N} \sum_{R_A, R'_A} e^{ik(R'_A - R_A)} \langle \phi_A(r - R_A) | H | \phi_A(r - R'_A) \rangle \end{aligned}$$

$$\begin{aligned}
&= \frac{1}{N} \sum_{R_A, R_0} e^{ikR_0} \langle \phi_A(r - R_A) | H | \phi_A(r - R_A - R_0) \rangle \\
&= \frac{1}{N} \left\{ \sum_{R_A, R_0=0} \langle \phi_A(r - R_A) | H | \phi_A(r - R_A) \rangle + \sum_{R_A, R_0 \neq 0} e^{ikR_0} \langle \phi_A(r - R_A) | H | \phi_A(r - R_A - R_0) \rangle \right\}
\end{aligned}$$

Finally,

$$H_{AA}(r) = \langle \phi_A(r) | H | \phi'_A(r) \rangle = \epsilon_{2p} \quad (1.41)$$

In the equation above the maximum contribution to the matrix element H_{AA} comes from $R = R'$, and this gives the orbital energy of the $2p$ level, ϵ_{2p} . The next order contribution to H_{AA} comes from terms in $R = R' \pm a$, which will be neglected for simplicity. Similarly, $H_{BB} = H_{AA}$.

Next let us consider the matrix element $H_{AB}(r)$. The larger contribution to $H_{AB}(r)$ arises when atoms A and B are nearest neighbors.

$$\begin{aligned}
H_{AB}(r) = \langle \phi_A(r) | H | \phi_B(r) \rangle &= \frac{1}{N} \sum_{R_A, R_B} e^{ik(R_B - R_A)} \langle \varphi_A(r - R_A) | H | \varphi_B(r - R_B) \rangle \\
&= \frac{1}{N} \sum_{R_A, R_B} e^{ikR_j} \langle \varphi_A(r - R_A) | H | \varphi_B(r - R_A - R_j) \rangle
\end{aligned}$$

Then,

$$H_{AB}(r) = \langle \phi_A(r) | H | \phi_B(r) \rangle = t e^{ikR_j} \quad (1.42)$$

Here $R_B = R_A + R_j$ and we define $t = \frac{1}{N} \langle \varphi_A(r - R_A) | H | \varphi_B(r - R_A - R_j) \rangle$

Otherwise, we consider the three nearest-neighbor B atoms relative to an A atom, which are denoted by the vectors \vec{R}_1, \vec{R}_2 and \vec{R}_3 .

$$H_{AB} = t(e^{ikR_1} + e^{ikR_2} + e^{ikR_3}) = tf(k) \quad (1.43)$$

where $f(k)$ is a function of the sum of the phase factors of e^{ikR_j} ($j = 1, 2, 3$).

It is noticed that $H_{BA} = H_{AB}^*$. So, the explicit form for H can be written as

$$H = \begin{bmatrix} \epsilon_{2p} & tf(k) \\ tf(k)^* & \epsilon_{2p} \end{bmatrix} \quad (1.44)$$

The calculations of overlap matrices $S_{\alpha\beta}$ are totally similar to that of $H_{\alpha\beta}$. We assume that the atomic wavefunction is normalized, so $S_{AA} = S_{BB} = 1$. Beside, $S_{AB} = sf(k)$ where s is the overlap integral between the nearest A and B atoms and is determined by $s = \frac{1}{N} \langle \varphi_A(r - R_A) | \varphi_B(r - R_A - R_j) \rangle$. We also have $S_{BA} = S_{AB}^*$. Finally, the explicit form for S is

$$S = \begin{bmatrix} 1 & sf(k) \\ sf(k)^* & 1 \end{bmatrix} \quad (1.45)$$

Solving the secular equation $\det(H - ES) = 0$ and using H and S above, the eigenvalues $E(\vec{k})$ are obtained as a function of $\omega(\vec{k})$, k_x and k_y

$$E_{g2D}(\vec{k}) = \frac{\epsilon_{2p} \pm t\omega(\vec{k})}{1 \pm s\omega(\vec{k})} \quad (1.46)$$

where the + signs in the numerator and denominator go together giving the bonding π energy band, and likewise for the - signs, which give the anti-bonding π^* band, while the function $\omega(\vec{k})$ is given by

$$\omega(\vec{k}) = \sqrt{|f(\vec{k})|^2} = \sqrt{3 + 2\cos(\sqrt{3}k_y a) + 4\cos(\frac{\sqrt{3}}{2}k_y a)\cos(\frac{3}{2}k_x a)} \quad (1.47)$$

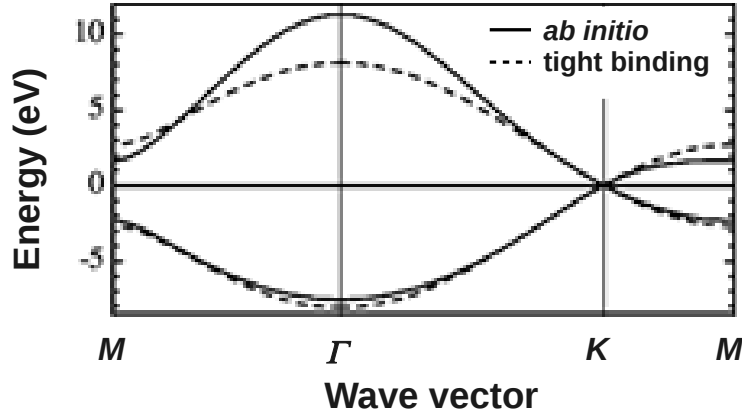


Figure 1.10: Ab initio and nearest-neighbor tight-binding dispersions of graphene. The converged ab initio calculation of the graphene π and π^* electronic bands is shown by the full lines. The dashed lines represent the tight-binding dispersion of Eq. 1.46 with $s = 0$ and $t = 2.7eV$ [57].

In the Eq. 1.46, the three parameters ϵ_{2p} , t and s are found by fitting experimental or first-principles data. The most common method is to adjust the tight-binding dispersion to obtain a correct description of the π bands at the K point. This yields $\epsilon_{2p} = 0$, t between -2.5 and -3.0 eV, and s below 0.1 [57]. Since s is small, it is usually neglected. In that case, the nearest neighbor Hamiltonian is able to produce bands which are symmetric with respect to the Fermi level. In addition, the Eq. 1.46 with $\omega(\vec{k})$ shown in Eq. 1.47 and zero s is given by

$$E_{g2D}(k_x, k_y) = \pm t \sqrt{3 + 2\cos(\sqrt{3}k_y a) + 4\cos(\frac{\sqrt{3}}{2}k_y a)\cos(\frac{3}{2}k_x a)} \quad (1.48)$$

Hence, when the overlap integral s becomes zero, the energy dispersion is linear around Dirac point, as shown in Fig. 1.10. Moreover, this figure is shown a result of an ab initio calculation of the graphene π and π^* electronic bands (full lines) to compare with the tight-binding dispersion in Eq. 1.48 [57], neglecting the overlap matrix (dashed lines). Clearly, the agreement between first-principles and the tight-binding band structure is very good close to the K point of Brillouin zone. In conclusion, the nearest neighbor tight-binding description of graphene is nearly perfect for the calculations to study the low-energy properties.

In other dispersions of energy equation with basic vectors

$$\vec{a}_1 = a\left(\frac{3}{2}, \frac{\sqrt{3}}{2}\right), \quad \vec{a}_2 = a\left(\frac{3}{2}, -\frac{\sqrt{3}}{2}\right)$$

$$\text{or } \vec{r}_1 = a\left(\frac{1}{2}, \frac{\sqrt{3}}{2}\right), \quad \vec{r}_2 = a\left(\frac{1}{2}, -\frac{\sqrt{3}}{2}\right), \quad \vec{r}_3 = a(1, 0)$$

finally, the description of energy bands can write as follows

$$E(k) = \pm t | e^{ik\vec{a}_1} + e^{ik\vec{a}_2} + 1 | \quad (1.49)$$

$$\text{or } E(k) = \pm t | e^{ik\vec{r}_1} + e^{ik\vec{r}_2} + e^{ik\vec{r}_3} | \quad (1.50)$$

1.8 Non-equilibrium Green's function technique

1.8.1 Basic equations

In this section, we present the NEGF equations for layer structures, i.e., single layer graphene. It has been shown that the NEGF formalism is a very efficient method in physics to solve the Schrodinger equation as well as the Poisson equation. First, we will reconsider the basic form of Green's function. Beginning from the Schrodinger equation, i.e.

$$(E - H)|\varphi\rangle = 0 \quad (1.51)$$

The relationship between the operator $(E-H)$ and the Green's function is defined by

$$(E - H)G(\vec{r}, \vec{r}'; E) = \delta(\vec{r} - \vec{r}') \quad (1.52)$$

where δ is the Dirac delta function. We can define a matrix form of the Green's function as follows

$$(E - H)G(E) = I \quad \text{or} \quad G(E) = (E - H)^{-1} \quad (1.53)$$



Figure 1.11: A general model of field effect transistor with a device channel connected to the source and drain contacts. The electrical current is modulated by a third electrode, the gate. The coupling to contacts is described by $\Sigma_{L,R}$ self energy.

where H is the matrix formed from the interactions between atoms in the system, it can be called atomistic Hamiltonian and the Green's function defined by Eq. 1.53 is called atomistic Green's function.

Now, we will consider the application of Green's function method in nanoscale devices. A schematic structure of typical simulated device is shown in Fig. 1.11. In principle, in the standard case of a transistor, it includes three main parts: a device channel (active region), contacts (left and right, or source and drain), and a gate electrode. The Green's function of the active region is now

$$G_D = (E - H_D - \Sigma_L - \Sigma_R)^{-1} \quad (1.54)$$

where H_D is the Hamiltonian of the active region. $\Sigma_{L(R)}$ is the self energy of left (right) contact and is determined by [58]

$$\Sigma_{L(R)}^s = H_{DL(R)} g_{0(N)}^{L(R)} H_{L(R)D} \quad (1.55)$$

where $H_{DL}(H_{LD})$ is the Hamiltonian describing the device-to-contact (contact-to-device) coupling, and $g_{0(N)}^{L(R)}$ is the surface Green's function of the left (right) contact, which is discussed in details below.

1.8.1.1 Transmission

In ballistic transport, the transmission of the system can be calculated via the Green's function [58, 59]

$$T = \text{trace}[\Gamma_L G_D \Gamma_R G_D^\dagger] \quad (1.56)$$

where $\Gamma_{L(R)} = i[\Sigma_{L(R)} - \Sigma_{L(R)}^\dagger]$ is the energy level broadening at the left (right) contact.

In principle, the Eq. 1.56 is the standard one for calculation of transmission. However, to calculate the transmission using this approach, we need all elements of

the Green's function matrix as well as all elements of Hamiltonian matrix H_D of the active region. Since the size of the tight binding matrix H_D can be very large it may require large computational resources. To reduce the computation time, the recursive Green's function algorithm [58] is very powerful. Using this technique, we do not need to calculate all elements of the Green's function matrix, but just some particular ones. Now, the transmission can be calculated efficiently with different techniques applied to reduce the size of the left (right) Green's function as well as of the device Green's function [58].

$$T(E) = \text{Trace}[\Gamma_L^s \{i(G_{11} - G_{11}^\dagger) - G_{11} \Gamma_L^s G_{11}^\dagger\}] \quad (1.57)$$

or

$$T(E) = \text{Trace}[\{i(G_{NN} - G_{NN}^\dagger) - G_{NN}^\dagger \Gamma_R^s G_{NN}\} \Gamma_R^s] \quad (1.58)$$

where $\Gamma_{L(R)}^s = i[\Sigma_{L(R)}^s - \Sigma_{L(R)}^{s\dagger}]$ with $\Sigma_{L(R)}^s = H_{DL(R)} g_{0(N)}^{L(R)} H_{L(R)D}$. Here, $g_{0(N)}^{L(R)}$ is the surface Green's function of left (right) contact.

1.8.1.2 Density of states (DOS) and local density of states (LDOS)

A. Density of states (DOS)

The density of states (DOS) is defined as the number of states per unit sample volume at an energy E inside an interval $[E, E + dE]$. The general form of DOS of a system is given as [59]

$$D(E) = \frac{dN(E)}{dE} = \sum_n \delta(E - E_n) \quad (1.59)$$

where $N(E)$ is the number of states between energies E and $E + dE$ in a given volume.

It has been demonstrated that the DOS can be computed via the Green's function thanks to the Lorentz form of the delta function as

$$D(E) = \sum_n \delta(E - E_n) = \lim_{\eta \rightarrow 0} \sum_n \frac{1}{\pi} \frac{\eta}{(E - E_n)^2 + \eta^2} \quad (1.60)$$

where η is a very small quantity (it is often noted as 0^+) and it has the physical meaning of a small broadening energy to avoid divergence in case of $E = E_n$.

Coming back to the common form of Green's function as mentioned above: $G(E) = (E - H)^{-1}$, we can rewrite this formula as follows

$$G(E) = (E + i\eta - H)^{-1} \quad (1.61)$$

With this form, if we use the basis eigen vectors of the Hamiltonian H , the Green's function contains the diagonal terms given by

$$G(E) = \begin{bmatrix} \frac{1}{E+i\eta-\varepsilon_1} & & & \\ & \frac{1}{E+i\eta-\varepsilon_2} & & \\ & & \ddots & \\ & & & \frac{1}{E+i\eta-\varepsilon_n} \end{bmatrix}$$

We define $A = i[G - G^\dagger]$, which is called spectral function. Then, we have

$$\text{trace}(A) = i \times \text{trace}[G - G^\dagger] = \sum_n \frac{2\eta}{(E - \varepsilon_n)^2 + \eta^2} \quad (1.62)$$

From Eq. 1.60 and Eq. 1.62, the DOS is finally given by

$$D(E) = \frac{\text{trace}(A)}{2\pi} = \frac{i \times \text{trace}[G - G^\dagger]}{2\pi} \quad (1.63)$$

B. Local density of states (LDOS)

The local density of states (LDOS) is very important for transport and device analysis. This quantity is associated with energy levels localized in the scattering region and especially important for instance in the presence of resonance effects where each peak of transmission corresponds to a confined state in the scattering region that can be observed clearly via LDOS spectrum.

The LDOS is defined as the DOS at a specific position in the space. So, the LDOS at the position of i^{th} layer in the device can be calculated via the Green's function as in Eq. 1.63. It is noted that the spectral function corresponding to the spectral function of i^{th} layer is $A_{ii} = i[G_{ii} - G_{ii}^\dagger] = -2\text{Im}(G_{ii})$ where $\text{Im}(G_{ii})$ is the imaginary part of G_{ii} . Therefore, the LDOS is now given by

$$D_{ii}(E) = \frac{\text{trace}(A_{ii})}{2\pi} = -\text{trace}\left[\frac{\text{Im}(G_{ii})}{\pi}\right] \quad (1.64)$$

1.8.1.3 Electric current

When a bias voltage is applied at source and drain, an electric field is generated along the transport direction and drives carriers in the channel. This leads to a flow or current in the device and it can be measured. The total current in ballistic regime can be calculated by the well-known Landauer's formula [59]

$$I = \frac{2e}{h} \int_{-\infty}^{+\infty} [f_L(E - \mu_L) - f_R(E - \mu_R)] T(E) dE \quad (1.65)$$

where $f(E, \mu, T_0) = [1 + \exp(\frac{E-\mu}{k_b T_0})]^{-1}$ is the Fermi function giving the distribution of electrons around the chemical energy μ . It is noted that here $\mu_R = E_{FR} + U_R$, $\mu_L = E_{FL} + U_L$, $U_L - U_R = eV_b$ (V_b : bias voltage) where $E_{FL(R)}$ is the Fermi energy in source (left contact) and drain (right contact). In common calculations, we often choose ($U_L = 0$ and $U_R = -eV_b$) or ($U_L = eV_b/2$ and $U_R = -eV_b/2$).

1.8.1.4 Conductance

The electronic conductance is usually defined at low bias and in ballistic regime it can be also calculated by a Landauer's formula [59]

$$G_e(\mu, T_0) = \lim_{V_b \rightarrow 0} \frac{I}{V_b} = \frac{2e^2}{h} \int_{-\infty}^{+\infty} \frac{\partial f(E, \mu, T_0)}{\partial E} T(E) dE \quad (1.66)$$

where $T(E)$ is the transmission of electrons and $f(E, \mu, T_0)$ is the Fermi function.

1.8.2 Numerical techniques for Green's function calculation

From the formula of device Green's function as shown above

$$G(E, k_y) = [E - H_D - \Sigma_L - \Sigma_R]^{-1} \quad (1.67)$$

We see that to determine the device's Green function it is first necessary to compute the coupling self-energies $\Sigma_{L,R}$. Afterwards, we can calculate the physical quantities of interest such as transmission, LDOS, conductance as well as current density.

1.8.2.1 Calculation of the self energy

In this work, we will study devices made of graphene material. It is noted that the Hamiltonian of graphene structures is constructed by the tight-binding method. This section will present some techniques used for this thesis work. First, to calculate the self-energies, the simulated structure is divided into layers as schematized in Fig. 1.12. The layer is a tiny part, which can form the whole structure by repeating it along x -direction (transport direction).

In this model, the device-to-contact coupling just appears between the device layer 1 and the layer l_0 of the left contact and between the device layer N and the layer r_0

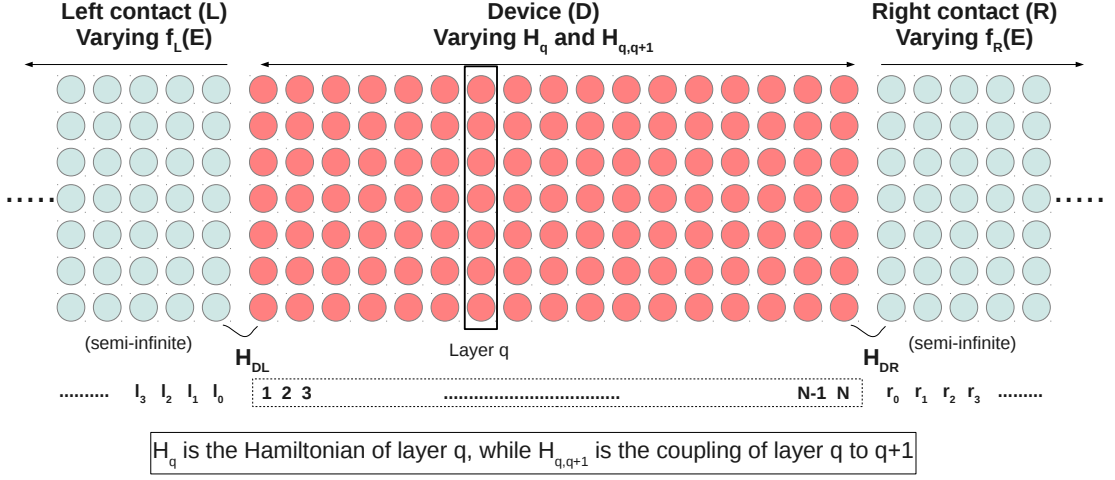


Figure 1.12: Layered description of a device.

of the right contact, we finally have the form:

$$H_D + \Sigma_L + \Sigma_R = \begin{bmatrix} H_1 + \hat{\Sigma}_L & H_{12} & & & 0 \\ H_{12} & H_2 & H_{23} & & \\ & H_{32} & H_3 & \ddots & \\ & & \ddots & \ddots & H_{N-1,N} \\ 0 & & & H_{N,N-1} & H_N + \hat{\Sigma}_R \end{bmatrix}$$

where,

$$\Sigma_L = \begin{bmatrix} \hat{\Sigma}_L & & & 0 \\ & 0 & & \\ & & 0 & \\ & & & \ddots \\ 0 & & & & 0 \end{bmatrix}$$

and,

$$\Sigma_R = \begin{bmatrix} 0 & & & 0 \\ & 0 & & \\ & & 0 & \\ & & & \ddots \\ 0 & & & & \hat{\Sigma}_R \end{bmatrix}$$

We now have to solve:

$$G(E) = [E + i0^+ - H_D - \Sigma_L - \Sigma_R]^{-1} \quad (1.68)$$

To do this, we have to compute the self energies by solving

$$\Sigma_L = H_{DL}g_0^l H_{LD} \quad \text{and} \quad \Sigma_R = H_{DR}g_0^r H_{RD} \quad (1.69)$$

with the surface Green's function g_0^l at the layer l_0 of the left contact and g_0^r at the layer r_0 of the right contact. We will present here an efficient scheme for finding the surface Green's function g_0^l and then the self energy Σ_L . This calculation can be of course used to determine the self energy Σ_R .

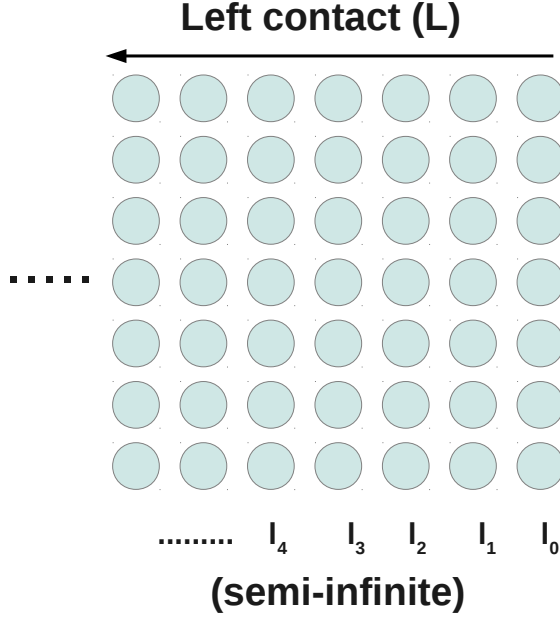


Figure 1.13: Schematic of semi-infinite left contact.

It has been shown [58] that the layer Green's functions in the contact are defined by the recursive relation as

$$g_n^l = [E + i0^+ - H_n^l - H_{n,n+1}^l g_{n+1}^l H_{n+1,n}^l]^{-1} \quad (1.70)$$

Normally, we assume that the contacts are semi-finite as illustrated in Fig. 1.13, $H_0^l = H_1^l = \dots = H_n^l$, $H_{01}^l = H_{12}^l = \dots = H_{n,n+1}^l$, and $H_{10}^l = H_{21}^l = \dots = H_{n+1,n}^l$. This leads to the fact that $g_0^l = g_1^l = \dots = g_n^l$ and thus we have

$$g_0^l = [E + i0^+ - H_0^l - H_{01}^l g_0^l H_{10}^l]^{-1} \quad (1.71)$$

In principle, this equation can be solved iteratively but the convergence is generally difficult. Here, we present two efficient methods: the fast iterative scheme developed by Sancho et al. (1984) and the analytical method which can be applied in some special cases.

A. Fast iterative scheme

First, we calculate the left self-energy. After Eq. 1.71 we have:

$$g_0 = [E^+ - H_0^l - H_{01}^l \Pi]^{-1} \quad (1.72)$$

where $\Pi = g_0 H_{10}^l = [E^+ - H_0^l - H_{01}^l \Pi]^{-1} H_{10}^l$, with $g_0 \equiv g_0^l$ and $E^+ \equiv E + i0^+$.

From the equation above, with note that $g_0^n = \Pi^n g_0$. We can then derive the following set of equations:

$$\begin{aligned} [E^+ - H_0^l - H_{01}^l \Pi] g_0 &= 1 \\ [E^+ - H_0^l] g_0 &= 1 + H_{01}^l \Pi g_0 \\ [E^+ - H_0^l] g_0 &= 1 + H_{01}^l g_0^1 \\ &\dots \\ \Pi [E^+ - H_0^l] g_0 &= \Pi (1 + H_{01}^l g_0^1) \\ [E^+ - H_0^l] \Pi g_0 &= \Pi + \Pi H_{01}^l g_0^1 \\ [E^+ - H_0^l] g_0^1 &= H_{10}^l g_0 + H_{01}^l g_0^2 \\ &\dots \\ [E^+ - H_0^l] g_0^n &= H_{10}^l g_0^{n-1} + H_{01}^l g_0^{n+1} \end{aligned}$$

from which we deduce that

$$g_0^n = [E^+ - H_0^l]^{-1} H_{10}^l g_0^{n-1} + [E^+ - H_0^l]^{-1} H_{01}^l g_0^{n+1} \quad (1.73)$$

By introducing the two quantities

$$\begin{aligned} t_0 &= [E^+ - H_0^l]^{-1} H_{10}^l \\ \tilde{t}_0 &= [E^+ - H_0^l]^{-1} H_{01}^l \end{aligned}$$

the Eq. 1.73 can be rewritten

$$g_0^n = t_0 g_0^{n-1} + \tilde{t}_0 g_0^{n+1}$$

with

$$\begin{aligned} g_0^{n-1} &= t_0 g_0^{n-2} + \tilde{t}_0 g_0^n \\ g_0^{n+1} &= t_0 g_0^n + \tilde{t}_0 g_0^{n+2} \end{aligned}$$

Now, we have

$$\begin{aligned} g_0^n &= t_0 (t_0 g_0^{n-2} + \tilde{t}_0 g_0^n) + \tilde{t}_0 (t_0 g_0^n + \tilde{t}_0 g_0^{n+2}) \\ g_0^n (1 - t_0 \tilde{t}_0 - \tilde{t}_0 t_0) &= t_0 t_0 g_0^{n-2} + \tilde{t}_0 \tilde{t}_0 g_0^{n+2} \end{aligned}$$

By defining

$$\begin{aligned} t_1 &= [1 - t_0\tilde{t}_0 - \tilde{t}_0t_0]^{-1}t_0^2 \\ \tilde{t}_1 &= [1 - t_0\tilde{t}_0 - \tilde{t}_0t_0]^{-1}\tilde{t}_0^2 \end{aligned}$$

We have

$$g_0^n = t_1g_0^{n-2} + \tilde{t}_1g_0^{n+2}$$

If we continue this iterative process, we have

$$\begin{aligned} g_0^{n-2} &= t_1g_0^{n-4} + \tilde{t}_1g_0^n \\ g_0^{n+2} &= t_1g_0^n + \tilde{t}_1g_0^{n+4} \\ g_0^n &= t_1(t_1g_0^{n-4} + \tilde{t}_1g_0^n) + \tilde{t}_1(t_1g_0^n + \tilde{t}_1g_0^{n+4}) \\ g_0^n(1 - t_1\tilde{t}_1 - \tilde{t}_1t_1) &= t_1^2g_0^{n-4} + \tilde{t}_1^2g_0^{n+4} \end{aligned}$$

Then,

$$\begin{aligned} t_2 &= [1 - t_1\tilde{t}_1 - \tilde{t}_1t_1]^{-1}t_1^2 \\ \tilde{t}_2 &= [1 - t_1\tilde{t}_1 - \tilde{t}_1t_1]^{-1}\tilde{t}_1^2 \\ g_0^n &= t_2g_0^{n-4} + \tilde{t}_2g_0^{n+4} \end{aligned}$$

To summarize:

$$\begin{aligned} g_0^n &= t_i g_0^{n-2^i} + \tilde{t}_i g_0^{n+2^i} \\ t_i &= [1 - t_{i-1}\tilde{t}_{i-1} - \tilde{t}_{i-1}t_{i-1}]^{-1}t_{i-1}^2 \\ \tilde{t}_i &= [1 - t_{i-1}\tilde{t}_{i-1} - \tilde{t}_{i-1}t_{i-1}]^{-1}\tilde{t}_{i-1}^2 \end{aligned}$$

Letting $n = 2^i$, the following chain of equations is obtained:

$$\begin{aligned} g_0^1 &= t_0g_0 + \tilde{t}_0g_0^2 \\ g_0^2 &= t_1g_0 + \tilde{t}_1g_0^4 \\ g_0^4 &= t_2g_0 + \tilde{t}_2g_0^8 \\ &\dots \\ g_0^{2^n} &= t_n g_0 + \tilde{t}_n g_0^{2^{n+1}} \end{aligned}$$

where

$$\begin{aligned}
g_0^1 &= t_0 g_0 + \tilde{t}_0 g_0^2 \\
&= t_0 g_0 + \tilde{t}_0 (t_1 g_0 + \tilde{t}_1 g_0^4) \\
&= (t_0 + \tilde{t}_0 t_1) g_0 + \tilde{t}_0 \tilde{t}_1 g_0^4 \\
&= (t_0 + \tilde{t}_0 t_1) g_0 + \tilde{t}_0 \tilde{t}_1 (t_2 g_0 + \tilde{t}_2 g_0^8) \\
&= (t_0 + \tilde{t}_0 t_1 + \tilde{t}_0 \tilde{t}_1 t_2) g_0 + \tilde{t}_0 \tilde{t}_1 \tilde{t}_2 g_0^8 \\
&\dots \\
&= (t_0 + \tilde{t}_0 t_1 + \tilde{t}_0 \tilde{t}_1 t_2 + \dots + \tilde{t}_0 \dots \tilde{t}_{n-1} t_n) g_0 + \tilde{t}_0 \dots \tilde{t}_{n-1} t_n g_0^{2^{n+1}}
\end{aligned} \tag{1.74}$$

This process is to be repeated until t_{n+1} , $\tilde{t}_{n+1} < \sigma$, as small as one wishes; then $g_0^{2^{n+1}} \sim 0$ and the equation above becomes (note that $g_0^1 = \Pi g_0$)

$$\Pi = t_0 + \tilde{t}_0 t_1 + \tilde{t}_0 \tilde{t}_1 t_2 + \dots + \tilde{t}_0 \dots \tilde{t}_{n-1} t_n \tag{1.75}$$

That means the self energy is calculated for left contacts.

$$\Sigma_L = H_{DL} g_0^l H_{LD} = H_{DL} \Pi g_0 H_{LD} \tag{1.76}$$

The self energy of the right contact is calculated in the same way.

B. Analytical method

This method can be used when we can find a transformation thanks to which all matrices H_0 , H_{01} and H_{10} can be diagonalized. After diagonalizing all matrices, the Eq. 1.71 becomes a set of equations of diagonal elements of the surface Green's function.

Now, we continue to determine the self-energies.

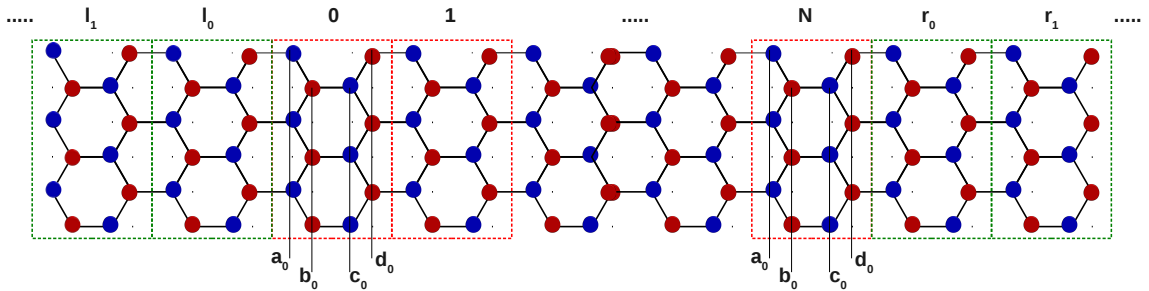


Figure 1.14: Schematic of a simple structure for analytical method.

$$\text{From the equation } g_n = [E^+ - H_n - H_{n,n+1} g_{n+1} H_{n+1,n}]^{-1}$$

We have the equation for surface Green's function at the right (after that to calculate for the right self-energy)

$$\begin{aligned}
g_{a_0} &= [E^+ - U_c - \alpha g_{b_0} \alpha^\dagger]^{-1} \\
g_{b_0} &= [E^+ - U_c - \beta g_{c_0} \beta]^{-1} \\
g_{c_0} &= [E^+ - U_c - \alpha g_{d_0} \alpha^\dagger]^{-1} \\
g_{d_0} &= [E^+ - U_c - \beta g_{a_1} \beta]^{-1} \\
&\dots
\end{aligned}$$

where α is the coupling of layer a_0 to b_0 , β is the coupling of layer b_0 to c_0 , as seen in Fig. 1.14. It is noted that here α is not diagonal matrix while β is diagonal.

The equation for surface Green's function at the left(after that to calculate for the left self-energy)

$$\begin{aligned}
g_{d_0} &= [E^+ - U_c - \alpha g_{c_0} \alpha^\dagger]^{-1} \\
g_{c_0} &= [E^+ - U_c - \beta g_{b_0} \beta]^{-1} \\
g_{b_0} &= [E^+ - U_c - \alpha g_{a_0} \alpha^\dagger]^{-1} \\
g_{a_0} &= [E^+ - U_c - \beta g_{d_1} \beta]^{-1} \\
&\dots
\end{aligned}$$

Within this technique, all matrices have to be diagonal, so they need to be diagonalized. This can be done as follows:

First, we find the eigenvectors of α and construct a transform matrix U : $U^\dagger \alpha U = \hat{\alpha}$. Here, $\hat{\alpha}$ is a diagonal matrix whose diagonal elements are eigenvalues of α . After that, using this transform, all matrices have diagonal forms. Hence, from the equation for surface Green's function at the right, we have

$$\begin{aligned}
\hat{g}_{a_0} &= [E^+ - U_c - |\hat{\alpha}|^2 \hat{g}_{b_0}]^{-1} \\
\hat{g}_{b_0} &= [E^+ - U_c - \beta^2 \hat{g}_{a_0}]^{-1}
\end{aligned}$$

So,

$$\hat{g}_{a_0} = [E^+ - U_c - \frac{|\hat{\alpha}|^2}{[E^+ - U_c - \beta^2 \hat{g}_{a_0}]}]^{-1}$$

Put: $\hat{g}_{a_0} \equiv \hat{g}_0$

$$\begin{aligned}
& \hat{g}_0[(E^+ - U_c)(E^+ - U_c - \beta^2 \hat{g}_0) - |\hat{\alpha}|^2] = (E^+ - U_c) - \beta^2 \hat{g}_0 \\
& -\hat{g}_0^2 \beta^2 (E^+ - U_c) + \hat{g}_0[(E^+ - U_c)^2 + \beta^2 - |\hat{\alpha}|^2] - (E^+ - U_c) = 0 \\
& \hat{g}_0^2 \beta^2 (E^+ - U_c) - \hat{g}_0[(E^+ - U_c)^2 + \beta^2 - |\hat{\alpha}|^2] + (E^+ - U_c) = 0 \\
& \Rightarrow \Delta = [(E^+ - U_c)^2 + \beta^2 - |\hat{\alpha}|^2]^2 - 4(E^+ - U_c)^2 \\
& \Delta = [(E^+ - U_c - \beta)^2 - |\hat{\alpha}|^2][(E^+ - U_c + \beta)^2 - |\hat{\alpha}|^2] \\
& \Rightarrow \hat{g}_0 = \frac{[(E^+ - U_c)^2 + \beta^2 - |\hat{\alpha}|^2] \pm \sqrt{\Delta}}{2\beta^2(E^+ - U_c)}
\end{aligned}$$

It is noted the real g_0 in the real space is determined as $g_0 = U\hat{g}_0U^\dagger$. From the determination of g_0 we can compute for the self energy.

1.8.2.2 Device Green's function calculation

The ballistic transmission coefficient can be computed from the equation

$$T(E) = \text{Trace}\{\Gamma_L[i(G_{11} - G_{11}^\dagger) - G_{11}\Gamma_L G_{11}^\dagger]\} \quad (1.77)$$

Or

$$T(E) = \text{Trace}\{[i(G_{NN} - G_{NN}^\dagger) - G_{NN}^\dagger\Gamma_R G_{NN}]\Gamma_R\} \quad (1.78)$$

We can compute $T(E)$ from G_{11} or G_{NN} . These elements of Green's function can be obtained as follows

For G_{11}

$$\begin{aligned}
& \text{Step 1: } G_{NN}^l = [E^+ - H_N - \Sigma_R]^{-1} \\
& \text{Step 2: for } q = N - 1, \dots, 2 \\
& G_{q,q}^l = [E^+ - H_q - H_{q,q+1}G_{q+1,q+1}^l H_{q+1,q}]^{-1} \\
& \text{Step 3: } G_{11}^l = [E^+ - H_1 - H_{12}G_{22}^l H_{21} - \Sigma_L]^{-1} \\
& \text{and } G_{11} \equiv G_{11}^l
\end{aligned}$$

For G_{NN}

$$\begin{aligned}
& \text{Step 1: } G_{11}^r = [E^+ - H_1 - \Sigma_L]^{-1} \\
& \text{Step 2: for } q = 2, \dots, N - 1 \\
& G_{q,q}^r = [E^+ - H_q - H_{q,q-1}G_{q-1,q-1}^r H_{q-1,q}]^{-1} \\
& \text{Step 3: } G_{NN}^r = [E^+ - H_N - H_{N,N-1}G_{N-1,N-1}^r H_{N-1,N} - \Sigma_R]^{-1} \\
& \text{and } G_{NN} \equiv G_{NN}^r
\end{aligned}$$

1.9 Conclusions

In this part, I have introduced some basic steps about tight binding model and Green's function techniques. Besides, some important physical quantities in energy and transport were also reviewed. Then, the calculating techniques are applied to investigate lots of characters such as energy band structure, transmission, LDOS, current, conductance, etc in the study of electronic and thermoelectric properties of unstrained/strained graphene systems in chapter 2 and 3.

Chapter 2

ELECTRONIC PROPERTIES OF STRAINED GRAPHENE JUNCTIONS

2.1 Introduction

In its simplest form, graphene is a flat single layer of carbon atoms that are tightly packed into a honeycomb-like crystalline lattice in a (2D) system. Thanks to lots of specific properties as mentioned above, graphene offers many advantages for electronic applications as well as thermal applications, such as high carrier mobility, exceeding $200\,000\text{ cm}^2\text{V}^{-1}\text{s}^{-1}$ [60], high current density 10^8 Acm^{-2} [1] and high thermal conductivity $5000\text{ Wm}^{-1}\text{K}^{-1}$ [61], etc. However, a single layer of graphene has a simple electronic spectra with zero-gap consisting of one conduction band and one valence band touching each other. As a result, the lack of energy gap between valence and conduction bands is a serious drawback of this material for practical applications. In particular, in graphene transistors it makes it very difficult to have a high ON/OFF current ratio and a really saturated current at high drain voltage. Regarding thermo-electric applications, the lack of bandgap makes it difficult to separate the opposite contributions of electrons and holes to the Seebeck coefficient. It results in a finite but small value of Seebeck coefficient $S < 100\text{V/K}$ in pristine graphene [62]. Therefore, a number of techniques to open a bandgap in graphene have been proposed, for instance, by cutting a graphene sheet into nanoribbons [63, 64], applying an electronic field perpendicular to a bilayer graphene sheet [65, 66], creating a system of many nanoholes on a 2D graphene sheet called graphene nanomesh [67, 68, 69, 70], applied strain engineering to monolayer [41, 42, 71] or twisted two layers graphene [72, 73, 74], stacking graphene with other 2D materials [75, 76], so on. The main features of these

graphene systems are reviewed and displayed in discussion below.

Otherwise, as mentioned in chapter 1, although many techniques have been suggested to open a bandgap in graphene, each of them still has its own issues. Hence, until now, bandgap engineering is still a timely and desirable topic for the development of graphene in nanoelectronics. In this work, we will use strain engineering as an alternative technique to modify the electronic bandstructure of graphene. In particular, we present the opening of bandgap in graphene by large strains, which is also studied by other groups. After that, our work focuses on the use of a small strain of a few percent, which is more achievable in experiments than a large strain. We will display the effects of a small strain to open a conduction gap, which can play in transport the same role as a real bandgap, in unstrained/strained junctions and the dependence of this conduction gap on the key parameters of the system.

The chapter 2 is organized as follows. After this first introductory section, the second section 2.2 presents the electronic structure of graphene and graphene nanostructures such as monolayer graphene, graphene nanoribbon, bilayer graphene, and graphene nanomesh. The section 2.3 shows the electronic structure of strained graphene, i.e., the bandgap opening under large strain and the shift of Dirac points in case of small strain of a few percent. In the section 2.4, we demonstrate a conduction gap of a few hundred meV can open in unstrained/strained graphene junctions with small strain. Moreover, we display the dependence of conduction gap on the strain amplitude, the direction of applied strain as well as the transport direction. Finally, a conclusion in section 2.5 to close the chapter 2.

2.2 Electronic properties of graphene nanostructures

In this section, we will introduce the main electronic features of monolayer graphene and its nanostructures, i.e., bilayer graphene, graphene nanoribbons, graphene nanomesh. It should be noticed that the overview of the electronic properties of graphene is described here using a simple nearest-neighbor tight-binding model.

2.2.1 Monolayer graphene

Graphene is made out of carbon atoms arranged in hexagonal structure, as seen in Fig. 2.1. The structure can be considered as a combination of two triangular lattices

with a basis of two atoms per unit cell. The lattice vector can be written as mentioned in chapter 1

$$\vec{a}_1 = a\left(\frac{3}{2}, \frac{\sqrt{3}}{2}\right), \quad \vec{a}_2 = a\left(\frac{3}{2}, -\frac{\sqrt{3}}{2}\right) \quad (2.1)$$

where $a \sim 1.42\text{\AA}$ is the carbon-carbon distance in graphene. The three nearest-neighbor vectors in real space are given by

$$\vec{r}_1 = -\frac{a}{2}(1, \sqrt{3}), \quad \vec{r}_2 = \frac{a}{2}(-1, \sqrt{3}), \quad \vec{r}_3 = a(1, 0) \quad (2.2)$$

while the six second-nearest neighbors are located at $\vec{r}_1' = \pm a_1$, $\vec{r}_2' = \pm a_2$ and $\vec{r}_3' = \pm(a_2 - a_1)$.

The reciprocal-lattice vectors are given by

$$\vec{b}_1 = \frac{2\pi}{3a}(1, \sqrt{3}), \quad \vec{b}_2 = \frac{2\pi}{3a}(1, -\sqrt{3}) \quad (2.3)$$

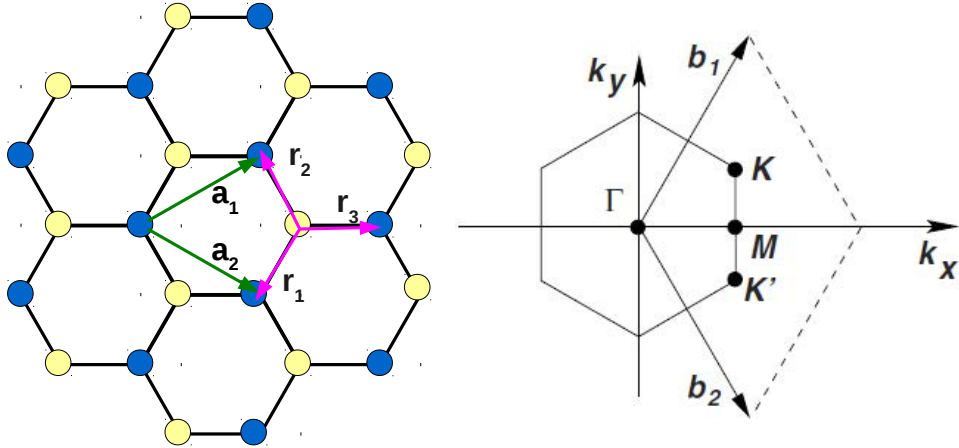


Figure 2.1: Honeycomb lattice of graphene and its Brillouin zone. Left panel: lattice structure made out of two triangular lattices (\vec{a}_1 and \vec{a}_2 are the unit vectors, and $\vec{r}_1, \vec{r}_2, \vec{r}_3$ are the nearest-neighbor vectors). Right panel: Brillouin zone in reciprocal space. The Dirac cones are located at the K and K' points.

Of particular importance for the physics of graphene are the two points K and K' at the corner of the graphene Brillouin zone (BZ). They are also called Dirac points. Their positions in momentum space are given by

$$\vec{K} = \left(\frac{2\pi}{3a}, \frac{2\pi}{3\sqrt{3}a}\right), \quad \vec{K}' = \left(\frac{2\pi}{3a}, -\frac{2\pi}{3\sqrt{3}a}\right) \quad (2.4)$$

In this work, we consider the lattice of graphene as a set of rectangular elementary cells of four carbon atoms, as can be seen in Fig. 2.2. The translation periods in

p and q directions are $L_x = 3a$ and $L_y = \sqrt{3}a$, respectively, where a is the carbon-carbon distance.

Generally, using the tight binding model, the Hamiltonian for graphene nanostructures is written as

$$H_{tb} = -t \sum_{n,m} (c_n^\dagger c_m + h.c.) \quad (2.5)$$

where c_n^\dagger and c_m are creation and annihilation operators, $\{n, m\}$ is the nearest neighbor index. Here, the hopping integral (t) corresponds to the transfer integral in tight binding model and the value of t is between -2.5 and -3.0 eV as mentioned in chapter 1.

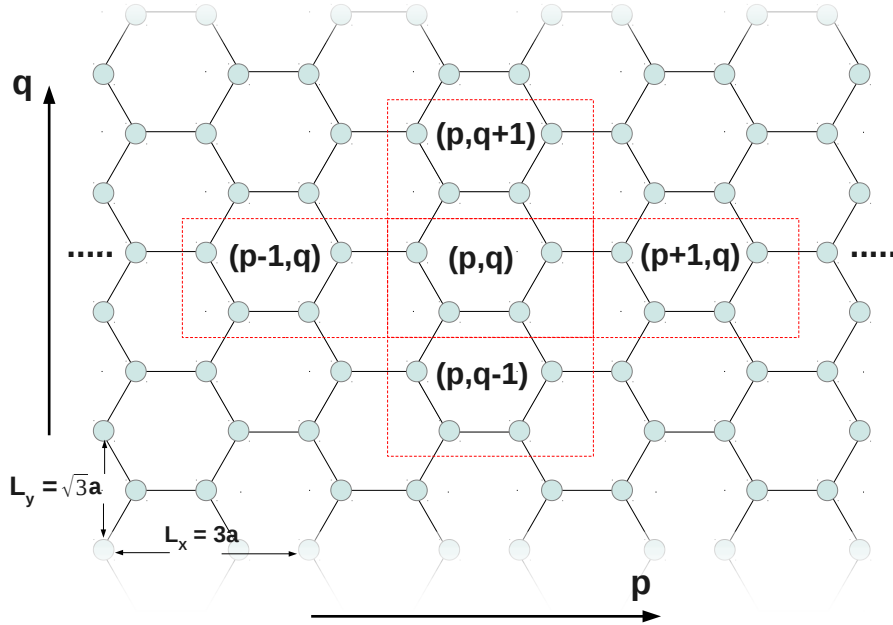


Figure 2.2: Sketch of 2D honeycomb lattice. The central block corresponds to an unit or elementary cell (p, q) consisting of four carbon atoms. The lengths $L_x = 3a$ and $L_y = \sqrt{3}a$ are the translation period in p and q directions, respectively. a is the nearest $C - C$ distance.

Otherwise, when the lattice is separated in unit cells as in Fig. 2.2 the Hamiltonian equation can be written as

$$H_{tb} = \sum_{p,q} H_{p,q \rightarrow q \pm 1} + H_{p,q} + H_{p \rightarrow p \pm 1, q} \quad (2.6)$$

where $H_{p,q}$ is the Hamiltonian of cell $\{p, q\}$, $H_{p,q \rightarrow q \pm 1}$ denotes the coupling of cell $\{p, q\}$ to cell $\{p, q \rightarrow q \pm 1\}$ along the direction OY and $H_{p \rightarrow p \pm 1, q}$ denotes the coupling of cell $\{p, q\}$ to cell $\{p \rightarrow p \pm 1, q\}$ along the transport direction OX.

We describe again the Hamiltonian in k -space ($\vec{k} = (k_x, k_y)$) by using the Fourier transform of the operators as

$$c_{n,p,q} = \frac{1}{\sqrt{M_{\text{cell}}}} \sum_{k_x, k_y} e^{ipk_x L_x + iqk_y L_y} c_{n, k_x, k_y} \quad (2.7)$$

Then,

$$\begin{aligned} \sum_{p,q} H_{p,q} &= \sum_{k_x, k_y} H_0(k_x, k_y) \\ \sum_{p,q} H_{p,q \rightarrow q \pm 1} &= \sum_{k_x, k_y} H_{0, \pm 1}(k_x, k_y), \quad \sum_{p,q} H_{p \rightarrow p \pm 1, q} = \sum_{k_x, k_y} H_{\pm 1, 0}(k_x, k_y) \end{aligned}$$

After that, we obtain

$$H_{tb} = \sum_{k_x, k_y} H_e(k_x, k_y) \quad (2.8)$$

with

$$H_e(k_x, k_y) = H_0(k_x, k_y) + H_{0, \pm 1}(k_x, k_y) + H_{\pm 1, 0}(k_x, k_y)$$

The Eq. 2.8 is a decoupled form of the Hamiltonian. Using this form we can easily find $E(k_x, k_y)$ by diagonalizing $H(k_x, k_y)$ independently for each vector \vec{k} .

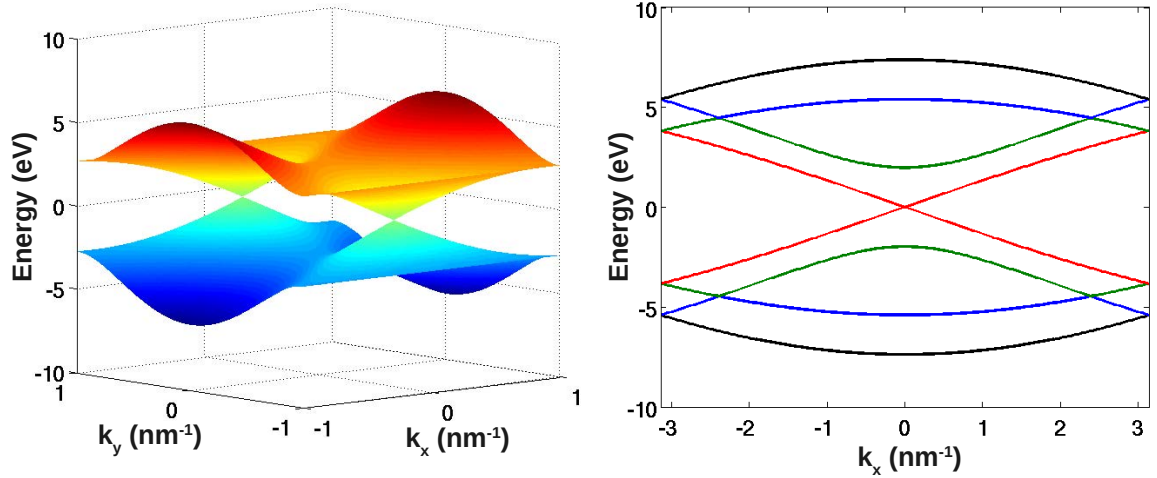


Figure 2.3: Electronic bandstructure in graphene lattice. Left panel: the full energy spectrum in 3 dimensions. Right panel: the energy bands along k_x direction.

In Fig. 2.3, we display the full band structure of graphene. As seen in the figure, the dispersion is (i) bounded by the energy interval $|E| \leq 3t$, (ii) symmetric (electron-hole symmetry) around zero energy, and (iii) linear in the vicinity of Dirac point. This dispersion can be written by expanding the full band structure, close to the K and K' points as

$$E(q) = \pm \hbar v_F \sqrt{q_x^2 + q_y^2} \quad (2.9)$$

with the Fermi velocity $v_F = 3at/2\hbar \sim 10^6 m/s$ and $\vec{q} = \vec{k} - \vec{K}$. This result was first obtained by Wallace in 1947. The most striking difference between this results and the usual case, $\epsilon(\vec{q}) = q^2/2m$, where m is the electron effective mass, is that the Fermi velocity in eq (2.9) does not depend on the energy or momentum, while for massive particles we have $v = q/m = \sqrt{2\epsilon/m}$ and hence this velocity changes substantially with carrier's energy or momentum.

2.2.2 Graphene nanoribbon structures

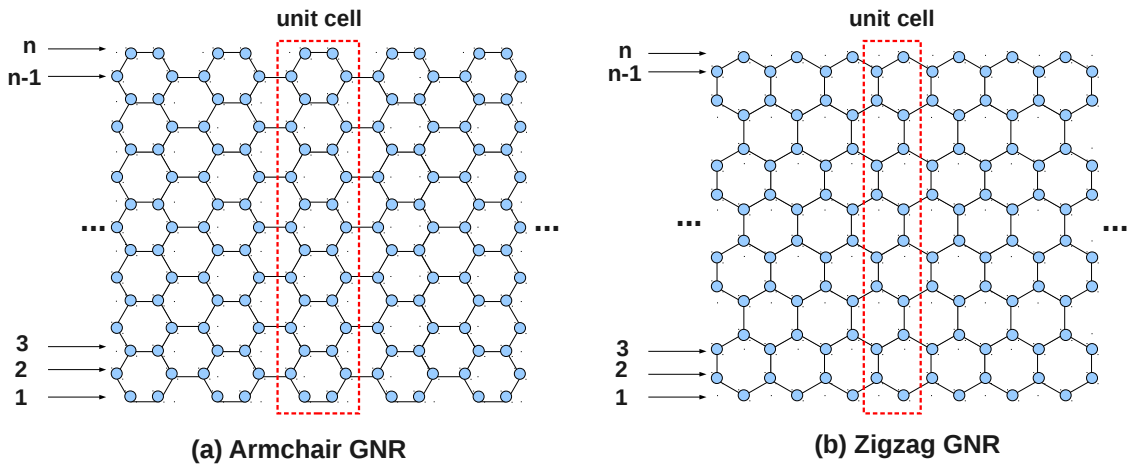


Figure 2.4: Sketch of graphene nanoribbons with (a) armchair and (b) zigzag edges. The GNRs are infinite following the direction of dots and the blocks in red rectangulars are the unit cells. n is number of carbon atom lines along the GNR width.

As mentioned above, thanks to its specific band structure and excellent carrier transport properties [3, 77], graphene has been expected to become an outstanding material for nanoscale electronics, specially for electronic applications [78, 79]. However, this wonderful material has also "an Achilles heel". The electric conduction cannot be turned off due to the lack of an energy bandgap, making it useless for designing transistors with high ON/OFF current ratio. The possibility of tuning the current is crucial for achieving the control of the current flow in electronic devices. Hence, opening a bandgap in graphene should overcome this drawback. Until now, so many different creative ways to do it have been proposed, as can be found in lots of Refs. in Section 2.1. One possible solution is to use narrow strips of graphene, also called graphene nanoribbons (GNRs).

In fact, graphene nanoribbons can be obtained by cutting a graphene sheet as shown in Fig. 2.4. There are two typical edge shapes: the armchair edge (Fig.

2.4(a)) and the zigzag edge (Fig. 2.4(b)). The atomic structure of nanoribbons with armchair and zigzag edge is represented in Fig. 2.5 and 2.6 respectively, along with their corresponding unit cells. Our results are in accordance with previous works [80, 81, 82, 83]. We denote here n the number of carbon lines along the width (as shown clearly in Fig. 2.4), which is the characteristic parameter that allows us to distinguish the metallic or semiconducting properties of nanoribbons.

In details, it is shown that two-thirds of armchair GNRs are semiconducting and the others are metallic, as can be seen in Fig. 2.5. The value of bandgap depends on the ribbon width, i.e., n . For $n = 3p + 2$ (p :integer), the bandgap is always equal to zero, meanwhile it is finite for $n = 3p$ or $n = 3p + 1$. Besides, as displayed in Fig. 2.5(a,b) the bandgap corresponding to the group of $3p$ is slightly larger than that in the group of $3p + 1$. By a similar way, the band structure of zigzag GNRs is also shown in three cases with $n = 3p$, $n = 3p + 1$ and $n = 3p + 2$ (Fig. 2.6). However, it is shown that zigzag GNRs are always metallic with zero bandgap. Since zigzag and armchair GNRs have different electronic structures, their transport properties are also very different. For instance, in zigzag GNRs, transport is dominated by dispersionless edge states, while no such edge state appears in perfect armchair ones.

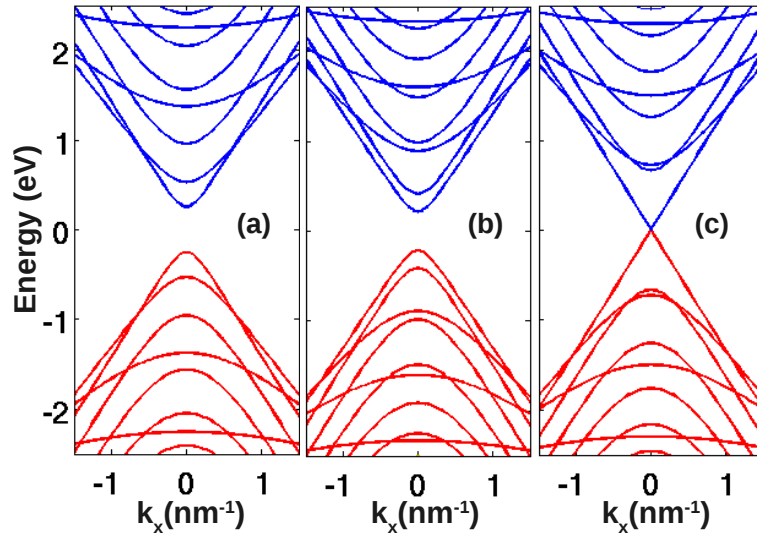


Figure 2.5: Electronic structure of armchair graphene nanoribbon is shown in three cases. (a) and (b) are semiconducting corresponding with $n = 3p$ and $n = 3p + 1$, respectively. (c) with $n = 3p + 2$ is metallic (p : an integer number).

However, the experiments have demonstrated that GNRs are always semiconducting with an energy bandgap depending on their width [63]. It was shown that the bandgap of GNRs does not depend on the orientation of lattice (in Fig. 2.7). That is

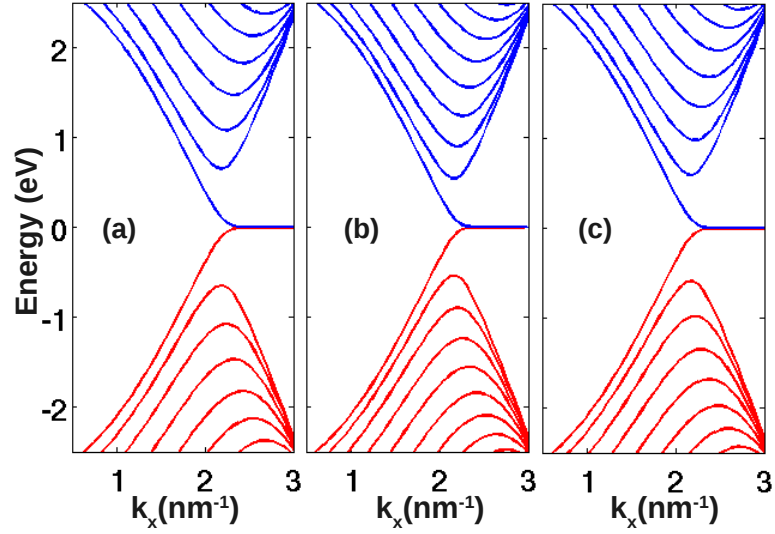


Figure 2.6: Electronic structure of zigzag graphene nanoribbon is shown in three cases with $n = 3p$, $n = 3p + 1$ and $n = 3p + 2$ (p : an integer number).

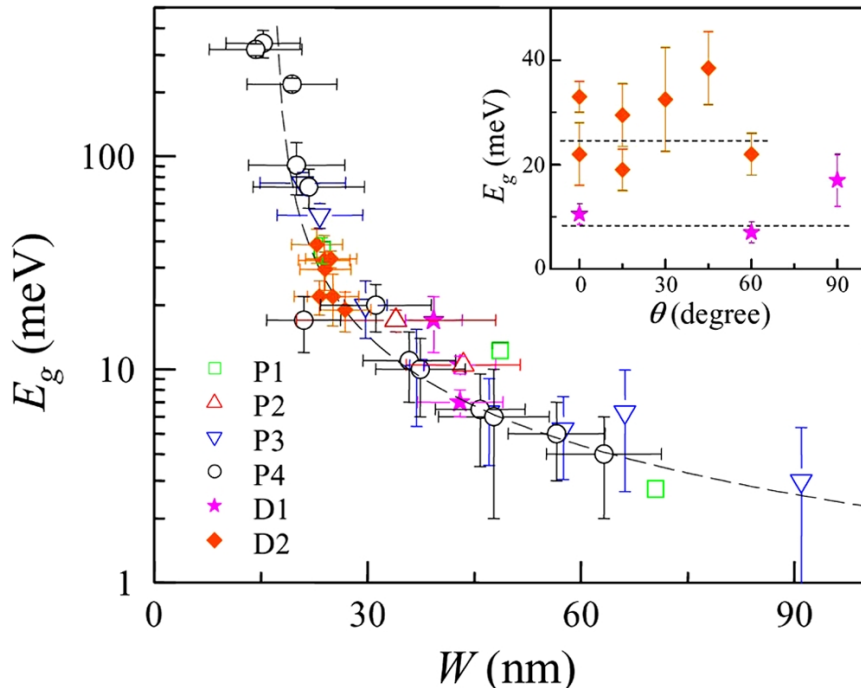


Figure 2.7: Energy bandgap E_g vs ribbon width W for six device sets with varying orientation. The inset shows E_g vs relative angle θ for the device sets D_1 and D_2 . Dashed line in the inset show the value of E_g as predicted by the empirical scaling of E_g vs W . From Y. Han *et al.* [63]

why there are lots of theoretical studies [80, 84, 85, 86, 87] dealing with this problem. Finally, it is demonstrated that features observed experimentally can be explained

by disorder effects, which are due to substrate or impurities, and especially edge roughness.

2.2.3 Bilayer graphene

The tight binding model developed for monolayer graphene can be easily extended to bilayer graphene. In fact, the case of bilayer graphene is interesting in itself, since with two graphene monolayers that are weakly coupled by interlayer carbon hopping, we have an intermediate case between graphene monolayer and bulk graphite, as shown in Fig. 2.8. In this bilayer structure, we assume that the layers are coupled with each other by a hopping energy between the atoms A_1 and A_2 , and all other possibilities are neglected. The tight binding Hamiltonian for this problem can be written as

$$H = -t \sum_{\langle i,j \rangle} (a_{i,p}^\dagger b_{j,p} + h.c.) - \gamma \sum_i (a_{i,1}^\dagger a_{i,2} + h.c.) \quad (2.10)$$

where the operators $a_{i,p}$ and $b_{j,p}$ act on the sites A and B, in plane $p = 1, 2$, respec-

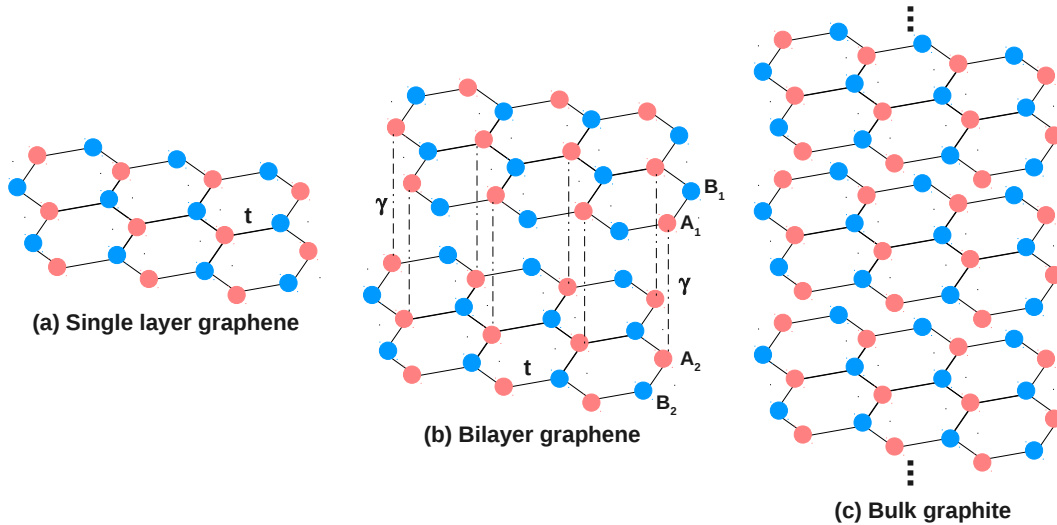


Figure 2.8: Lattice structure of single layer (a), bilayer graphene (b) and bulk graphite (c). t and γ are hopping parameters. The A and B sublattices are indicated with index 1,2 as shown in figure.

tively, and $\gamma = 0.39eV$ is the hopping energy between atoms A_1 and A_2 .

From this Hamiltonian, using a similar calculation to that described in the previous sections, the dispersion relation, by expanding the momentum close to the K -point in the Brillouin zone [88], is

$$E^2(k) = v_F^2 p^2 + \frac{\gamma^2}{2} + \frac{\Delta^2}{4} \pm \sqrt{\frac{\gamma^4}{4} + v_F^2 p^2 (\gamma^2 + \Delta^2)} \quad (2.11)$$

where $p = \hbar k$ is the magnitude of the momentum near the Dirac point, the potential

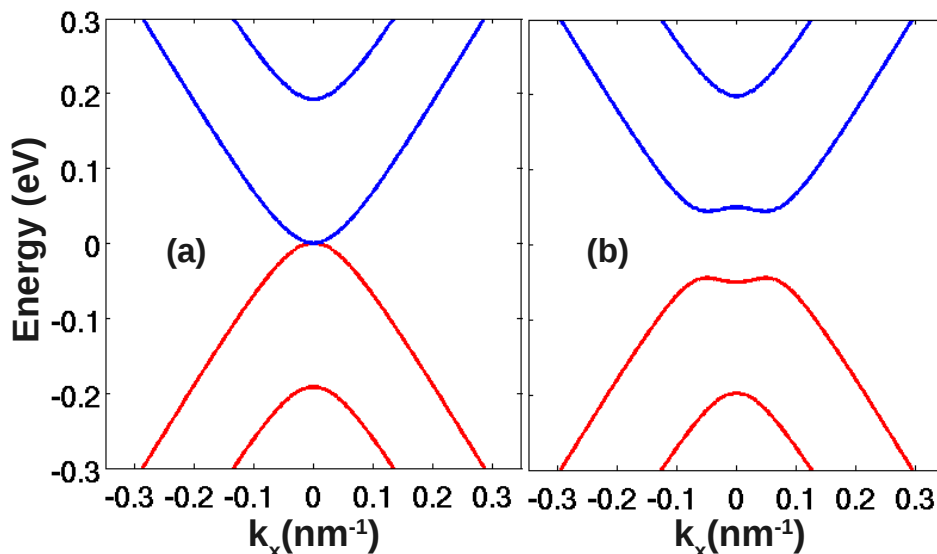


Figure 2.9: Energy bands of bilayer graphene calculated in two cases. Left panel (a): $\Delta = 0$ and right panel (b): $\Delta = 50\text{meV}$.

difference Δ between two graphene layers (this term will appear if an electric field is applied perpendicularly to the graphene sheet) has been introduced in the model. The energy bands are shown in Figs. 2.9 for $\Delta = 0$ and $\Delta = 50\text{ meV}$. Besides the electron-hole symmetry, differently from the case of monolayer graphene, carriers in the bilayer graphene are no longer massless but have a finite effective mass. If $\Delta = 0$ and $v_F p \ll \gamma$, one can eliminate the high energy states perturbatively, which gives

$$E(k) = \pm p^2/2m \quad (2.12)$$

with the effective mass $m = \gamma/2v_F^2 \approx 0.045m_e$. In the presence of finite Δ , the energy bandgap between the conduction and valence bands, occurring at $k \neq 0$, is

$$E_g = \frac{\gamma\Delta}{\sqrt{\Delta^2 + \gamma^2}} \quad (2.13)$$

For strong asymmetry $\Delta \gg \gamma$, it saturates at $E_g \approx \gamma$, and for weak asymmetry, we have $E_g \approx \Delta$. This behavior suggest a simple method to induce an energy bandgap in bilayer graphene. It consists in applying an electric field perpendicularly to the bilayer graphene sheet, which generates a potential difference between the two layers. This feature has been demonstrated experimentally [66]. The ability to open a gap makes bilayer graphene interesting for applications.

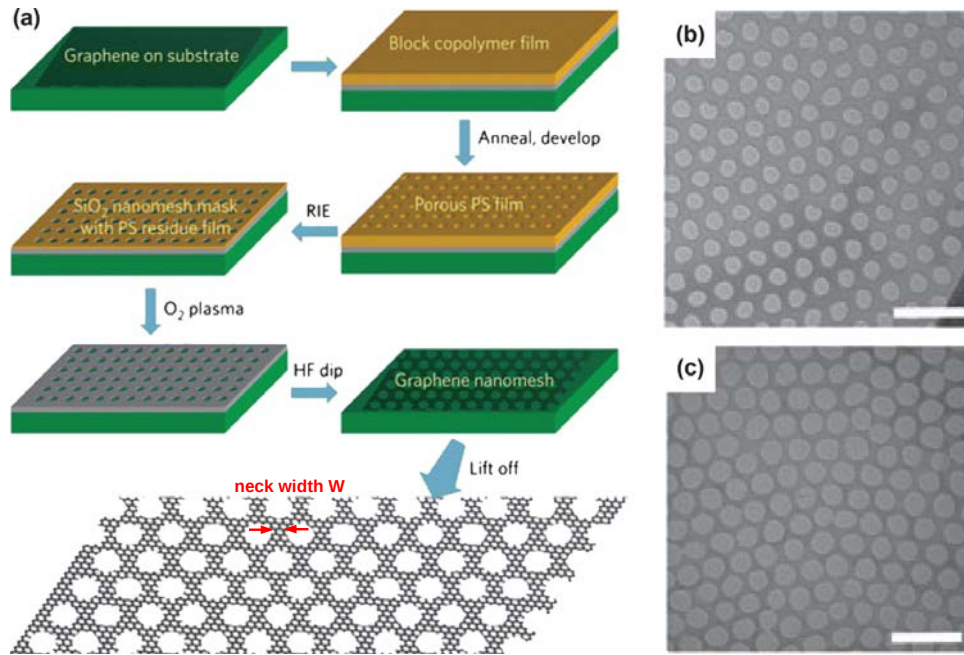


Figure 2.10: Example of fabrication of graphene nanomesh. (a) Schematics of the fabrication process by copolymer lithography. (b), (c) TEM images of graphene nanomesh with average neck width of 11.2 nm and 7.1 nm, respectively. From J. Bai et al. [67]

2.2.4 Graphene nanomesh

In GNRs, as discussed above, a bandgap may open and GNR-based FETs have been theoretically shown to give good performance. However, in practice these structures of graphene cannot be perfect and give rise to several issues as edge roughness-induced localization effect and Coulomb blockade effect [see in reviews [89] and references therein]. Especially, GNRs with a very narrow width to achieve a large bandgap are challenging to fabricate. For instance, a bandgap of 0.67 eV (like Ge) requires a GNR width of 2-3 nm. To overcome this limitation, a new graphene nanostructure with nonzero bandgap called graphene nanomesh (GNM) has been fabricated experimentally. It consists in a graphene sheet with a periodic array of nanoholes. The size of nanoholes and the neck width (the shortest distance between neighbor nanoholes) have to be controlled down to the sub-10 nm scale [67, 68, 90, 91], as can be seen in Fig. 2.10. This type of nanostructuring can open up a finite bandgap in large graphene sheets and hence GNM-based FETs had *ON/OFF* current ratio similar to those of GNR devices. However, GNM devices are able to carry electric currents about 100 times greater than a single GNR. Furthermore, the interest of GNMs is additionally due to the possibilities of bandgap engineering when varying the shape

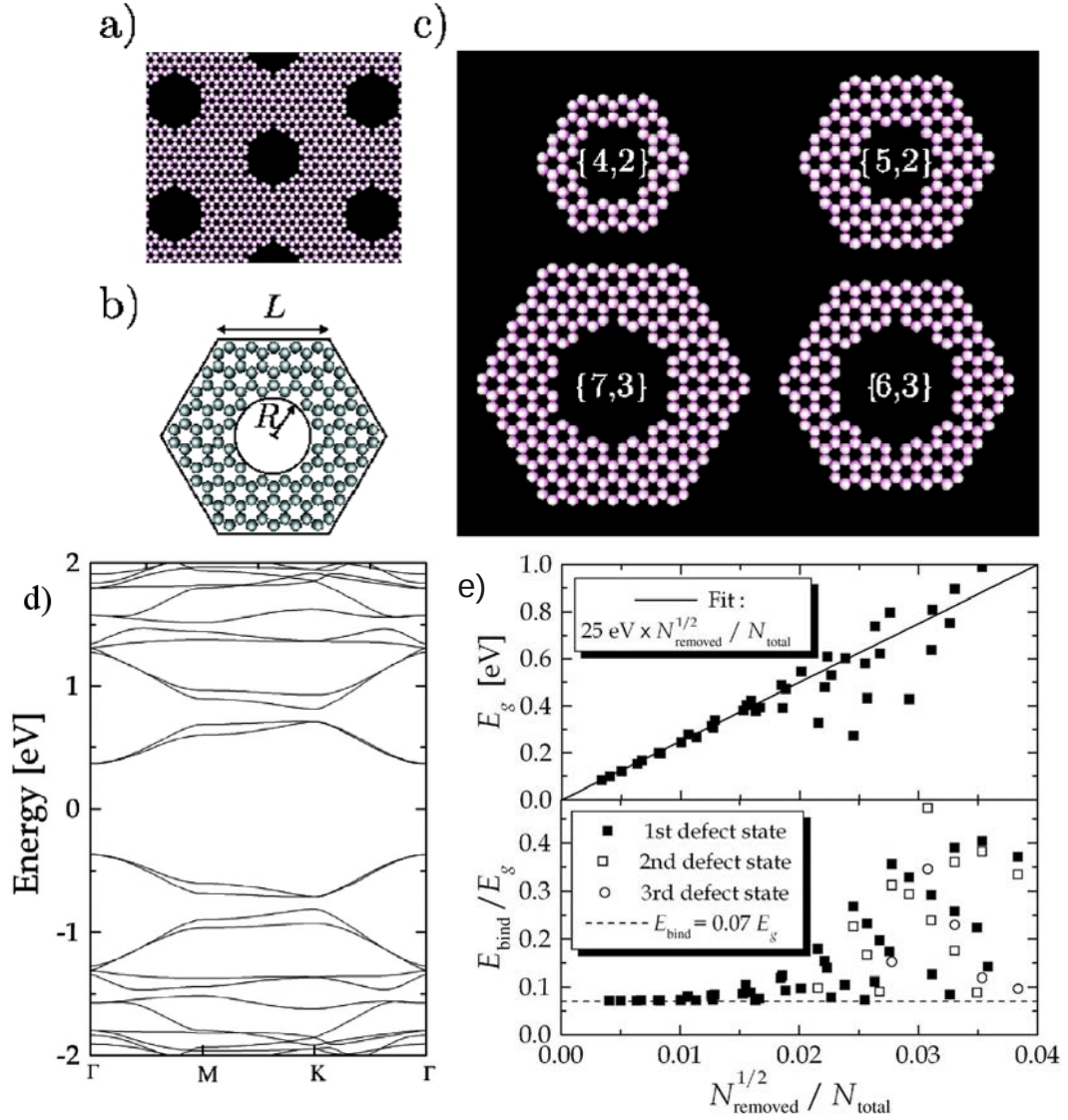


Figure 2.11: Illustration of the triangular antidot lattice (a) with a unit cell characterized by side length L and hole radius R (b). In (c), several examples with corresponding (L, R) parameters are shown. In (d), energy band structure for a $(7, 3)$ antidot lattice. (e) compilation of energy gaps, displayed versus $\sqrt{N_{\text{removed}}}/N_{\text{total}}$, very simple scaling is observed. From T. G. Pedersen *et al.* [93]

of nanoholes and the neck width.

A number of works [69, 70, 93, 94, 95, 96, 97, 98] have explored this subject. The studies in Refs. [69, 70, 93, 94, 95] have focused on the electronic structure of perfect GNM lattices, especially, on the property of bandgap depending on the lattice constant, the hole shape and the orientation (i.e., holes along zigzag or armchair direction). Scaling rules have been proposed in some of these works to explain and predict the behavior of bandgap (E_g) when varying the lattice parameters. However, the

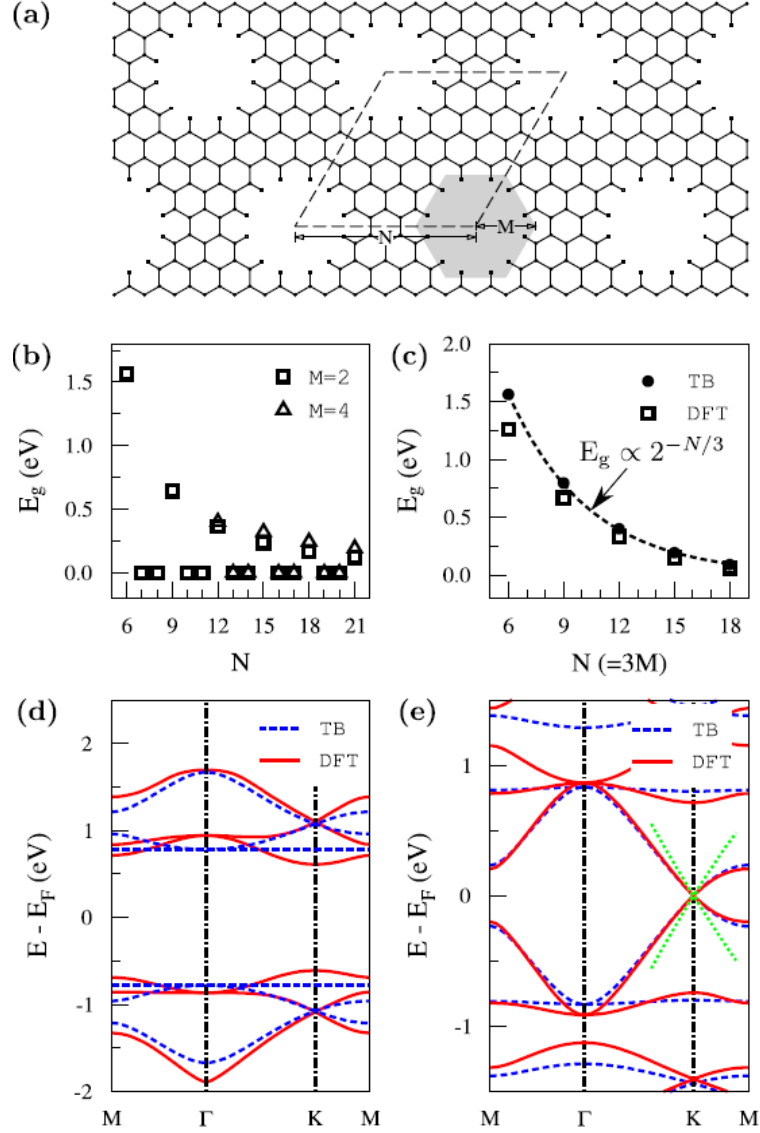


Figure 2.12: (a) Schematic of a triangular graphene antidot lattice. The unit cell indicated by dashed lines can be characterized by (N, M) , where N is the periodicity and M is the side length of the hexagonal hole. (b) The variation of bandgaps as a function of N with $M = 2$ and $M = 4$. (c) The variation of bandgaps as a function N with $M = N/3$. (d) The band structure of a $(6, 2)$ antidot lattice. (e) The band structure of a $(7, 2)$ antidot lattice. From A. Zhang *et al.* [69]

obtained results are very different. In particular, Pedersen *et al.* [93] considered the lattice of armchair circular hole and found the scaling rule $E_g \sim K\sqrt{N_{removed}}/N_{total}$ (constant $K \sim 25$ eV), where $N_{removed}$ is the number of removed carbon atoms in a super-cell containing originally N_{total} atoms, as can be seen in Fig. 2.11. However, this rule does not work well for large $\sqrt{N_{removed}}/N_{total}$ when E_g fluctuates very strongly

with the change of this ratio. Besides, together with the results obtained in Ref. [94], it has been shown that the scaling of E_g is also strongly dependent on the hole shape (circular holes in Ref. [93], triangular and rhombus holes in Ref. [94]). Furthermore, it was reported for different hole shapes that only one-third of considered GNMs in Ref. [69] have a significant bandgap, as can be seen in Fig. 2.12, while all GNMs in Ref. [94] are semiconductors. The authors of Ref. [69] also predicted the scaling rule $E_g \sim 2^{-N/3}$ for this kind of GNM lattice, where N is the super-cell lattice constant in the unit of $a = 1.42A^\circ$. Thus, the properties of E_g of perfect GNM lattice are very sensitive to the hole shape and to the lattice orientation, i.e., to whether we have zigzag or armchair holes.

Experimentally, Liang *et al.* [68] reported the bandgap scaling rule $E_g \sim 1/W_{nw}$ (W_{nw} is the neck width), which can be explained by the important role on the GNM bandgap of the quantum confinement in the multiple graphene nanoribbon network. A theoretical work [95] found the same rule for E_g (different from the rule proposed by Pedersen *et al.* [93]) when studying the lattices of irregular holes. However, the distribution of E_g is statistically quite wide at each W_{nw} . The work indicates that the GNM bandgap is very sensitive to even a small change in the hole edges. It is important to note that neither metallic GNMs nor the orientation effects have been experimentally observed [67, 68, 90, 91]. In those structures, the edge disorder of holes in the GNM lattice is inevitable. In addition, as suggested by the studies [86, 87] on disorder GNR structures, the mentioned disorder may be an important factor to explain the discrepancies between theoretical predictions and experiments.

The disagreement between theoretical and experimental studies motivated us to investigate the general feature of the bandgap in GNM lattices depending on the shape and size of holes as well as the effect of disorder of edges. Our results have been published in Ref. [98]. First, we have computed the bandgap E_g of the lattice of perfectly periodic holes to understand its dependence on the lattice parameters. In Fig. 2.13, we plot E_g as a function of the super-cell lattice constant W for different hole shapes and for different orientations (zigzag holes in Fig. 2.13(a) and armchair holes in Fig. 2.13(b)). In general, it is shown that E_g of semiconducting GNMs decreases with an increase of the super-cell lattice constant W . Qualitatively, this is in agreement with the experiments. However, it confirms again a big difference between the lattice of zigzag and armchair holes. In the case of zigzag holes, the results for the hole shape of type (1) in Fig. 2.13 (already studied in Ref. [69]) show that a finite bandgap is observed when the index Q (note that $Q = W/a_c$ with $a_c = 2.46A^\circ$) is a multiple of 3, while all other GNMs are semimetallic. This feature

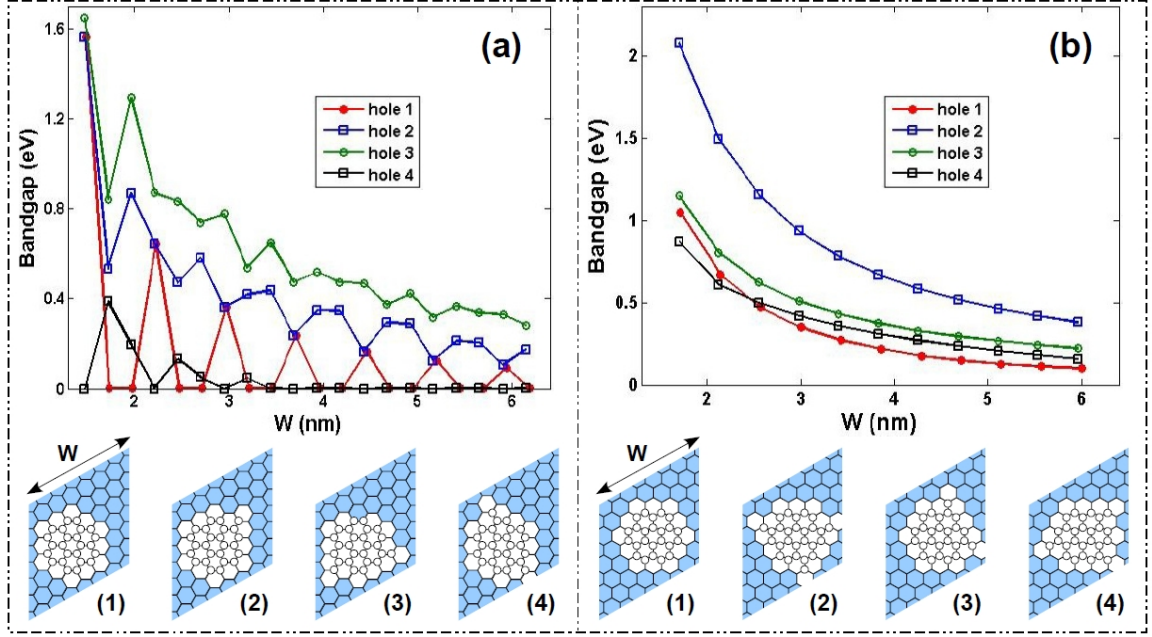


Figure 2.13: Energy gap of GNM lattices as a function of the super-cell lattice constant for different hole shapes. (a) is for zigzag holes while (b) is for armchair holes. The super-cells of considered GNM lattices, where white circles indicate the removed carbon atoms, are presented in the bottom of the two sub-figures. From Nguyen *et al.* [98]

has been explained in Ref. [69] as a consequence of the intervalley scattering between different Dirac points of pristine graphene when the holes are created. However, our results in Fig. 2.13 (a) demonstrate that this is not the case of other hole shapes even with a small change compared to the holes of type (1) and, additionally, the scaling rule $E_g \sim 2^{-Q/3}$ (here $Q \equiv N$ in Ref. [69]) is not applicable. For instance, the lattice with the hole shape (4) behave contrary to the previously suggested law, i.e., they are semimetals when Q is a multiple of 3, while others are semiconductors. In this case, the GNM bandgap decreases very rapidly with an increase of W . Besides, no semi-metallic GNMs with holes of type 2 and 3 are observed. Considering the lattices of armchair holes, we find from the results displayed in Fig. 2.13(b) that all studied GNMs are semiconducting. However, E_g is also sensitive to the change in the hole shape. It is important to note that the bandgap E_g in the case of holes of type (1), which have been studied by Pedersen *et al.* in Ref. [93], is fitted accurately with the scaling rule $E_g \sim \sqrt{N_{removed}}/N_{tot}$. However, this rule does not work well for other cases of holes (2), (3) and (4) shown in Fig. 2.13(b). Consistently with the previous works, our results demonstrate two important points for the lattices of perfectly periodic holes: (1) the GNM bandgap is very sensitive to the change

in the hole shape and the lattice orientation, (2) it is hence difficult to determine theoretically a unique scaling rule to describe the bandgap for all kinds of perfect GNM lattice.

In the next step of this study of GNMs lattice, we go to consider the disorder effects on the energy gap of GNM lattices. Here, we choose to present the results obtained for the lattices wherein the holes numbered (1) in Fig. 2.13, which are close to the holes fabricated in experiments [67, 68] are original holes. As explained above, the other holes (e.g., see Fig. 2.13) probably occur in the considered lattices with a few percent fraction. As done in [87, 99], we compute the conductance at zero temperature and then measure the transport gap around the zero energy point, which is an image of the bandgap of the considered lattice. Note that all transport quantities are computed averagely over 40 disordered samples. In Fig. 2.14(a), we plot the conductance of the GNM lattices as a function of energy computed using different disorder strengths. In this figure, the lattices of zigzag holes with $Q = 13$ are used. Similarly to the metallic GNRs studied in [86, 87, 99], the ordered GNM lattice is a semimetal, i.e., no conduction gap is observed for $P_D = 0\%$ in Fig. 2.14(a). When the disorder is present, the conductance is strongly suppressed, especially near the neutrality (zero energy) point, and a deep conduction gap develops near this point when the disorder strength increases. The same feature is obtained for the samples originating from the semiconducting lattices of perfectly periodic holes, but the enhancement of conduction gap is weaker than that in the metallic ones.

In Fig. 2.14(b), we display the energy (conduction) gap as a function of the super-lattice constant W for different orientations (zigzag and armchair holes) and different disorder strengths. In what follows, we use the terms semiconducting (metallic) GNMs to identify the lattices originating from semiconducting (metallic) GNMs of perfectly periodic holes. As mentioned above, while the conduction gap of semiconducting GNMs is slightly enlarged, the gap of metallic ones strongly broadens when increasing the disorder strength. Therefore, no metallic GNMs of zigzag holes are detected and the dependence of energy gap on W tends to a unique scaling rule in the case of strong disorder. Additionally, the results presented in Fig. 2.14(b) also show that the orientation effects are suppressed and the same scaling rule is obtained for two different orientations in strongly disordered lattices, e.g., see the case of $P_D = 8\%$. As an important result, the energy gap in this case is fitted very well with the scaling rule $E_g = \alpha/W_{nm}$ [68] where $\alpha \sim 0.6$ eV nm. The difference between the value of α obtained here and $\alpha = 0.8 - 0.95$ eV nm in [68] can be attributed to the fact that the holes we consider are smaller and the disorder seems to be weaker

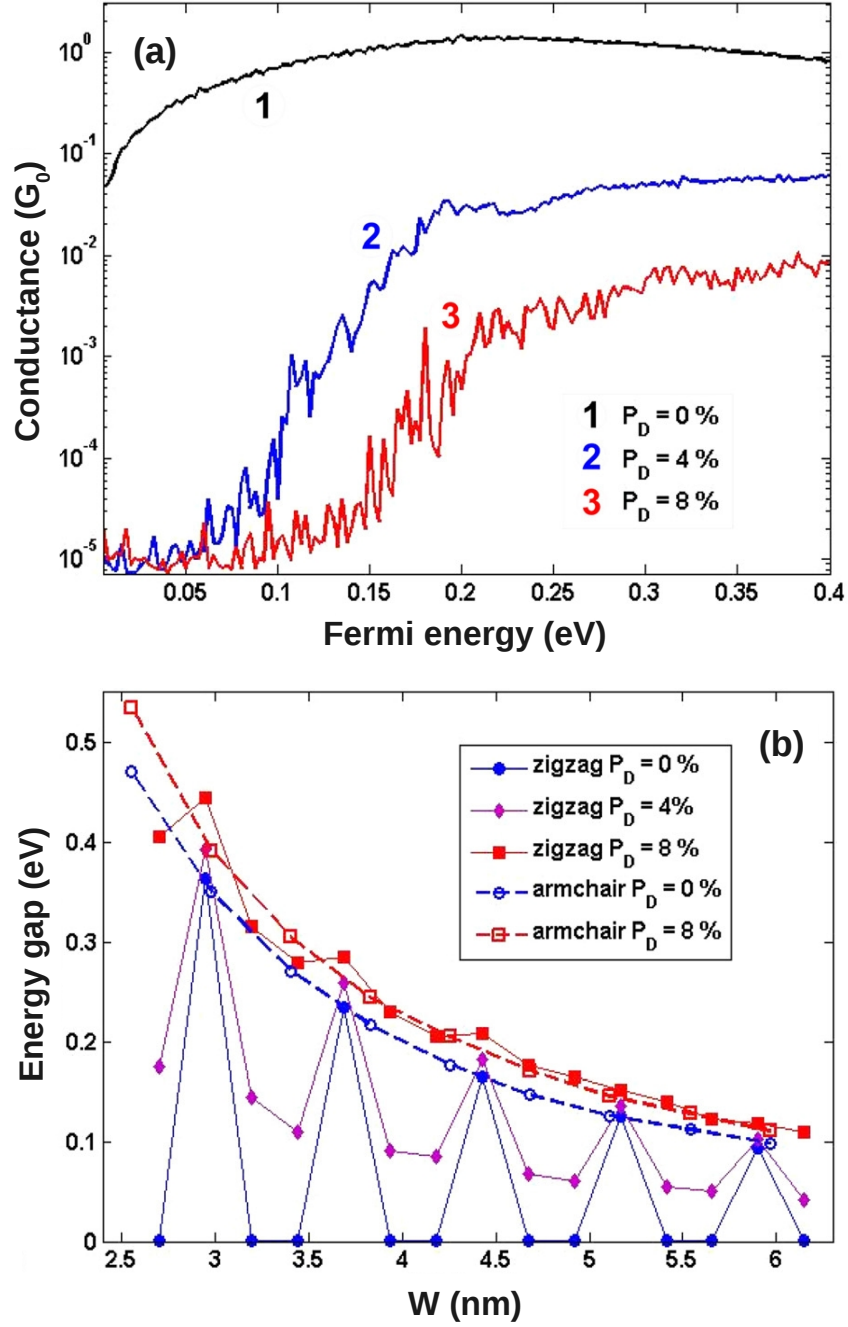


Figure 2.14: (a) Conductance in the unit of $G_0 = e^2W_G/hW$ as a function of Fermi energy for different disorder strengths. (b) Energy gap of the GNM lattices as a function of the super-cell lattice constant with disorder effects. From Nguyen *et al.* [98]

than in the case studied in [68]. Moreover, the simulation of different original holes (results not displayed here) shows that not only the orientation effects but also the sensitivity of E_g to the shape of original holes are significantly suppressed, especially

when the disorder is sufficiently strong for the holes of different shapes to contribute equivalently to the electronic properties of the sample. We find again that the scaling rule proposed by Pedersen *et al* [93] works well only for small values of $\sqrt{N_{rem}}/N_{tot}$ (i.e., $\lesssim 0.01$) but not for large $\sqrt{N_{rem}}/N_{tot}$. However, the energy gap E_g is fitted better (and well) with the rule, experimentally verified in [68], $E_g = \alpha/W_{nm}$ in all different cases of strongly disordered lattices examined.

These results are very similar to those observed for disordered GNRs in [86, 87, 99] and demonstrate that the edge disorder of holes is one of the important factors, which weakens the lattice symmetry effects and makes the effects of quantum confinement in the nanoribbon crossing network of GNM lattices dominant. It explains well the behavior of energy gap observed in experiments [68].

2.3 Electronic properties of strained graphene

As mentioned above, many techniques to open a bandgap in graphene have been suggested. However, as shown in lots of discussions, each method still has its Achilles heel, in particular in their fabrication, and need to be further confirmed by experiments. In this section, we consider strain engineering, which has been shown to be an

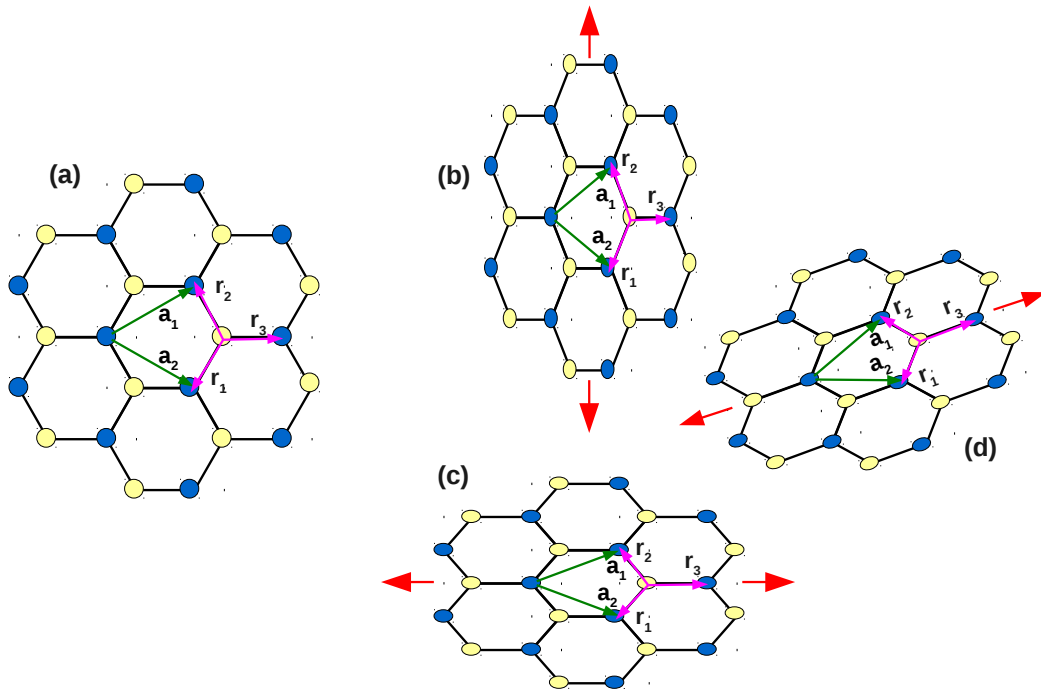


Figure 2.15: Graphene (a) and strain graphene (b, c, d). The strain is applied along a zigzag axis in (b), a armchair axis in (c) and any axis in (d).

alternative/promising approach to modulating the electronic properties of graphene material.

2.3.1 Basic equations

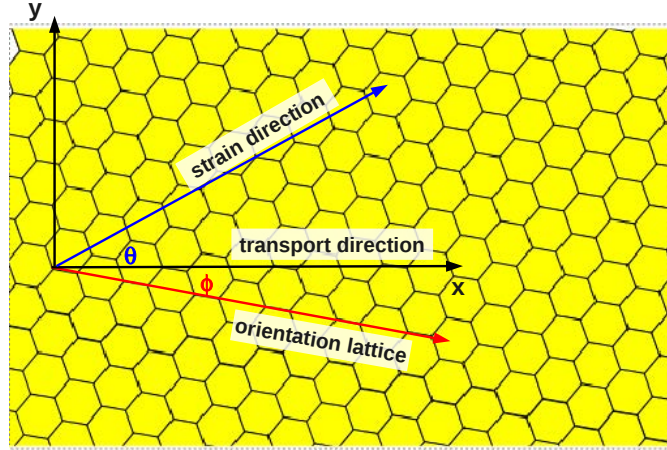


Figure 2.16: Schematic of strained graphene lattice. (θ, ϕ) are the angles of strain direction with respect to transport direction and of transport direction with respect to armchair direction.

We illustrate in Fig. 2.15 some graphene sheets stretched by strain. We show graphene lattices strained along armchair direction (Fig. 2.15(b)), zigzag direction (Fig. 2.15(c)) or any direction (Fig. 2.15(d)). Clearly, the basis vectors and vectors of unit cell are changed under the effect of strain. Hence, in this part, we show the method and corresponding equations to compute the feature of band structure as well as transport characters in strained graphene sections.

First, we describe strained graphene lattice in detail with its key parameters in Fig. 2.16. It is noted that (θ, ϕ) are the angles of strain direction with respect to transport direction and of transport direction with respect to armchair direction. The Hamiltonian in the π -orbital tight binding model is $H_{tb} = \sum_n U_n c_n^\dagger c_n - \sum_{nm} t_{nm} c_n^\dagger c_m$. Here, U_n is the on-site/potential energy that can be modulated by the external voltage, $c_n(c_n^\dagger)$ is the operator which annihilates (creates) an electron on the n th site of the graphene lattice, and the sum in (n,m) is restricted to the nearest-neighbor atoms with a hopping energy t_{nm} .

The application of a uniaxial strain of angle (θ) causes the following changes in

the $C - C$ bond vectors:

$$\begin{aligned} \vec{r}_{nm}(\sigma) &= \{1 + M_s(\sigma, \theta)\} \vec{r}_{nm}(0) \\ M_s(\sigma, \theta) &= \sigma \begin{bmatrix} \cos^2\theta - \gamma\sin^2\theta & (1 + \gamma)\sin\theta\cos\theta \\ (1 + \gamma)\sin\theta\cos\theta & \sin^2\theta - \gamma\cos^2\theta \end{bmatrix} \end{aligned} \quad (2.14)$$

where σ represents the strain amplitude and $\gamma \simeq 0.165$ is the Poisson ratio [100]. The hopping parameters are defined as $t_{nm}(\sigma) = t_0 \exp[-3.37(r_{nm}(\sigma)/r_0 - 1)]$, where the hopping energy $t_0 = -2.7$ eV and the bond length $r_{nm}(0) \equiv r_0 = 0.142$ nm in the unstrained case. Therefore, there are three different hopping parameters $t_{1,2,3}$ corresponding to the three bond vectors $\vec{r}_{1,2,3}$, respectively, in the strained graphene part of the structure in Fig. 2.17. It is noticed that in the specific cases where the strain is applied along a zigzag axis ($\theta = 90^\circ, \phi = 0^\circ$) or an armchair axis ($\theta = 0^\circ, \phi = 0^\circ$), we only have to consider two different hopping parameters $t_{1,2}$ in the armchair and zigzag directions, respectively, corresponding to two bond vectors $\vec{r}_{1,2}$ in strained graphene section.

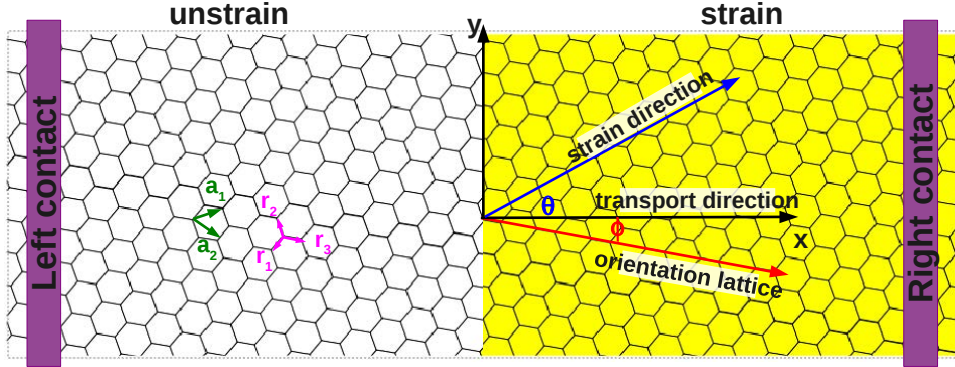


Figure 2.17: Schematic of unstrained/strained graphene junctions.

In this work, we investigate a 2D graphene channel as seen in Fig. 2.17, i.e., the lateral size W (along the Oy direction) of the graphene sheet is much larger than the length (along the Ox direction and, e.g., \sim a few tens of nm) of the active region. We assume a 1D profile of applied strain, i.e., the strain tensor, is a function of position along the transport direction while it is constant along the perpendicular one. Note that here, Ox (resp. Oy)-axis is parallel (resp. perpendicular) to the transport direction. The transport direction, ϕ , and strain direction, θ , are defined as shown in Fig. 2.16 as well as Fig. 2.17. Based on the tight binding model, the conduction gap in strained junctions which is a finite gap of conductance can be described by using two possible methods as follows:

Green's function calculations. We split the graphene sheet into the smallest possible unit cells periodically repeated along the Ox and Oy directions with the indices p and q , as shown in Fig. 2.2, respectively [97]. The tight-binding Hamiltonian can therefore be expressed in the following form (similar to in section 2.2):

$$H_{tb} = \sum_{p,q} H_{p,q \rightarrow q-1} + H_{p \rightarrow p-1,q} + H_{p,q} + H_{p,q \rightarrow q+1} + H_{p \rightarrow p+1,q} \quad (2.15)$$

where $H_{p,q}$ is the Hamiltonian of cell $\{p, q\}$, and $H_{p,q \rightarrow q \pm 1}$ denotes the coupling of cell $\{p, q\}$ to cell $\{p, q \pm 1\}$ and $H_{p \rightarrow p \pm 1,q}$ denotes the coupling of cell $\{p, q\}$ to cell $\{p \pm 1, q\}$.

In the simulated devices, we assume the lateral size (along the Oy direction) of the graphene sheet to be much larger than the length (along the Ox direction) of the active region between the two contacts (which will be investigated in chapter 3). Therefore, the potential energy U_n in equation of Hamiltonian can be modeled as a function of x only. Here, the channel, i.e., unstrained/strained graphene channel, is considered as an infinite sheet and the translational symmetry of the crystal lattice can be applied along the Oy direction. Hence, we can Fourier transform the operators in Eq. 2.15 as follows:

$$c_{n,p,q} = \frac{1}{\sqrt{M_{cell}}} \sum_{\kappa_y} e^{iq\kappa_y} \hat{c}_{p,\kappa_y} \quad (2.16)$$

where the indices n,p,q denote the n th site in the cell p,q and M_{cell} is the number of unit cells and $\kappa_y \equiv k_y L_y$ with the size L_y of unit cells along the Oy direction. The Hamiltonian Eq. 2.15 is finally rewritten as a sum of κ_y -dependent 1D-components:

$$\begin{aligned} H_{tb} &= \sum_{\kappa_y} \hat{H}(\kappa_y) \\ \hat{H}(\kappa_y) &= \sum_p \hat{H}_{p \rightarrow p-1}(\kappa_y) + \hat{H}_p(\kappa_y) + \hat{H}_{p \rightarrow p+1}(\kappa_y) \end{aligned} \quad (2.17)$$

In this form, since the terms $\hat{H}_{p \rightarrow p \pm 1}$ are obtained by Fourier transform of the operators $H_{p \rightarrow p \pm 1,q}$ which describe only the coupling between the cells of the same index q , they are k_y -independent. In contrast, the term $\hat{H}_p(\kappa_y)$ determined from the Fourier transform of the first three operators in Eq. 2.15 is k_y -dependent.

From the Hamiltonian Eq. 2.17, the non-equilibrium Green's function formalism can be easily applied to study the charge transport in graphene junctions. With the assumption that left and right contacts are semi-infinite along transport direction Ox, the problem of device-to-contact coupling has been detailed in chapter 1, within the

concept of self-energy. The device retarded Green's function for a given momentum k_y is then defined as

$$G(E, k_y) = [E + i0^+ - \hat{H}(k_y) - \Sigma_L(E, k_y) - \Sigma_R(E, k_y)]^{-1} \quad (2.18)$$

where $\Sigma_{L(R)}$ is the self-energy describing the device-to-left (-right) contact coupling. The transmission probability needed to define the conductance is calculated as

$$\mathcal{T}_\epsilon(\epsilon, k_y) = \text{Tr} \{ \Gamma_L G \Gamma_R G^\dagger \}$$

where $\Gamma_{L(R)} = i(\Sigma_{L(R)} - \Sigma_{L(R)}^\dagger)$ is the transfer rate at the left (right) contact. Then, we can compute the transport quantities in the graphene-strained junction with different transport directions. In particular, the conductance at zero temperature is determined as:

$$\mathcal{G}(\epsilon) = \frac{e^2 W}{\pi h L_y} \int_{BZ} d\kappa_y \mathcal{T}(\epsilon, \kappa_y) \quad (2.19)$$

where $W \equiv M_{cell} L_y$ and $\mathcal{T}(\epsilon, \kappa_y)$ is the transmission probability computed from the Green's functions. The integration over κ_y is performed in the whole first Brillouin zone. As in ref. [98, 101], the gap of conductance (conduction gap or transport gap) is then measured from the obtained data of conductance.

Bandstructure analysis. To determine the conduction gap of strained junctions, we find that another simple way based on the analysis of graphene bandstructures could be efficiently used. It is described as follows. Since the conductance is computed from Eq. 2.19, the appearance of conduction gap is essentially governed by the gaps of transmission probability, which is determined from the energy gaps in the unstrained and strained graphene sections. These energy gaps can be defined directly from the graphene bandstructures. Therefore, our calculation is in two steps, similarly to that in [101, 102]. From the graphene bandstructures obtained using the tight-binding Hamiltonian above, we first look for the energy gaps $E_{unstrain}^{gap}(\kappa_y)$ and $E_{strain}^{gap}(\kappa_y)$ for a given κ_y of both graphene sections. The maximum of these energy gaps determines the gap $E_{junc}^{gap}(\kappa_y)$ of transmission probability through the junction. Finally, the conduction gap $E_{cond.gap}$ is obtained by looking for the minimum value of $E_{junc}^{gap}(\kappa_y)$ when varying κ_y in the whole Brillouin zone.

In particular, the equation of energy bands in pristine graphene is given by

$$E(k) = \pm |t_0 e^{i\vec{k}\vec{a}_1} + t_0 e^{i\vec{k}\vec{a}_2} + t_0| \quad (2.20)$$

where the plus/minus sign corresponds to the conduction/valence band, respectively.

This equation is changed in strained graphene as follows

$$E(k) = \pm |t_1 e^{i\vec{k}\vec{a}_1} + t_2 e^{i\vec{k}\vec{a}_2} + t_3| \quad (2.21)$$

where \vec{a}_1 and \vec{a}_2 are two basis vectors of the lattice, as shown in 2.15.

It is noted that when the transport direction is the armchair orientation ($\phi = 0^\circ$) or the zigzag orientation ($\phi = 30^\circ$), it is straightforward to determine the basis vectors and the unit cell of the lattice. However, for any given direction (ϕ), in principle, the vectors $\vec{L}_{x,y}$ defining the size of unit cells along the Ox and Oy directions, respectively, can be always expressed as

$$\begin{cases} \vec{L}_x = n_1 \vec{a}_1 + n_2 \vec{a}_2 \\ \vec{L}_y = m_1 \vec{a}_1 + m_2 \vec{a}_2 \end{cases} \quad (2.22)$$

With condition

$$\vec{L}_x \vec{L}_y = 0$$

So, we have the relationship among n_1, n_2, m_1 and m_2 given by

$$\frac{m_1}{m_2} = -\frac{n_1 + 2n_2}{2n_1 + n_2} \quad (2.23)$$

* In case of armchair direction: $n_1 = n_2 = 1; m_1 = 1; m_2 = -1$ ($\phi = 0^\circ$)

$$\vec{a}_1 = \frac{\vec{L}_x + \vec{L}_y}{2} \quad ; \quad \vec{a}_2 = \frac{\vec{L}_x - \vec{L}_y}{2} \quad (2.24)$$

The energy bands are given by

$$E(\vec{k}) = \pm |t_1 e^{i\vec{k}\vec{L}_y/2} + t_2 e^{-i\vec{k}\vec{L}_y/2} + t_3 e^{-i\vec{k}\vec{L}_x/2}| \quad (2.25)$$

* In case of zigzag direction: $n_1 = 1; n_2 = 0; m_1 = 1; m_2 = -2$ ($\phi = 30^\circ$)

$$\vec{a}_1 = \vec{L}_x \quad ; \quad \vec{a}_2 = \frac{\vec{L}_x - \vec{L}_y}{2} \quad (2.26)$$

The energy bands are given by

$$E(\vec{k}) = \pm |t_1 e^{i\vec{k}\vec{L}_x/2} + t_2 e^{-i\vec{k}\vec{L}_y/2} + t_3 e^{-i\vec{k}\vec{L}_x/2}| \quad (2.27)$$

2.3.2 Opening of bandgap under large strain

We calculate directly the energy bands of 2D strained graphene lattice in the case of transport direction ($\phi = 0$) (that means the transport direction is the armchair orientation of lattice). As mentioned above, the energy bands in that case are given by

$$E(\vec{k}) = \pm |t_1 e^{i\vec{k}\vec{L}_y/2} + t_2 e^{-i\vec{k}\vec{L}_y/2} + t_3 e^{-i\vec{k}\vec{L}_x/2}|$$

That means

$$E(\vec{k})^2 = (t_1 \cos \frac{\vec{k}\vec{L}_y}{2} + t_2 \cos \frac{\vec{k}\vec{L}_y}{2} + t_3 \cos \frac{\vec{k}\vec{L}_x}{2})^2 + (t_1 \sin \frac{\vec{k}\vec{L}_y}{2} - t_2 \sin \frac{\vec{k}\vec{L}_y}{2} - t_3 \sin \frac{\vec{k}\vec{L}_x}{2})^2$$

$$E(\vec{k})^2 = (t_1 - t_2)^2 + t_3^2 + 4t_1 t_2 \cos^2 \frac{\vec{k}\vec{L}_y}{2} + 2t_3 [(t_1 + t_2) \cos \frac{\vec{k}\vec{L}_y}{2} \cos \frac{\vec{k}\vec{L}_x}{2} - (t_1 - t_2) \sin \frac{\vec{k}\vec{L}_y}{2} \sin \frac{\vec{k}\vec{L}_x}{2}]$$

For a given kL_y , the bottom of conduction bands (BCB) $E_{BCB}(kL_y)$ is obtained for

$$\begin{cases} \cos(\frac{kL_x}{2}) = \frac{t_1 + t_2}{\sqrt{(t_1 - t_2)^2 + 4t_1 t_2 \cos^2 \theta_y}} \cos(\frac{kL_y}{2}) \\ \sin(\frac{kL_x}{2}) = \frac{t_2 - t_1}{\sqrt{(t_1 - t_2)^2 + 4t_1 t_2 \cos^2 \theta_y}} \sin(\frac{kL_y}{2}) \end{cases}$$

Introducing the parameter $\kappa_y = kL_y$, the description of energy bands of strain graphene becomes

$$E(\kappa_y) = 2 \left| \sqrt{(t_1 - t_2)^2 + 4t_1 t_2 \cos^2 \frac{\kappa_y}{2}} + t_3 \right| \quad (2.28)$$

Strain graphene has no bandgap ($E(\kappa_y) = 0$) when the equation below has a solution

$$\cos^2 \frac{\kappa_y}{2} = \frac{t_3^2 - (t_1 - t_2)^2}{4t_1 t_2} \quad (2.29)$$

which corresponds to

$$0 \leq \frac{t_3^2 - (t_1 - t_2)^2}{4t_1 t_2} \leq 1 \quad (2.30)$$

As a consequence, the opening of bandgap in strained graphene depends on the solution of equation (2.29). Otherwise, if we put $f(t) = \frac{t_3^2 - (t_1 - t_2)^2}{4t_1 t_2}$, then $f(t)$ depends on the amplitude of strain σ and its applied direction θ . The relationship (2.29) is displayed in Fig. 2.18 as a function of strain direction for different strain amplitudes. Here, the function $f(t)$ is described for both tensile and compressive strain cases with a range of strain amplitude from 0 to 30% and the angle θ changing from 0 to 180°. It can be seen that the value of cosin function varies from 0 to 1 when the amplitude of strain varies from 0 to $\sim 23\%$. It means that equation (2.29) can be solved and 2D

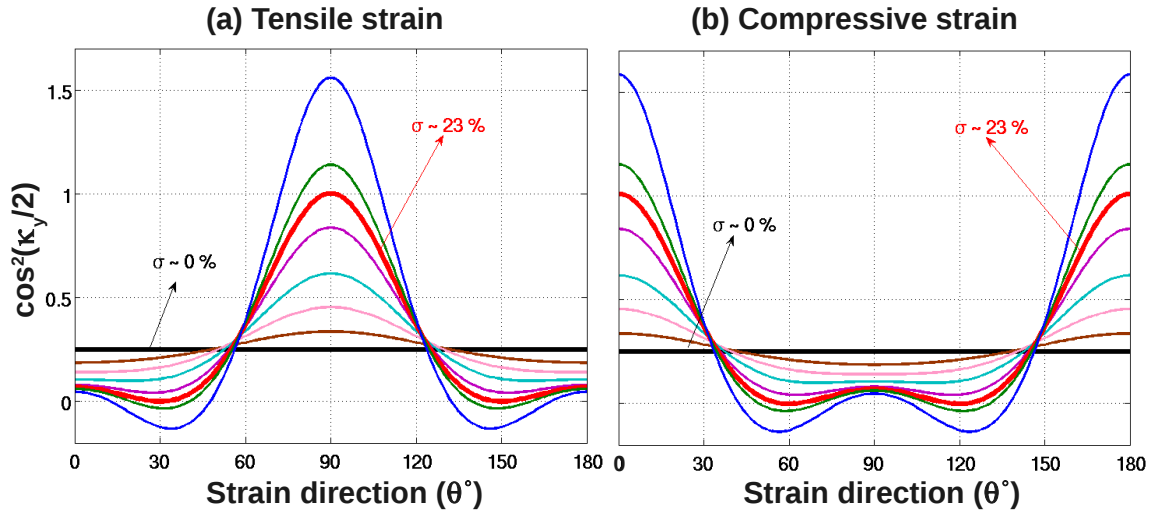


Figure 2.18: Sketch of the relationship (2.29) as a function of strain direction for different strain amplitudes. A strain $\sigma > 23\%$ is required to open a bandgap in graphene.

strained graphene lattice has no bandgap. Therefore, a strain ($\sigma \geq 23\%$) is required to open a bandgap in a graphene sheet. This result has been shown first by V. M. Pereira *et al* as illustrated in Fig. 2.19 [71]. These authors have concluded that (i) the gap threshold is at strain ($\sim 23\%$), (ii) the behavior of the system is periodic in the angle of applied strain (θ) with period $\pi/3$, in accordance with the symmetry of the lattice; (iii) tension along the zigzag direction ($\theta = 0, \pi/3, \dots$) is more effective in overcoming the gap threshold, and (iv) tension along the armchair direction never generates any gap.

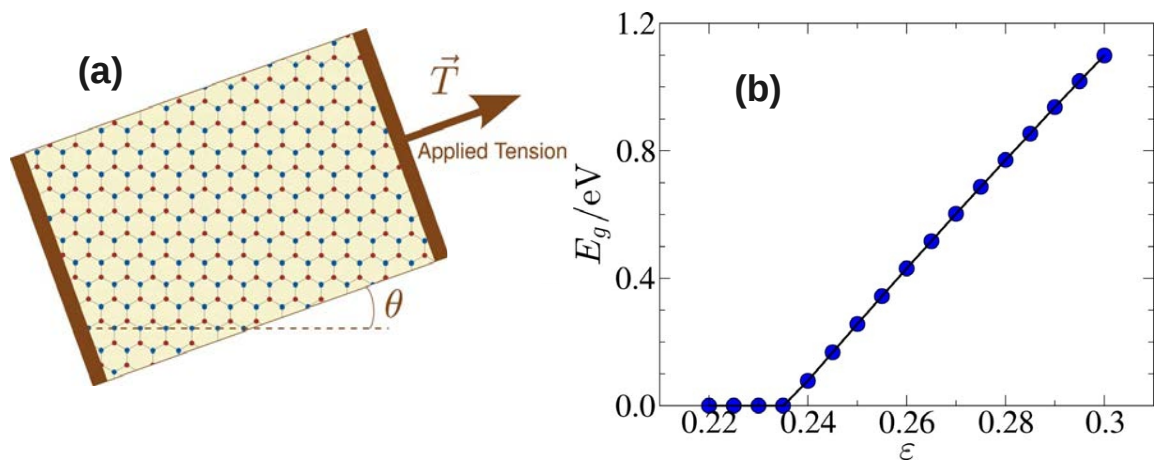


Figure 2.19: Strain is applied on a 2D graphene sheet in (a). The strain dependence of bandgap (E_g) is shown in (b). From V. M. Pereira *et al.* [71]

Next, we examine the formation of the bandgap of graphene under a uniaxial strain and compare these results with Pereira's results. First, we display the feature of bandgap in 2D graphene sheet in Fig. 2.20 with strain strength ranging from 0 to 30%. It can be seen clearly in Fig. 2.20(a) that, in case of *tensile strain*, a finite bandgap opens only for strain larger than $\sim 23\%$ and the zigzag (not armchair) is the preferred direction for bandgap opening. This result is in agreement with the result of V. M. Pereira *et al* [71]. Then, we extend our investigation to the case of *compressive*

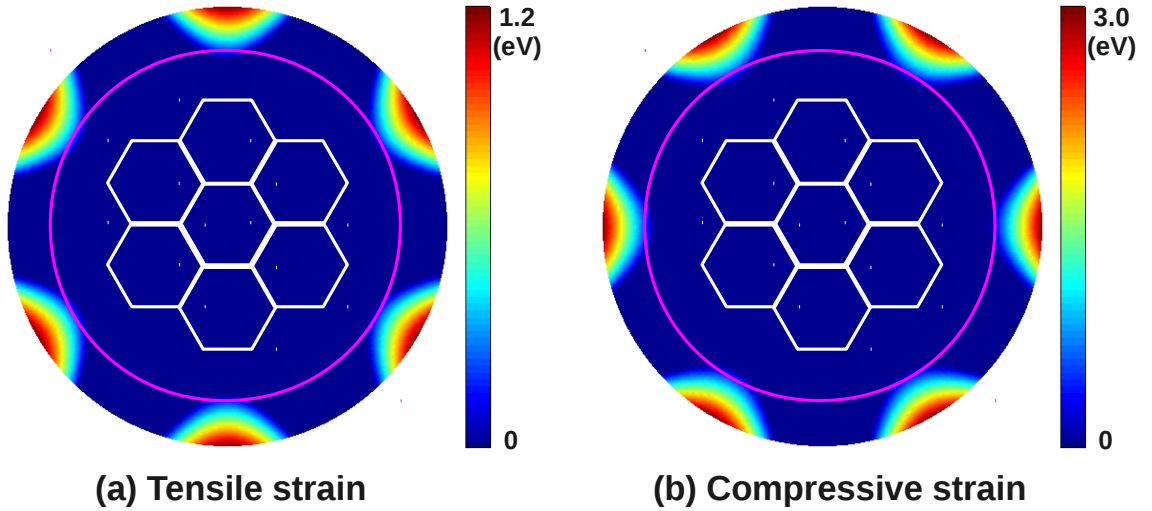


Figure 2.20: Dependence of graphene bandgap on the applied strain and its direction: tensile (a) and compressive (b). The radius from the central point indicates strain strength ranging from 0 (center) to 30% (edge of maps), while the graphene lattice is superimposed to show visibly the strain direction. The pink circle corresponds to the strains of $\sigma = 23\%$.

strain, as seen in Fig. 2.20(b) and find that (i) the same gap threshold of $\sigma \sim 23\%$ is observed but (ii) the preferred direction to open the gap under a *compressive strain* is the armchair direction, not the zigzag one, as in the case of *tensile strain*. This implies that the properties of graphene bandstructure at low energy should be qualitatively the same when applying strains of $\{\sigma, \theta\}$ and of $\{-\sigma, \theta + 90^\circ\}$. This feature can be understood by considering, for example, strain of $\{\sigma, \theta = 0^\circ\}$ and of $\{-\sigma, \theta = 90^\circ\}$. This property is proved in Appendix A. Indeed, these strains result in the same qualitative changes on the bond-lengths, i.e., an increased bond-length r_3 and reduced bond-length $r_{1,2}$. However, for the same strain amplitude, because of the exponential dependence of hopping energies on the bond-lengths, the *tensile strain* generally induces a smaller bandgap than the *compressive strain*, as can be seen when comparing the data displayed in figure 2.20(a) and (b). Clearly in the case of same

strain amplitude, i.e., strain of 30%, the maximum of bandgap in the former cannot reach to $2.0eV$ while the maximum of bandgap in the latter is larger than $3.0eV$. To conclude this part, we would like to emphasize again that a large strain ($\geq 23\%$) is necessary to open a bandgap in graphene.

2.3.3 The shift of Dirac point by a small strain of a few percent

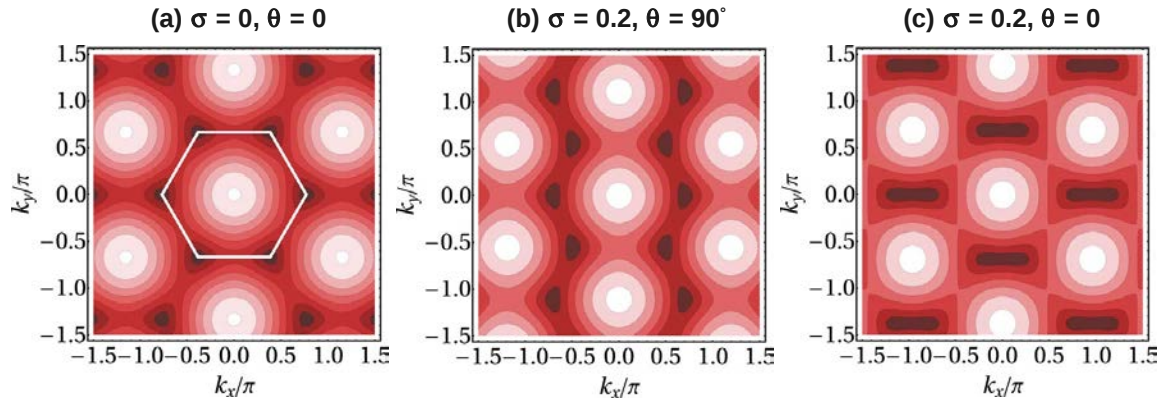


Figure 2.21: Schematic show density plots of the energy dispersion, $E(k_x, k_y)$, for $\{\sigma = 0, \theta = 0\}$ (a), $\{\sigma = 0.2, \theta = 90^\circ\}$, and $\{\sigma = 0.2, \theta = 0\}$. From V. M. Pereira *et al.* [71]

As shown in the previous subsection, a large strain ($\geq 23\%$) is required to open a bandgap in a graphene sheet and a small strain of a few percent cannot change its gapless character. However, some studies in Ref. [71, 101, 102, 103] have shown that a small strain causes the shift of Dirac points in k -space which may lead to dramatic changes of electronic transport features. In particular, Pereira *et al.* [71] concluded that under a real deformation both lattice and hopping parameters are affected. The lattice deformation causes the distortion of Brillouin zone, as can be seen in Fig. 2.21. Clearly, in case of Fig. 2.21(a) without strain, the position of Dirac points is fixed in the density plot of energy dispersion, and hence the Brillouin zone is known to be a hexagon. By applying a strain of 20% along Oy axis (Fig. 2.21(b)) or along Ox axis (Fig. 2.21(c)), the Dirac cones move in opposite directions (they never meet) in the former case while they always approach each other (they eventually merge) in the latter case [71]. The shift of Dirac points has been observed experimentally by M. Huanget *al* [104], as seen in Fig. 2.22.

Regarding unstrained/strained graphene junctions in our work (on the top of Fig. 2.23), the position of Dirac points in each part and their strain-induced shift

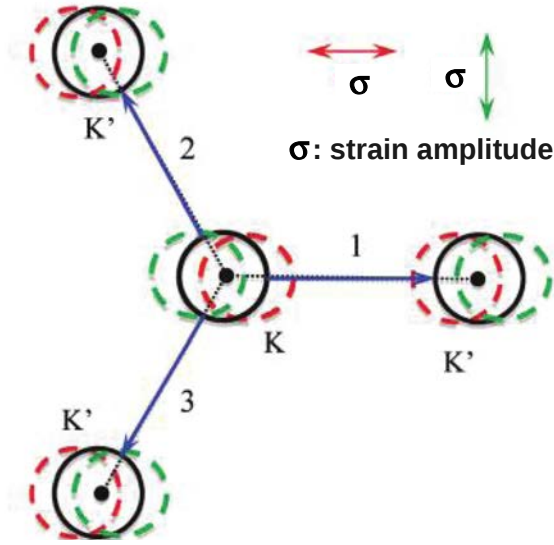


Figure 2.22: Three Raman scattering paths (arrows labeled by 1, 2, 3) from the Dirac cone at K point to the three nearest Dirac cones at K points (circles). The dashed red and green circles indicate the strain-induced movement of the Dirac cone for the zigzag and armchair sample, respectively. The double headed arrows show the strain directions. From M. Huang *et al.* [104]

are described in the bottom of Fig. 2.23. Here, this shift leads to the opening of conduction gap in graphene heterojunctions which is discussed in details in the next parts.

2.4 Opening of a conduction gap (transport gap) in strained graphene junctions

A small strain of a few percent cannot change the gapless character of graphene, i.e., there is no gap of conductance in case of uniformly strained graphene though Dirac points are displaced, as experimentally demonstrated in [104, 105]. As reported in our recent work [101], a significant conduction gap of a few hundreds meV can open in the unstrained/strained graphene junctions. The appearance of this conduction gap is due to the strain-induced shift of Dirac points. This phenomenon will be discussed detailed in this part.

Throughout this section, the junction of unstrained/strained graphene (as can be seen in the Fig. 2.23) is studied. In fact, to create this junction on a 2D graphene sheet, a small strain of a few percent is applied on one half section. The key parameters are the strain amplitude (σ), the direction of applied strain (θ) and the transport

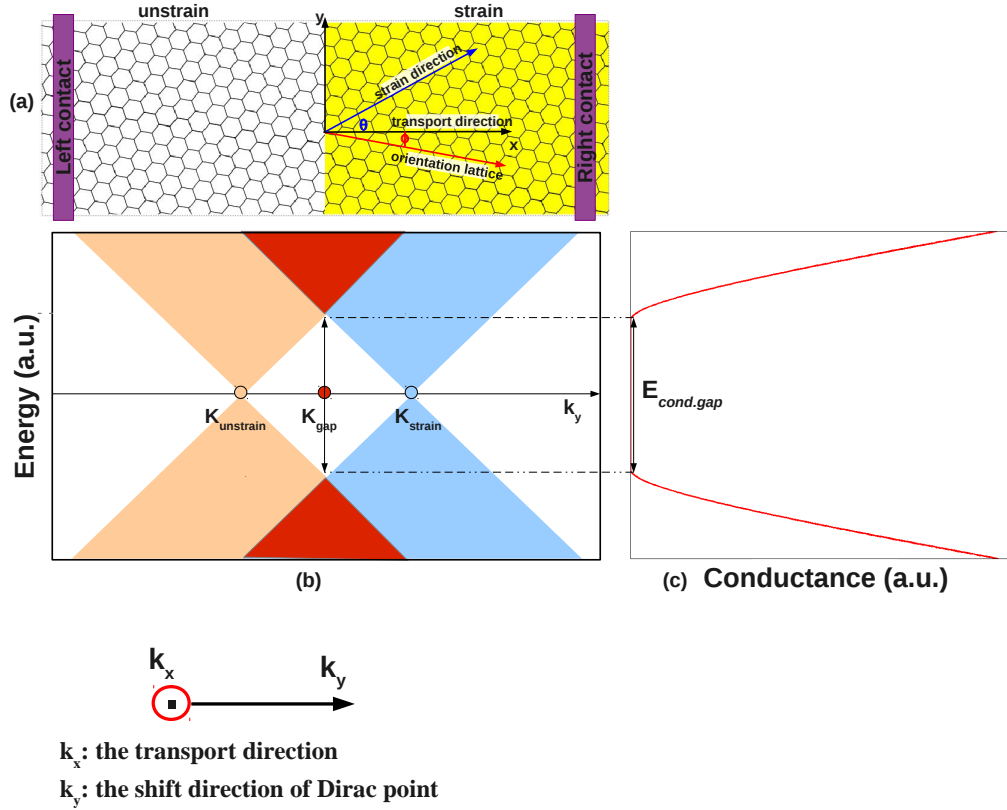


Figure 2.23: (a) unstrained/strained graphene junctions. (b) bandedges illustrating the strain-induced shift of Dirac points along the k_y -direction that leads to the opening of a conduction gap (c).

direction (ϕ).

2.4.1 The opening of conduction gap with strain of a few percent

We now go to explore the properties of the conduction gap in unstrained/strained graphene junctions. In Fig. 2.24, we display the conductance as a function of energy computed from Eq. 2.19 using the Green's function technique. First, we study uniform junctions in two cases: no strain ($\sigma = 0\%$) and strain ($\sigma = 5\%$). The result in Fig. 2.24 shows clearly that there is no energy gap of conductance in both cases. Hence, a small strain of a few percent (e.g., 5% here) cannot change the gapless character of graphene as previously discussed. However, for the case of hetero junction in Fig. 2.24, when strain of 5% is only applied in one half-sheet. A significant conduction gap (~ 400 meV) can open. The appearance of this conduction gap, as mentioned previously, is due to the strain-induced shift of Dirac points. This phenomenon can be

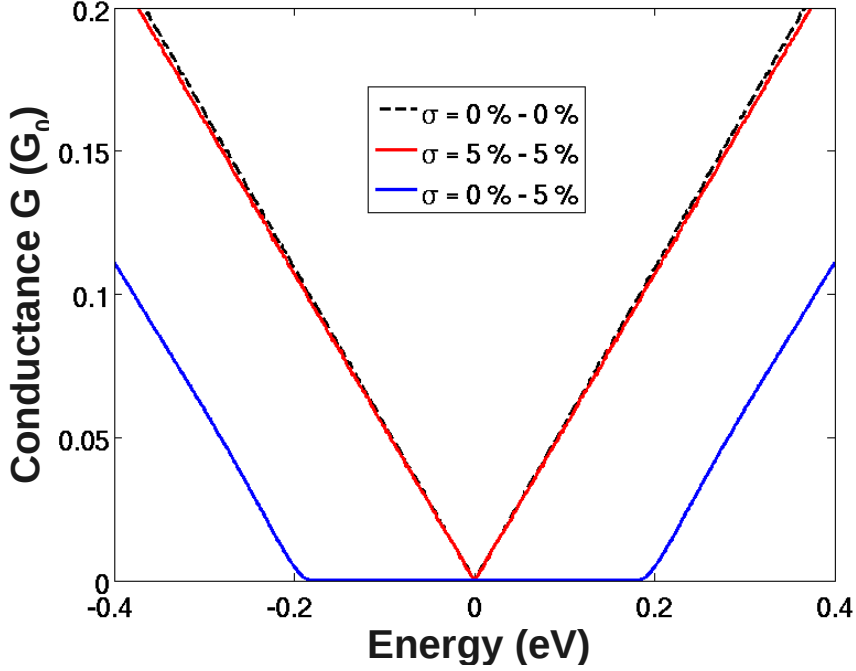


Figure 2.24: Conductance ($G_0 = e^2W/hL_y$) as a function of energy in strained graphene heterostructures. The comparison of the conductance in unstrained, uniformly strained and strained heterostructures is shown. The transport along the armchair direction ($\phi = 0$) with a strain applied along the Ox axis ($\theta = 0$) are considered here.

described as follows. Actually, the bandedges as a function of wave-vector k_y in unstrained and strained graphene sections can be illustrated schematically in Fig. 2.23. As one can see, the shift of Dirac points in strained graphene leads to a situation where there is no value of κ_y , for which the energy gap $E_{unstrain}^{gap}(\kappa_y)$ and $E_{strain}^{gap}(\kappa_y)$ are simultaneously equal to zero. This means that the transmission probability always exhibits a finite gap, $E_{junc}^{gap}(\kappa_y) = \max[E_{unstrain}^{gap}(\kappa_y), E_{strain}^{gap}(\kappa_y)]$, for any κ_y . In particular, these energy gaps are zero (or small) in the unstrained (resp strained) graphene section, but are finite in strained (resp unstrained) sections in the vicinity of Dirac point $k_y = K_{unstrain}$ (K_{strain}).

Have a look at pictures of local density of states in the left panels of Fig. 2.25 and reinforced in the corresponding transmission functions in the right panels. Well-defined gaps $E_{junc}^{gap}(\kappa_y)$ of transmission are still obtained. Far from the values of k_y above, $E_{unstrain}^{gap}(\kappa_y)$ and $E_{strain}^{gap}(\kappa_y)$ are both finite (e.g., see the LDOS plotted for $k_y = K_{gap}$) and hence a finite gap of conductance, which is determined from Eq. 2.19, is achieved as shown in Fig. 2.24. This gap is simply given by $E_{cond.gap} = \min[E_{junc}^{gap}(\kappa_y)]$ for all κ_y as discussed above.

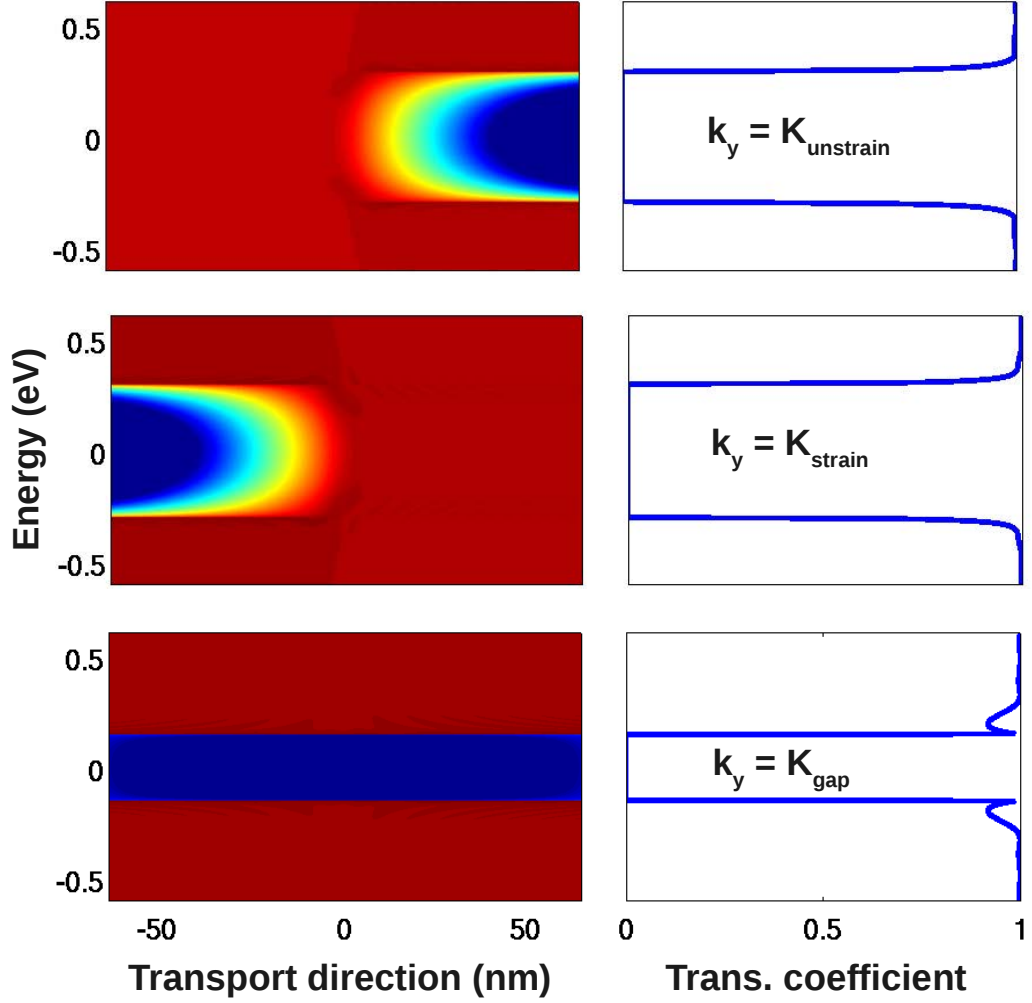


Figure 2.25: Local density of states (left panels) and corresponding transmission coefficient (right panels) for three different wave-vectors k_y obtained in an unstrained/strained graphene junction of $\sigma = 5\%$ and $\theta \equiv \phi = 0$.

Additionally, Fig. 2.26 shows that besides the amplitude of strain, the strain effect is also strongly dependent on the applied direction. For instance, the conduction gap takes the values of 295, 172 and 323 meV for $\theta = 0^\circ, 30^\circ$ and 90° , respectively. We will discuss the properties of the conduction gap with respect to the strain amplitude, its applied direction, and the direction of transport. Note that due to the lattice symmetry, the transport directions ϕ and $\phi + 60^\circ$ are equivalent while the applied strain of angle θ is identical to that of $\theta + 180^\circ$. Hence, the data obtained for ϕ ranging from -30° to 30° and θ from 0° to 180° covers the properties of the conduction gap with all possibilities.

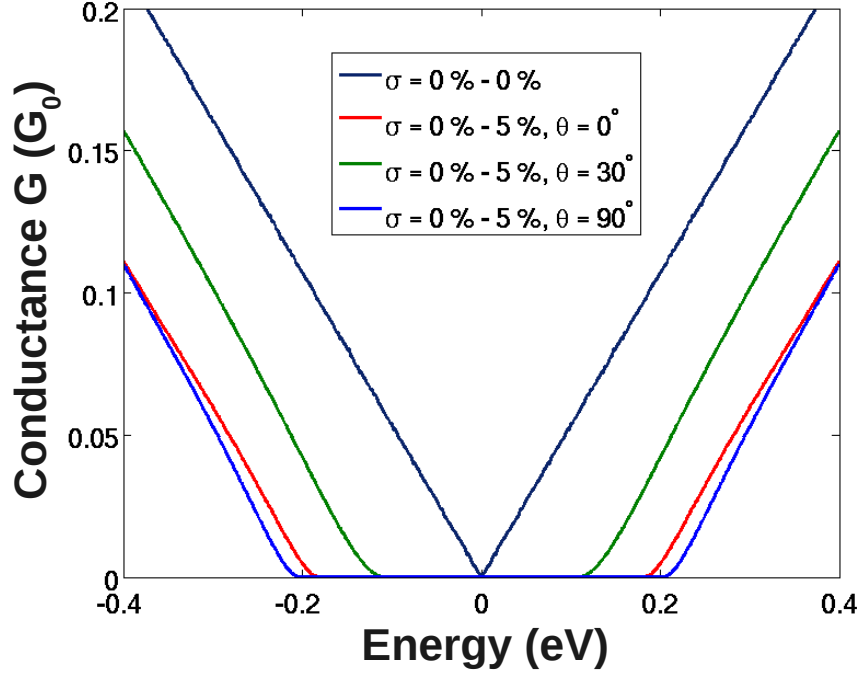


Figure 2.26: Conductance ($G_0 = e^2W/hL_y$) as a function of energy in graphene-strained junctions for $\sigma = 5\%$ with different strain directions. The transport along the armchair direction ($\phi = 0$) is considered. The data obtained in a uniformly strained graphene are displayed for the comparison.

2.4.2 The dependence of conduction gap on strain amplitude (σ), direction of applied strain (θ) and transport direction (ϕ) in both of tensile and compressive cases

Now, we present the figures of conduction gap with respect to the strain amplitude and its applied direction in two particular cases where the transport is either along the armchair ($\phi = 0$) or the zigzag ($\phi = 30^\circ$) directions, as can be seen in Fig. 2.27 and Fig. 2.28.

2.4.2.1 Armchair transport direction ($\phi = 0$)

The term "armchair transport direction" corresponds to the case where the transport direction and the armchair orientation of lattice coincide, i.e., $\phi = 0$. First, we only study three cases of strain, i.e., strain of 2%, 4% and 6%. It is noted that both tensile and compressive strain are considered here. Let us first discuss the results obtained in the armchair case. Figures 2.27(a) and (b) show that the value of conduction gap increases with the strain amplitude and can reach up to ~ 500 meV for a strain of 6%. Besides, these results display clearly the θ -dependence of conduction gap.

In particular, its peaks (maximum) occur at $\theta = 0$ or 90° while the gap is zero at $\theta = 47^\circ$ and 133° for tensile strain and at $\theta = 43^\circ$ and 137° for compressive strain. In principle, the conduction gap is larger if the shift of Dirac points in the k_y -axis is larger, as previously discussed about Fig. 2.22 and 2.21. We notice that the strain-

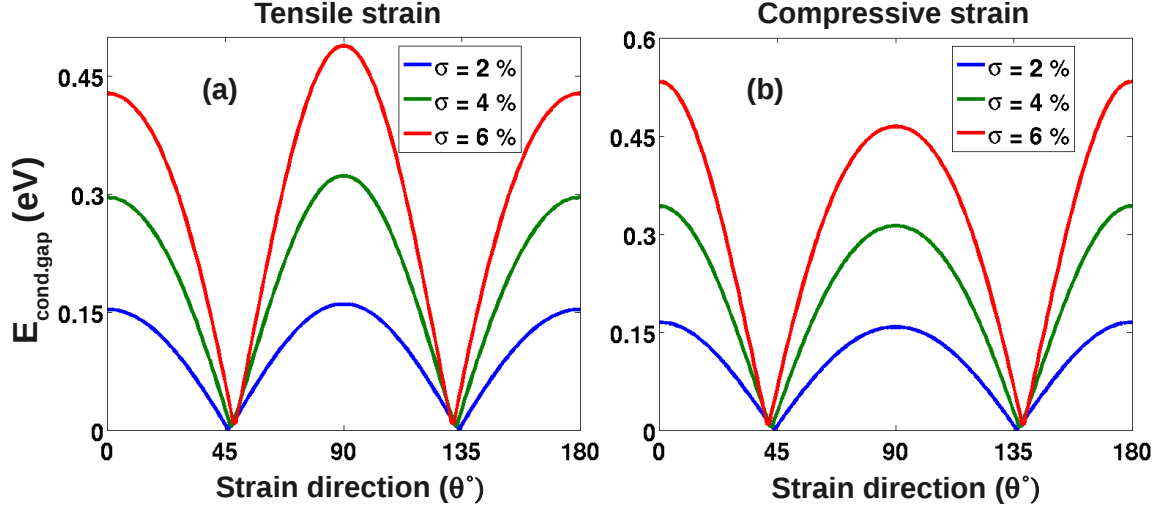


Figure 2.27: Maps of conduction gap in unstrained/strained graphene junctions: tensile (a) and compressive cases (b). The transport is along the armchair directions, $\phi = 0$. The strain of 2%, 4%, 6% is considered.

induced shifts can be different for the six Dirac points of graphene [106] and the gap is zero wherever the Dirac points are observed at the same values of κ_y in the two graphene sections. From Eq. 2.29, we find that the Dirac points are determined by the following set of equations:

$$\cos\left(\frac{\kappa_y}{2}\right) = \pm \frac{1}{2} \sqrt{\frac{t_3^2 - (t_1 - t_2)^2}{t_1 t_2}} \quad (2.31)$$

$$\cos\left(\frac{\kappa_x}{2}\right) = \frac{t_1 + t_2}{|t_3|} \cos\left(\frac{\kappa_y}{2}\right), \quad \sin\left(\frac{\kappa_x}{2}\right) = \frac{t_1 - t_2}{|t_3|} \sin\left(\frac{\kappa_y}{2}\right) \quad (2.32)$$

which simplifies into $\cos(\frac{\kappa_y}{2}) = \pm \frac{1}{2}$ and, $\cos(\frac{\kappa_x}{2}) = \pm 1$ in the unstrained case. Hence, the zero conduction gap obtained above satisfies the condition

$$\frac{t_3^2 - (t_1^2 - t_2^2)}{4t_1 t_2} = \frac{1}{4} \quad (2.33)$$

i.e., there is no shift of Dirac points along the κ_y -axis. Additionally, it is shown that the effects of a strain (σ, θ) are qualitatively similar to those of a strain $(-\sigma, \theta + 90^\circ)$, i.e., the peaks and zero values of conduction gap are obtained at the same θ values in

these two situations. To understand this, we analyze the strain matrix $M_s(\sigma, \theta)$ and find that in the case of small strains studied here, the relationship between the bond lengths under these two strains is approximately given by

$$r(\sigma, \theta) - r(-\sigma, \theta + 90^\circ) \simeq \sigma(1 - \gamma)r_0 \quad (2.34)$$

which is θ -independent for all $C - C$ bond vectors. It implies that there is a fixed ratio between the hopping energies $t_i(\sigma, \theta)$ and $t_i(-\sigma, \theta + 90^\circ)$ and hence a similar shift of Dirac points happens in these two cases.

2.4.2.2 Zigzag transport direction ($\phi = 30^\circ$)

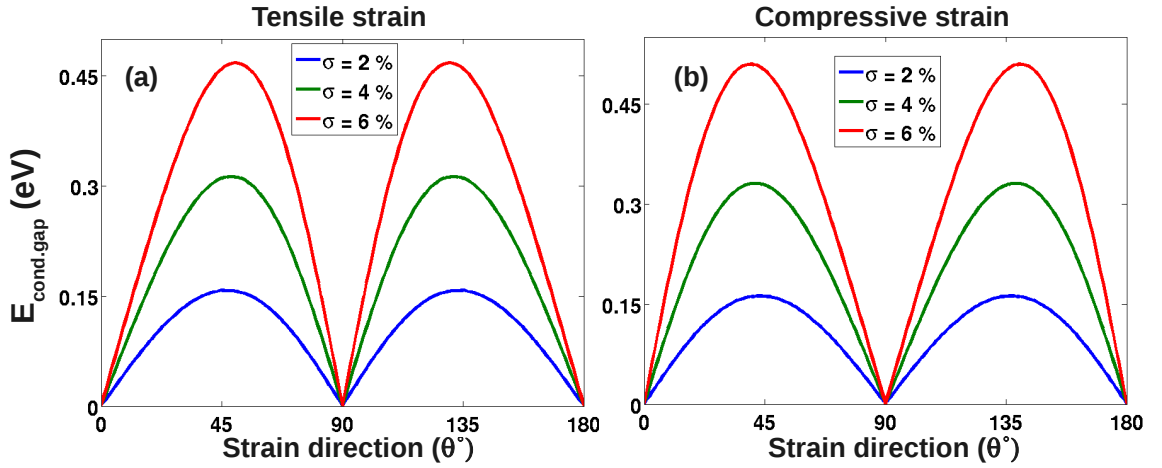


Figure 2.28: Maps of conduction gap in unstrained/strained graphene junctions: tensile (a) and compressive cases (b). The transport is along the zigzag directions, $\phi = 30^\circ$. The strain of 2%, 4%, 6% is considered.

The definition of "zigzag transport direction" here is quite similar to that of "armchair transport direction", i.e. the zigzag orientation of lattice is along the transport direction (also along Ox direction). We thus analyze the properties of conduction gap displayed in Fig. 2.28(a) and (b) where the transport is along the zigzag direction $\phi = 30^\circ$. In fact, the conduction gap in this case can also reach a value as high as that of the case of $\phi = 0$ but with a different θ -dependence. In particular, the conduction gap has peaks at $\theta \approx 47^\circ$ and 133° for tensile strain and at $\theta = 43^\circ$ and 137° for compressive strain, while it is zero in the case of $\phi = 0$. It is also equal to zero at $\theta = 0$ and $\theta = 90^\circ$ where we had peaks of conduction gap in the previous case of $\phi = 0$.

The relationship between these two transport directions can be explained as follows. On the one hand, based on the analysis above for $\phi = 0$, we find that for a given

amplitude of strain, a maximum shift of Dirac points along the k_y -axis corresponds to a minimum shift along the k_x -one and vice versa when varying the strain direction θ . On the other hand, as schematized in Fig. 2.29, the change in transport direction results in the rotation of the first Brillouin zone, i.e., the k_x (resp. k_y) axis in the case of $\phi = 30^\circ$ is identical to the k_y (resp. k_x) axis in the case of $\phi = 0$. These two features explain essentially the opposite θ -dependence of conduction gap for $\phi = 30^\circ$, compared to the case of $\phi = 0$, as mentioned. Again, we found the same qualitative behavior of the conduction gap when applying the strains of σ, θ and $\sigma, \theta + 90^\circ$.

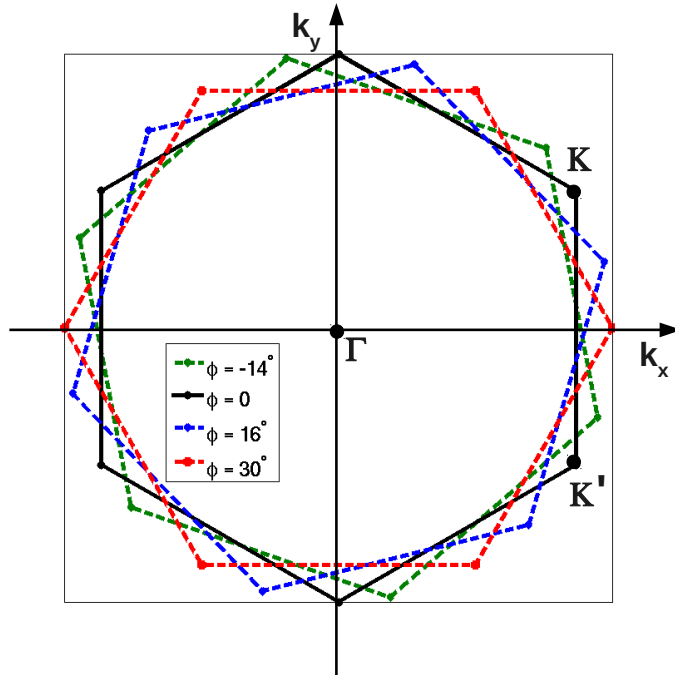


Figure 2.29: The diagram illustrating the rotation of Dirac points in the k -space with the change in the transport direction ϕ .

The full map of (σ, θ) -dependence of conduction gap is shown in Fig. 2.30 for both cases of tensile and compressive strain with the transport direction of armchair and zigzag. Here, strain varies continuously from 0 (at the center) to 6% (at the edge) with θ varying from 0 to 360° .

2.4.2.3 Any transport direction ($0 < \phi < 30^\circ$)

Now, we investigate the conduction gap with respect to different transport directions ϕ . A number of ϕ -cases are shown in table in Fig. 2.31 with several configurations of different unit cells described in Fig. 2.32. We display a (θ, ϕ) -picture of conduction

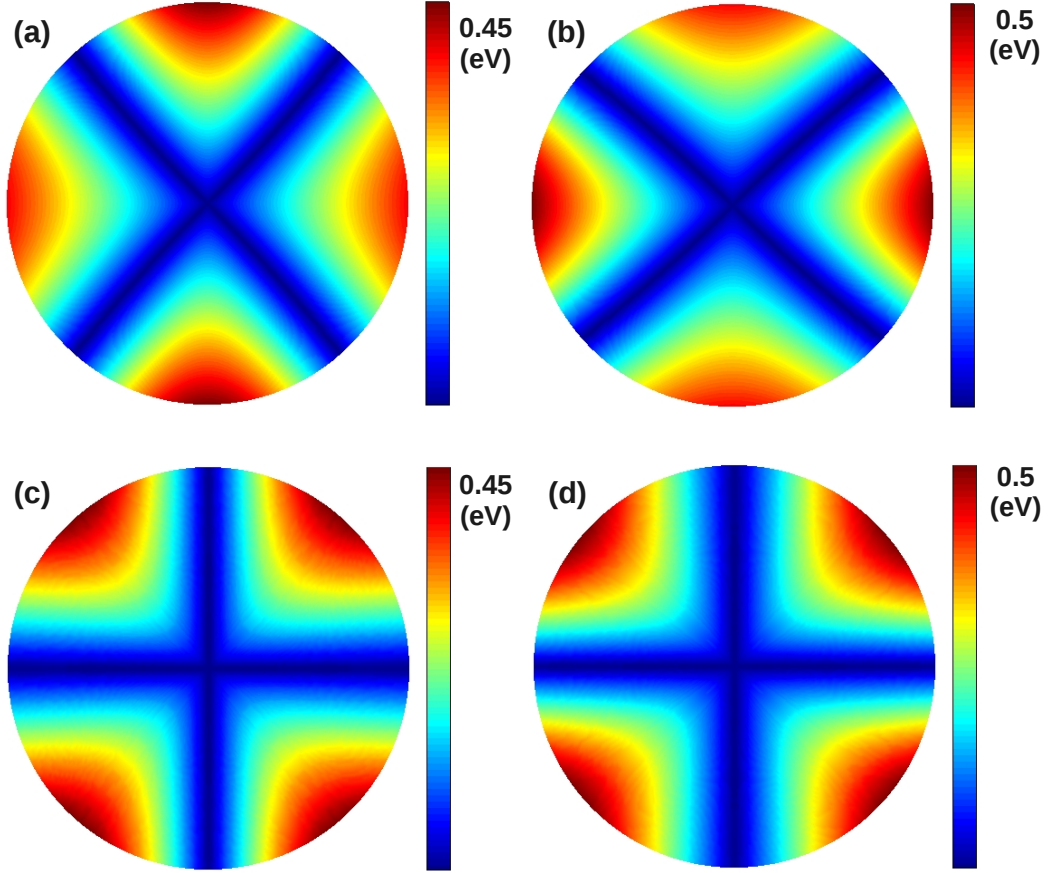


Figure 2.30: Maps of conduction gap in unstrained/strained graphene junctions: tensile (a, c) and compressive cases (b, d). The transport is along the armchair $\phi = 0$ (a, b) and zigzag $\phi = 30^\circ$ directions (c, d). The strain strength ranges from 0 (center) to 6% (edge of maps) in all cases.

gap for $\sigma = 4\%$ in Fig. 2.33. It is clearly shown that (i) a similar scale of conduction gap is obtained for all different transport directions, (ii) there is a smooth and continuous shift of $E_{cond.gap}-\theta$ behavior with the value of ϕ considered here, and (iii) the same behavior of $E_{cond.gap}$ is also observed when comparing the two transport directions of ϕ and $\phi + 30^\circ$, similarly to the comparison previously made for the cases of $\phi = 0^\circ$ and 30° . The data plotted in Fig. 2.33 additionally show that $E_{cond.gap}$ takes the same value, as in both cases of (ϕ, θ) and $(-\phi, -\theta)$ with a remark that the strains of $-\theta$ and $180^\circ - \theta$ are identical. It can be said that all these features are essentially a consequence of the rotation of Dirac point in k -space with respect to the transport direction (ϕ) illustrated in the diagram in the Fig. 2.29, and of the lattice symmetry of graphene.

In this part, we have only considered the twelve values of transport direction (ϕ)

	n_1	n_2	m_1	m_2	$N_p = n_2 m_1 - n_1 m_2$	$\phi(^{\circ})$	$N_{\text{atoms}}/\text{unit cell}$
1	1.0	1.0	1.0	-1.0	2.0	0°	4.0
2	4.0	3.0	10.0	-11.0	74.0	4.7°	148.0
3	3.0	2.0	7.0	-8.0	38.0	6.6°	76.0
4	7.0	4.0	5.0	-6.0	62.0	8.9°	124.0
5	2.0	1.0	4.0	-5.0	14.0	10.9°	28.0
6	5.0	2.0	3.0	-4.0	26.0	13.9°	52.0
7	3.0	1.0	5.0	-7.0	26.0	16.1°	52.0
8	4.0	1.0	2.0	-3.0	14.0	19.1°	28.0
9	5.0	1.0	7.0	-11.0	62.0	21.0°	124.0
10	7.0	1.0	3.0	-5.0	38.0	23.4°	76.0
11	10.0	1.0	4.0	-7.0	74.0	25.3°	148.0
12	1.0	0.0	1.0	-2.0	2.0	30.0°	4.0

Figure 2.31: The value of different transport directions (ϕ).

given in table in Fig. 2.31. All these values correspond to unit cells of small size leading to strain-induced shift of Dirac point within the Brillouin zone. As a consequence, the trend of conduction gap towards increasing and decreasing is quite simple and nearly follows a general rule for all of these cases of (ϕ) listed in the table. However, in other cases, especially for small angles (ϕ) (i.e., less than 5°), the size of primitive cells is large which leads to a small size of Brillouin zone. When displacement of Dirac point in the first Brillouin zone is large enough, it can reach the first Brillouin zone's edge and then enter the second zone. As a result, the behavior of conduction gap is much more complicated than in the cases shown in table in Fig. 2.31, i.e., the conduction gap can decrease when increasing the strain amplitude. It is noted, the move of Dirac point from the first Brillouin zone to the second one is only predicted in the cases where the size of the Brillouin zone is small. A detailed picture of this phenomenon has been displayed in the system of strained vertical devices by V. H. Nguyen *et al* [73]. We have planned to study this situation in a next work to present a full map of the dependence of conduction on the key parameters of the present system.

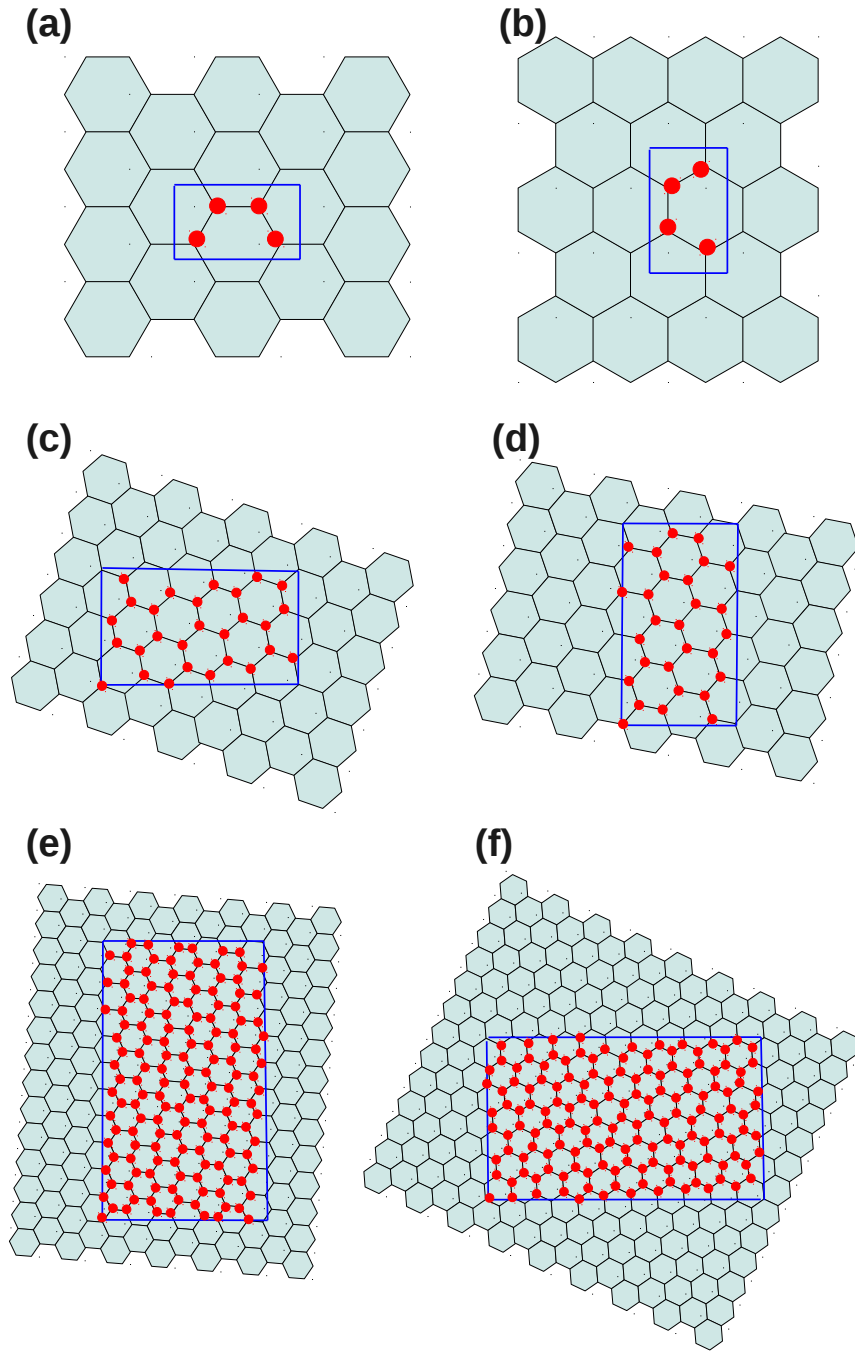


Figure 2.32: Sketch of 2D graphene lattice with different unit cell for six cases of different transport directions from the table. (a) $\{N_{atom} = 4, \phi = 0\}$, (b) $\{N_{atom} = 4, \phi = 30^\circ\}$, (c) $\{N_{atom} = 28, \phi = 19.1^\circ\}$, (d) $\{N_{atom} = 28, \phi = 10.9^\circ\}$, (e) $\{N_{atom} = 148, \phi = 4.7^\circ\}$, and (f) $\{N_{atom} = 148, \phi = 25.3^\circ\}$.

2.4.2.4 Compressive and tensile-strained graphene junctions

As an alternative, we investigate another kind of strained junction based on both compressive and tensile-strained graphene sheets. The idea is that in this type of

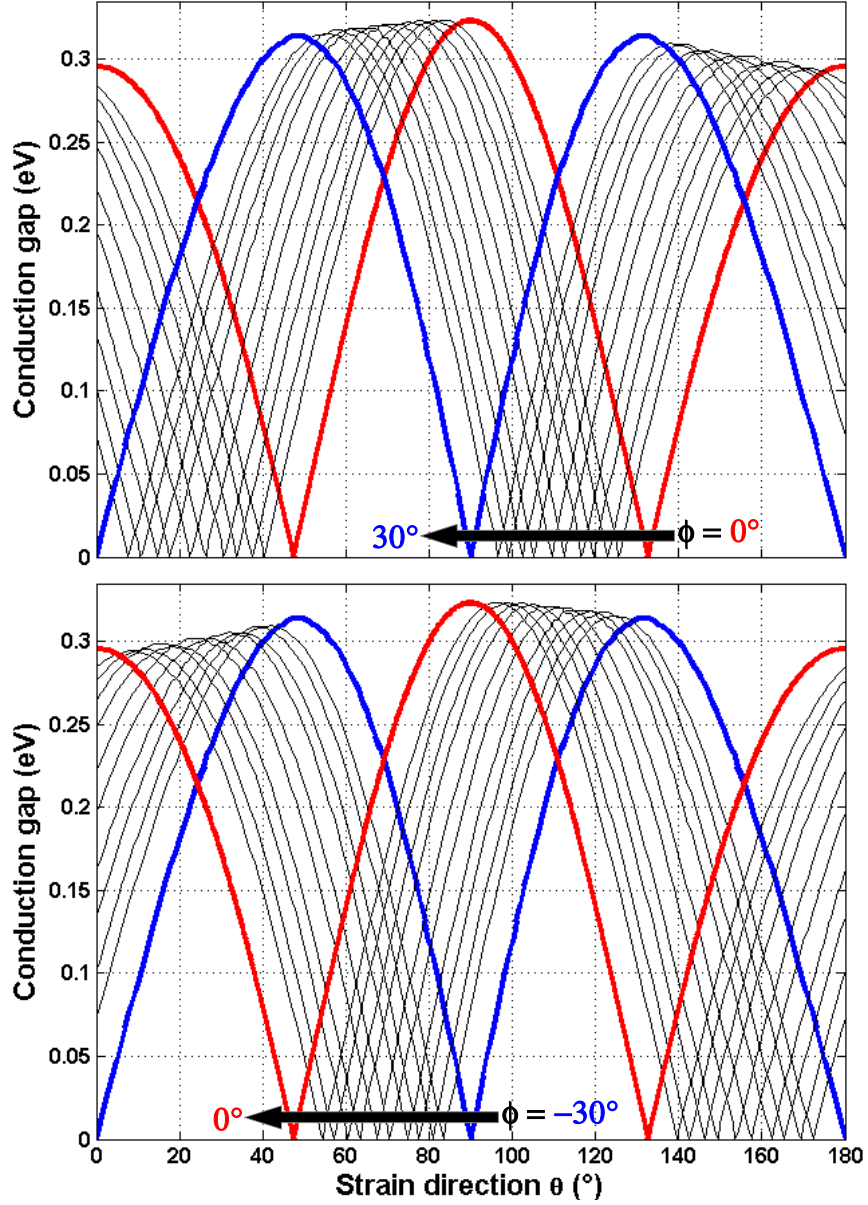


Figure 2.33: Dependence of conduction gap on the directions (θ, ϕ) for $\sigma = 4\%$.

strained junction, the shifts of the Dirac points are different in the two graphene sections of different strains, which offers the possibility of using smaller strains to achieve a similar conduction gap, compared to the case of unstrained/strained junctions. In Fig. 2.34, we display the maps of the conduction gap with respect to the directions of compressive and tensile strains in two cases of transport direction: $\phi = 0$ (armchair) and 30° (zigzag) for given strain strengths. Indeed, as seen in Fig. 2.34 (a) and (b), with smaller strains $(\sigma_c, \sigma_t) = (-2\%, 2\%)$ or $(-1\%, 3\%)$, similar conduction gap of about 310 meV can be achieved while it requires a strain of 4% in the

unstrained/strained junctions studied above. However, since the shift of the Dirac points is strongly dependent on the direction of applied strains and the transport direction, the properties of conduction gap in this case are more complicated. In particular, our calculations show that the preferred transport directions to achieve large conduction gaps are close to the armchair one. Otherwise, the conduction gap is generally smaller, similarly to the data for $\phi = 30^\circ$ compared to $\phi = 0$, as displayed in Fig. 2.34. Additionally, the preferred directions of applied strains for $\phi = 0$ are $\theta_c = \theta_t = 0$ or 90° .

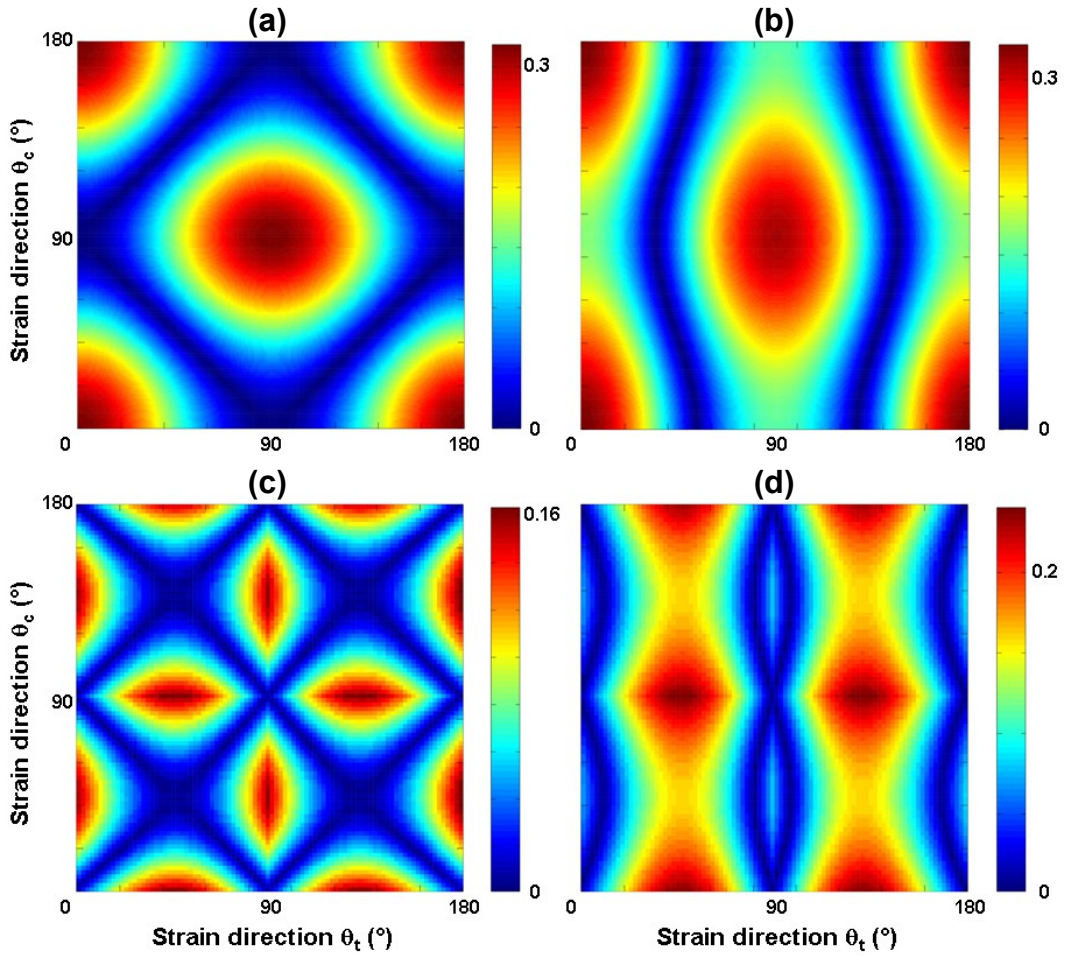


Figure 2.34: Maps of conduction gap obtained in tensile/compressive strained junctions. The transport along the armchair/zigzag directions is considered in (a, b)/(c, d), respectively. The strains $\sigma_c = 2\%$ and $\sigma_t = 2\%$ are applied in (a, c) while $\sigma_c = 1\%$ and $\sigma_t = 3\%$ in (b, d).

In this section, we have investigated the effects of uniaxial strain on the transport properties of graphene strained junctions and have discussed systematically the possibilities of achieving a large conduction gap with respect to the strain, its applied di-

rection and the transport direction. It has been shown that due to the strain-induced deformation of graphene lattice and hence of graphene bandstructure, a finite conduction gap higher than 500 meV can be achieved for a strain of only 6%. Moreover, as a consequence of the shift of Dirac points along the k_y -axis, the conduction gap is strongly dependent not only on the strain strength but also on the direction of applied strain and the transport direction. A full picture of these properties of conduction gap has been presented and explained. The study hence could be a good guide for the use of this type of unstrained/strained graphene junction in electronic applications.

2.5 Conclusion

In the chapter 2, we have introduced a new way to open a conduction energy gap in pristine graphene, using strain engineering. It is based on the displacement of Dirac cones in the k-space under the effect of strain. Such displacement has been demonstrated both experimentally and theoretically. In this work, we have displayed the full feature of electronic band structure of strained graphene. Then, we also have introduced a new structure, which consists in an unstrained/strained graphene junction that takes advantage of the resulting mismatch of band structure between both sections to open a sizable conduction gap. In the next chapter, such junctions will be explored for designing the channel of several types of devices. We will see that such a conduction gap can be used like a real bandgap to strongly improve some electrical effects like the switching-off of the transistors, the Seebeck coefficient of graphene and the peak-to-valley ratio of negative differential conductance in diodes.

Chapter 3

APPLICATION OF STRAINED JUNCTIONS IN GRAPHENE HETEROCHANNELS

3.1 Introduction

For many years, the traditional scaling rules of complementary metal oxide semiconductor (CMOS) have led to improvements in device performance, with lower cost as well as higher yield. However, as physical limits on device scaling are approaching, technological innovations are required to deliver continuous device performance improvements over traditional scaling. That is why in recent years scientists have looked for new types of materials, which can replace or complement conventional semiconductors thanks to specific, and eventually outstanding, properties.

Graphene (a single layer of atoms) can be considered as one of the most promising of these new materials. However, it is still limited in practical applications due to its gapless character. Until now, many different ways to open a bandgap in graphene have been investigated to introduce graphene in technological innovations, i.e., in designing device channels.

In chapter 2, we mentioned the possible use of strain engineering to open a conduction gap (transport gap) in graphene junctions. These junctions with sizeable gap are believed to be good candidates for graphene devices in electronic applications. In particular, in this chapter, we discuss the capability to use strained graphene junctions in designing FETs with high ON/OFF ratio in section 3.2. Next, in section 3.3, we present the enhancement of Seebeck effect in strained heterochannels. In section 3.4, the advantages of strained heterochannels is discussed in view to improving strongly the negative differential conductance (NDC) effect in single gate-induced

barrier structure and in p-n junctions. Finally, a conclusion is given in section 3.5.

3.2 Improved performance of graphene transistors

Nowadays, computers are widespread in the world. Each computer contains more than a billion transistors, making transistors more numerous than any other object we could think of. In fact, there are many different types of transistors, i.e., bipolar junction transistors (small signal transistors, small switching transistors, power transistors, high frequency transistors, etc), and field effect transistors (junction gate field-effect transistors, metaloxidesemiconductor field-effect transistors, etc). They have their own characteristics and each type has also its own advantages and disadvantages in applications. However, in this work we will refer only to the most common one in use today, i.e., the field effect transistor (FET), which is made up of 3 regions, a gated channel, a source, and a drain. FETs are voltage-controlled devices. A voltage placed at the gate controls current flow from the source to the drain of the transistor.

For many years, the Moore's law has given the trend in the time evolution of between metal oxide semiconductor FET (MOSFET) technology, in terms of gate length and number of transistors per processor chip. Today, processors even containing more than two billion MOSFETs, many of them with gate lengths of just 30 nm [107, 108, 109], are in mass production (see in Fig. 3.1 [107]). Here, as gate lengths have decreased, the number of transistors per processor chip has increased. Maintaining these trends is a significant challenge for the semiconductor industry, which is why new materials such as graphene are being investigated. Making MOSFETs smaller is still required and it has been the key to the progress in digital logic.

As discussed below, graphene with its interesting properties is expected to become a new material of choice for electron devices. Regarding FET application, the drawback of this material is its gapless character, so that devices with channels made of large-area graphene cannot be switched off efficiently and therefore are not suitable for logic application. However, the band structure of graphene can be modified in several ways such as by forming one-dimensional graphene nanoribbons, by biasing bilayer graphene, by creating a sublattice of nanoholes into a graphene sheet or by applying strain to graphene. In this section 3.2, we will discuss the positive properties of transistors made from these structures of graphene in comparison with pristine graphene transistors. This section is organized as follows. The first subsection 3.2.1 introduces the structure of pristine graphene-based field-effect transistor

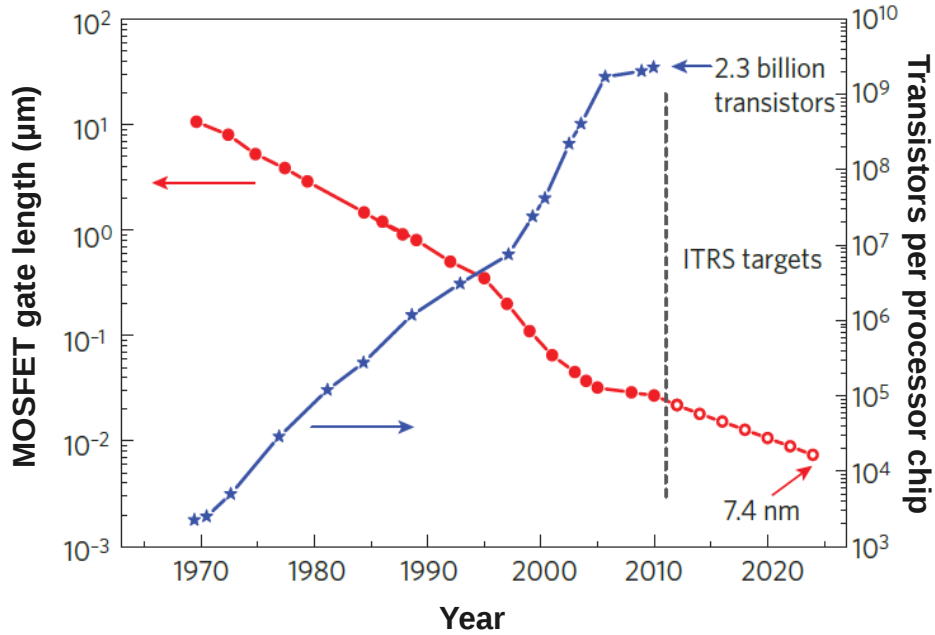


Figure 3.1: Trends in digital electronics [107].

and its characteristic properties. Then, the second subsection shows the general features of FETs based on graphene nanostructures, like bilayer graphene and graphene nanomesh. Finally, we present a study of graphene FET with the heterochannel made from unstrained/strained junctions in subsection 3.2.3.

3.2.1 Field-effect transistor (FET)

A conventional field-effect transistor consists of a gate, a channel region connecting source and drain electrodes, and an insulating barrier separating the gate from the channel, as schematized in Fig. 3.2. Here, when the voltage applied between the source and gate electrodes exceeds a threshold voltage, a conducting channel is formed and a drain current flows. The length of the channel is defined by the length of the gate electrode, the thickness of the gate-controlled channel region is the depth through which the electronic properties of the semiconductor (p-doped Si in this case) are electrostatically controlled by the gate [107]. The operation of a conventional FET relies on the control of the channel conductivity, and thus the drain current, by the voltage V_{GS} applied between gate and source. For high-speed application, FETs are expected to respond quickly to variations in V_{GS} , which requires short gate and fast carriers in the channel. However, it has been shown that FETs with short gates have many possible problem such as degraded electrostatics, threshold-voltage roll-off, drain-induced barrier lowering and impaired drain-current saturation (see in [107]

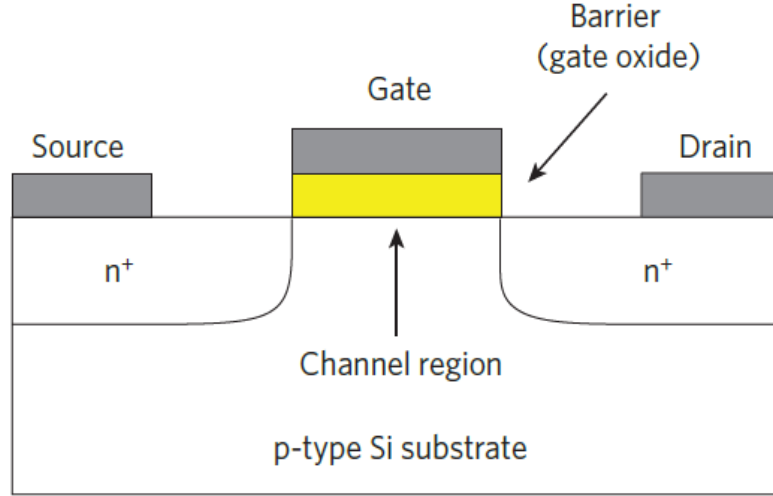


Figure 3.2: Schematic of conventional field-effect transistor [107].

and Refs. therein). Theoretical studies predict that a FET with thin barrier and a thin gate region should be robust against short channel effects down to very short gate length. Hence, the possibility of having channels that are just one atomic layer-thick is perhaps the most attractive property of graphene for fabricating transistors [110]. Besides, the high mobility in graphene makes it very appealing to replace conventional materials.

Otherwise, the ratio between the ON-current (I_{on}) and the OFF-current (I_{off}) in FETs is an important parameter. The ON-current, corresponding to on-state, is defined at the maximum of V_{GS} while the OFF-current is corresponding to the leakage current in off-state at $V_{GS} = 0$. In general, a large number of MOSFETs in CMOS circuits are always switched off, which means with almost no current flowing through the device (to the exception of the small I_{off} that must be as small as possible). Silicon CMOS has been introduced in all logic technologies due to the ability of silicon MOSFETs to switch off very well. Therefore, any generation of post-silicon MOSFETs that is to be used in CMOS-like logic must have excellent switching capabilities as well as a high ON/OFF ratio (I_{on}/I_{off}), typically between 10^4 and 10^7 (see in [107] and Refs. therein). In a conventional FET, this requires semiconducting channels with a bandgap about 0.4 eV or more. Thus, pristine graphene with its gapless character is not a good candidate from this viewpoint. Hence, a new generation of transistor with attractive characteristics, i.e., small and thin size and shape, high ON/OFF current ratio, is a challenge in science and technology.

3.2.2 Different types of graphene transistors

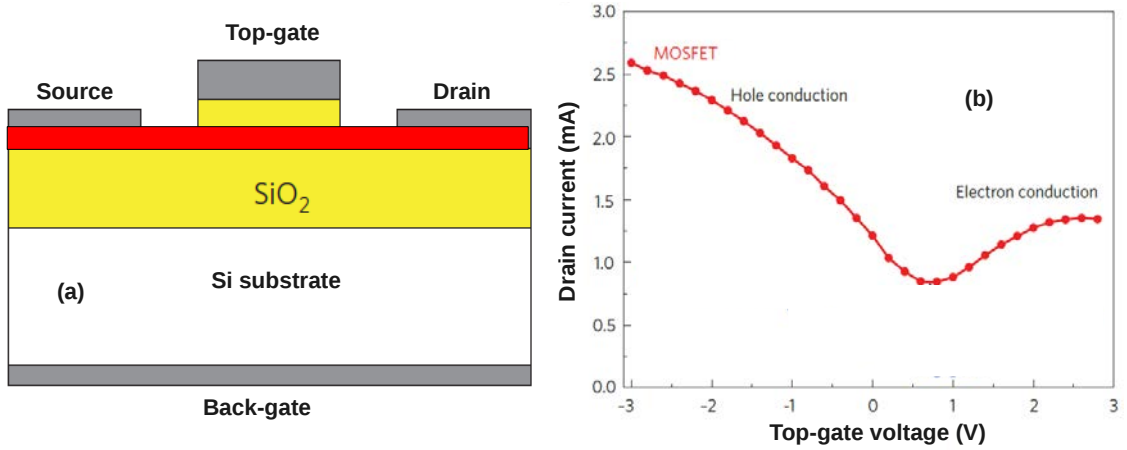


Figure 3.3: Schematics of transistor with graphene channel in red region is shown in figure (a) [107] and the characteristics of current is displayed in figure (b) [111, 112].

Graphene is the thinnest material ever known to exist. It is really attractive for fabricating transistors as mentioned above. In this part, we would like to discuss the properties of transistor made of graphene and graphene nanostructures, i.e., pristine graphene transistor, graphene nanoribbon transistor and graphene nanomesh transistor. Then, we will review some main results on the use of unstrained/strained junctions likely to improve the performance of transistors.

The simplest design of conventional transistor made of 2D graphene lattice is shown in Fig. 3.3(a) [107]. The current character through this channel (see in Fig. 3.3(b)) is measured [111, 112]. The carrier density and the type of carrier (electrons and holes) in the channel are governed by the potential differences between the channel and the gates (top gate and/or back gate).

It is shown that the current displayed in Fig. 3.3(b) is a typical transfer characteristics for a MOSFET with large-area-graphene channel. The ON-OFF current ratio is about 3 [111, 112]. Clearly, this ratio is quite low due to the gapless character of graphene. Therefore, the graphene field-effect transistor (FET) cannot be turned off effectively due to the absence of a bandgap, leading to an ON/OFF current ratio typically lower than 10 in top-gated graphene FETs [113]. To improve the OFF-state behavior in more conventional field-effect architecture, it is necessary to open a finite bandgap in graphene. Hence, nanostructures of graphene with real bandgaps are alternative methods.

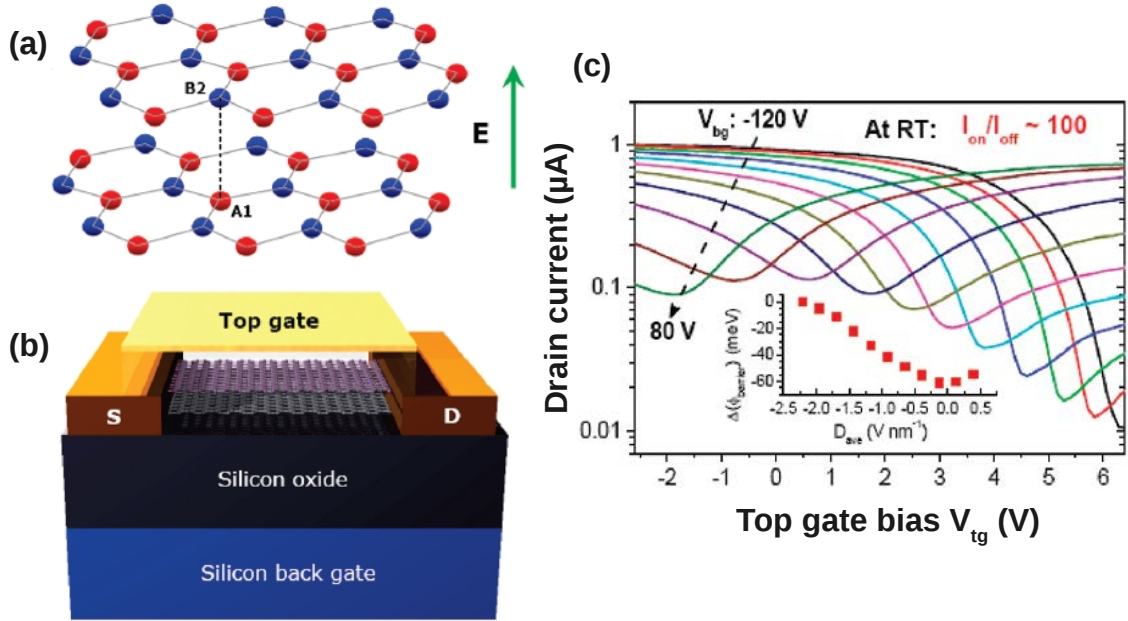


Figure 3.4: Structure of the bilayer graphene FET. Figure (a) shows the bilayer graphene structure in a perpendicular E-field. A three-dimensional schematic view of the dual-gate bilayer graphene FET in (b). The room temperature transfer characteristics of a dual-gate bilayer graphene FET in (c) [114].

First, we can think about the bilayer graphene FET shown in Fig. 3.4(b) [114]. As already mentioned, theoretical investigations predict a sizable bandgap opening up to 300 meV in bilayer graphene using a perpendicular E-field between the A_1 and B_2 sites, as can be seen Fig. 3.4(a). However, experimental measurements were not able to find such a large bandgap. In fact, F. Xia *et al.* have fabricated the bilayer graphene FET [114] which allowed them to observe an electrical bandgap (> 130 meV). In this work, the FET with a channel $1.6 \mu\text{m}$ wide by $3 \mu\text{m}$ long was investigated. The back gate bias (V_{bg}) was fixed and the top gate bias (V_{tg}) was changed from -2.6 to 6.4 V. V_{bg} was varied from -120 to 80 V by steps of 20 V as shown in Fig. 3.4(c). As a result at room temperature, the ON/OFF current ratio can reach about 100. In comparison, an ON/OFF ratio of only about 4 was observed in a single layer graphene FET with similar device structure as seen in Fig. 3.4(b). Obviously, the ON/OFF current ratio is enhanced significantly in bilayer graphene FET, i.e., it is 25 times larger than that in a single layer graphene FET.

Next, we would like to discuss about another alternative method, the opening of a bandgap in a large sheet of graphene by a system of periodic nanoholes. In this model, a bandgap higher than 0.5 eV can be achieved depending on the size, the shape and the periodicity of nanoholes forming a graphene nanomesh. Transistor

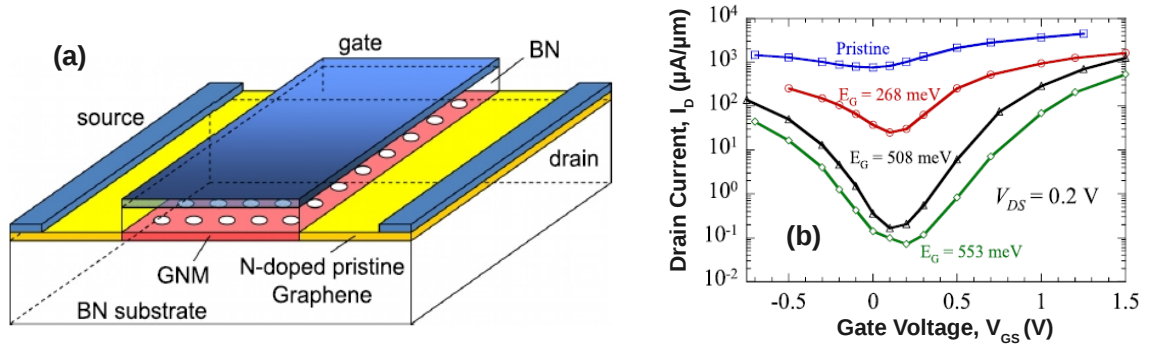


Figure 3.5: Schematic view of the GNM transistor is considered in figure (a). Transfer characteristics is displayed in figure (b) [92].

with gated region of graphene nanomesh is schematized in Fig. 3.5(a). S. Berrada *et al* [92] have shown that by increasing the bandgap of graphene nanomesh, the overall current is reduced but the OFF-current at the Dirac point is drastically suppressed. In particular, the ON/OFF current ratio increases from 7 for pristine graphene FET to more than 7400 for graphene nanomesh FET with a bandgap > 500 meV, seen in Fig. 3.5(b). Besides, the possibility to get a good saturation current in GNM FETs is realizable for a sub-50 nm while a good saturation behavior has been observed previously in bilayer graphene FETs but with a gate length as long as $4\mu m$. It even leads to excellent frequency behavior, not only in terms of cutoff frequency f_T but also in terms of maximum oscillation frequency f_{max} , that is usually very weak in pristine GFET due to high output conductance [92]. So in conclusion, graphene nanomesh FET is really a brilliant candidate for fabricating excellent transistors to overcome the serious drawback of conventional transistors. However, it requires a good control of nanoholes size and periodicity at the nanometer scale.

3.2.3 A high ON/OFF ratio in strained graphene transistor

For this thesis project, I have focused on the effect of uniaxial strain applied in a 2D monolayer graphene sheet and explored the possibility of using the unstrained/strained hetero-channel to enhance performance of devices. First, we would like to mention the ability of unstrained/strained channel to achieve a good operation of FETs. Though I contributed with some simulations and analyses, this work has been mainly conducted by V. H. Nguyen *et al* [102], with main results shown in Fig. 3.6. In fact, local strain has been realized in experiments (lots of Refs. in chapter 1 and [115, 116]) and theoretically demonstrated to improve the electrical performance of various graphene devices [71, 117, 118]. For instance, the local strain has been shown to enhance the

ON current in a GNR tunneling FET by a factor of ten [117] and to increase the conduction gap in strained GNR junctions [118]. It has also been shown in [102] that the use of a strained heterostructure with a moderately small strain of 5% can greatly improve the performance of graphene FETs with respect to a high ON/OFF ratio and good saturation of the current.

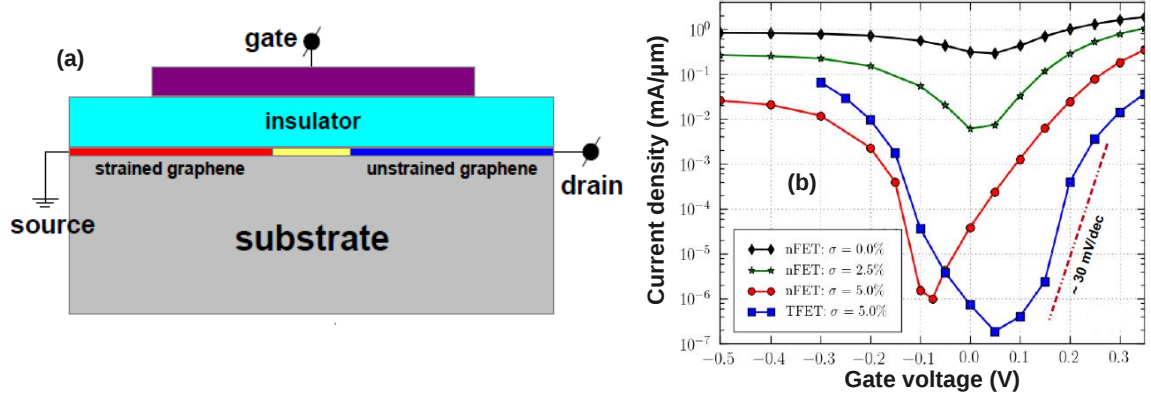


Figure 3.6: Schematic of graphene FET with unstrained/strained junction (a). The channel of the simulated device is based on strained graphene heterostructures. The yellow zone in the graphene layer indicates the transition region between strained and unstrained sections. (b) I - V_{gs} characteristics of simulated graphene FETs at the value of drain voltage $V_{ds} = 0.1$ V with different strain amplitudes.

Indeed, a conduction gap of 360 meV can be achieved with a strain of only 5% and higher value can even be obtained with larger strain [102]. This gap is the important key leading to the possibility of switching off the current, which allows us to achieve high ON/OFF current ratio. In particular, it is found in Fig. 3.6(b) that when increasing the strain (or conduction gap), the OFF-current is strongly reduced and by defining arbitrarily the ON-current as the current obtained at $V_{gs} = 0.35$ V, the ON/OFF current ratio increases significantly to over 10^5 for $\sigma = 5\%$. Such a high ratio seems to be at variance with what was shown for bilayer graphene [114] and graphene nanomesh FETs [92], where an energy gap of ~ 300 meV is not enough to switch off the current efficiently, i.e., to obtain a large ON/OFF ratio. This may be because, in those devices, the energy gap occurs locally in the gated region and is, therefore, not sufficient to fully suppress the band-to-band tunneling components. This situation here, with unstrained/strained junctions, is different and is explained below.

In fact, the transport modes k_y that contribute significantly to the current are the values k_y around the range from $K_{unstrain}$ to K_{strain} , as schematized in Fig. 3.7. Far from this range to the left and to the right, the energy gap $E_{gap}(k_y)$ in the strained

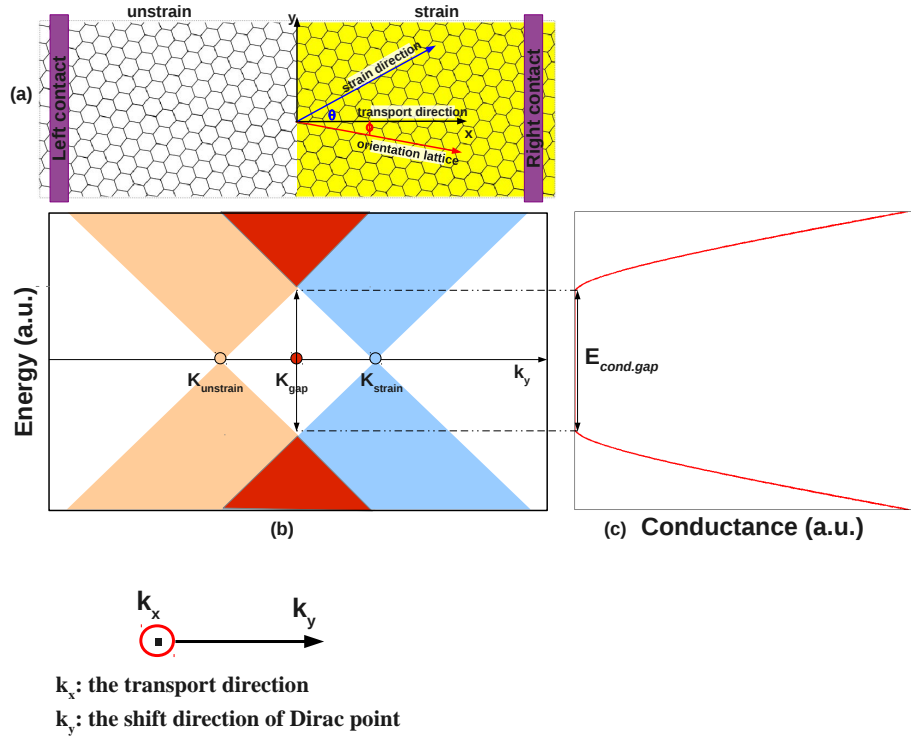


Figure 3.7: (a) unstrained/strained graphene junctions. (b) bandedges illustrating the strain-induced shift of Dirac points along the k_y -direction that leads to the opening of a conduction gap (c) [chapter 2].

(source and half of the gated zone) and unstrained (drain and half of the gated zone) graphene sections, respectively, is very large, which very strongly suppresses the corresponding current component even in the ON state. Close to $k_y = K_{unstrain}$ or K_{strain} , the energy gap mentioned is still large, but the corresponding current component starts to have a significant contribution to the ON current, while it remains almost negligible in the OFF-state. For other modes k_y , e.g., around K_{gap} , the energy gap of $\sim E_{cond.gap}$, though smaller than the gap of modes discussed above, occurs along the whole channel and is thus enough to switch off the corresponding component of current in the OFF-state. The combined effect of these k_y -dependent energy gaps makes high the ON/OFF current ratio, at the price of a reduced ON-current. The result obtained demonstrates that strained heterochannels are excellent candidates for graphene devices in electric applications. The full analysis of this device can be found in [102].

3.3 Enhanced thermoelectric effect

Recent studies have shown that the potential of graphene as thermoelectric material is quite intriguing (seen in review [119] and Refs. therein). This single layer of carbon atoms offers fascinating electronic properties resulting in high mobility for massless chiral particles [3, 60]. Regarding thermoelectric properties, graphene has the advantage of a strong energy-dependence of the conductivity near the charge neutrality point [1]. However, it has the strong drawback to be gapless, which makes it difficult to separate the opposite contributions of electrons and holes to the Seebeck coefficient. It results in a finite but small value of $S < 100 \mu V/K$ in pristine graphene [62].

So far, many studies have suggested different ways to open a bandgap in graphene as mentioned in chapter 2. As a direct consequence, it has been shown that the Seebeck effect can be significantly enhanced in graphene nanostructures with finite energy gap such as armchair graphene nanoribbons [120], hybrid structures combining zigzag graphene nanoribbon with zigzag boron nitride nanoribbon [121], graphene nano-hole lattices [122], graphene nanoribbons consisting of alternate zigzag and armchair sections [123], vertical graphene junctions [124], and graphene p-n junctions [125]. However, each method has its own drawbacks and still need to be confirmed by experiments. Some of them will be mentioned in more detail in the discussion below.

Furthermore, we repeat that graphene has been demonstrated to be conformable and able to sustain large strain [41, 42], making it a promising candidate for flexible devices. Also, strain engineering has been proposed to be an alternative approach to modulating the electronic properties of this material. In particular, it has been shown that an energy gap can be opened in pristine graphene for deformations beyond 20% [71]. In the previous chapter, we have investigated the effects of uniaxial strain on the transport properties of 2D graphene heterochannels and found that a significant conduction gap of a few hundred meV can be achieved with a small strain of a few percent. This result motivated us to investigate here the possible strain-induced enhancement of Seebeck coefficient in graphene nanostructures. In addition, doping engineering has been included in our investigation since it is likely to increase strongly the conduction gap, and thus the Seebeck coefficient, in graphene doped heterojunctions. All these interesting points will be discussed in detail in this section.

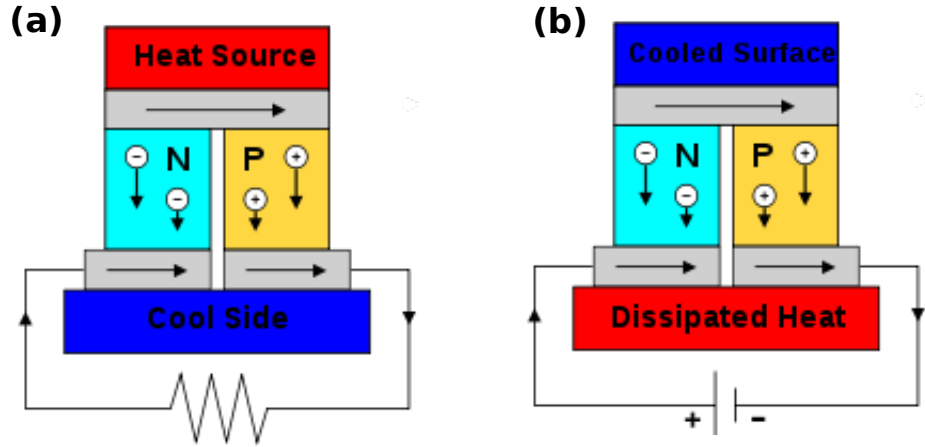


Figure 3.8: Left panel: a thermoelectric circuit composed of materials of different Seebeck coefficient (p-doped and n-doped semiconductors), configured as a thermoelectric generator (a). Right panel: the Seebeck circuit configured as a thermoelectric cooler (b).

3.3.1 What is the thermoelectric effect?

The thermoelectric effect is the direct conversion of temperature differences to electric voltage and vice versa. A thermoelectric device creates a voltage when there is a different temperature on each side. Conversely, when a voltage is applied to it, it creates a temperature difference. At the atomic scale, applying a temperature gradient induces a diffusion of charge carriers in the material from the hot side to the cold side. This effect can be used to generate electricity, measure temperature or change the temperature of objects. Because the direction of heating and cooling is determined by the polarity of the applied voltage, thermoelectric devices can be used as temperature controllers, as illustrated in Fig. 3.8.

In particular, when a conductor is connected to a hot and a cold reservoir with a temperature difference ΔT , an electrical voltage ΔV is established across the conductor according to

$$\Delta V = S\Delta T \quad (3.1)$$

where S is the Seebeck coefficient characterizing the thermoelectric sensitivity of the conductor. The use of materials with high Seebeck coefficient is thus one of important factors to design efficient thermoelectric generators and coolers or thermal sensors. It is also important to maximize the power factor $G_e S^2$ where G_e is the conductivity of the material. In a conductor in weak scattering regime, the linear

response thermoelectric coefficient is given by the Mott's formula [126]

$$S = \frac{1}{G_e} \frac{k_B}{e} \int G_e(\epsilon) \frac{\epsilon - E_F}{k_B T} \left(-\frac{\partial f}{\partial \epsilon} \right) d\epsilon \quad (3.2)$$

where $G_e(\epsilon)$ is the energy-dependent conductivity associated to the density $n(\epsilon)$ of electrons that fill energy states between ϵ and $\epsilon + d\epsilon$, and $f(\epsilon)$ is the Fermi-Dirac distribution function with the Fermi energy E_F . In conventional materials, a high Seebeck coefficient is usually found in low carrier density semiconductors while a high conductivity is found in metals. The best compromise is often to use heavily-doped semiconductors where, thanks to the finite bandgap, electrons and holes can be separated and the Seebeck coefficient is not reduced by their opposite contributions.

However, since the pioneering works of Hicks and Dresselhaus [127], nanostructuring materials into low-dimensional systems are now widely investigated to enhance the thermoelectric properties. To basically understand this size effect on the Seebeck coefficient, it is convenient to start from the simplified form of Eq. 3.2 derived for degenerately doped materials, i.e.

$$S = -\frac{\pi^2 k_B^2 T}{3e} \frac{1}{G_e} \left. \frac{\partial G_e(\epsilon)}{\partial \epsilon} \right|_{\epsilon=E_F} \quad (3.3)$$

This expression suggests that any effect that can enhance the energy-dependence of the conductivity should enhance the Seebeck coefficient, e.g., by enhancing the energy-dependence of the density $n(\epsilon)$ that is directly dependent on the density of states $D(\epsilon)$. Hence, compared to bulk materials, low-dimensional systems are expected to provide higher Seebeck coefficient and power factor thanks to much higher $dD(\epsilon)/d\epsilon$. For instance, it has been confirmed experimentally first in PbTe/Pb_{1-x}Eu_xTe quantum well structures [128].

Regarding some thermoelectric applications, the figure of merit ZT is another important parameter. The figure of merit ZT determines the efficiency of energy conversion in thermoelectric device [119]

$$\eta = \eta_0 \frac{\sqrt{1 + ZT} - 1}{\sqrt{1 + ZT} + (T_c/T_h)} \quad (3.4)$$

where T_h and T_c are temperatures of hot and cold end, and $\eta_0 = 1 - T_c/T_h$ is the Carnot efficient for an ideal system. The thermoelectric figure of merit is defined as $ZT = G_e S^2 T / \kappa$, where κ is the thermal conductivity. Actually, strain engineering is not an efficient technique to modulate the phonon bandstructure [129] and to strongly reduce the thermal conductivity in the junctions studied here. Hence, though the

Seebeck coefficient and the power factor $G_e S^2$ are strongly improved, we believe that the combination of this design with additional nanostructuring (e.g., as in [124]) or more complex design would be required to achieve high ZT . For this reason, we focus here our investigation on the Seebeck coefficient that is an essential ingredient.

3.3.2 The Seebeck effect in monolayer and bilayer graphene, graphene nanoribbons and graphene nanomesh

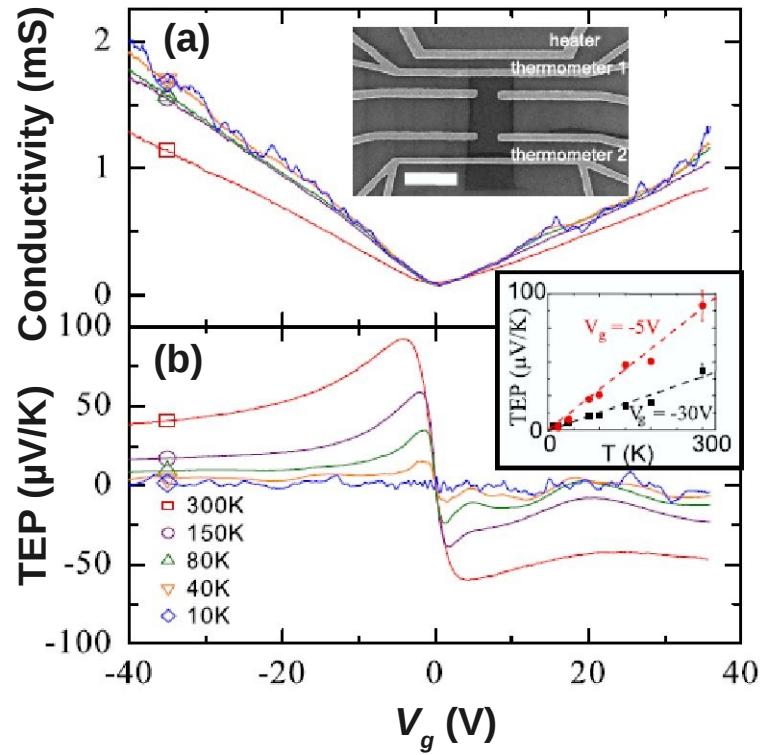


Figure 3.9: (a) Electrical conductivity and (b) thermoelectric power (TEP) of a graphene sample as a function of V_g (for different temperatures) for single graphene. From Y. M. Zuev *et al* [62].

As discussed in [130], compared to bulk materials, low-dimensional systems are expected to provide higher Seebeck coefficient and power factor. Graphene is truly a 2D lattice of carbon atoms. Beside, nanostructures of this material have been fabricated in experiment, i.e., graphene nanoribbons, graphene nanomesh or a few heterostructures of graphene with other 2D materials. Therefore, some nanostructures of graphene are expected to be good candidates for thermoelectric applications. In this sub-section we review briefly the performance of some graphene structures in terms of Seebeck effect.

First, let's look again at the results of Seebeck effect in monolayer, bilayer graphene, graphene nanoribbons as well as graphene nanomesh. The first measurement of the thermoelectric properties of graphene were published in 2009 [131]. In these experiments, the structures consisted of a single-layer graphene sheet exfoliated onto a 300 nm-thick SiO_2 layer grown on degenerately doped Si substrate, with a back gate to control the carrier density. All measurements have confirmed that at room temperature the peak value of thermopower reaches about $80 \mu V K^{-1}$, as seen in Fig. 3.9.

Next, these results of thermoelectric power (TEP) measurements in bilayer graphene in zero magnetic field is shown in Fig. 3.10 by Seung-Geol Nam *et al* [132]. Here, it is seen that the dependence of TEP on temperature is similar to the case of monolayer graphene because bilayer graphene has also no bandgap.

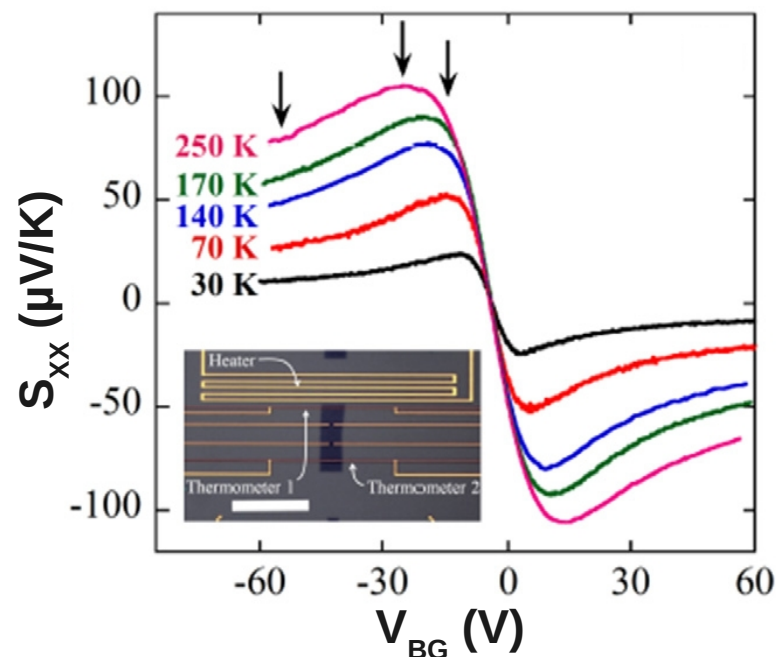


Figure 3.10: Thermoelectric power (S_{xx}) as a function of the backgate voltage V_{BG} in zero magnetic field and at various temperatures: $T = 30, 50, 70, 140, 170,$ and $250 K$. From Seung-Geol Nam *et al* [132].

Y. Yokomizo *et al* have suggested to use structures combining zigzag graphene nanoribbons (ZGNR) with hexagonal boron nitride (h-BN) to create superlattices. This ZGNR/h-BN superlattices can open a bandgap and hence enhance significantly the Seebeck coefficient, compared with graphene strips. In particular, as seen in Fig. 3.11, the Seebeck coefficients in ZGNR/BNNRs is higher than in ZGNRs. Moreover,

the superlattice (2,2) has the highest Seebeck coefficient of 1.78 mV/K at maximum, while ZGNR ($n = 2$) has the Seebeck coefficient of 0.282 mV/K. Hence, the Seebeck coefficient of superlattice is 6.3 times larger than that of ZGNR and 22 times as large as in monolayer graphene. However, the drawback of these superlattices is the decreasing of bandgap by increasing the width of graphene/h-BN strip, which leads to the strong decrease of Seebeck coefficient.

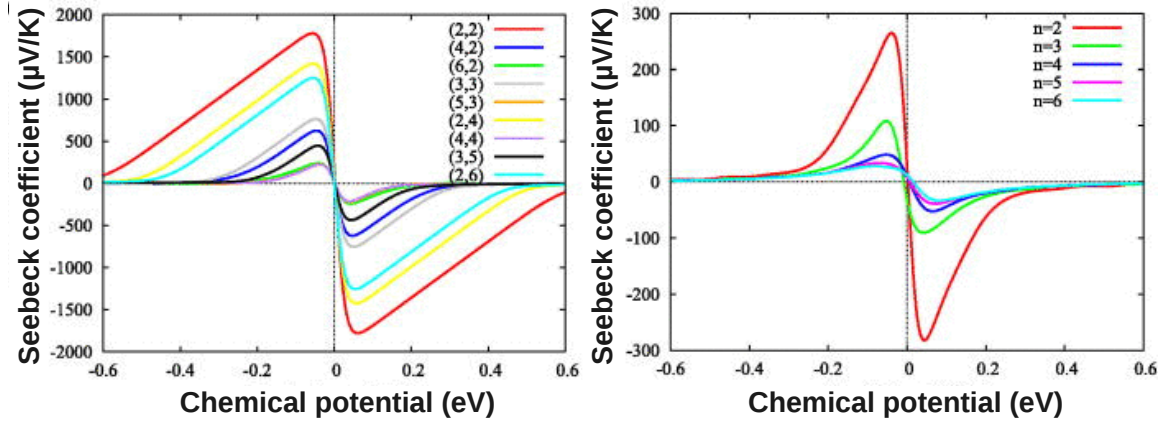


Figure 3.11: Seebeck coefficients of (a) the ZGNR/BNNR superlattices and (b) free-standing ZGNRs at 300 K as a function of the chemical potential felt by electrons. From Y. Yokomizo *et al* [121].

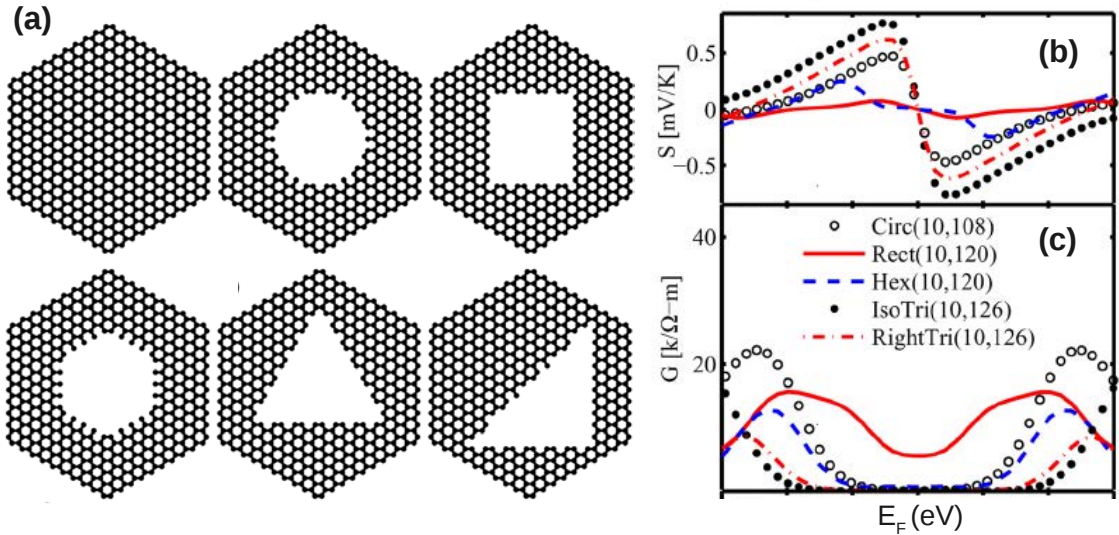


Figure 3.12: Geometrical structures of different graphene antidot lattices (GALs) in (a) with Circ(10, 108), Rect(10, 120), Hex(10, 120), IsoTri(10, 126), and RightTri(10, 126), respectively. Seebeck coefficient and electrical conductance are displayed in figure (b) and (c). From H. Karamitaheri *et al* [133].

The enhancement of Seebeck effect has been suggested in graphene nanomesh systems (also called graphene antidot lattice) by H. Karamitaheri *et al* [133]. In these systems, the zero bandgap graphene can be converted into a narrow bandgap semiconductor as seen in Fig. 3.12. This positive point is useful in thermoelectric applications. In contrast to a pristine graphene sheet, graphene nanomeshes have a beneficial bandgap, so that one can suppress either the electron or the hole current to obtain unipolar conductance. As a result, these systems with finite bandgap have a high Seebeck coefficient and a low electrical conductance. However, similarly as ZGNR/BNNRs, graphene nanomesh has also the drawback that the value of Seebeck coefficient is very sensitive the size and the shape of nanoholes.

3.3.3 The enhancement of Seebeck effect in graphene heterochannels by strain and doping engineering

In this part, we would like to discuss about 2D graphene doped heterojunctions with a strain area of finite length as schematized in Fig. 3.13. The strain area covers symmetrically both doped sides and its length L_S is assumed to be much longer than the length of the transition region L_T between left and right doped sections. In this work, the doping profile can be generated/controlled by chemical doping or electrostatic methods, e.g., as seen in refs. [134, 135]. Though expected to be short for achieving high band-to-band tunneling current, the transition length is always finite in devices with chemical doping [134]. In the case of electrostatic doping [135], this length is also finite but can be controlled by tuning the properties of insulator layer, i.e., its thickness and dielectric constant. Throughout this work, unless otherwise stated our calculations were performed at room temperature for $L_S = 70 \text{ nm}$ and $L_T = 10 \text{ nm}$.

In this part, we still use the p_z -orbital tight-binding model to calculate electronic and thermoelectric properties of the device with Hamiltonian H_{tb} [as mentioned in chapter 2]. In particular, here we consider a local uniaxial strain applied along the Oy direction. Accordingly, the strain-dependence of $C - C$ bond vectors is given by

$$\begin{cases} r_x(\sigma) = (1 - \sigma\gamma) r_x(0) \\ r_y(\sigma) = (1 + \sigma) r_y(0) \end{cases} \quad (3.5)$$

where σ is the strain amplitude and $\gamma = 0.165$ is the Poisson's ratio, as described in chapter 2. In the specific case of this study, where the strain is applied along a zigzag axis, we have to consider two different hopping parameters $t_{1,2}$ in the armchair

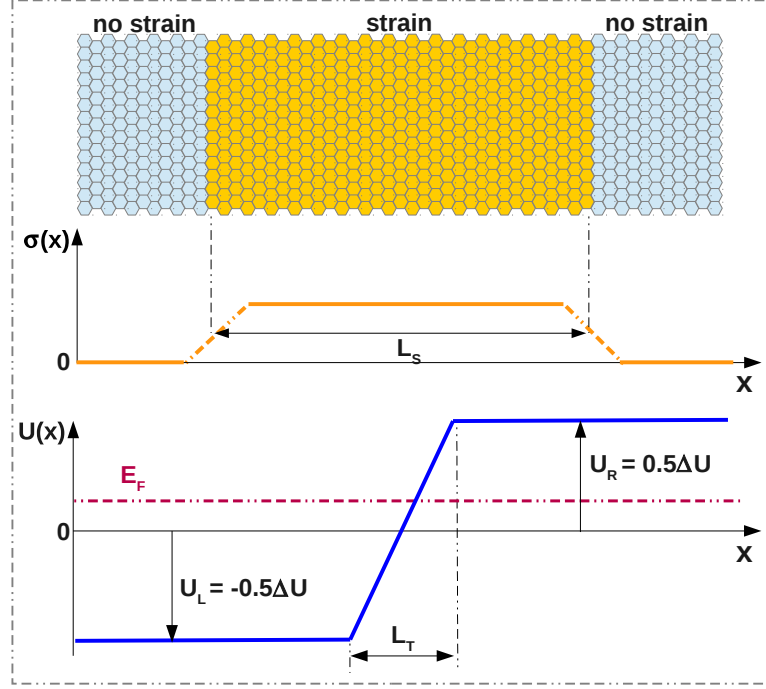


Figure 3.13: Schematic view of the graphene structure investigated in this work, consisting of a PN diode with a locally strained area of length L_S that covers symmetrically both doped sides. The bottom shows its strain and potential profiles where the doping is characterized by the potential difference $\Delta U = U_R - U_L$ and the length L_T of transition region.

and zigzag directions, respectively, corresponding to two bond vectors $\vec{r}_{1,2}$ in strained graphene as in [102].

Next, the tight-binding Hamiltonian was solved by the Green's function technique: $\mathcal{G}(\epsilon, k_y) = [\epsilon + i0^+ - H_{tb}(k_y) - \Sigma_L(\epsilon, k_y) - \Sigma_R(\epsilon, k_y)]^{-1}$, where $H_{tb}(k_y)$ is the Hamiltonian rewritten in the wavevector k_y -dependent (quasi-1D) form as in [101] and $\Sigma_{L(R)}$ is the self energy describing the left (right) contact-to-device coupling. The local density of states and the transmission probability needed to evaluate the transport quantities are determined as $\mathcal{D}(\epsilon, k_y, \vec{r}_n) = -\text{Im} \{ \mathcal{G}_{n,n}(\epsilon, k_y) \} / \pi$ and $\mathcal{T}_e(\epsilon, k_y) = \text{Tr} \{ \Gamma_L \mathcal{G} \Gamma_R \mathcal{G}^\dagger \}$, respectively, where $\Gamma_{L(R)} = i \left(\Sigma_{L(R)} - \Sigma_{L(R)}^\dagger \right)$ is the energy level broadening at the left (right) contact. The electrical conductance and the Seebeck coefficient were calculated by

$$G(E_F) = G_0 L_0(E_F, T) \quad (3.6)$$

$$S(E_F) = \frac{1}{eT} \frac{L_1(E_F, T)}{L_0(E_F, T)} \quad (3.7)$$

where

$$L_n(E_F, T) = \frac{1}{\pi} \int d\kappa_y d\epsilon \mathcal{T}_e(\epsilon, \kappa_y) (\epsilon - E_F)^n \left(-\frac{\partial f}{\partial \epsilon} \right). \quad (3.8)$$

Here, $G_0 = e^2 W/hL_y$ and the channel width $W = M_{cell}L_y$ with the size of unit cells L_y ($\equiv r_0\sqrt{3}$) and the number of cells M_{cell} along Oy direction. The integral over κ_y ($\kappa_y \equiv k_y L_y$) is performed in the whole Brillouin zone. The distribution function $f(\epsilon, E_F) = (1 + \exp[(\epsilon - E_F)/k_B T])^{-1}$ is the Fermi-Dirac function with the Fermi energy E_F .

3.3.3.1 Strained device with uniform doping ($\Delta U = 0$)

First, let us examine the basic effect of strain on the transport properties of graphene. Actually, for a small strain of a few percent, graphene is still metallic [71], i.e., its gapless character does not change [as discussed in chapter 2]. However, even a small strain causes a shift of Dirac points in the k -space [71]. As a consequence, it may lead to the opening of a conduction gap in strained/unstrained graphene junctions [101] [explained detail in chapter 2]. The appearance of conduction gap is in principle an important factor in the enhancement of Seebeck coefficient, which is discussed in next parts.

In Figs. 3.14(a) and 3.14(b), we plot the conductance and Seebeck coefficient, respectively, as a function of Fermi energy for different strain amplitudes σ ranging from 0 to 10 %. While the minimum value of conductance is finite in pristine graphene ($\sigma = 0$), a finite conduction gap is achieved when a local strain is applied to the structure. Actually, E_{gap} increases almost linearly as a function of strain amplitude and, particularly, it takes the value of 0.162 eV, 0.324 eV, 0.486 eV, 0.654 eV, 0.822 eV for $\sigma = 2\%$, 4%, 6%, 8%, 10%, respectively, as can be seen in table in Fig. 3.15. As expected from this gap enhancement, the maximum value S_{max} of Seebeck coefficient increases from 0.086 mV/K for $\sigma = 0$, in agreement with experimental data [62], to 0.803 mV/K for $\sigma = 6\%$. We find as shown in Fig. 3.14(c) that the conductance in the OFF state, i.e., the minimum of conductance when varying E_F (practically, at $E_F = 0$), decreases exponentially when the strain amplitude increases, in accordance with the linear increase of conduction gap. This effect is at the origin of the enhancement of ON/OFF current ratio in the transistors based on this type of strain heterochannels [102], where the OFF and ON currents are the minimum and maximum currents, respectively, obtained when tuning the gate voltage. It is shown concomitantly in Fig. 3.14(c) that S_{max} increases linearly as a function of strain amplitude and reaches up to 1.353 mV/K for $\sigma = 10\%$. However, practically it may

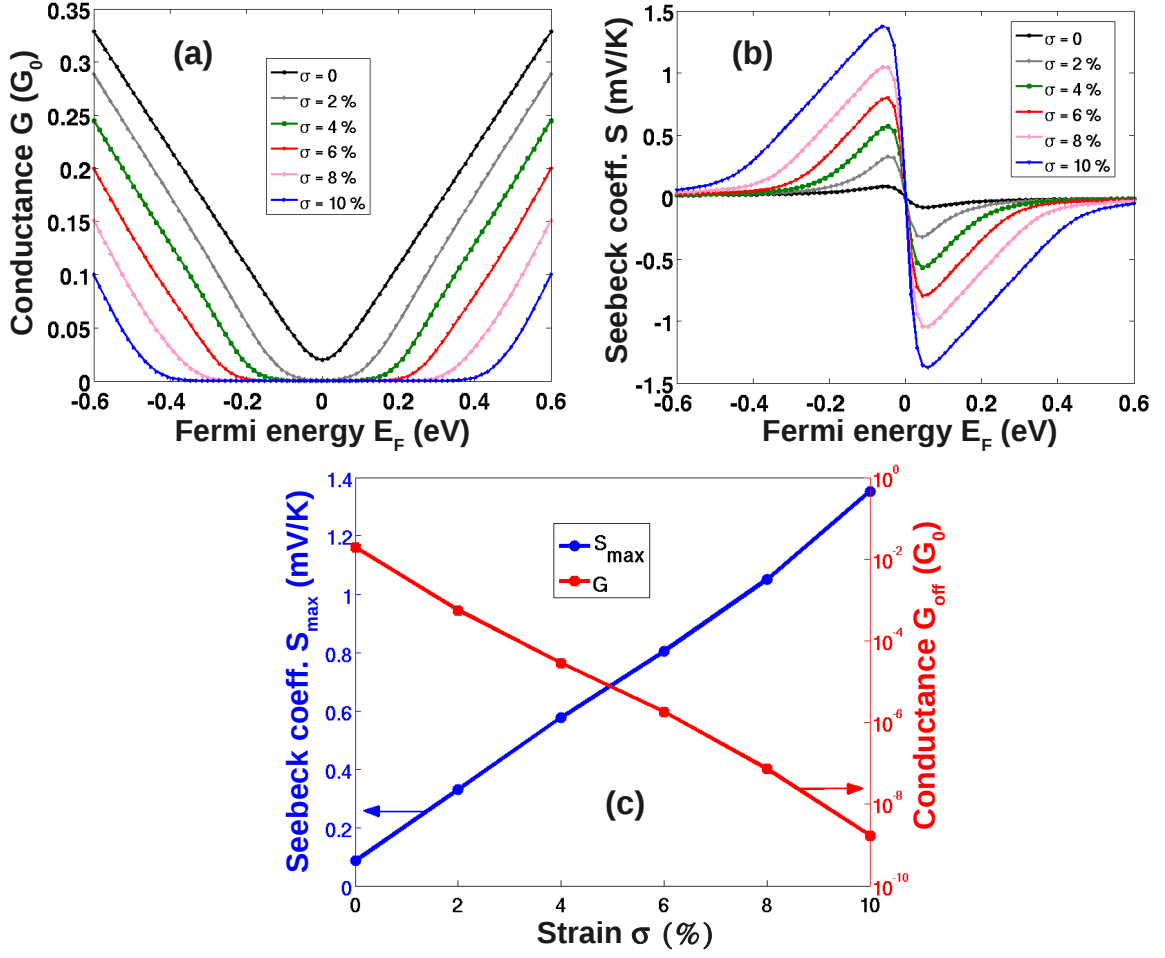


Figure 3.14: (a) Conductance and (b) Seebeck coefficient as a function of Fermi energy E_F for different strain amplitudes in the device with uniform doping. (c) Maximum value of Seebeck coefficient (S_{max}) and conductance (G_{off}) in OFF state (i.e., at $E_F = 0$) as a function of strain amplitude.

be difficult to apply locally such a large strain in this type of structure. Hence, we propose here to introduce appropriate doping engineering in this device to enhance the conduction gap with a reasonable strain amplitude.

3.3.3.2 Strained device with both strain and doping engineering ($\Delta U \neq 0$)

In this subsection, we discuss the effects of doping engineering schematized in Fig. 3.13 on the transport properties of this strain heterostructure. The structure now consists of three sections: differently doped-graphene sections in both sides and a transition region between them. Note that within the condition $L_S \gg L_T$, left and right doped sections are actually formed by two different strain junctions. In Fig. 3.16, we display the conductance G and the Seebeck coefficient as a function of Fermi

Strain (%)	Conduction gap (eV)	Maximum Seebeck coefficient (mV/K)
0	0	0.086
2%	0.162	0.328
4%	0.324	0.576
6%	0.486	0.803
8%	0.654	1.050
10%	0.822	1.353

Figure 3.15: The value of conduction gap E_{gap} corresponding with maximum of Seebeck coefficient for strain amplitude from 0 to 10%.

energy E_F for different doping profiles. The strain amplitude is fixed to 5% and the doping profile is characterized by a finite potential difference $\Delta U = U_R - U_L$ (see Fig. 3.13). The doping engineering consists here in controlling the carrier density profile, which is characterized and determined by both the potential ΔU and the Fermi level E_F . The results in Fig. 3.16(a) show that for small ΔU , the conduction gap increases with this potential difference, which can be explained as follows. When ΔU increases, E_{gap} of strained/unstrained junctions in the left and right sides are shifted in opposite directions, which results in the enlargement of the transmission gap (i.e., conduction gap). Indeed, this phenomenon is clearly illustrated in the pictures of local density of states (LDOS) and transmission coefficient in Fig. 3.18, obtained for $k_y = (K_y^{unstrain} + K_y^{strain})/2$ where $K_y^{unstrain/strain}$ is the wavevector at the Dirac points of unstrained/strained graphene, respectively. Note that at this k_y point, $E_{gap}^{unstrain}(k_y) \simeq E_{gap}^{strain}(k_y) \simeq E_{gap}$ for $\Delta U = 0$. Actually, the conduction gap $E_{gap}(\Delta U)$ of the whole device in the range of small ΔU (i.e., $\Delta U < E_{gap}(0)$) is basically determined as $E_{gap}(\Delta U) = E_{gap}(0) + \Delta U$, as shown in Fig. 3.18(c) and confirmed in Fig. 3.16(c) where we observe a linear dependence of E_{gap} as a function of ΔU . As a consequence, S is significantly enhanced when increasing ΔU (see Fig. 3.16(b)) and S_{max} reaches the value of 0.689, 0.839, 0.999, 1.160 and 1.315 mV/K for $\Delta U = 0, 0.1, 0.2, 0.3$ and 0.4 eV, respectively, as can be seen in table of Fig. 3.17. It is worth noting here that the result obtained for $\eta = 5\%$, $\Delta U = 0.4$ eV is almost similar to that obtained for $\sigma = 10\%$, $\Delta U = 0$, which is about 15 times greater than S_{max} in pristine graphene. Thus, it is demonstrated that the doping engineering can be an effective way to further enlarge E_{gap} without the requirement of too large

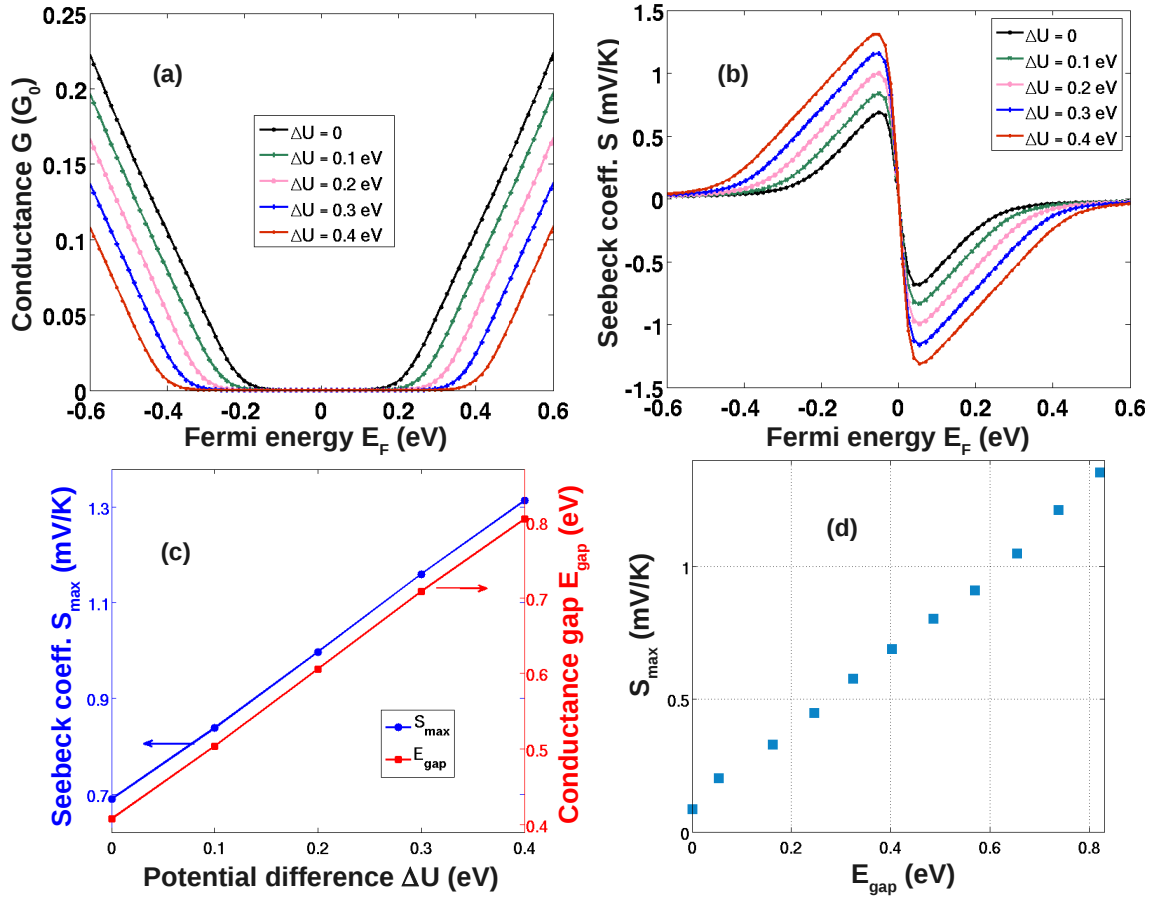


Figure 3.16: (a) Conductance and (b) Seebeck coefficient as a function of Fermi energy E_F for different ΔU . (c) Maximum Seebeck coefficient (S_{max}) and conduction gap (E_{gap}) as a function of ΔU . (d) S_{max} as a function of E_{gap} . $\sigma = 5\%$ is considered here.

Doping potential (eV)	Conduction gap (eV)	Maximum Seebeck coefficient (mV/K)
0	0.402	0.689
0.1	0.504	0.839
0.2	0.606	0.999
0.3	0.708	1.160
0.4	0.804	1.315

Figure 3.17: The value of conduction gap E_{gap} corresponding with maximum of Seebeck coefficient for doping potential from 0 to 0.4 eV.

strain. All the features above are clearly summarized in Fig. 3.16(d). In addition, the Fig. 3.16(d) confirms that whatever the technique of energy gap opening S_{max}

always depends linearly on E_{gap} , as predicted theoretically in ref. [121].

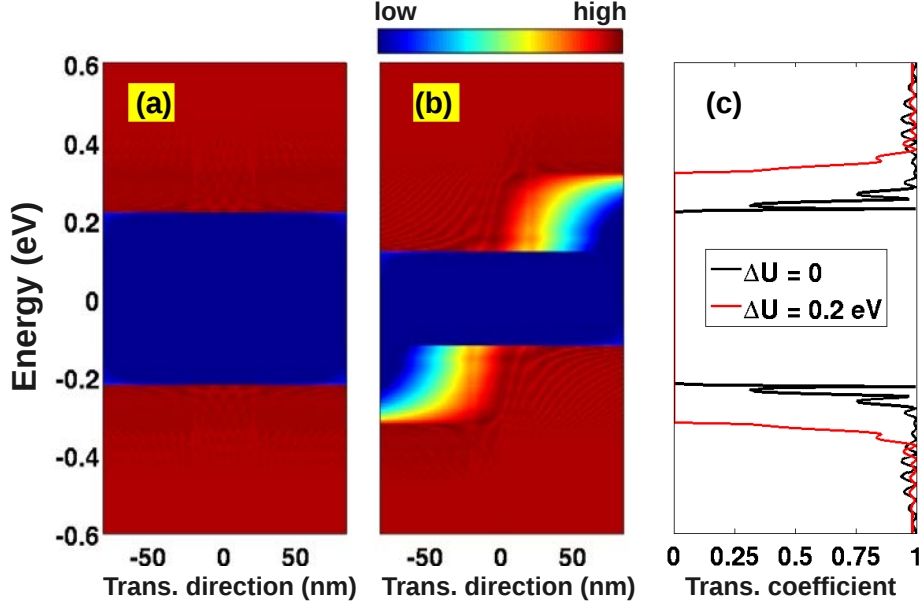


Figure 3.18: Local density of states in the devices of different ΔU : 0 (a) and 0.2 eV (b). The blue color regions correspond to energy-gaps, i.e., low density of states. (c) shows the transmission coefficient in these two cases. $k_y = (K_y^{unstrain} + K_y^{strain})/2$ and $\sigma = 5\%$ are considered here.

3.3.3.3 Strained device with large doping

Next, we go to analyze the effects of large ΔU , i.e., values greater than $E_{gap}(0)$. In Figs. 3.19(a) and 3.19(b) we plot the conductance and Seebeck coefficient as a function of E_F for large values of ΔU increasing from 0.4 eV to 0.6 eV. It is shown that the conduction gap is separated in two smaller ones that correspond to the conduction gap of each strained/unstrained junction of the structure. Between these two gaps, a region of finite conductance is recovered due to the band-to-band tunneling (BTBT), as in a standard doped tunnel diode, which is illustrated clearly in Figs. 3.20(a,b) and 3.20(c) where we plot the map of LDOS and transmission coefficient, respectively, for $\Delta U = 0.4$ eV and $\Delta U = 0.6$ eV. As a consequence, at large ΔU the Seebeck coefficient exhibits two positive (negative) peaks with a maximum value S_{max} that reduces and tends finally to a finite value S_∞ when increasing ΔU , as shown in the Fig. 3.19(c). Note that the value S_∞ is generally higher than the value of S_{max} obtained for $\Delta U = 0$ but tends to this value when the transition length L_T is reduced. This is explained by the detrimental contribution of band-to-band tunneling current, which is significantly reduced when increasing L_T (see further comments below). It

is additionally shown that $S_{max}(\Delta U)$ has a peak at $\Delta U \equiv E_{gap}(0)$, e.g., $\Delta U \simeq 0.4 \text{ eV}$ for $\sigma = 5\%$ here.

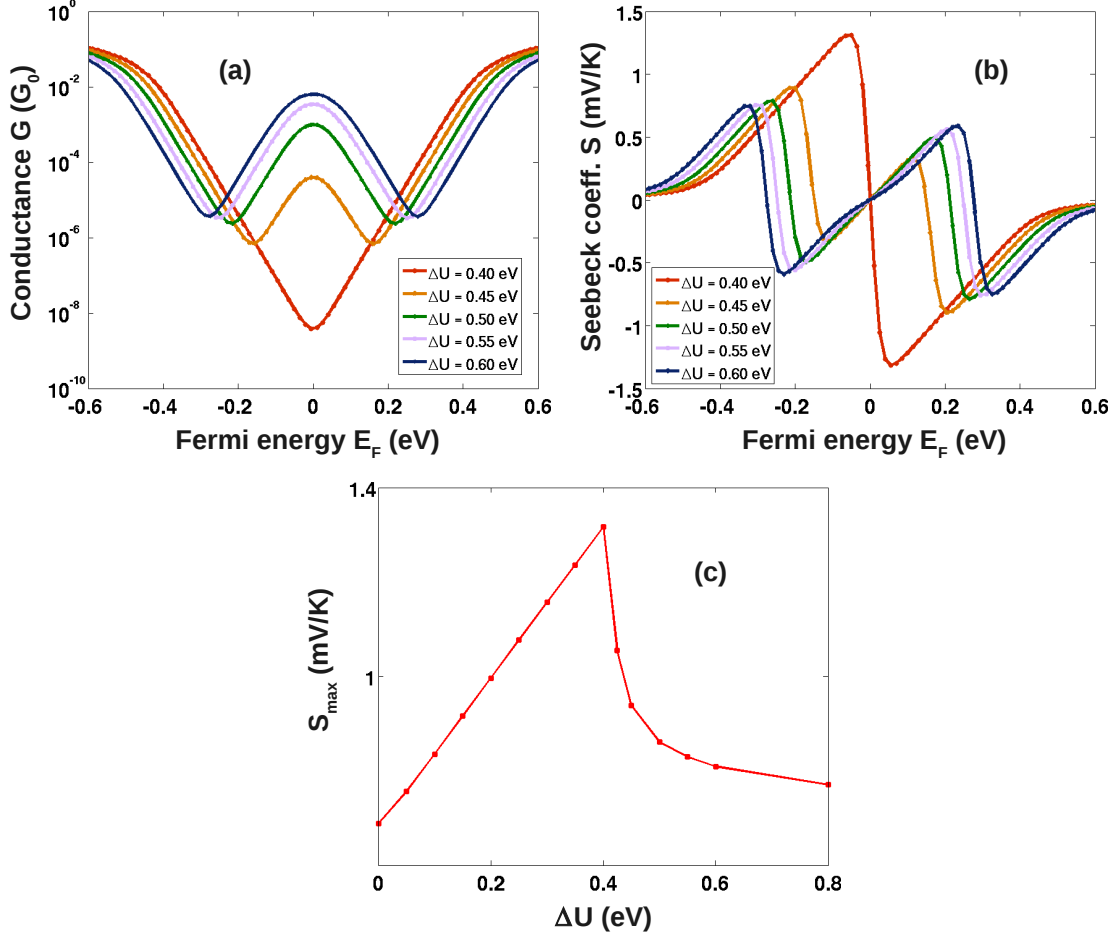


Figure 3.19: (a) conductance and (b) Seebeck coefficient as a function of Fermi energy E_F with high values of ΔU . The relationship between S_{max} and ΔU is shown in (c). $\sigma = 5\%$ is considered here.

Now, we would like to clarify the roles of device parameters L_S and L_T on the obtained results. Note that in this work, we consider only the case $L_S \gg L_T$. Within this condition, each doped section contains by a strain junction and hence has a finite conduction gap. In principle, this conduction gap is strongly dependent on the length of the strained graphene part in these two doped sections, i.e., the transmission probability in the gap increases exponentially when reducing the length of strained graphene area. Hence, to ensure that the transmission is fully suppressed in the gap, the length L_S should be much larger than L_T . Moreover, the required length L_S is basically dependent on the value of energy gap, i.e., the larger L_S is required for the smaller E_{gap} (i.e., smaller strain). In particular, in the case of $\sigma = 5\%$,

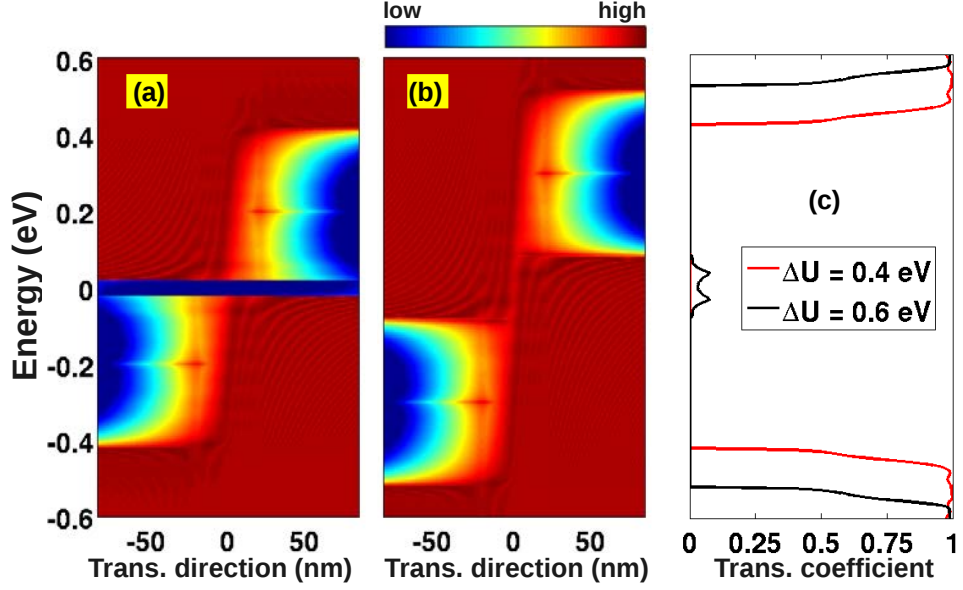


Figure 3.20: Local density of states in the devices of different ΔU : 0.4 (a) and 0.6 eV (b) (the blue color regions correspond to energy-gaps, i.e., low density of states). The transmission coefficient in these cases is shown in (c). $k_y = (K_y^{unstrain} + K_y^{strain})/2$ and $\sigma = 5\%$ are considered here.

$L_S > L_T + 20 \text{ nm}$ should be used. Additionally, it has been shown that the length L_T of the transition region between n - and p -doped sections plays an important role on the BTBT current [136], i.e., this current is exponentially reduced when increasing L_T as seen in Fig. 3.21(a). More interestingly, based on this reduction of BTBT current, the Seebeck coefficient in the case of $\Delta U > E_{gap}(0)$ is significantly enhanced when increasing L_T , i.e., S_{max} reaches 1.48 mV/K for $L_T = 40 \text{ nm}$ as shown in Fig. 3.21(b) while it is only about 0.77 mV/K for $L_T = 5 \text{ nm}$. We notice that in the case of small ΔU , the BTBT current is negligible as shown for $\Delta U = 0$ and 0.2 eV in Fig. 3.18 and hence S is very weakly dependent on L_T .

In conclusion of this work, we have proposed to make appropriate use of strain and doping engineering to generate and enlarge a conduction gap in graphene heterochannels and to benefit from this feature to enhance the Seebeck effect. The maximum value S_{max} of the Seebeck coefficient was shown to increase linearly with the conduction gap. Remarkably, with a small strain of 5% and an appropriate doping profile, the Seebeck coefficient can reach a value higher than 1.4 mV/K, i.e., 17 times higher than the value in gapless pristine graphene. Besides its use in strain sensors, this design strategy is thus promising to achieve good performance in graphene devices based on the Seebeck effect, as thermal sensors.

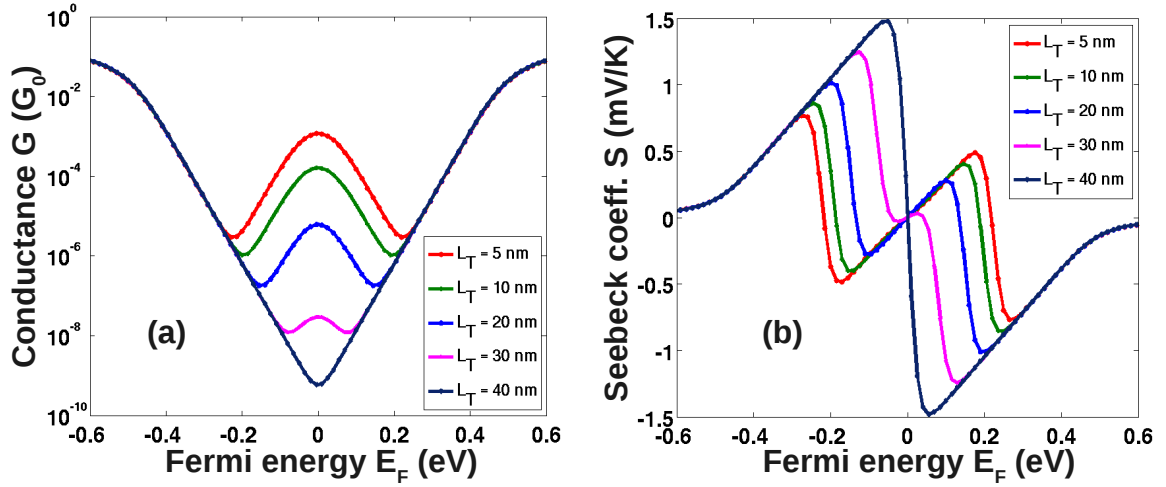


Figure 3.21: (a) conductance and (b) Seebeck coefficient as a function of Fermi energy E_F for the different lengths L_T . $\sigma = 5\%$ and $\Delta U = 0.5 eV$.

3.4 Enhanced negative differential conductance (NDC) effect

3.4.1 What is the NDC effect?

Negative resistance (NR) is a property of some electrical circuits and devices in which an increase in voltage across the device's terminal results in a decrease in electric current through it. While a positive resistance consumes power from current passing through it, a negative resistance may produce power [138, 139]. Under certain conditions, it can increase the power of an electrical signal. It can be seen that the conductance has the same sign as its corresponding resistance: a negative resistance will correspond to a negative conductance while a positive resistance will correspond to a positive conductance.

Beyond the usual linear or saturation behaviors expected to occur in transistors, non-linear effects as negative differential conductance (NDC) in the current-voltage characteristics may be of strong interest to design devices for high-speed analog applications and memories [140]. Hence, a lot of works have been devoted recently to investigate the possibility to generate a negative differential conductance or transconductance in graphene devices, based on various physical mechanisms.

For 2D graphene sheets, an NDC behavior has been observed experimentally in graphene transistors [141, 142] and explained theoretically as a possible consequence of chiral tunneling regime [142, 143, 144]. However, the effect is relatively weak due to the gapless character of graphene. The gapless bandstructure leads to the fact that

the band-to-band tunneling can give important contributions to the current, making the valley current relatively high [145, 146]. Recently, a strong NDC effect has been demonstrated in graphene/Boron Nitride/graphene van der Waals heterostructures in resonant tunneling regime [147, 148, 149]. An NDC behavior can be also obtained in tunnel diodes by controlling the interband tunneling between the conduction band of the n-doped side and the valence band in the p-doped side of the junction. Though small in gapless monolayer and bilayer graphene sheets [150], this effect increases significantly if a finite bandgap can be generated in graphene, as discussed below. The NDC has been predicted also in double-barrier resonant tunneling diodes [151, 152, 153], in diodes made of graphene/Boron Nitride heterochannels [154] and in graphene nanoribbon (GNR) superlattices with different ballistic transport regimes, including the resonant tunneling through the minibands and the Wannier-Stark ladder regime [155].

Nanostructuring graphene into nanoribbons offers promising possibilities to enhance non-linear effects in the I - V characteristics. The NDC effect has been predicted in different kinds of armchair GNRs working in resonant tunnelling regime [156, 157] and in heterochannels made of GNR sections of different widths [158, 159]. The effect of parity selective rule [160] in zigzag GNRs with an even number of zigzag lines has been also predicted to generate an NDC behavior [161]. Regardless of the width of zigzag GNR, the mismatch of modes between left and right sides of a zigzag GNR junction may also induce an NDC [162, 163]. Actually, the strongest NDC effect, with high peak-to-valley ratio (PVR) of several hundreds, has been predicted to occur in tunnel diodes made of GNR heterochannels with alternating sections of different widths [164]. This large PVR is essentially due to the enhancement of the peak current. Another graphene nanostructure, i.e. nanomesh lattices, has been also demonstrated as a good channel for NDC devices [97].

In this work we explore a new possibility to generate a strong NDC effect in graphene devices by exploiting the transport gap that can arise at strained/unstrained graphene junctions. It has been experimentally demonstrated that a 2D graphene sheet is conformable and able to sustain large strain of over 20% [165] (also mentioned in chapter 2). Therefore, modifying the electronic structure of this material by strain engineering has been proposed to overcome the lack of bandgap in graphene.

Different techniques to generate local strains at the nanoscale in graphene and 2D materials have been discussed in chapter 1. In this section, we will show that in the considered devices with a local strain of a few percent, the PVR can reach high values, i.e., a few hundreds. Additionally, in the case of a p-n tunnel diode, this ratio

will be shown to be not strongly sensitive to the transition length, i.e., the length of the region across which the charge density changes monotonically from n-type to p-type, that is usually difficult to control.

3.4.2 Enhanced NDC effect in strained graphene channels

In this work, we investigate the possibility to obtain a strong NDC behavior in 2D graphene devices by employing strain engineering. In particular, we focus on two structures: (i) single potential barriers with a finite strained graphene section inserted into the potential barrier region and (ii) graphene p–n junctions where strain is applied locally and symmetrically to both sides of the junction.

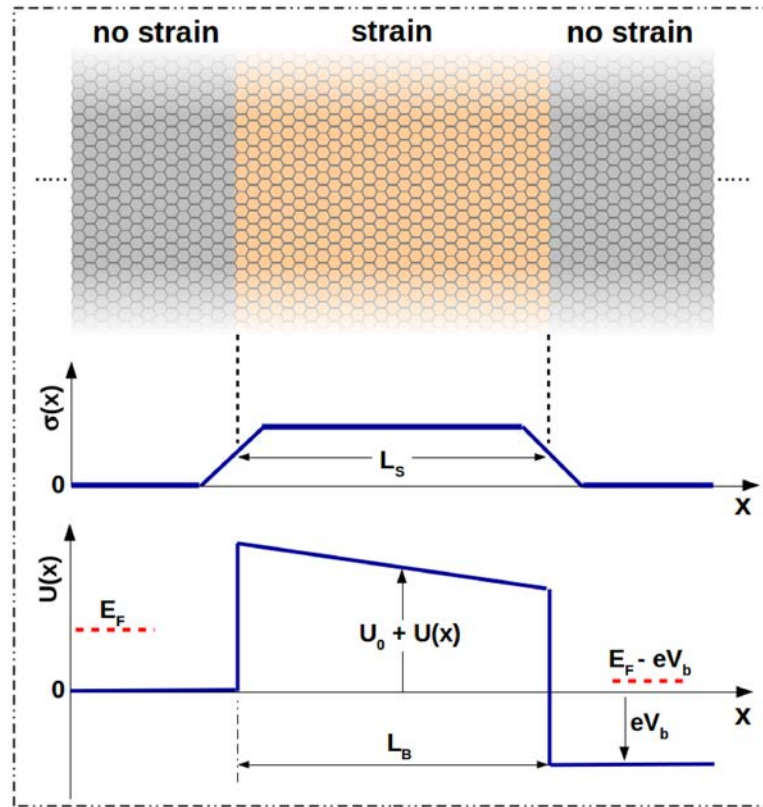


Figure 3.22: Schematic of single potential barrier structures studied in this work. Strain is applied locally in an area of length L_S and the potential barrier of length L_B can be generated and controlled by an external gate voltage. The middle panel shows the strain profile $\sigma(x)$. The bottom one is the potential energy along the device channel when a bias voltage V_b is applied.

An atomistic tight-binding model was still used to describe the electronic transport through the devices (similar as in previous section). Under a uniaxial strain applied

along the Ox direction, the $C - C$ bond vectors in Eq. 3.5 change as

$$\begin{cases} r_x(\sigma) \rightarrow (1 + \sigma)r_x(0), \\ r_y(\sigma) \rightarrow (1 - \gamma\sigma)r_y(0), \end{cases} \quad (3.9)$$

In general, there are three different hopping parameters $t_{1,2,3}$ corresponding to three bond vectors $r_{1,2,3}$ respectively, in the strained graphene region [101] (as mentioned in chapter 2). However, in this section, we consider the case where both the transport direction (Ox axis) and the direction of strain are parallel to the armchair line of graphene sheet so as to have a large transport gap for a given strain magnitude [101]. Therefore, there are only two different hopping parameters in strained graphene, i.e., $t_1 \equiv t_2$.

Throughout the work, the transition zone of ~ 10 nm between unstrained and strain sections (as seen in Fig. 3.22) is considered [101]. As in [101, 137], to investigate the electronic transport properties of the devices, we employed the non equilibrium Green's function formalism.

Given the large mean free path of charge carriers with respect to the typical device size and low defect density achievable in high-quality graphene on appropriate substrate [167, 168, 169, 170, 60], scattering (i.e., on phonon, defects, etc...) is not expected to affect strongly the physics of transport and the performance of the devices under investigation. On this basis, our simulations here were made in the ballistic approximation and the graphene channel was assumed to be free of defects and impurities. To this end, the tight-binding Hamiltonian H_{tb} is rewritten in the wavevector k_y -dependent (quasi-1D) form $H_{tb}(k_y)$ [101]. The Green's function is then computed using the equation [58]:

$$\mathcal{G}(\epsilon, k_y) = [\epsilon + i0^+ - H_{tb}(k_y) - \Sigma(\epsilon, k_y)]^{-1}, \quad (3.10)$$

where the self-energy $\Sigma(\epsilon, k_y) = \Sigma_L(\epsilon, k_y) + \Sigma_R(\epsilon, k_y)$ with $\Sigma_{L(R)}$ being the self-energies that describe the left (right) contact-to-device couplings. The transmission probability needed to evaluate the current is calculated as $\mathcal{T}_e(\epsilon, k_y) = \text{Tr} \{ \Gamma_L \mathcal{G} \Gamma_R \mathcal{G}^\dagger \}$, with $\Gamma_{L(R)} = i(\Sigma_{L(R)} - \Sigma_{L(R)}^\dagger)$ (as described in previous section or in chapter 1). The current density is obtained by the Landauer formula:

$$J = \frac{e}{\pi h} \int_{BZ} dk_y \int d\epsilon \mathcal{T}_e(\epsilon, k_y) \{ f_L(\epsilon) - f_R(\epsilon) \}. \quad (3.11)$$

In this expression, the integral over k_y is performed in the whole Brillouin zone and $f_{L(R)} = 1/[1 + \exp((E - E_{FL(R)})/k_b T)]$ are the Fermi functions in the left (right) contact with the Fermi energies $E_{FL(R)}$. The local density of states is computed from the Green's function as $\mathcal{D}(\epsilon, k_y, \vec{r}_n) = -\text{Im} \{ \mathcal{G}_{n,n}(\epsilon, k_y) \} / \pi$ [58].

3.4.2.1 Enhanced NDC effect in single potential barrier structure

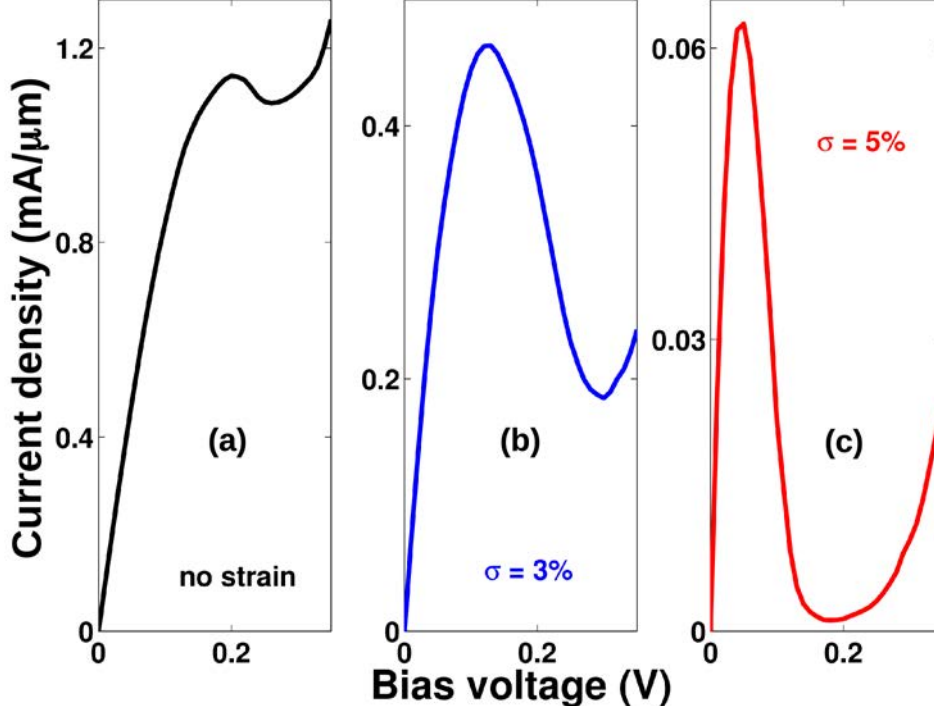


Figure 3.23: $I - V$ characteristics of a single potential barrier structure for different strain amplitudes. Other parameters of the structure are: $L_S = L_B = 40$ nm, $U_0 = 0.45$ eV, and $E_F = 0.25$ eV.

Clearly, a small strain of a few percent cannot change the gapless character of pristine graphene, but it is emphasized to lead to the shift of Dirac points in k -space [101, 118]. Thus, the appearance of transport gap in unstrained/strained junctions, i.e. the vanishing of the conductance over a finite range of energy, has been described in Chapter 2. Additionally, when a potential barrier is applied to the strained graphene regions, the energy bandstructure is shifted in energy. The combination of these shifts of graphene bandstructure both in k -space and in energy may lead to interesting features in the transport picture of single barrier structures as well as p-n tunnel diodes. In particular, not only does NDC behavior appear in these structures, but the effect is also significantly enhanced even with a relatively small strain of a few percent. This will be demonstrated and discussed in details below.

Important parameters that characterize the single potential barrier structure schematized in Fig. 3.22 are the length of strained region, L_S , the length of barrier, L_B , and the height of potential barrier, U_0 , which can be generated and controlled by a gate electrode [143, 144, 142]. First, we display in Fig. 3.23 the $I - V$ characteristics of

the device with $L_S = L_B = 40$ nm calculated for different values of strain amplitude while the values of U_0 and Fermi energy E_F are kept fixed at 0.45 eV and 0.25 eV, respectively. The appearance of NDC effect is clearly shown and its behavior is moreover strongly dependent on strain amplitude. Without strain ($\sigma = 0$), the NDC effect is weak with the PVR being only marginally larger than 1 (see Fig. 3.23(a)). When strain is applied, the overall current is reduced as seen in Fig. 3.23(b,c) and the general trend is that the larger the strain amplitude, the smaller the overall current. However, the valley current decreases much more significantly than the peak current, leading to a strong increase of the PVR with strain amplitude. For instance, with a strain of 3% PVR is slightly increased ($\sim 2 \div 3$), but it reaches a value of about 56 with a strain of 5%. Note that the increase of PVR is also strongly dependent on other device parameters (i.e., U_0 , E_F , and $L_{S,B}$) as discussed later. To explain

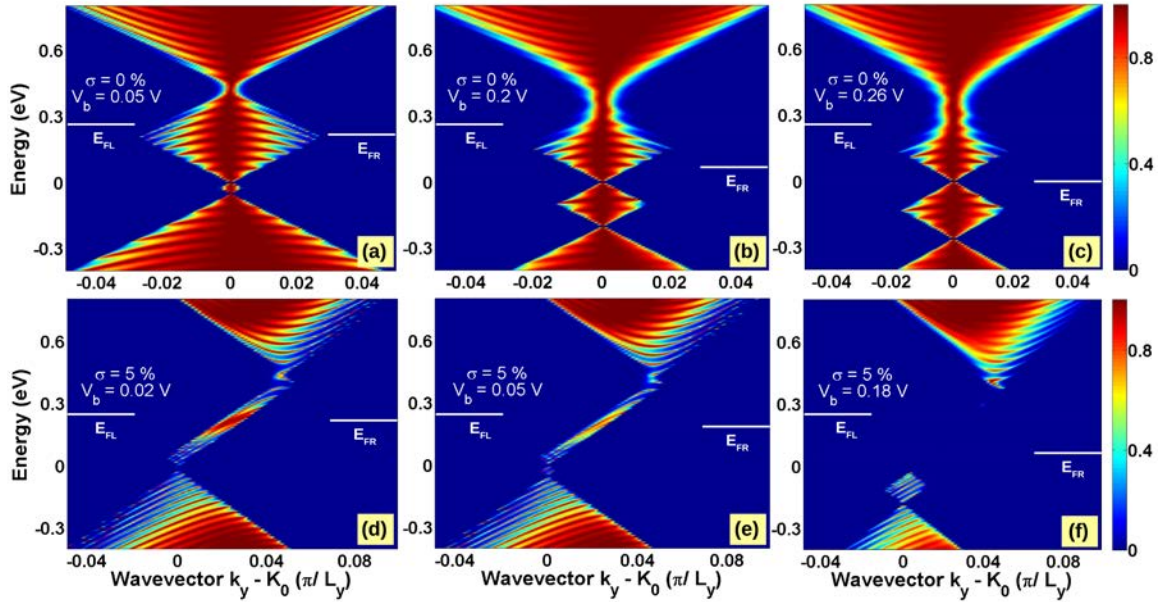


Figure 3.24: $(E - k_y)$ maps of transmission probability in two cases of unstrained (top) and strained (bottom) devices with different applied bias. K_0 denotes the position of Dirac point of unstrained graphene and $U_0 = 0.45$ eV is considered here.

the appearance of NDC effect in this structure and its enhancement when strain is applied, we display in Fig. 3.24 the $(E - k_y)$ maps of transmission probability at different values of bias voltage, V_b , for two cases: without strain (top panel, $\sigma = 0$) and with strain (bottom panel, $\sigma = 5\%$). The values of V_b for the two maps on the left panels are somehow arbitrarily chosen in the linear regions of $I - V$ characteristics in Figs. 3.23(a,c), while those for the maps in the middle and right columns are the values corresponding to the peak and valley positions of the current, respectively.

Let us first recall the reason for the appearance of NDC effect for the case of pristine graphene (i.e. without strain). When increasing the bias voltage, the energy window between two Fermi energies, $[E_{FR}, E_{FL}]$, that provides the main contributions to the flow of current is widened, thus making the current larger as can be seen when comparing Figs. 3.24(a) and 3.24(b). However, increasing the bias voltage also causes the extension of the bottleneck effect [143, 144] in the transmission probability (see Figs. 3.24(b) and 3.24(c)). When the bottlenecks of transmission probability enter into the energy window $[E_{FR}, E_{FL}]$, the current is reduced, which is the origin of the appearance of the NDC behavior observed in Fig. 3.23(a). It is noted that the bottleneck effect is here rather weak, hence the valley current can not be completely/strongly suppressed. This explains the small PVR observed in the case of unstrained graphene devices.

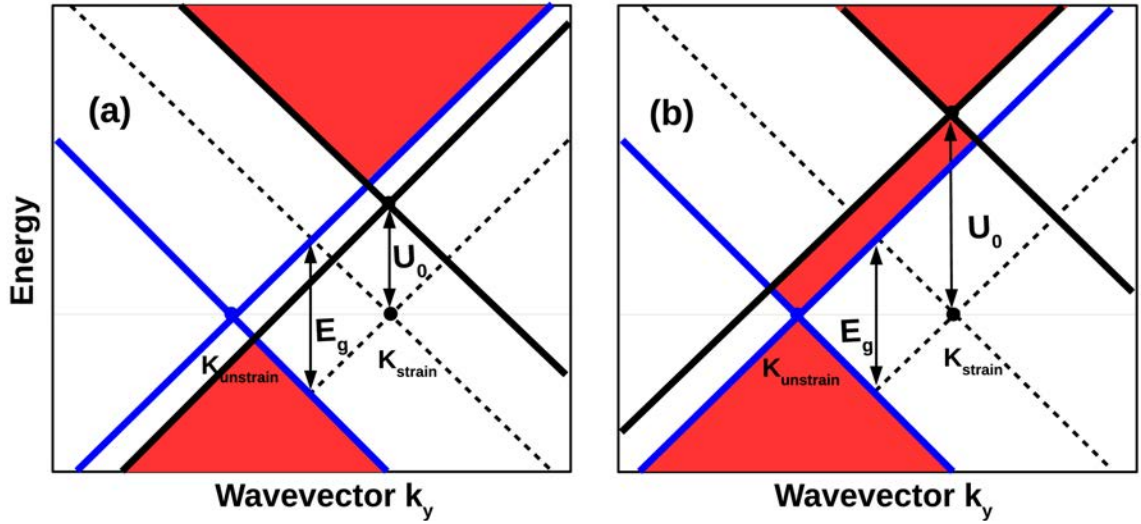


Figure 3.25: Schematics of graphene band profile illustrating the shift of Dirac cone along k_y axis (due to strain) and in energy (due to potential barrier U_0) when $U_0 < E_g$ (a) and $U_0 > E_g$ (b) where E_g is the transport gap obtained for $U_0 = 0$. The blue lines are the bandedges in unstrained graphene while the (dashed/solid) black lines are the bandedges (for $U_0 = 0/U_0 > 0$) in strained graphene. $K_{unstrain}$ and K_{strain} denote the positions of Dirac point in the k_y axis in these two cases, respectively.

When strain is applied, the picture of transmission probability is dramatically changed as seen in Figs. 3.24(d,e,f). This can be understood from the schematics of energy band profile shown in Fig. 3.25. Essentially, when strain is applied, the Dirac points and bandstructure are shifted in k -space (dashed line) and hence the Klein tunneling can be strongly suppressed. This causes the appearance of a transport gap, E_g (see in Fig. 3.25), in strained graphene junctions, the magnitude of which

depends on the direction and amplitude of strain (see [101] for details), e.g., in the case considered here E_g takes the value of 0.246 eV and 0.402 eV for a strain amplitude of 3% and 5%, respectively. Actually, this transport gap corresponds to the energy interval where the Dirac cones of the strained and unstrained areas do not overlap. When a potential barrier of height U_0 is further applied, the bandstructure is shifted upwards by the same energy amount. There are two possibilities here. If $U_0 < E_g$, the bandstructures of the two graphene sections overlap only in two regions (marked in red in Fig. 3.25(a)). However, when $U_0 > E_g$, there is another overlap region in the center, which corresponds to transitions between electron states outside the barrier and hole states in the barrier region. It is important to note that, in ballistic transport regime, the transmission probability can get a finite value only in these overlap regions. This explains the results obtained for the map of transmission probability at low bias voltage (Fig. 3.24(d)). Among the three overlap regions, only the middle one can be strongly modulated, i.e., it can be suppressed completely when increasing the bias voltage (Figs. 3.24(e,f)). Thus this middle region plays a decisive role in the occurrence of NDC effect while the contribution of other regions always makes the current increase with the bias. Indeed, it is clearly seen that the transmission probability in the energy window $[E_{FR}, E_{FL}]$ is largely reduced (even to zero as in Fig. 3.24(f)). This effect, on the one hand, reduces the overall current, but, on the other hand, leads to a significant increase of PVR due to the strong suppression of valley current.

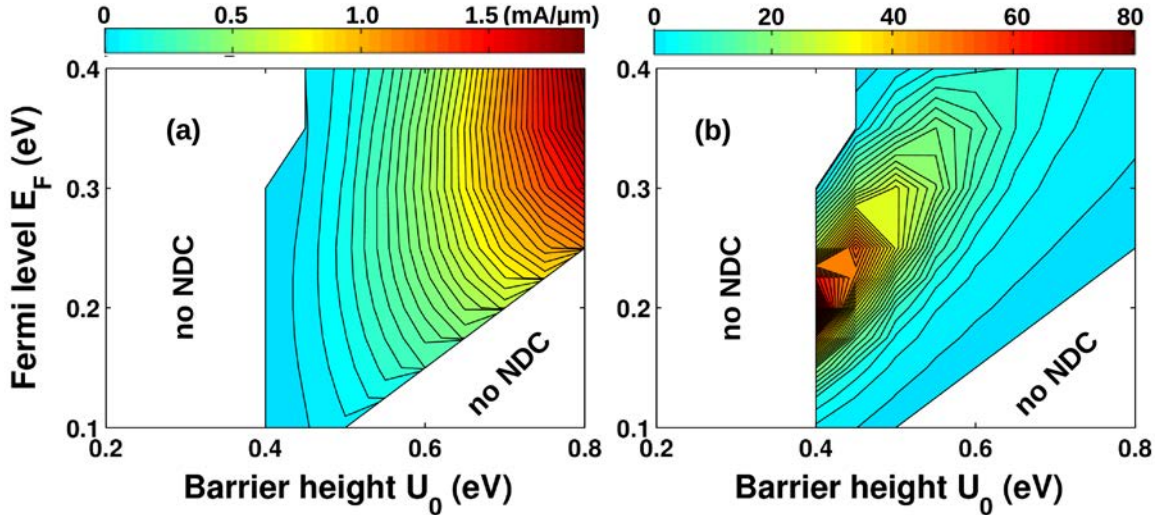


Figure 3.26: $(E_F - U_0)$ maps of peak current (a) and PVR (b) in the single potential barrier structure with $L_S = L_B = 40$ nm and $\sigma = 5\%$. Other parameters: $E_F = 0.25$ eV, $U_0 = 0.45$ eV, and $\sigma = 5\%$.

To investigate the dependence of NDC behavior on the barrier height, U_0 , and Fermi level, E_F , we plot (E_F-U_0) maps of peak current (Fig. 3.26(a)) and PVR (Fig. 3.26(b)) for a strain of 5%. The result shows that NDC effect does not appear in two regions where U_0 is low (regardless of the value of Fermi energy) or U_0 is high and E_F is small. It is noted that here we only consider $E_F \leq 0.4$ eV, i.e. in the range corresponding to realistic doping concentrations. The disappearance of NDC in the region of small U_0 ($U_0 < E_g$) is due to the fact that at zero bias, the two bandstructures do not overlap in the middle region as discussed above and illustrated in Fig. 3.25(a). For higher U_0 ($U_0 > E_g$), there are three overlap regions and it is convenient to decompose the current into two components as

$$J_{tot} = J_{mid} + J_{other}, \quad (3.12)$$

where J_{mid} is the contribution from the middle region and J_{other} is due to the top and bottom regions. Note that while J_{mid} can be reduced, J_{other} always increases when raising the bias. At high bias, J_{other} dominates and hence the current always increases with the bias. For small Fermi energies, this is also true in the region of low bias and, hence, NDC behavior can not be observed in these cases. The situation changes when E_F is larger, i.e., the contribution of the middle region, J_{mid} , becomes more important in the low bias region and thus the NDC effect occurs. Moreover, the higher the potential barrier U_0 the larger the middle overlap region, i.e. the larger the peak current as can be seen in Fig. 3.26(a). However, the valley current is also high in this case because the middle region is so large that it can not be completely suppressed at the low bias while, as mentioned, the component J_{other} can have an important contribution to J_{tot} when raising the bias. This explains the fact that the maximum of PVR occurs in the region with moderate U_0 and E_F in Fig. 3.26(b). Therefore, the moderate values of barrier height and Fermi level are the best compromise to have a high PVR while the peak current is still large, e.g., $U_0 \cong 0.45$ eV and $E_F \cong 0.25$ eV in Fig. 3.27.

Another important parameter that can affect the NDC behavior of the considered device is the length of strained region, L_S . In our study, we always keep L_S equal to the length of barrier region, L_B , to avoid the complication arising from other unstrained/strained junctions when these two lengths are not equal. It is worth to note that in the case where $L_S \neq L_B$, one can anticipate that the NDC behavior is still observed, but the transport gaps resulting from the complicated profile of junctions should affect the peak current. The $I-V$ characteristics obtained using $U_0 = 0.45$ eV, $E_F = 0.25$ eV, and $\sigma = 5\%$ with different values of L_S are displayed in Fig. 3.27(a).

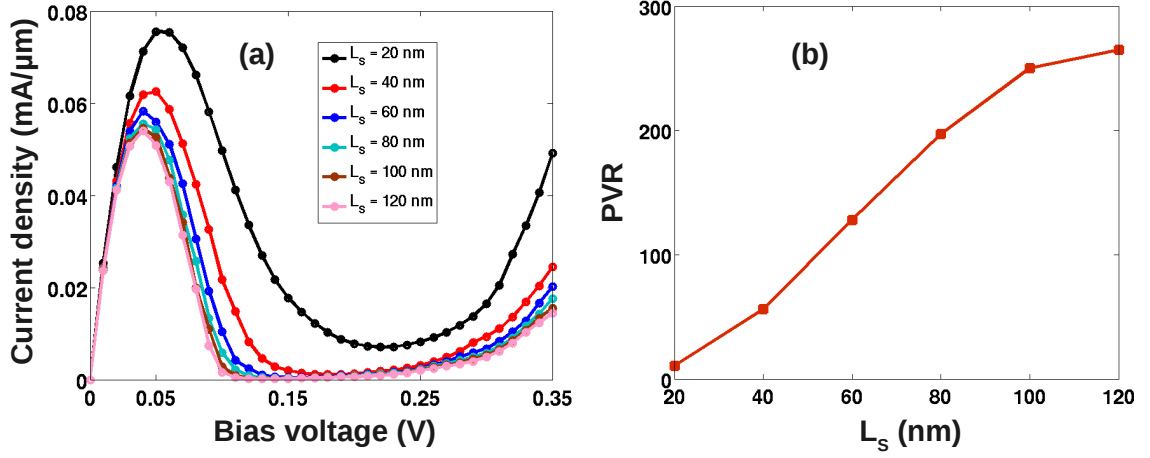


Figure 3.27: $I - V$ characteristics computed for different lengths of strained region L_S (a). The PVR as a function of L_S is shown in (b). Other parameters: $E_F = 0.25$ eV, $U_0 = 0.45$ eV, and $\sigma = 5\%$.

The general trend is that increasing L_S leads to a decrease of overall current, but the valley current is suppressed much more significantly than the peak current. This is due to the fact that both propagating and evanescent states contribute to the latter while the former has contributions from evanescent states only. As a consequence, the PVR increases with L_S and can reach a value of a few hundred when L_S is of the order of 100 nm as can be seen in Fig. 3.27(b). It is noted however that this trend is only valid in the limit of ballistic approximation, i.e., if L_S is less than a few hundred nm [60, 167, 168, 169, 170]. When the device length is too large, the current can be affected by scatterings, which is predicted to reduce the peak current and hence the PVR.

3.4.2.2 Enhanced NDC effect in PN junction

It is known that opening a bandgap in graphene is also a key ingredient to have a strong NDC behavior in graphene p-n junctions. Indeed, several proposals based on this strategy have been investigated previously, e.g., in refs. [150, 154, 164]. In this section, we will show that a significant enhancement of NDC effect in graphene p-n junctions can also be achieved by applying a local strain in the active region of the device channel. A schematic of the structure under study is shown on the top panel of Fig. 3.28 where p-doped and n-doped regions can be generated by electrostatic [134] or by chemical doping [171]. The structure is characterized by the potential difference, U_0 , the length of strain area, L_S and the length of transition region, L_T . It is noted

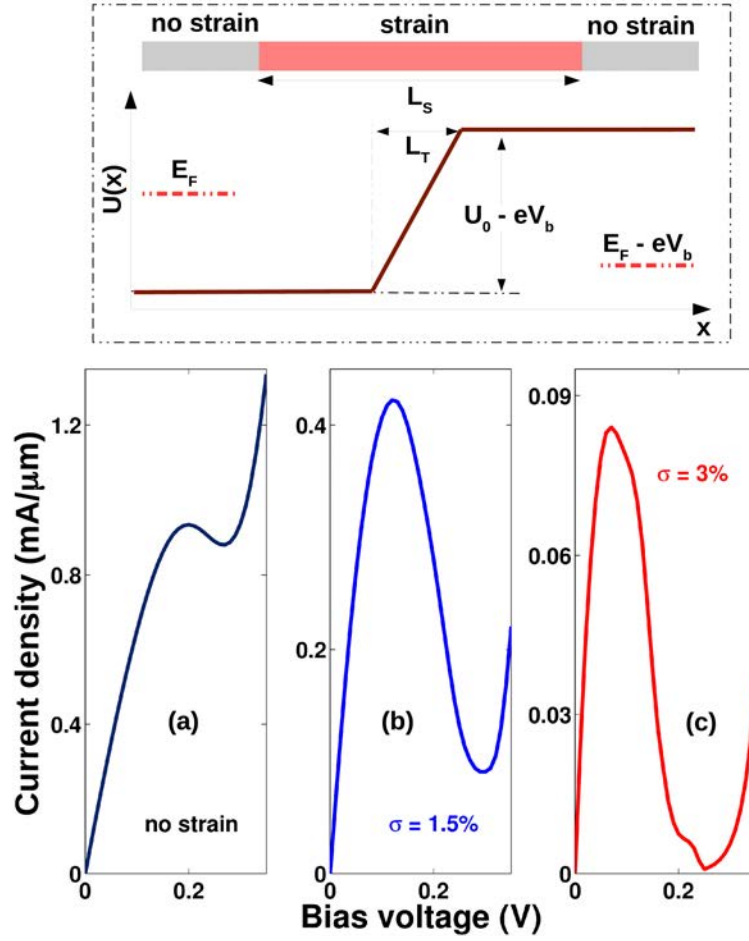


Figure 3.28: The top panel shows the model of graphene p–n junctions studied in this work. The bottom panel shows the $I - V$ characteristics obtained with different strain amplitudes. Other parameters of the device: $U_0 = 0.5$ eV, $L_S = 40$ nm and $L_T = 10$ nm.

that L_S must be considerably larger than L_T so as to generate two strained/unstrained junctions, i.e., one in each doping section [137].

The enhancement of NDC behavior due to local strain is demonstrated in the bottom panel of Fig. 3.28 where $I - V$ characteristics of a p–n junction with $L_S = 40$ nm and $L_T = 10$ nm calculated for different strain amplitudes are displayed. Not surprisingly, the NDC behavior is weak in the junction without strain ($\sigma = 0$), while the effect is enhanced significantly when strain is applied. Remarkably, PVR can reach a value of one hundred for a small strain of 3%. The enhancement of NDC effect can be understood noting that the two unstrained/strained junctions formed in the channel create two different energy gaps in the transmission function [137]. The energy window between the gaps has a non zero transmission probability due

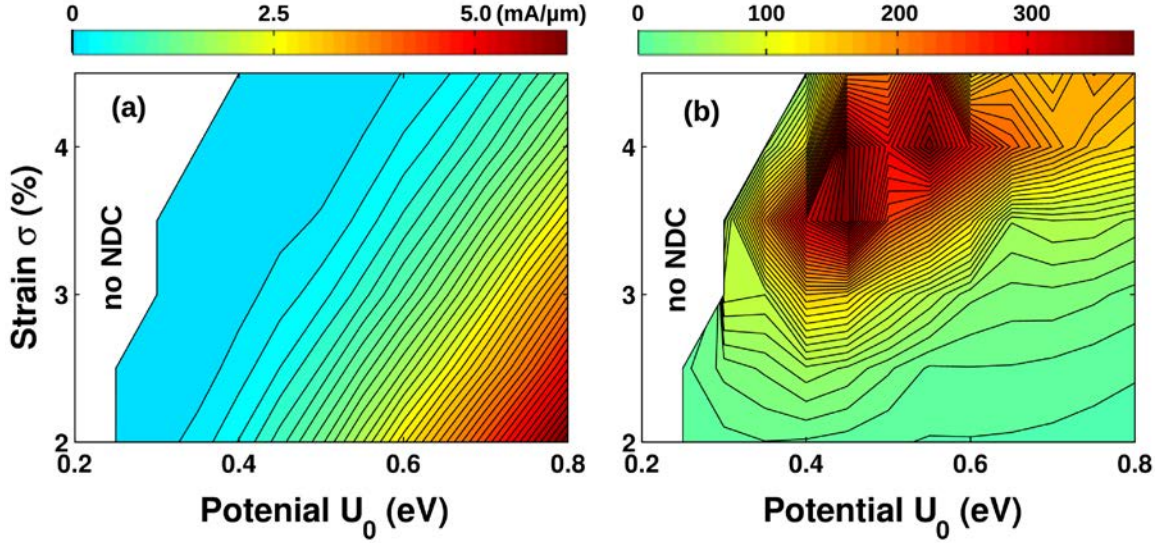


Figure 3.29: $(\sigma - U_0)$ maps of peak current (a) and PVR (b) in the p-n junction with $L_S = 40$ nm and $L_T = 10$ nm.

to the band-to-band tunneling (BTBT) that provides an important contribution to the current. When raising the bias voltage, this energy window is narrowed and the BTBT contribution to the current is reduced. This is the origin of the NDC behavior observed in this device.

Now, we go to investigate the effect of changing some device parameters on the NDC behavior of the structure. In Fig. 3.29(a,b) we plot the maps of peak current and PVR for different strain amplitudes and potential heights. In the range of strain amplitude considered here, the NDC behavior is not observed in the regime of low potential difference, i.e., $U_0 \lesssim 0.25$ eV, because there is no BTBT current in this case [137]. The dependence of peak current and PVR on strain and potential are rather complex. For instance, while the peak current is large in the region with high U_0 and small σ , the maximum of PVR, that depends on both the peak and valley currents, occurs at moderate potential height and at large strain. Therefore, we suggest to use moderate values of strain and potential, such as, for instance $\sigma = 3\%$ and $U_0 = 0.5$ eV, to obtain a high PVR with a still large peak current in this structure.

It has been shown that the peak current in the p-n devices made of simple semiconducting materials is very sensitive to the length of transition region L_T [164, 154]. Therefore, we go to examine, in Fig. 3.30 (a), the $I - V$ characteristics at different lengths L_T while keeping the value of L_S fixed at 40 nm (the above mentioned optimized values of strain and potential were used). It is clearly shown that, because of the decrease of BTBT current, the peak current is reduced when increasing L_T . How-

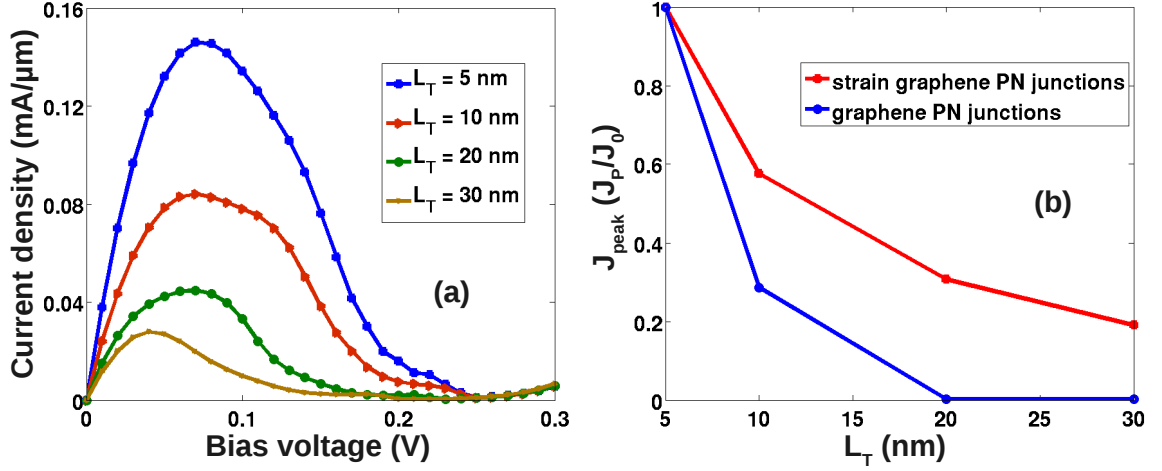


Figure 3.30: $I-V$ characteristics of the device with different lengths L_T while $L_S = 40$ nm is fixed in (a). The evolution of peak current J_{peak} when increasing L_T , compared to that in the case of normal semiconducting (gapped) graphene channel in (b), where J_0 is the current obtained for $L_T = 5$ nm. Other parameters: $\sigma = 3\%$ and $U_0 = 0.5$ eV.

ever, the decrease of peak current in the structure considered here is not very strong compared to other p-n junction devices made of a simple gapped graphene channel as seen in the Fig. 3.30 (b).

As a result, the PVR is weakly degraded when increasing L_T , namely, PVR is about 148 for $L_T = 5$ nm and reduces slightly to ~ 100 for $L_T = 30$ nm. To explain this weak sensitivity of the peak current to L_T , we display in Fig. 3.31 the maps of local density of states (LDOS) and the transmission probability for two different modes k_y . For the mode $k_y = K_{strain}$, i.e. corresponding to the position of a Dirac point in the strained section, the BTBT current is less sensitive to L_T (Fig. 3.31(b)) due to the zero bandgap in the transition region as seen in Fig. 3.31(a). For the other mode where k_y is far from K_{strain} (Fig. 3.31(c)), the BTBT is strongly reduced as shown in Fig. 3.31(d) because the gap in the transition region is finite. It is the contribution of modes around K_{strain} that makes the peak current less sensitive to L_T , compared to the case of devices made of uniform gapped graphene channels. Hence, the PVR here is not strongly degraded when increasing L_T .

In conclusion, we have shown that due to the effects of local strain, the Klein tunneling is strongly suppressed and hence a transport gap can occur in the graphene channels with strained/unstrained junctions. This gap can be modulated in k -space and in energy by strain and doping engineering, respectively. Thanks to this effect, a strong NDC can be achieved in the considered graphene devices (single gate-induced

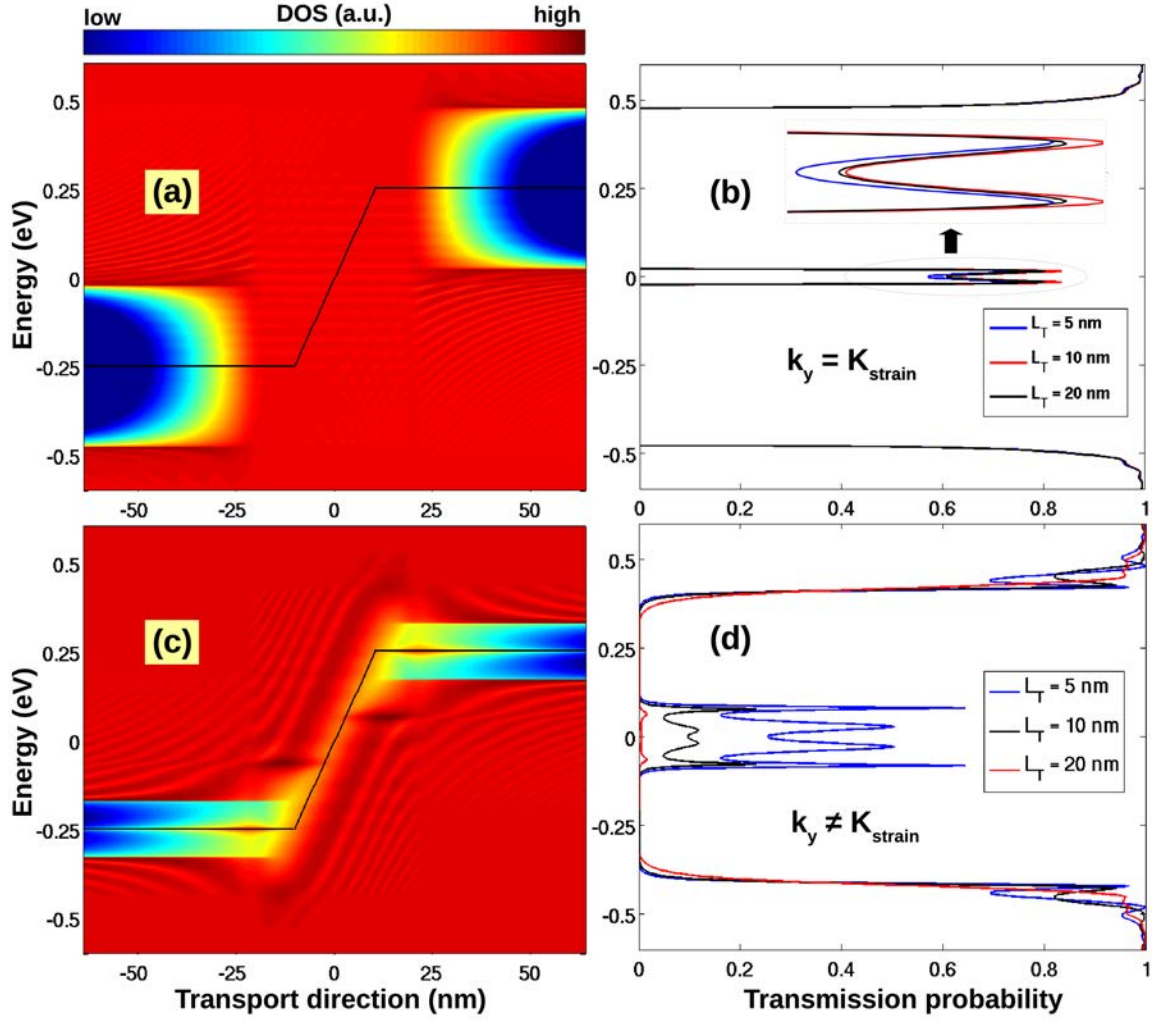


Figure 3.31: Maps of local density of states (left) and corresponding transmission probability (right) obtained for two different wavevectors k_y . In the right side, devices with different lengths L_T are considered. The inset in (b) shows a zoomed image of the transmission probability around the zero energy point. Other device parameters: $L_S = 40$ nm, $\sigma = 3$ % and $U_0 = 0.5$ eV.

barrier and p–n structures) when a local strain is suitably applied. Remarkably, with a small strain of a few percent the PVR can reach a value of a few hundreds at room temperature. The dependence of NDC behavior on the device parameters has been systematically analyzed. It is shown that a strong NDC effect can be achieved in single barrier structures with large strain area while it is nicely weakly sensitive to the change in the length of transition region in p–n devices. These results suggest that strain engineering can be a promising way to overcome the lack of bandgap in graphene and to enlarge the route towards high-performance graphene-based electronic devices.

3.5 Conclusion

In this chapter, we have demonstrated that strained graphene junctions are really excellent candidates for designing channels with good qualities. First, it has been shown the performance of strained GFETs is improved significantly in comparison with conventional GFETs. In particular, an ON/OFF current higher than 10^5 can be achieved. Next, the combination of strain and doping engineering can generate graphene heterochannels in which the Seebeck effect is strongly enhanced. We have presented the maximum value S_{max} of the Seebeck coefficient increases linearly with the opening of conduction gap. These results show that with a small strain of only 5% and an appropriate doping profile, the Seebeck coefficient can reach a value higher than 1.4 mV/K. In comparison, it is 17 times higher than the value in gapless pristine graphene channel. Moreover, we also see that strained heterochannels enhance remarkably the NDC effect in graphene devices, i.e., single gate-induced barrier and p-n structures. It has been shown when the local strain is suitably applied, the peak to valley ratio (PVR) of the current-voltage characteristics can be as high as a few hundreds.

Summary and perspectives

Summary: during the last decade, just after the experimental discovery of graphene and its fascinating properties, research on this material and applications rapidly became a hot topic. This single layer material seems to be very promising for many practical applications in high performance electronics. However, the lack of an energy gap makes graphene not directly suitable for common devices such as transistors and diodes. Although that drawback can be overcome by different ways, i.e., using a transverse electric field (in bilayer graphene), by cutting a graphene sheet in narrow strips (nanoribbons), by creating a lattice of nanoholes (graphene nanomesh) or by even stacking graphene with other 2D materials (graphene boron nitride), etc, each technique still has an Achilles heel and/or need experimental confirmation.

Strain engineering is believed to be one of the most simple and efficient approaches thanks to excellent mechanical properties of graphene, in particular to its the ability of sustaining stretch with the deformation beyond 20%. However, though a strain over 20% opens a bandgap in graphene, experiments have to face up several issues in the case of such large deformation. That is why in this work we always focused our study towards strain of only a few percent. Such a small strain is much easier to manage experimentally and we have shown that it may lead to the opening of a conduction gap in graphene junctions with strain/unstrain interface. These junctions with sizable energy gap lead to graphene applications in designing device channels.

The main contributions of this Ph.D project (from November 2013 to October 2016) are summarized as follows:

1. **Methodologies.** I have developed systematically calculations and numerical simulation codes with a combination of different models and methodologies, i.e., tight binding model and Green's function method to draw a good physics picture including various properties of electrons in unstrained/strained graphene nanostructures. These approaches allowed us to obtain all the results displayed in chapter 2 and 3. To be honest, the codes here are not perfect yet and still need some improvements, but at present calculating the techniques have been shown to be effective for the devices

considered. In the future, these techniques should be developed further to take into account effects of defects, impurities, electron phonon interaction, etc., in graphene devices.

2. The opening of conduction gap in strained graphene junctions. Using strain engineering to modify the electronic band structure, we have shown that a bandgap can open in pristine graphene with a strain over 20%. More important, a small strain of only a few percent causes the shift of Dirac points, leading to a conduction gap in unstrained/strained graphene junctions, e.g., a conduction gap ~ 400 meV with a strain of 5%. In addition, the dependences of conduction gap on the amplitude of strain, the direction of applied strain and the transport direction have been discussed and displayed in details.

3. Enhancement of the ON/OFF current ratio in transistors, the Seebeck coefficient and the peak to valley ratio of negative differential conductance effect. The unstrained/strained junctions with sizable energy gap have been used to design channels in devices. First, it is demonstrated that a strain of 5% can significantly improve the performance of graphene FETs. As a results, the ON/OFF current ratio increases remarkably to over 10^5 while it is less than 10 in pristine graphene transistors. Next, we suggest a simple channel using local strain combining doping engineering for the enhancement of Seebeck effect. It is observed that the appearance of energy gap with again 5% of strain separates the opposite contributions of electrons and holes to the Seebeck coefficient. As a consequence, the Seebeck coefficient can reach a value higher than 1.4 mV/K, i.e., 17 times higher than the value in gapless graphene. Finally in applications of strained heterojunctions, we mention the negative differential conductance effect. It is also based on the idea that in an unstrained/strained junction, the strained-induced displacement of Dirac cones generates a transport gap (conduction gap) that can be used similarly as a bandgap in an electron device. We have demonstrated that with a small strain of only 3 – 5% this transport gap can suppress strongly the Klein (chiral) tunneling through a single-barrier structure and can be exploited to modulate efficiently the interband tunneling in a pn tunnel diode. In both cases it results in strongly non-linear $I - V$ characteristics with peak to valley current ratio reaching a few hundred at room temperature. In conclusion of all obtained results we believe that they can be useful to enlarge the route towards high-performance graphene-based electronic devices.

Perspectives: though the work is closed here, there are still some works that can be further performed. Based on the results and physics obtained from the current

works, we propose here some interesting ideas in the view of optimizing electronic and thermoelectric properties such as

(i) In chapter 2, the dependence of transport gap on the orientation of lattice has been studied only for some values of ϕ . So in next works, we will consider more the effects of direction of lattice. We believe that the full picture of these effects is not as simple as in Fig. 2.33. It means that the conduction gap can eventually decrease when increasing the amplitude of strain. Besides, we will investigate the effect of other kinds of strain on the transport gap in graphene junctions, i.e., shear strain or pure shear strain. Therefore, the dependence of conduction gap will be displayed in its full dependences.

(ii) The problems such as electron transport in the presence of electron-phonon interaction can become important at high temperature or for longer devices. Hence, it is necessary to extend the techniques of Green's function calculations for that cases.

(iii) In future works without the use of strain engineering to modulate the electronic properties, we think about other graphene nanostructures with the effect of grain boundaries which appears in realistic samples. Besides, graphene can also be developed in conjunction with other two-dimensional (2D) crystals to create some even more amazing compounds to suit an even wider range of applications.

Appendix A

The relationship between the bond lengths in cases of (σ, θ) and $(-\sigma, \theta + 90^\circ)$

It has been shown in Eq. 2.47 that the effects of a strain (σ, θ) are quite similar to those of a strain $(-\sigma, \theta + 90^\circ)$. To clarify, we analyze it here in details as follows

In the case of zero strain ($\sigma = 0$), we choose the unit vector $\vec{r}_0(x, y)$ within $|\vec{r}_0| = \sqrt{x^2 + y^2}$.

In the case of a finite tensile strain (σ) with an angle (θ), the bond lengths are given by

$$\vec{r}_1 = M_s(\sigma, \theta)\vec{r}_0 \quad (\text{A.1})$$

here $M_s(\sigma, \theta)$ is the strain matrix defined by

$$M_s(\sigma, \theta) = I + \sigma \begin{bmatrix} \cos^2\theta - \gamma\sin^2\theta & (1 + \gamma)\sin\theta\cos\theta \\ (1 + \gamma)\sin\theta\cos\theta & \sin^2\theta - \gamma\cos^2\theta \end{bmatrix}$$

Similarly in the case of compressive strain ($-\sigma$) with an angle ($\theta' = \theta + 90^\circ$), the bond lengths are given by

$$\vec{r}_2 = M'_s(\sigma, \theta')\vec{r}_0 \quad (\text{A.2})$$

wherein

$$M'_s(\sigma, \theta') = I - \sigma \begin{bmatrix} \cos^2\theta' - \gamma\sin^2\theta' & (1 + \gamma)\sin\theta'\cos\theta' \\ (1 + \gamma)\sin\theta'\cos\theta' & \sin^2\theta' - \gamma\cos^2\theta' \end{bmatrix}$$

First, we have

$$\vec{r}_1 = M_s(\sigma, \theta)\vec{r}_0 = \begin{bmatrix} 1 + \sigma(\cos^2\theta - \gamma\sin^2\theta) & \sigma(1 + \gamma)\sin\theta\cos\theta \\ \sigma(1 + \gamma)\sin\theta\cos\theta & 1 + \sigma(\sin^2\theta - \gamma\cos^2\theta) \end{bmatrix} \begin{bmatrix} x \\ y \end{bmatrix} \quad (\text{A.3})$$

$$\vec{r}_1 = M_s(\sigma, \theta)\vec{r}_0 = \begin{bmatrix} [1 + \sigma(\cos^2\theta - \gamma\sin^2\theta)]x + \sigma(1 + \gamma)\sin\theta\cos\theta y \\ \sigma(1 + \gamma)\sin\theta\cos\theta x + [1 + \sigma(\sin^2\theta - \gamma\cos^2\theta)]y \end{bmatrix} \quad (\text{A.4})$$

Then

$$|\vec{r}_1| \simeq \sqrt{(x^2 + y^2)} \left\{ 1 + \frac{\sigma}{x^2 + y^2} [x^2(\cos^2\theta - \gamma \sin^2\theta) + y^2(\sin^2\theta - \gamma \cos^2\theta) + 2xy(1 + \gamma)\sin\theta\cos\theta] \right\} \quad (\text{A.5})$$

Similarly,

$$\vec{r}_2 = M'_s(\sigma, \theta')\vec{r}_0 = \begin{bmatrix} 1 - \sigma(\cos^2\theta' - \gamma \sin^2\theta') & -\sigma(1 + \gamma)\sin\theta'\cos\theta' \\ -\sigma(1 + \gamma)\sin\theta'\cos\theta' & 1 - \sigma(\sin^2\theta' - \gamma \cos^2\theta') \end{bmatrix} \begin{bmatrix} x \\ y \end{bmatrix} \quad (\text{A.6})$$

$$\vec{r}_2 = M'_s(\sigma, \theta')\vec{r}_0 = \begin{bmatrix} [1 - \sigma(\cos^2\theta' - \gamma \sin^2\theta')]x - \sigma(1 + \gamma)\sin\theta'\cos\theta'y \\ -\sigma(1 + \gamma)\sin\theta'\cos\theta'x + [1 - \sigma(\sin^2\theta' - \gamma \cos^2\theta')]y \end{bmatrix} \quad (\text{A.7})$$

Now,

$$|\vec{r}_2| \simeq \sqrt{(x^2 + y^2)} \left\{ 1 - \frac{\sigma}{x^2 + y^2} [x^2(\cos^2\theta' - \gamma \sin^2\theta') + y^2(\sin^2\theta' - \gamma \cos^2\theta') + 2xy(1 + \gamma)\sin\theta'\cos\theta'] \right\} \quad (\text{A.8})$$

It is noted that $\theta' = \theta + 90^\circ$, hence $\cos\theta' = -\sin\theta$ and $\sin\theta' = \cos\theta$

$$|\vec{r}_2| \simeq \sqrt{(x^2 + y^2)} \left\{ 1 - \frac{\sigma}{x^2 + y^2} [x^2(\sin^2\theta - \gamma \cos^2\theta) + y^2(\cos^2\theta - \gamma \sin^2\theta) + 2xy(1 + \gamma)\sin\theta\cos\theta] \right\} \quad (\text{A.9})$$

From Eq. A.5 and Eq. A.9 we can deduce

$$|\vec{r}_1| - |\vec{r}_2| \simeq \frac{\sigma}{x^2 + y^2} [x^2(1 - \gamma) + y^2(1 - \gamma)] \sqrt{(x^2 + y^2)} = \sigma(1 - \gamma) \sqrt{(x^2 + y^2)} \quad (\text{A.10})$$

Hence,

$$|\vec{r}_1| - |\vec{r}_2| \simeq \sigma(1 - \gamma) |\vec{r}_0| \quad (\text{A.11})$$

With $\mathbf{r}(\sigma, \theta) \equiv |\vec{r}_1|$, $\mathbf{r}(-\sigma, \theta + 90^\circ) \equiv |\vec{r}_2|$ and $\mathbf{r}_0 \equiv |\vec{r}_0|$

$$\mathbf{r}(\sigma, \theta) - \mathbf{r}(-\sigma, \theta + 90^\circ) \simeq \sigma(1 - \gamma) \mathbf{r}_0 \quad (\text{A.12})$$

So, the Eq. 2.34 in chapter 2 has been proved.

Appendix B

The equation of transmission

In principle, the transmission is calculated via Eq. 1.56. However, to avoid the use of matrix of device Green's function with large size, we introduce the formula in Eq. 1.57. In this appendix, we analyze here the derivation (1.57) from Eq. 1.56 in details.

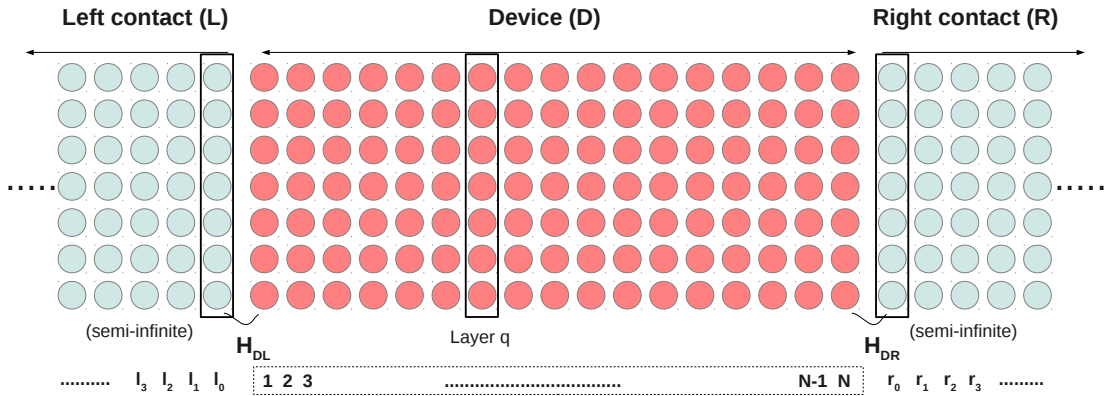


Figure B.1: Schematic of device connected to two semi-infinite contacts. The device and the contacts are split into different layers. Here, one layer only interacts with its nearest neighbor layers.

As mentioned in Part I of chapter 1, the system is divided into layers. Here, we only consider the couple of one layer with its nearest neighbor layers. Hence, the Hamiltonian of the system can be written as a tri-diagonal matrix block of layers. That means only the first layer (l_0 or r_0) of each contact interacts into the first (end) layer of device, as seen in Fig. B.1. As a result, the self-energy of left (right) contact is given by

$$\Sigma_{L(R)}^s = H_{DL(R)} g_{0(N)}^{L(R)} H_{L(R)D} \quad (\text{B.1})$$

where $g_{0(N)}^{L(D)}$ is the surface Green's function of the left (right) contact (all blocks is zero except the block of the surface layer).

Thus the left (right) energy level broadening only has one valuable block, i.e.,

$$\Gamma_L = \begin{bmatrix} \Gamma_L^s & & & 0 \\ & 0 & & \\ & & 0 & \\ & & & \ddots \\ 0 & & & & 0 \end{bmatrix} \quad (\text{B.2})$$

and

$$\Gamma_R = \begin{bmatrix} 0 & & & 0 \\ & 0 & & \\ & & 0 & \\ & & & \ddots \\ 0 & & & & \Gamma_R^s \end{bmatrix} \quad (\text{B.3})$$

where $\Gamma_{L(R)}^s = i[\Sigma_{L(R)}^s - \Sigma_{L(R)}^{s\dagger}]$.

The full size of device Green's function G_D writes

$$G_D = \begin{bmatrix} G_{11} & G_{12} & G_{13} & \dots & G_{1N} \\ G_{21} & G_{22} & G_{23} & \dots & G_{2N} \\ G_{31} & G_{32} & G_{33} & \dots & G_{3N} \\ \vdots & \vdots & \vdots & \vdots & \vdots \\ G_{N1} & G_{N2} & G_{N3} & \dots & G_{NN} \end{bmatrix} \quad (\text{B.4})$$

In this form, G_{ii} is the Green's function of i^{th} layer.

Now, we have

$$\Gamma_L G_D \Gamma_R G_D^\dagger = \begin{bmatrix} 0 & & & 0 \\ & 0 & & \\ & & 0 & \\ & & & \ddots \\ 0 & & & & \Gamma_R^s \end{bmatrix} \begin{bmatrix} G_{11} & G_{12} & G_{13} & \dots & G_{1N} \\ G_{21} & G_{22} & G_{23} & \dots & G_{2N} \\ G_{31} & G_{32} & G_{33} & \dots & G_{3N} \\ \vdots & \vdots & \vdots & \vdots & \vdots \\ G_{N1} & G_{N2} & G_{N3} & \dots & G_{NN} \end{bmatrix} \begin{bmatrix} 0 & & & 0 \\ & 0 & & \\ & & 0 & \\ & & & \ddots \\ 0 & & & & \Gamma_R^s \end{bmatrix} \\ \times \begin{bmatrix} G_{11}^\dagger & G_{12}^\dagger & G_{13}^\dagger & \dots & G_{1N}^\dagger \\ G_{21}^\dagger & G_{22}^\dagger & G_{23}^\dagger & \dots & G_{2N}^\dagger \\ G_{31}^\dagger & G_{32}^\dagger & G_{33}^\dagger & \dots & G_{3N}^\dagger \\ \vdots & \vdots & \vdots & \vdots & \vdots \\ G_{N1}^\dagger & G_{N2}^\dagger & G_{N3}^\dagger & \dots & G_{NN}^\dagger \end{bmatrix} \quad (\text{B.5})$$

Then,

$$\Gamma_L G_D \Gamma_R G_D^\dagger = \begin{bmatrix} \Gamma_L^s G_{1N} \Gamma_R^s G_{1N}^\dagger & \Gamma_L^s G_{1N} \Gamma_R^s G_{2N}^\dagger & \Gamma_L^s G_{1N} \Gamma_R^s G_{3N}^\dagger & \dots & \Gamma_L^s G_{1N} \Gamma_R^s G_{NN}^\dagger \\ 0 & 0 & 0 & \dots & 0 \\ 0 & 0 & 0 & \dots & 0 \\ \vdots & \vdots & \vdots & \vdots & \vdots \\ 0 & 0 & 0 & \dots & 0 \end{bmatrix} \quad (\text{B.6})$$

Hence,

$$T = \text{trace}[\Gamma_L G_D \Gamma_R G_D^\dagger] = \text{trace}[\Gamma_L^s G_{1N} \Gamma_R^s G_{1N}^\dagger] \quad (\text{B.7})$$

The calculation in Eq. B.7 is really better than the calculation in Eq. 1.56 because Γ_L^s, Γ_R^s and G_{1N} are just the matrices with one layer size. Hence, they are much smaller than the matrix system in Eq. 1.56.

However, we still need to determine three elements (Γ_L^s, Γ_R^s and G_{1N}) in Eq. B.7 while we only compute two elements in Eq. 1.57. That is why the equation (1.57) is more efficient for the calculation of transmission. Now, we analyze main steps to get the equation (1.57).

We use here the spectral function which is defined by

$$A = i(G - G^\dagger) \quad (\text{B.8})$$

where $G = [E^+ - H_D - \Sigma_L - \Sigma_R]^{-1}$

It is noted that

$$(G^+)^{-1} - G^{-1} = (\Sigma_L - \Sigma_L^\dagger) + (\Sigma_R - \Sigma_R^\dagger) = -i(\Gamma_L + \Gamma_R) = -i\Gamma \quad (\text{B.9})$$

$$[(G^+)^{-1} - G^{-1}]G^+ = -i\Gamma G^+$$

$$1 - G^{-1}G^+ = -i\Gamma G^+$$

$$G - G^+ = -iG\Gamma G^+ \quad (\text{B.10})$$

So,

$$A = i(G - G^\dagger) = G\Gamma G^+ \quad (\text{B.11})$$

Now, we compute

$$\begin{aligned} G\Gamma G^+ &= G(\Gamma_L + \Gamma_R)G^+ = \begin{bmatrix} G_{11} & G_{12} & G_{13} & \dots & G_{1N} \\ G_{21} & G_{22} & G_{23} & \dots & G_{2N} \\ G_{31} & G_{32} & G_{33} & \dots & G_{3N} \\ \vdots & \vdots & \vdots & \vdots & \vdots \\ G_{N1} & G_{N2} & G_{N3} & \dots & G_{NN} \end{bmatrix} \\ &\times \begin{bmatrix} \Gamma_L^s & & & & 0 \\ & 0 & & & \\ & & 0 & & \\ & & & \ddots & \\ 0 & & & & \Gamma_R^s \end{bmatrix} \begin{bmatrix} G_{11}^\dagger & G_{12}^\dagger & G_{13}^\dagger & \dots & G_{1N}^\dagger \\ G_{21}^\dagger & G_{22}^\dagger & G_{23}^\dagger & \dots & G_{2N}^\dagger \\ G_{31}^\dagger & G_{32}^\dagger & G_{33}^\dagger & \dots & G_{3N}^\dagger \\ \vdots & \vdots & \vdots & \vdots & \vdots \\ G_{N1}^\dagger & G_{N2}^\dagger & G_{N3}^\dagger & \dots & G_{NN}^\dagger \end{bmatrix} \quad (\text{B.12}) \end{aligned}$$

$$G\Gamma G^+ = G(\Gamma_L + \Gamma_R)G^+ = \begin{bmatrix} G_{11}\Gamma_L^s G_{11}^\dagger + G_{1N}\Gamma_R^s G_{1N}^\dagger & \cdots & \cdots \\ \vdots & \vdots & \vdots \\ \cdots & \cdots & G_{N1}\Gamma_L^s G_{N1}^\dagger + G_{NN}\Gamma_R^s G_{NN}^\dagger \end{bmatrix} \quad (\text{B.13})$$

Otherwise,

$$i(G - G^\dagger) = \begin{bmatrix} i(G_{11} - G_{11}^\dagger) & \cdots & \cdots \\ \vdots & \vdots & \vdots \\ \cdots & \cdots & i(G_{NN} - G_{NN}^\dagger) \end{bmatrix} \quad (\text{B.14})$$

From Eq. B.13 and Eq. B.14 we have

$$\begin{aligned} i(G_{11} - G_{11}^\dagger) &= G_{11}\Gamma_L^s G_{11}^\dagger + G_{1N}\Gamma_R^s G_{1N}^\dagger \\ i(G_{NN} - G_{NN}^\dagger) &= G_{N1}\Gamma_L^s G_{N1}^\dagger + G_{NN}\Gamma_R^s G_{NN}^\dagger \end{aligned} \quad (\text{B.15})$$

From these, it is easy to see that

$$G_{1N}\Gamma_R^s G_{1N}^\dagger = i(G_{11} - G_{11}^\dagger) - G_{11}\Gamma_L^s G_{11}^\dagger \quad (\text{B.16})$$

Or

$$G_{N1}\Gamma_L^s G_{N1}^\dagger = i(G_{NN} - G_{NN}^\dagger) - G_{NN}\Gamma_R^s G_{NN}^\dagger \quad (\text{B.17})$$

Thus,

$$\Gamma_L^s G_{1N}\Gamma_R^s G_{1N}^\dagger = \Gamma_L^s [i(G_{11} - G_{11}^\dagger) - G_{11}\Gamma_L^s G_{11}^\dagger] \quad (\text{B.18})$$

$$G_{N1}\Gamma_L^s G_{N1}^\dagger \Gamma_R^s = [i(G_{NN} - G_{NN}^\dagger) - G_{NN}\Gamma_R^s G_{NN}^\dagger] \Gamma_R^s \quad (\text{B.19})$$

Finally, we can compute the transmission in the simple way

$$T = \text{trace}\{\Gamma_L^s [i(G_{11} - G_{11}^\dagger) - G_{11}\Gamma_L^s G_{11}^\dagger]\} \quad (\text{B.20})$$

Or

$$T = \text{trace}\{[i(G_{NN} - G_{NN}^\dagger) - G_{NN}\Gamma_R^s G_{NN}^\dagger] \Gamma_R^s\} \quad (\text{B.21})$$

Bibliography

- [1] K. S. Novoselov, A. K. Geim, S. V. Morozov, D. Jiang, Y. Zang, S. V. Dubonos, I. V. Grigorieva, and A. A. Firsov, "Electric Field Effect in Atomically Thin Carbon Films", *Science* **306**, 666 (2004).
- [2] A. K. Geim, "Graphene: Status and Prospects", *Science* **324**, 15301534 (2009).
- [3] A. H. Castro Neto, F. Guinea, N. M. R. Peres, K. S. Novoselov, and A. K. Geim, "The electronic properties of graphene", *Rev. Mod. Phys.* **81**, 109 (2009).
- [4] X. Wan, Y. Huang and Y. Chen, "Focusing on Energy and Optoelectronic Applications: A Journey for Graphene and Graphene Oxide at Large Scale", *Acc. Chem. Res.* **45**, 598607 (2012).
- [5] A. H. Castro Neto, F. Guinea, and N. M. R. Peres, "Drawing conclusions from graphene", *Physics World.* **19**, 33 (2006).
- [6] M. I. Katsnelson, K. S. Novoselov, and A. K. Geim, "Chiral tunnelling and the Klein paradox in graphene", *Nat. Phys.* **2**, 620 (2006).
- [7] V. P. Gusynin and S. G. Sharapov, "Unconventional Integer Quantum Hall Effect in Graphene", *Phys. Rev. Lett.* **95**, 146801 (2005).
- [8] Y. Zhang, Y. W. Tan, H. L. Stormer, and P. Kim, "Experimental observation of the quantum Hall effect and Berry's phase in graphene", *Nature* **438**, 201 (2005).
- [9] K. S. Novoselov, Z. Jiang, Y. Zhang, S. V. Morozov, H. L. Stormer, U. Zeitler, J. C. Maan, G. S. Boebinger, P. Kim, and A. K. Geim, "Room-Temperature Quantum Hall Effect in Graphene", *Science* **315**, 1379 (2007).
- [10] A. F. Young and P. Kim, "Quantum interference and Klein tunnelling in graphene heterojunctions", *Nat. Phys.* **5**, 222 (2009).

- [11] P. Krekora, Q. Su, and R. Grobe, "Klein Paradox in Spatial and Temporal Resolution", *Phys. Rev. Lett.* **92**, 040406 (2004).
- [12] H. Wang, X. Yuan, Y. Wu, H. Huang, X. Peng, G. Zeng, H. Zhong, J. Liang, and M. Ren, "Graphene-based materials: Fabrication, characterization and application for the decontamination of wastewater and wastegas and hydrogen storage/generation", *J. Colloid Interface Sci.* **195-196**, 19-40 (2013).
- [13] G. Brumfiel, A. Geim, "In Praise of Graphene", October 7, (2010). <http://www.nature.com/news/2010/101007/full/news.2010.525.html>
- [14] Sherry Mazzocchi, "Five Things You Need to Know about the Big Little Substance Graphene", October 8, 2010. <http://www.pbs.org/wnet/need-to-know/five-things/the-big-little-substance-graphene/4146/>
- [15] C. Lee, X. Wei, J. W. Kysar, and J. Hone, "Measurement of the elastic properties and intrinsic strength of monolayer graphene", *Science* **321**, 385 (2008).
- [16] F. Liu, P. Ming, and J. Li, "Ab initio calculation of ideal strength and phonon instability of graphene under tension", *Phys. Rev. B* **76**, 064120 (2007).
- [17] H. H. Hall, J. Bardeen, and G. L. Pearson, "The Effects of Pressure and Temperature on the Resistance of pn Junctions in Germanium", *Phys. Rev.* **84**, 129 (1951).
- [18] C. S. Smith, "Piezoresistance Effect in Germanium and Silicon", *Phys. Rev.* **94**, 42 (1954).
- [19] J. Welser, J. Hoyt, and J. Gibbons, "Electron mobility enhancement in strained-Si n-type metal-oxide-semiconductor field-effect transistors", *IEEE Electron Device Lett.* **15**, 100 (1994).
- [20] K. Rim, J. Chu, H. Chen, K. Jenkins, T. Kanarsky, K. Lee, A. Mocuta, H. Zhu, R. Roy, J. Newbury, J. Ott, K. Petrarca, P. Mooney, D. Lacey, S. Koester, K. Chan, D. Boyd, M. Jeong, and H. Wong, "Characteristics and device design of sub-100 nm strained Si n- and p-MOSFETs", In *VLSI Symp. Tech.Dig.*, 98-99 (2002).

- [21] Z. Y. Cheng, M. T. Currie, C. W. Leitz, G. Taraschi, E. A. Fitzgerald, J. L. Hoyt, and D. A. Antoniadis, "Electron mobility enhancement in strained-Si n-MOSFETs fabricated on SiGe-on-insulator (SGOI) substrates", *IEEE Electron Device Lett.* **22**, 321-323 (2001).
- [22] F. Andrieu, T. Ernst, O. Faynot, O. Rozeau, Y. Bogumilowicz, J. M. Hartmann, L. Brevard, A. Toffoli, D. Lafond, and B. Ghyselen, "Performance and physics of sub-50 nm strained Si on Si_{1-x}Ge_x on insulator (SGOI) nMOSFETs", *Solid-State Electron.* **50**, 566-572 (2006).
- [23] V. Sverdlov, "Strain-Induced Effects in Advanced MOSFETs" (Springer Wien New York, 2011)
- [24] E. Ungersboeck, "Advanced Modeling of Strained CMOS Technology", (Ph.D. thesis, 2007).
- [25] Y. Sun, S. E. Thompson, and T. Nishida, "Strain Effect in Semiconductors" (Springer New York Dordrecht Heidelberg London, 2010).
- [26] Andres Castellanos-Gomez, Rafael Roldán, Emmanuele Cappelluti, Michele Buscema, Francisco Guinea, Herre S. J. van der Zant, and Gary A. Steele, "Local Strain Engineering in Atomically Thin *MoS₂*", *Nano Lett.* **13**, 5361-5366 (2013).
- [27] S. Yang, C. Wang, H. Sahi, H. Chen, Y. Li, S. S. Li, A. Suslu, F. M. Peeters, Q. Liu, J. Li, and S. Tongay, "Tuning the Optical, Magnetic, and Electrical Properties of *ReSe₂* by Nanoscale Strain Engineering", *Nano Lett.* **15**, 1660-1666 (2015).
- [28] S. Richard, F. Aniel, G. Fishman, and N. Cavassilas, "Energy-band structure in strained silicon: A 20-band $k \cdot p$ and BirPikus Hamiltonian model", *J. Appl. Phys.* **94**, 1795 (2003).
- [29] X. Peng and S. Velasquez, "Strain modulated band gap of edge passivated armchair graphene nanoribbons", *Appl. Phys. Lett.* **98**, 023112 (2011).
- [30] Z. H. Ni, T. Yu, Y. H. Lu, Y. Y. Wang, Y. P. Feng and Z. X. Shen, "Uniaxial Strain on Graphene: Raman Spectroscopy Study and Band-Gap Opening", *ACS Nano* **2**, 23012305 (2008).

- [31] W. Shockley and J. Bardeen, "Energy Bands and Mobilities in Monatomic Semiconductors", *Phys. Rev.* **77**, 407 (1950).
- [32] J. Bardeen and W. Shockley, "Deformation Potentials and Mobilities in Non-Polar Crystals", *Phys. Rev.* **80**, 72 (1950).
- [33] C. Herring and E. Vogt, "Transport and Deformation-Potential Theory for Many-Valley Semiconductors with Anisotropic Scattering", *Phys. Rev.* **101**, 944 (1956).
- [34] C. K. Maiti, N. B. Chakrabarti and S. K. Ray, "Strained silicon heterostructures: materials and devices", (*IEE circuits, devices and systems series*; No. 12, 2001).
- [35] S. Thompson, N. Anand, M. Armstrong, C. Auth, B. Arcot, M. Alavi, P. Bai, J. Bielefeld, R. Bigwood, J. Brandenburg, M. Buehler, S. Cea, V. Chikarmane, C. Choi, R. Frankovic, T. Ghani, G. Glass, W. Han, T. Hoffmann, M. Hussein, P. Jacob, A. Jain, C. Jan, S. Joshi, C. Kenyon, J. Klaus, S. Klopčič, J. Luce, Z. Ma, B. McIntyre, K. Mistry, A. Murthy, P. Nguyen, H. Pearson, T. Sandford, R. Schweinfurth, R. Shaheed, S. Sivakumar, M. Taylor, B. Tufts, C. Wallace, P. Wang, C. Weber, and M. Bohr, "A 90 nm Logic Technology Featuring 50nm Strained Silicon Channel Transistors", *Int. Electron Devices Meet. Tech. Dig., San Francisco* (2002).
- [36] M. Yang, A. Nurbawono, C. Zhang, R. Wu, Y. Feng and Ariando, "Manipulating absorption and diffusion of H atom on graphene by mechanical strain", *AIP Adv.* **1**, 032109 (2011).
- [37] T. Low and F. Guinea, "Strain-Induced Pseudomagnetic Field for Novel Graphene Electronics", *Nano Lett.* **10**, 35513554 (2010).
- [38] W. Pan, J. Xiao, J. Zhu, C. Yu, G. Zhang, Z. Ni, K. Watanabe, T. Taniguchi, Y. Shi and X. Wang, "Biaxial Compressive Strain Engineering in Graphene/Boron Nitride Heterostructures", *Sci. Rep.* **2**, 893 (2012).
- [39] N. Petrone, I. Meric, J. Hone and K. L. Shepard, "Graphene Field-Effect Transistors with Gigahertz-Frequency Power Gain on Flexible Substrates", *Nano Lett.* **13**, 121-125 (2013).

- [40] S. K. Lee, H. Y. Jang, S. Jang, E. Choi, B. H. Hong, J. Lee, S. Park and J. H. Ahn, "All Graphene-Based Thin Film Transistors on Flexible Plastic Substrates", *Nano Lett.* **12**, 3472-3476 (2012).
- [41] H. H. P. Garza, E. W. Kievit, G. F. Schneider and U. Staufer, "Controlled, Reversible, and Nondestructive Generation of Uniaxial Extreme Strains ($> 10\%$) in Graphene", *Nano Lett.* **14**, 4107 (2014).
- [42] H. Shioya, M. F. Craciun, S. Russo, M. Yamamoto and S. Tarucha, "Straining Graphene Using Thin Film Shrinkage Methods", *Nano Lett.* **14**, 1158 (2014).
- [43] K. S. Kim, Y. Zhao, H. Jang, S. Y. Lee, J. M. Kim, K. S. Kim, J. H. Ahn, P. Kim, J. Y. Choi and B. H. Hong, "Large-scale pattern growth of graphene films for stretchable transparent electrodes", *Nature.* **457**, 706-710 (2009).
- [44] J. Li, T. F. Chung, Y. P. Chen, and G. J. Cheng, "Nanoscale Strainability of Graphene by Laser Shock-Induced Three-Dimensional Shaping", *Nano Lett.* **12**, 4577-4583 (2012).
- [45] W. Bao, F. Miao, Z. Chen, H. Zhang, W. Jang, C. Dames, C. N. Lau, "Controlled ripple texturing of suspended graphene and ultrathin graphite membranes" *Nat. Nanotechnol.* **4**, 562-566 (2009).
- [46] H. Mi, S. Mikael, C. C. Liu, J. H. Seo, G. Gui, A. L. Ma, P. F. Nealey, and Z. Ma, "Creating periodic local strain in monolayer graphene with nanopillars patterned by self-assembled block copolymer", *Appl. Phys. Lett.* **107**, 143107 (2012).
- [47] S. K. Lee, B. J. Kim, H. Jang, S. C. Yoon, C. Lee, B. H. Hong, J. A. Rogers, J. Ho Cho and J. H. Ahn, "Stretchable Graphene Transistors with Printed Dielectrics and Gate Electrodes", *Nano Lett.* **11**, 4642-4646 (2011).
- [48] G. Tsoukleri, J. Parthenios, K. Papagelis, R. Jalil, A. C. Ferrari, A. K. Geim, K. S. Novoselov, C. Galiotis, "Subjecting a Graphene Monolayer to Tension and Compression", *Small* **5**, 23972402 (2009).
- [49] J. Lu, A.H. C. Neto, and K. P. Loh, "Transforming moiré blisters into geometric graphene nano-bubbles", *Nature Communications* **3**, 823 (2013).

- [50] E. Kogan, V. U. Nazarov, V. M. Silkin and M. Kaveh, "Energy bands in graphene: Comparison between the tight-binding model and ab initio calculations", *Phys.Rev. B*, **89**, 165430 (2014).
- [51] S. Richard, F. Aniel, and G. Fishman, "Energy-band structure of Ge, Si, and GaAs:A thirty-band k.p method", *Phys.Rev. B*, **70**, 235204 (2004).
- [52] J. R. Chelikowsky and M. L. Cohen, "Nonlocal pseudopotential calculations for the electronic structure of eleven diamond and zinc-blende semiconductors", *Phys.Rev. B*, **14**, 556-582 (1976).
- [53] Y. M. Niquet, C. Delerue, G. Allan, and M. Lannoo, "Method for tight-binding parametrization: Application to silicon nanostructures", *Phys.Rev. B*, **62**, 5109-5116 (2000).
- [54] M. Bescond, N. Cavassilas, K. Nehari, and M. Lannoo, "Tight-binding calculations of Ge-nanowire bandstructures", *J Comput Electron*, **6**, 341344 (2007).
- [55] J. C. Slater and G. F. Koster, "Simplified LCAO Method for the Periodic Potential Problem", *Phys.Rev.* **94**, 1498 (1954).
- [56] R. Saito, G. Dresselhaus, M. S. Dresselhaus, "Physical Properties of Carbon Nanotubes" (Imperial College Press, 1998)
- [57] S. Reich, J. Maultzsch, C. Thomsen, and P. Ordejon, "Tight-binding description of graphene", *Phys.Rev. B*, **66**, 035412 (2002).
- [58] M. P. Anantram, M. S. Lundstrom, and D. E. Nikonov, "Modeling of Nanoscale Devices", *Proc. IEEE* **96**, 1511-1550 (2008).
- [59] S. Datta, "Quantum Transport : Atom to Transistor" (Cambridge: Cambridge University Press, 2005)
- [60] K. I. Bolotin, K. J. Sikes, Z. Jiang, M. Klima, G. Fudenberg, J. Hone, P. Kim, and H. L. Stormer, "Ultrahigh electron mobility in suspended graphene", *Solid State Commun.* **146**, 351 (2008).
- [61] S. Ghosh, I. Calizo, D. Teweldebrhan, E. P. Pokatilov, D. L. Nika, A. A. Balandin, W. Bao, F. Miao and C. N. Lau, "Extremely high thermal conductivity of graphene: Prospects for thermal management applications in nanoelectronic circuits", *Appl. Phys. Lett.* **92**, 151911 (2008).

- [62] Y. M. Zuev, W. Chang, and P. Kim, "Thermoelectric and Magnetothermoelectric Transport Measurements of Graphene", *Phys. Rev. Lett.* **102**, 096807 (2009).
- [63] M. Y. Han, B. zyilmaz, Y. Zhang, and P. Kim, "Energy Band-Gap Engineering of Graphene Nanoribbons", *Phys. Rev. Lett.* **98**, 206805 (2007).
- [64] J. Bai, X. Duan and Y. Huang, "Rational Fabrication of Graphene Nanoribbons Using a Nanowire Etch Mask", *Nano Lett.* **9**, 2083 (2009).
- [65] E. V. Castro, K. S. Novoselov, S. V. Morozov, N. M. R. Peres, J. M. B. Lopes dos Santos, J. Nilsson, F. Guinea, A. K. Geim, and A. H. Castro Neto, "Biased Bilayer Graphene: Semiconductor with a Gap Tunable by the Electric Field Effect", *Phys. Rev. Lett.* **99**, 216802 (2007).
- [66] Y. Zhang, T. T. Tang, C. Girit, Z. Hao, M. C. Martin, A. Zettl, M. F. Crommie, Y. R. Shen and F. Wang, "Direct observation of a widely tunable bandgap in bilayer graphene", *Nature* **459**, 820 (2009).
- [67] J. Bai, X. Zhong, S. Jiang, Y. Huang and X. Duan, "Graphene nanomesh", *Nature Nanotechnology* **4**, 190194 (2010).
- [68] X. Liang, Y. S. Jung, S. Wu, A. Ismach, D. L. Olynick, S. Cabrini and J. Bokor, "Formation of Bandgap and Subbands in Graphene Nanomeshes with Sub-10 nm Ribbon Width Fabricated via Nanoimprint Lithography", *Nano Lett.* **10**, 24542460 (2010).
- [69] A. Zhang, H. F. Teoh, Z. Dai, Y. P. Feng and C. Zhang, "Band gap engineering in graphene and hexagonal BN antidot lattices: A first principles study", *Appl. Phys. Lett.* **98**, 023105 (2011).
- [70] W. Oswald and Z. Wu, "Energy gaps in graphene nanomeshes", *Phys. Rev. B* **85**, 115431 (2012).
- [71] V. M. Pereira and A. H. Castro Neto, "Tight-binding approach to uniaxial strain in graphene", *Phys. Rev. B* **80**, 045401 (2009).
- [72] W. Yan, W. Y. He, Z. D. Chu, M. Liu, L. Meng, R. F. Dou, Y. Zhang, Z. Liu, J. C. Nie and L. He, "Strain and curvature induced evolution of electronic band structures in twisted graphene bilayer", *Nature Communications* **4**, 2159 (2013). and Y. R. Li, "Observation of tunable electrical bandgap in large-area

- twisted bilayer graphene synthesized by chemical vapor deposition”, *Scientific Reports* **5**, 15285 (2015).
- [73] V. H. Nguyen, H. V. Nguyen, J. Saint-Martin and P. Dollfus, ”Strain-induced conduction gap in vertical devices made of misoriented graphene layers”, *Nanotechnology* **26**, 115201 (2015).
- [74] F. Symalla, S. Shallcross, I. Beljakov, K. Fink, W. Wenzel and V. Meded, ”Band-gap engineering with a twist: Formation of intercalant superlattices in twisted graphene bilayers”, *Phys. Rev. B* **91**, 205412 (2015).
- [75] Z. Liu, L. Song, S. Zhao, J. Huang, L. Ma, J. Zhang, J. Lou and P. M. Ajayan, ”Direct Growth of Graphene/Hexagonal Boron Nitride Stacked Layers”, *Nano Lett.* **11**, 2023 (2011).
- [76] X. D. Li, S. Yu, S. Q. Wu, Y. H. Wen, S. Zhou, and Z. Z. Zhu, ”Structural and Electronic Properties of Superlattice Composed of Graphene and Monolayer MoS_2 ”, *J. Phys. Chem. C* **117**, 15347 (2013).
- [77] A. K. Geim and K. S. Novoselov, ”The rise of graphene”, *Nature Materials* **6**, 183 (2007).
- [78] Y.-M. Lin, C. Dimitrakopoulos, K. A. Jenkins, D. B. Farmer, H.-Y. Chiu, A. Grill and Ph. Avouris, ”100-GHz Transistors from Wafer-Scale Epitaxial Graphene”, *Science* **327**, 662 (2011).
- [79] F. Schwierz, ”Graphene transistors”, *Nature Nanotechnology* **5**, 487 (2010).
- [80] Y. W. Son, M. L. Cohen, and S. G. Louie, ”Energy Gaps in Graphene Nanoribbons”, *Phys. Rev. Lett.* **97**, 216803 (2006).
- [81] H. Raza and E. C. Kan, ”Armchair graphene nanoribbons: Electronic structure and electric-field modulation”, *Phys. Rev. B.* **77**, 245434 (2008).
- [82] D. A. Areshkin, D. Gunlycke, and C. T. White, ”Ballistic Transport in Graphene Nanostrips in the Presence of Disorder: Importance of Edge Effects”, *Nano Lett.* **7**, 204 (2007).
- [83] M. Ezawa, ”Peculiar width dependence of the electronic properties of carbon nanoribbons”, *Phys. Rev. B.* **73**, 045432 (2006).

- [84] K. Nakada, M. Fujita, G. Dresselhaus, and M. S. Dresselhaus, "Edge state in graphene ribbons: Nanometer size effect and edge shape dependence", *Phys. Rev. B* **54**, 17954 (1996).
- [85] L. Yang, C. H. Park, Y. W. Son, M. L. Cohen, and S. G. Louie, "Quasiparticle Energies and Band Gaps in Graphene Nanoribbons", *Phys. Rev. Lett.* **99**, 186801 (2007).
- [86] D. Querlioz, Y. Apertet, A. Valentin, K. Huet, A. Bournel, S. Galdin-Retailleau and P. Dollfus, "Suppression of the orientation effects on bandgap in graphene nanoribbons in the presence of edge disorder", *Appl. Phys. Lett.* **92**, 042108 (2008).
- [87] E. R. Mucciolo, A. H. Castro Neto, and C. H. Lewenkopf, "Conductance quantization and transport gaps in disordered graphene nanoribbons", *Phys. Rev. B* **79**, 075407 (2009).
- [88] E. McCann "Asymmetry gap in the electronic band structure of bilayer graphene", *Phys. Rev. B* **74**, 161403 (2006).
- [89] J. Yang, M. Ma, L. Li, Y. Zhang, W. Huang and X. Dong, "Graphene nanomesh: new versatile materials", *Nanoscale* **6**, 13301 (2014).
- [90] M. Kim, N. S. Safron, E. Han, M. S. Arnold and P. Gopalan, "Fabrication and Characterization of Large-Area, Semiconducting Nanoperforated Graphene Materials", *Nano Lett.* **10**, 11251131 (2010).
- [91] A. Sinitskii and J. M. Tour, "Patterning Graphene through the Self-Assembled Templates: Toward Periodic Two-Dimensional Graphene Nanostructures with Semiconductor Properties", *J. Am. Chem. Soc.* **132**, 1473014732 (2010).
- [92] S. Berrada, V. H. Nguyen, D. Querlioz, J. Saint-Martin, A. Alarcon, C. Chassat, A. Bournel and P. Dollfus, "Graphene nanomesh transistor with high on/off ratio and good saturation behavior", *Appl. Phys. Lett.* **103**, 183509 (2013).
- [93] T. G. Pedersen, C. Flindt, J. Pedersen, N. A. Mortensen, A. P. Jauho, and K. Pedersen, "Graphene Antidot Lattices: Designed Defects and Spin Qubits", *Phys. Rev. Lett.* **100**, 189905 (2008).
- [94] W. Liu, Z. F. Wang, Q. W. Shi, J. Yang, and F. Liu, "Band-gap scaling of graphene nanohole superlattices", *Phys. Rev. B* **80**, 233405 (2009).

- [95] H. Jippo, M. Ohfuchi, and C. Kaneta, "Theoretical study on electron transport properties of graphene sheets with two- and one-dimensional periodic nanoholes", *Phys. Rev. B* **84**, 075467 (2011).
- [96] Y. Yana, Q. F. Lianga, H. Zhaob, C. Q. Wuc and B. Lid, "Thermoelectric properties of one-dimensional graphene antidot arrays", *Phys. Lett. A* **376**, 24252429 (2012).
- [97] V Hung Nguyen, F Mazzamuto, J Saint-Martin, A Bournel and P Dollfus, "Graphene nanomesh-based devices exhibiting a strong negative differential conductance effect", *Nanotechnology* **23**, 065201 (2012).
- [98] V. H. Nguyen, M. C. Nguyen, H. V. Nguyen, and P. Dollfus, "Disorder effects on electronic bandgap and transport in graphene-nanomesh-based structures", *J. Appl. Phys.* **113**, 013702 (2013).
- [99] M. Evaldsson, I. V. Zozoulenko, Hengyi Xu and T. Heinzl, "Disorder effects on electronic bandgap and transport in graphene-nanomesh-based structures", *Phys. Rev. B* **78**, 161407 (2008).
- [100] O. L. Blakslee, D. G. Proctor, E. J. Seldin, G. B. Spence¹ and T. Weng, "Elastic Constants of Compression Annealed Pyrolytic Graphite", *J. Appl. Phys.* **41**, 3373 (1970).
- [101] M. C. Nguyen, V. H. Nguyen, H. V. Nguyen and P. Dollfus, "Conduction gap in graphene strain junctions: direction dependence", *Semicond. Sci. Technol.* **29**, 115024 (2014).
- [102] V. H. Nguyen, H. V. Nguyen and P. Dollfus, "Improved performance of graphene transistors by strain engineering", *Nanotechnology* **25**, 165201 (2014).
- [103] Y. Hasegawa, R. Konno, H. Nakano, and M. Kohmoto, "Zero modes of tight-binding electrons on the honeycomb lattice", *Phys. Rev. B* **74**, 033413 (2006).
- [104] M. Huang, H. Yan, T. F. Heinz and J. Hone, "Probing Strain-Induced Electronic Structure Change in Graphene by Raman Spectroscopy", *Nano Lett.* **10**, 4074 (2010).
- [105] Z. H. Ni, T. Yu, Y. H. Lu, Y. Y. Wang, Y. P. Feng and Z. X. Shen, "Uniaxial Strain on Graphene: Raman Spectroscopy Study and Band-Gap Opening", *ACS Nano* **3**, 438 (2009).

- [106] A. L. Kitt, V. M. Pereira, A. K. Swan, and B. B. Goldberg, "Lattice-corrected strain-induced vector potentials in graphene", *Phys. Rev. B* **85**, 115432 (2012).
- [107] F. Schwierz, "Graphene transistors", *Nature Nanotechnology* **5**, 487496 (2010).
- [108] M. Shin, M. Shi, M. Mouis, A. Cros, E. Josse, G. T. Kim, G. Ghibaudo, "In depth characterization of electron transport in 14 nm FD-SOI CMOS devices", *Solid-State Electronics* **112**, 13-18 (2015).
- [109] J. Widiez, T. Poiroux, M. Vinet, M. Mouis, and S. Deleonibus, "Experimental Comparison Between Sub-0.1 μ m Ultrathin SOI Single- and Double-Gate MOS-FETs: Performance and Mobility", *IEEE Transactions on Nanotechnology* **6**, 643-648 (2006).
- [110] C. Sire, F. Ardiaca, S. Lepilliet, J. W. T. Seo, M. C. Hersam, G. Dambrine, H. Happy, and V. Derycke, "Flexible Gigahertz Transistors Derived from Solution-Based Single-Layer Graphene", *Nano Lett.* **12**, 11841188 (2012).
- [111] J. Kedzierski, P. L. Hsu, P. Healey, P. Wyatt, C. Keast, M. Sprinkle, C. Berger, W. de Heer, "Epitaxial graphene transistors on SiC substrates", *IEEE Trans. Electron. Dev.* **55**, 2078-2085 (2008).
- [112] J. Kedzierski, P. L. Hsu, P. Healey, P. Wyatt, C. Keast, M. Sprinkle, C. Berger, W. de Heer, "Graphene-on-Insulator Transistors Made Using C on Ni Chemical-Vapor Deposition", *IEEE Electron Dev. Lett* **30**, 745-747 (2009).
- [113] A. Alarcón, V. H. Nguyen, S. Berrada, D. Querlioz, J. Saint-Martin, A. Bournel, P. Dollfus, "Pseudosaturation and negative differential conductance in graphene field-effect transistors", *IEEE Trans. Electron. Dev.* **60**, 985-991 (2013).
- [114] F. Xia, D. B. Farmer, Y. M. Lin and P. Avouris, "Graphene Field-Effect Transistors with High On/Off Current Ratio and Large Transport Band Gap at Room Temperature", *Nano Lett.* **10**, 715718 (2010).
- [115] J. S. Bunch, S. S. Verbridge, J. S. Alden, A. M. van der Zande, J. M. Parpia, H. G. Craighead and P. L. McEuen, "Impermeable atomic membranes from graphene sheets", *Nano Lett.* **8**, 2458-62 (2008).
- [116] J. Lu, A. C. Neto and K. P. Loh, "Transforming moire blisters into geometric graphene nano-bubbles", *Nature Commun.* **3**, 823 (2012).

- [117] Y. Lu and J. Guo, "Local strain in tunneling transistors based on graphene nanoribbons", *Appl. Phys. Lett.* **91**, 073105 (2010).
- [118] D. A. Bahamon and V. M. Pereira, "Conductance across strain junctions in graphene nanoribbons", *Phys. Rev. B* **88**, 195416 (2013).
- [119] P. Dollfus, V. H. Nguyen, J. Saint-Martin, "Thermoelectric effects in graphene nanostructures", *J Phys Condens Matter* **27**, 133204 (2015).
- [120] H. Zheng, H. J. Liu, X. J. Tan, H. Y. Lv, L. Pan, J. Shi, X. F. Tang, "Enhanced thermoelectric performance of graphene nanoribbons ", *Appl. Phys. Lett.* **100**, 093104 (2012).
- [121] Y. Yokomizo and J. Nakamura, "Giant Seebeck coefficient of the graphene/h-BN superlattices", *Appl. Phys. Lett.* **103**, 113901 (2013).
- [122] H. Karamitaheri, M. Pourfath and R. Faez, H. Kosina, "Geometrical effects on the thermoelectric properties of ballistic graphene antidot lattices", *J. Appl. Phys.* **110**, 054506 (2011).
- [123] F. Mazzamuto, V. H. Nguyen, Y. Apertet, C. Caer, C. Chassat, J. Saint-Martin, and P. Dollfus, "Enhanced thermoelectric properties in graphene nanoribbons by resonant tunneling of electrons", *Phys. Rev. B* **83**, 235426 (2011).
- [124] V. H. Nguyen, M. C. Nguyen, H. V. Nguyen, J. Saint-Martin, and P. Dollfus, "Enhanced thermoelectric figure of merit in vertical graphene junctions ", *Appl. Phys. Lett.* **105**, 133105 (2014).
- [125] S. -H. Lv, S. -B. Feng, and Y. -X. Li, "Thermopower and conductance for a graphene p-n junction", *J. Phys.: Condens. Matter* **24**, 145801 (2012).
- [126] M. Cutler and N. F. Mott, "Observation of Anderson Localization in an Electron Gas", *Phys. Rev.* **181**, 1336 (1969).
- [127] L. D. Hicks and M. S. Dresselhaus, "Effect of quantum-well structures on the thermoelectric figure of merit", *Phys. Rev. B* **47**, 12727 (1993).
- [128] L. D. Hicks, T. C. Harman, X. Sun, and M. S. Dresselhaus, "Experimental study of the effect of quantum-well structures on the thermoelectric figure of merit", *Phys. Rev. B* **53**, R10493 (1996).

- [129] M. G. Xia and S. L. Zhang, "Modulation of specific heat in graphene by uniaxial strain", *Eur. Phys. J. B* **84**, 385 (2011).
- [130] I. B. Akram, B. Yuri, T. K. Jamil, J. K. Yu, A. G. William and R. H. James, "Silicon nanowires as efficient thermoelectric materials", *Nature* **451**, 168171 (2008).
- [131] Y. M. Zuev, W. Chang, and P. Kim, "Thermoelectric and Magnetothermoelectric Transport Measurements of Graphene", *Phys. Rev. Lett.* **102**, 096807 (2009).
- [132] S. G. Nam, D. K. Ki, and H. J. Lee, "Thermoelectric transport of massive Dirac fermions in bilayer graphene", *Phys. Rev. B* **82**, 245416 (2010).
- [133] H. Karamitaheri, M. Pourfath, R. Faez and H. Kosina, "Geometrical effects on the thermoelectric properties of ballistic graphene antidot lattices", *J. Appl. Phys.* **110**, 054506 (2011).
- [134] D. B. Farmer, Y.-M. Lin, A. Afzali-Ardakani, P. Avouris, "Behavior of a chemically doped graphene junction", *Appl. Phys. Lett.* **94**, 213106 (2009).
- [135] J. R. Williams, L. DiCarlo, C. M. Marcus, "Quantum Hall Effect in a Gate-Controlled p-n Junction of Graphene", *Science* **317**, 638 (2007).
- [136] V. H. Nguyen, F. Mazzamuto, J. Saint-Martin, A. Bournel, P. Dollfus, "Giant effect of negative differential conductance in graphene nanoribbon pn heterojunctions", *Appl. Phys. Lett.* **99**, 042105 (2011).
- [137] M. C. Nguyen, V. H. Nguyen, H. V. Nguyen, J. Saint-Martin and P. Dollfus, "Enhanced Seebeck effect in graphene devices by strain and doping engineering", *Physica E* **73**, 207 (2015).
- [138] J. J. Carr, "Microwave and Wireless Communications Technology", (Newnes, pp. 313-314, ISBN 0750697075).
- [139] J. Groszkowski, "Frequency of Self-Oscillations", (Panstwowe Wydawnictwo Naukowe (PWN), pp. 4551. ISBN 1483280306).
- [140] H. Mizuta and T. Tanoue, "The Physics and Applications of Resonant Tunneling Diodes", (Cambridge University Press, Cambridge, 1995).

- [141] Y. Wu, D. B. Farmer, W. Zhu, S. J. Han, C. D. Dimitrakopoulos, A. A. Bol, P. Avouris, and Y.-M. Lin, "Three-Terminal Graphene Negative Differential Resistance Devices", ACS Nano **6**, 2610-2616 (2012).
- [142] P. Sharma, L. S. Bernard, A. Bazigos, A. Magrez, and A. M. Ionescu, "Room-Temperature Negative Differential Resistance in Graphene Field Effect Transistors: Experiments and Theory", ACS Nano **9**, 620-625 (2015).
- [143] A. Alarcón, V. H. Nguyen, S. Berrada, D. Querlioz, J. Saint-Martin, A. Bournel, P. Dollfus, "Pseudosaturation and Negative Differential Conductance in Graphene Field-Effect Transistors", IEEE Trans. Electron Dev. **60**, 985-991 (2013).
- [144] R. Grassi, T. Low, A. Gnudi, and G. Baccarani, "Contact-Induced Negative Differential Resistance in Short-Channel Graphene FETs", IEEE Trans. Electron Dev. **60**, 140-146 (2013).
- [145] D. Dragoman and M. Dragoman, "Negative differential resistance of electrons in graphene barrier", Appl. Phys. Lett. **90**, 143111 (2007).
- [146] V. N. Do, V. H. Nguyen, P. Dollfus and A. Bournel, "Electronic transport and spin-polarization effects of relativisticlike particles in mesoscopic graphene structures", J. Appl. Phys. **104**, 063708 (2008).
- [147] L. Britnell *et al.*, "Resonant tunnelling and negative differential conductance in graphene transistors", Nature Commun. **4**, 1794 (2013).
- [148] A. Mishchenko *et al.*, "Twist-controlled resonant tunnelling in graphene/boron nitride/graphene heterostructures", Nature Nanotechnol. **9**, 808-813 (2014).
- [149] Y. Zhao, Z. Wan, X. Xu, S. R. Patil, U. Hetmaniuk and M. P. Anantram, "Negative Differential Resistance in Boron Nitride Graphene Heterostructures: Physical Mechanisms and Size Scaling Analysis", Scientific Rep. **5**, 10712 (2015)
- [150] G. Fiori, "Negative Differential Resistance in Mono and Bilayer Graphene p-n Junctions", IEEE Electron Device Lett. **32**, 1334-1336 (2011).
- [151] J. Milton Pereira Jr., P. Vasilopoulos and F. M. Peeters, "Graphene-based resonant-tunneling structures", Appl. Phys. Lett. **90**, 132122 (2007).

- [152] Y. Song, H. C. Wu and Y. Guo, "Negative differential resistances in graphene double barrier resonant tunneling diodes", *Appl. Phys. Lett.* **102**, 093118 (2013).
- [153] I. Rodríguez-Vargas, J. Madrigal-Melchor and O. Oubram, "Resonant tunneling through double barrier graphene systems: A comparative study of Klein and non-Klein tunneling structures", *J. Appl. Phys.* **112**, 073711 (2012).
- [154] V. H. Nguyen, F. Mazzamuto, A. Bournel and P. Dollfus, "Resonant tunneling diode based on graphene/h-BN heterostructure", *J. Phys. D: Appl. Phys.* **45**, 325104 (2012).
- [155] G. J. Ferreira, M. N. Leuenberger, D. Loss and J. Carlos Egues, "Low-bias negative differential resistance in graphene nanoribbon superlattices", *Phys. Rev. B* **84**, 125453 (2011).
- [156] H. Ren, Q. X. Li, Y. Luo and J. Yang, "Graphene nanoribbon as a negative differential resistance device", *Appl. Phys. Lett.* **94**, 173110 (2009).
- [157] H. Teong, K. T. Lam, S. B. Khalid and G. Liang, "Shape effects in graphene nanoribbon resonant tunneling diodes: A computational study", *J. Appl. Phys.* **105**, 084317 (2009).
- [158] J. W. González, M. Pacheco, L. Rosales and P. A. Orellana, "Transport properties of graphene quantum dots", *Phys. Rev. B* **83**, 155450 (2011).
- [159] S. Li, C. K. Gan, Y.-W. Son, Y. P. Feng and S. Y. Quek, "Low-bias negative differential resistance effect in armchair graphene nanoribbon junctions", *Appl. Phys. Lett.* **106**, 013302 (2015).
- [160] A. Cresti, G. Grosso and G. P. Parravicini, "Valley-valve effect and even-odd chain parity in p-n graphene junctions", *Phys. Rev. B* **77**, 233402 (2008).
- [161] Z. F. Wang, Q. Li, Q. W. Shi, X. Wang, J. Yang, J. G. Hou and J. Chen, "Chiral selective tunneling induced negative differential resistance in zigzag graphene nanoribbon: A theoretical study", *Appl. Phys. Lett.* **92**, 133114 (2008).
- [162] V. N. Do and P. Dollfus, "Negative differential resistance in zigzag-edge graphene nanoribbon junctions", *J. Appl. Phys.* **107**, 063705 (2010).

- [163] H. Cheraghchi and H. Esmailzade, "A gate-induced switch in zigzag graphene nanoribbons and charging effects", *Nanotechnol.* **21**, 205306 (2010).
- [164] V. H. Nguyen, F. Mazzamuto, J. Saint-Martin, A. Bournel, and P. Dollfus, "Giant effect of negative differential conductance in graphene nanoribbon p-n hetero-junctions", *Appl. Phys. Lett.* **99**, 042105 (2011).
- [165] K. S. Kim¹, Y. Zhao, H. Jang, S. Y. Lee, J. M. Kim, K. S. Kim, J. H. Ahn, P. Kim, J. Y. Choi and B. H. Hong, "Large-scale pattern growth of graphene films for stretchable transparent electrodes", *Nature* **457**, 706 (2009).
- [166] A. Castellanos-Gomez, R. Roldán, E. Cappelluti, M. Buscema, F. Guinea, H. S. J. van der Zant, and G. A. Steele, "Local Strain Engineering in Atomically Thin MoS₂", *Nano Lett.* **13**, 5361 (2013).
- [167] R. Decker, Y. Wang, V. W. Brar, W. Regan, H. Z. Tsai, Q. Wu, W. Gannett, A. Zettl and M. F. Crommie, "Local Strain Engineering in Atomically Thin MoS₂", *Nano Lett.* **11**, 2291 (2011).
- [168] J. Xue, J. Sanchez-Yamagishi, D. Bulmash, P. Jacquod, A. Deshpande, K. Watanabe, T. Taniguchi, P. Jarillo-Herrero and B. J. LeRoy, "Scanning tunnelling microscopy and spectroscopy of ultra-flat graphene on hexagonal boron nitride", *Nature Materials* **10**, 282 (2011).
- [169] P. J. Zomer, S. P. Dash, N. Tombros and B. J. van Wees, "A transfer technique for high mobility graphene devices on commercially available hexagonal boron nitride ", *Appl. Phys. Lett.* **99**, 232 (2011).
- [170] A. S. Mayorov, R. V. Gorbachev, S. V. Morozov, L. Britnell, R. Jalil, L. A. Ponomarenko, P. Blake, K. S. Novoselov, K. Watanabe, T. Taniguchi, and A. K. Geim, "Micrometer-Scale Ballistic Transport in Encapsulated Graphene at Room Temperature", *Nano Lett.* **11**, 2396-2399 (2011).
- [171] J. R. Williams, L. DiCarlo and C. M. Marcus, "Quantum Hall Effect in a Gate-Controlled p-n Junction in Graphene", *Science* **317**, 638 (2007).

List of publications and conferences

Publications

1. **M. Chung Nguyen**, V. Hung Nguyen, H. Viet Nguyen, and P. Dollfus "*Strong negative differential conductance in strained graphene devices*", Journal of Applied Physics **118**, 234306 (2015).
2. **M. Chung Nguyen**, V. Hung Nguyen, H. Viet Nguyen, J. Saint-Martin and P. Dollfus "*Enhanced Seebeck effect in graphene devices by strain and doping engineering*", Physica E **73**, 207212 (2015).
3. V. Hung Nguyen, **M. Chung Nguyen**, H. Viet Nguyen, J. Saint-Martin and P. Dollfus "*Enhanced thermoelectric figure of merit in vertical graphene junctions*", Applied Physics Letters **105**, 133105 (2014).
4. **M. Chung Nguyen**, V. Hung Nguyen, H. Viet Nguyen, and P. Dollfus "*Conduction gap in graphene strain junctions: direction dependence*", Semicond. Sci. Technol. **29**, 115024 (2014).
5. V. Hung Nguyen, **M. Chung Nguyen**, H. Viet Nguyen and P. Dollfus "*Disorder effects on electronic bandgap and transport in graphene-nanomesh-based structures*", Journal of Applied Physics **113**, 013702 (2013).

International conferences with proceedings

1. V. Hung Nguyen, J. Saint-Martin, P. Dollfus, **M. Chung Nguyen**, H. Viet Nguyen "*High thermoelectric figure of merit in vertical devices made of stacked graphene layers*", 20th International Conference on Simulation of Semiconductor Processes and Devices (SISPAD), 20150909–20150911, Washington DC, USA.
2. **M. Chung Nguyen**, H. Viet Nguyen, V. Hung Nguyen, J. Saint-Martin and P. Dollfus "*Strong Negative Differential Resistance in Graphene Devices with Local*

Strain”, 18th International Workshop on Computational Electronics (IWCE 2015), 20150902–20150904, West Lafayette-USA.

3. **M. Chung Nguyen**, V. Hung Nguyen, Huy-Viet Nguyen and P. Dollfus ”*Conduction gap in unstrained/strained graphene junctions: direction dependence*”, 17th International Workshop of Computational Electronics (IWCE 2014), 20140603–20140606, Paris-France.

Others conferences

1. Viet-Hung Nguyen, **Mai-Chung Nguyen**, Jérôme Saint-Martin, Huy-Viet Nguyen, Jean-Christophe Charlie, and Philippe Dollfus, ”*Conduction Gap in Graphene Systems: Strain-Induced Enhancement and Application to Electron Device*”, the 5th International Symposium on Graphene Devices (ISGD-5), Brisbane-Australia.
2. **M. Chung Nguyen**, H. Viet Nguyen, V. Hung Nguyen and P. Dollfus ”*Transport gap in graphene strain heterochannels*”, the 3rd International Workshop on Theoretical and Computational Physics, Dalat-Vietnam.
3. **M. Chung Nguyen**, H. Viet Nguyen, V. Hung Nguyen, J. Saint-Martin and P. Dollfus ”*Enhancement of Seebeck effect in strained graphene PN junctions*”, 19th International Conference on Electron Dynamics in Semiconductors, Optoelectronics and Nanostructures (EDISON19), 20150629–20150702, Salamanca-Spain.
4. **M. Chung Nguyen**, H. Viet Nguyen, V. Hung Nguyen and P. Dollfus ”*Strain engineering to enhance conduction gap and Seebeck effect in graphene devices*”, Journées Nationales du Réseau Doctoral en Micro-nanoelectronique, Bordeaux-France.
5. V. Hung Nguyen, **M. Chung Nguyen**, Huy-Viet Nguyen and P. Dollfus ”*Strain-induced improvement of graphene transistors*”, 17th International Workshop of Computational Electronics (IWCE 2014), 20140603–20140606, Paris-France.
6. **M. Chung Nguyen**, H. Viet Nguyen, V. Hung Nguyen and P. Dollfus ”*Conduction gap in unstrained/strained graphene junctions: direction dependence*”, Journées Nationales du Réseau Doctoral en Micro-nanoelectronique, Lille-France.

Titre: Etude théorique de nanodispositifs électroniques et thermoélectriques à base de jonctions contraintes de graphène

Mots clés: Électroniques et thermoélectriques, nanodispositifs, l'ingénierie de contrainte, jonctions graphène contraint /graphène non contraint, gap de conduction.

Résumé: De par ses extraordinaires propriétés physiques, on s'attend à ce que le graphène devienne un matériau de nouvelle génération, susceptible de compléter les semiconducteurs traditionnels dans les technologies de dispositifs électroniques. Depuis sa découverte expérimentale en 2004, de nombreux travaux ont cherché à en évaluer les potentialités. Toutefois, en vue d'applications en électronique, le graphène souffre d'un inconvénient majeur: l'absence de bande interdite dans sa structure de bandes. Dans ce travail, je me suis focalisée sur une autre approche : l'ingénierie de contrainte, qui offre un large éventail de possibilités pour moduler les propriétés électroniques des nanostructures de graphène. Pour ce travail théorique, tous les calculs ont été faits en utilisant essentiellement deux méthodes: un modèle atomistique de Hamiltonien de liaisons fortes pour décrire les propriétés électroniques du matériau et l'approche des fonctions de Green hors-équilibre pour le calcul du transport quantique.

En fait, une contrainte d'amplitude supérieure à 23% est nécessaire pour ouvrir un gap dans la structure de bande du graphène. Mais je montre qu'avec une contrainte de quelques pourcents, le décalage du point de dirac induit par la contrainte peut suffire à ouvrir un gap de conduction très significatif (500 meV ou plus) dans des hétérostructures de graphène constituées de jonctions graphène contraint / graphène non contraint, alors que chacun des matériaux reste semi-métallique.

Après l'analyse détaillée de cette propriété en fonction de l'amplitude de la contrainte, de sa direction et de la direction du transport, j'exploite cet effet dans des jonctions appropriées pour améliorer le comportement et les performances de différents types de dispositifs. En particulier, je montre qu'avec une contrainte de seulement 5% il est possible de couper efficacement le courant dans les transistors, de sorte que le rapport ON/OFF peut atteindre 10^5 , ce qui constitue une très forte amélioration par rapport aux transistors de graphène pristine où ce rapport ne peut pas excéder 10. Puis, nous montrons qu'en combinant ingénieries de contrainte et de dopage dans de telles jonctions, le coefficient Seebeck peut atteindre des valeurs aussi fortes que 1.4 mV/K, ce qui est 17 fois plus élevé que dans le graphène sans gap. Cela peut contribuer à faire du graphène un excellent matériau thermoélectrique. Enfin, j'ai étudié l'effet de conductance différentielle négative (CDE) dans des diodes de graphène, constituées soit d'une simple-barrière contrainte contrôlée par une grille, soit d'une jonction PN. Je montre qu'une ingénierie de contrainte appropriée peut induire de forts effets de CDE, avec un rapport pic/vallée de quelques centaines à température ambiante.



Title: Theoretical study of electronic and thermoelectronic nanodevices based on strained graphene junctions

Keywords: Electronic and thermoelectronic, nanodevices, strain engineering, unstrained/strained graphene junctions, conduction gap.

Abstract : Due to its outstanding physical properties, graphene is expected to become a new generation material, able to replace or complement traditional semiconductors in device technology. Hence, many studies have been led to explore the potential of this material immediately after the successful fabrication of a single layer of graphene in 2004. However, applications of graphene in electronic devices are still questionable due to the gapless character of this material. In this work, we focus on strain engineering, which offers a wide range of opportunities for modulating the electronic properties of graphene nanostructures. For this theoretical work, all calculations were performed using essentially two main methods, i.e., an atomistic tight binding Hamiltonian model to describe the electronic structure and the non-equilibrium Green's function approach of quantum transport. The main aim is to analyze in details the strain effects in graphene and to provide strategies of strain engineering to improve the performance of both electronic (transistors and diodes) and thermoelectric devices.

After analyzing in details this property according the amplitude and direction of strain and the direction of transport, we exploit this effect using appropriate strain junctions to improve the behavior and performance of several types of devices. In particular, we show that with a strain of only 5%, it is possible to switch-off transistors efficiently, so that the ON/OFF current ratio can reach 10^5 , which is a strong improvement with respect to pristine graphene transistors where this ratio cannot exceed 10. Then we show that by combining strain and doping engineering in such strain junctions the Seebeck coefficient can reach values higher than 1.4 mV/K, which is 17 times higher than in gapless pristine graphene. It can contribute to make graphene an excellent thermoelectric material. Finally, we study the effect of negative differential conductance (NDC) in graphene diodes made of either as single gate-induced strained barrier or a p-n junction. We show that appropriate strain engineering in these devices can lead to very strong NDC effects with peak-to-valley ratios of a few hundred at room temperature.

Actually, if uniformly applied, a strain of large amplitude ($> 23\%$) is required to open a bandgap in the band structure of graphene. However, we show that with a strain of only a few percent, the strain-induced shift of the Dirac point in k-space may be enough to open a sizable conduction gap (500 meV or more) in graphene heterojunctions made of unstrained/strained junctions, though the strained material remains gapless.

